FATIGUE TEST OF A THREE-SPAN COMPOSITE HIGHWAY BRIDGE STUDY 73-1

Prepared for

MISSOURI STATE HIGHWAY DEPARTMENT

by

JAMES W. BALDWIN, JR.

HAROLD J. SALANE

ROGER C. DUFFIELD

DEPARTMENT OF CIVIL ENGINEERING

UNIVERSITY OF MISSOURI-COLUMBIA

COLUMBIA, MISSOURI

June 1978

in cooperation with

U.S. DEPARTMENT OF TRANSPORTATION

FEDERAL HIGHWAY ADMINISTRATION

The opinions, findings, and conclusions in this publication are not necessarily those of the Department of Transportation, Federal Highway Administration. This report does not constitute a standard, Specification, or Regulation.

ABSTRACT

A three-span continuous composite bridge of modern design was field tested under fatigue loading which produced stresses equal to or greater than design stresses. Both the primary fatigue loading and loading for dynamic-property tests were imposed by a moving-mass closed-loop electrohydraulic-actuator system. During the fatigue loading the bridge was inspected periodically by eight different inspection methods. Inspection methods included visual, ultrasonic, radiographic, acoustic emission, and dynamic-signature techniques.

Ultrasonic inspection was the most reliable and in the regions which were inspected regularly, no cracks are known to have grown to a length greater than 1.5 inches before detection. Radiography was nearly as reliable as ultrasonic inspection where it could be used, but more than half of the material to be inspected was inaccessible to radiography.

Stiffness coefficients were calculated from the experimental mode shapes on the basis of a multi degree of freedom system with modified coupling. Mechanical impedance plots were made from frequency sweep tests which included five resonant modes. Changes in the bridge stiffness and vibration signatures in the form of mechanical impedance plots were indicators of structural deterioration due to the fatigue. The average reduction in stiffness due to a combination of deck deterioration and steel girder cracking was approximately 20%.

A total of 18 fatigue cracks developed at the ends of welded cover plates and two fatigue cracks developed in base metal which was not adjacent to welds. At 471,000 cycles of loading, these cracks had propagated far enough to completely sever the girder flanges at five different sections. The fatigue life in regions where the stress range was 22.5 ksi was considerably longer than would be predicted on the basis of current code requirements. However, the fatigue life in other regions where the stress range was only 8.7 ksi was considerably shorter than would be predicted on the basis of current code requirements.

ACKNOWLEDGEMENTS

A research project of this magnitude cannot be conducted without the cooperation of many organizations and their personnel. The authors are deeply indebted to everyone who aided them in this investigation.

Special gratitude must be expressed to the Army Corps of Engineers, Memphis District, for providing the bridge and the site preparation. Sincere thanks are due Mr. Lionel T. Murray, District Engineer, and Mr. C. P. Bennett, District Maintenance Engineer, of the 10th Missouri Highway District for their help and cooperation during the field test.

The authors are grateful to the Federal Highway Administration (FHWA) for the loan of data acquisition equipment and for providing the able assistance of Mr. Harry Latz, Engineering Technician. We would also like to express a sincere appreciation to our own technicians, Messrs. Delbert Morton, William Ballard, and Donald Ausburn, for their valuable help with this project.

Nielsen Engineering and Research, Inc. and their Research Engineer, Robert E. Reed are owed a special acknowledgment for their aid and cooperation with the Randomdec portion of the study.

Finally, the authors wish to extend special recognition to the following graduate assistants for both the research reported and the authorship of appendicies:

Robert K. Brady, Research Assistant in Mechanical and Aerospace Engineering - Appendices A and D

Ivan E. Lindner, Research Assistant in Civil Engineering - Appendix B

Stanley T. Samborski, III, Research Assistant in Civil Engineering - Appendices C and G.

TABLE OF CONTENTS

CHAPTER		PAGE
	ABSTRACT	ii
	ACKNOWLEDGEMENTS	iv
	LIST OF FIGURES	ix
	LIST OF TABLES	xvi
1.	INTRODUCTION	1
	1.1 PREFACE	1
	1.2 PURPOSE AND SCOPE	4
	1.3 DESCRIPTION OF TEST BRIDGE	5
	1.4 DESCRIPTION OF FIELD TEST	7
	1.4.1 Fatigue Loading	8
	1.4.2 Crack Detection Techniques	12
2.	SUMMARY, CONCLUSIONS AND RECOMMENDATIONS	19
	2.1 RESPONSE	19
	2.2 FATIGUE	20
	2.3 FATIGUE CRACK DETECTION	21
	2.3.1 Ultrasonic Inspection	21
	2.3.2 Visual Inspection	22
	2.3.3 Radiography	22
	2.3.4 Dynamic Properties - Equivalent Single Degree of Freedom Analysis	22
	2.3.5 Dynamic Properties Multi Degree-of-Freedom Damping	23
	2.3.6 Dynamic Properties - Multi Degree-of-Freedom Stiffness	23
	2.3.7 Mechanical Impedance	23
	2.3.8 Randomdec	24
	2.3.9 Acoustic Emission	24
	2.4 RECOMMENDATIONS	24
	2.4.1 Composite Action	24
	2.4.2 Stenciling	25
	2.4.3 Fatigue Stresses	25
	2.4.4 Detection Methods	26
3.	BEHAVIOR UNDER FATIGUE LOADING	27
	3.1 DYNAMIC RESPONSE	27
	3.2 COMPOSITE ACTION	34
	3.3 CONCRETE DECK	41
	3.4 STEEL GIRDERS	44
	3.5 SUPPORTING STRUCTURE	52

CHAPTER PAGE

4. CRACK DETECTION METHODS 56

4.1 ULTRASONICS. 56
4.2 DYE PENETRANT. 61
4.3 RADIOGRAPHY. 62
4.4 ACOUSTIC EMISSION. 64
4.5 RANDOMDEC. 68
4.6 FHWA ACOUSTIC AND MAGNETIC CRACK DETECTOR UNITS. . 71
4.7 DAMPING RATIOS, RESONANT FREQUENCIES AND VIBRATION SIGNATURES 73
4.8 MULTI DEGREE-OF-FREEDOM. 82

ADDENDUM 89

REFERENCES 95

APPENDIX A SINGLE DEGREE OF FREEDOM DYNAMIC PROPERTIES. . . A 1
A.1 ANALYSIS TECHNIQUES AND EXPERIMENTAL PROCEDURES. . A 1
A.1.1 Transient Vibration Test. . . . . A 1
A.1.1.1 The Logarithmic Decrement Method . . A 1
A.1.1.2 Transform Decay Method . . . . . A 4
A.1.1.3 Experimental Procedures for the Transient Test . . . . . A 8
A.1.2 Frequency Response Generation Test. . . . . A 8
A.1.2.1 Dynamic Properties . . . . . A 8
A.1.2.2 Experimental Procedure for the Frequency Response Curve Generation Test . . . . . A 10
A.1.3 Sweep Test. . . . . A 12
A.1.3.1 Introduction . . . . . A 12
A.1.3.2 Mechanical Impedance . . . . . A 13
A.1.3.3 Experimental Procedure for the Sweep Test . . . . . A 16

A.1.4 Peak Amplitude Method . . . . . A

A.2 EXPERIMENTAL RESULTS . . . . . A 17
A.2.1 Transient Response. . . . . A 17
A.2.1.1 Damping Ratio Results (Logarithmic Decrement). . . . . A 18
A.2.1.2 Damping Ratio Results (Fourier Transform Decay Method). . . . . A 25
A.2.2 Results Based on the Frequency Response Curves . . . . . A 27
A.2.3 Results from the Sweep Test . . . . . A 33
A.2.4 Discussion of Experimental Results. . . . . A 44

REFERENCES. . . . . A 45

CHAPTER PAGE

APPENDIX B MULTI-DEGREE OF FREEDOM DYNAMIC PROPERTIES . . . B 1
B.1 INTRODUCTION AND PROBLEM STATEMENT . . . . . B 1
B.2 PROCEDURE . . . . . B 1
B.3 DESCRIPTION OF NORMAL MODE DYNAMIC TESTS . . . . . B 2
B.3.1 General. . . . . B 2
B.4 PRELIMINARY ANALYSES. . . . . B 3
B.4.1 General. . . . . B 3
B.4.2 Bridge Properties. . . . . B 5
B.5 COMPARISON OF PREDICTED AND EXPERIMENTAL RESULTS. . B 6
B.5.1 General. . . . . B 6
B.5.2 Tabulation of Experimental Results . . . . . B 6
B.5.3 Tabulation of Comparisons. . . . . B 9
B.6 RESULTS OF DYNAMIC ANALYSIS . . . . . B 9
B.6.1 General. . . . . B 9
B.6.2 Study of Data. . . . . B 16
B.6.2.1 Raw Data. . . . . B 16
B.6.2.2 Spectral Analysis . . . . . B 17
B.6.2.3 Mode Shapes . . . . . B 29
B.6.3 Dynamic Properties . . . . . B 39
B.6.3.1 Damping Ratio . . . . . B 39
B.6.3.2 Stiffness Matrix. . . . . B 40
B.6.3.3 Damping Matrix. . . . . B 51

REFERENCES . . . . . B 54

APPENDIX C ULTRASONICS . . . . . C 1
C.1 INTRODUCTION. . . . . C 1
C.2 TYPE OF EQUIPMENT . . . . . C 1
C.2.1 Scope. . . . . C 2
C.2.2 Probes . . . . . C 2
C.3 MECHANICS OF SOUND WAVES. . . . . C 5
C.3.1 Piezo-electric Effect. . . . . C 5
C.3.2 Reflection and Refraction. . . . . C 5
C.3.3 Skip Distance. . . . . C 7
C.3.4 Attenuation. . . . . C 8
C.3.5 Minimum Detectable Flaw. . . . . C 9
C.3.6 Ultrasonic Couplant. . . . . C 9
C.4 INSPECTION FOR FATIGUE CRACKS . . . . . C 12
C.4.1 Calibration of the Angle Probes. . . . . C 12
C.4.2 Calibration of the Split-Crystal Normal Probe . . . . . C 13
C.4.3 Technique... . . . . C 13
C.4.4 Limitations. . . . . C 17
C.5 PRESENTATION OF FIELD DATA. . . . . C 19
C.5.1 Introduction . . . . . C 19
C.5.2 Location of Fatigue Cracking in Bottom Critical Sections. . . . . C 23
C.5.3 Location of Fatigue Cracks in Top Critical Sections. . . . . C 27
C.5.4 Additional Fatigue Cracking. . . . . C 35
C.5.5 Ultrasonic Flaw Size vs. Actual Flaw Size. . C 35

REFERENCES. . . . . C 39

CHAPTER PAGE

APPENDIX D EXPERIMENTAL SETUP . . . . . D 1
D.1 INTRODUCTION. . . . . D 1
D.2 VIBRATIONAL EXCITATION SYSTEM . . . . . D 1
D.2.1 Ballast. . . . . D 3
D.2.2 Moving Weights . . . . . D 3
D.2.3 Hydraulic and Electronic Control Systems . . D 3
D.3 TRANSDUCERS. . . . . D 6
D.3.1 Accelerometers . . . . . D 6
D.3.2 Deflection Gauges. . . . . D 7
D.3.3 Strain Gauges. . . . . D 7
D.3.4 LVDT. . . . . D 9
D.3.5 DC Differential Transformer. . . . . D 9
D.4 ELECTRONIC DATA ACQUISITION SYSTEMS . . . . . D 9
D.4.1 Signal Conditioning System . . . . . D 12
D.4.1.1 Accelerometer System. . . . . D 12
D.4.1.2 Deflection and Strain Gauges. . . . D 12
D.4.1.3 LVDT. . . . . D 16
D.4.1.4 DCDT. . . . . D 16
D.4.2 Data Recording Equipment . . . . . D 16
D.4.2.1 Digital Recording System. . . . . D 16
D.4.2.2 Oscillograph. . . . . D 18
D.4.3 Resonant Monitoring . . . . . D 19

APPENDIX E ACOUSTIC EMISSION . . . . . E 1
E.1 INTRODUCTION. . . . . E 1
E.2 EXPERIMENTAL PROCEDURE. . . . . E 2
E.3 RESULTS . . . . . E 9
E.4 DISCUSSION OF RESULTS . . . . . E 10

REFERENCES. . . . . E 12

APPENDIX F COMPOSITE COMPUTATION . . . . . F 1
F.1 INTRODUCTION. . . . . F 1
F.2 ANALYSIS. . . . . F 1
F.3 RESULTS . . . . . F 7

APPENDIX G A FATIGUE ANALYSIS OF FIELD DATA. . . . . G 1
G.1 INTRODUCTION. . . . . G 1
G.2 APPLIED STRESSES AT CRITICAL SECTIONS . . . . . G 4
G.2.1 Loading at Critical Sections . . . . . G 4
G.2.2 Residual Tensile Stress. . . . . G 12
G.3 CORRELATION OF TEST RESULTS WITH PRIOR STUDIES. . G 13

REFERENCES. . . . . G 17

LIST OF FIGURES

FIGURE		PAGE
1-1	TEST BRIDGE.	3
1-2	ELEVATION AND SECTION VIEWS OF TEST BRIDGE	6
1-3	PHYSICAL LAYOUT OF TEST SITE	7
1-4	HYDRAULIC ACTUATOR AND LOAD DISTRIBUTION FRAME . . .	9
1-5	LOCATION OF BALLAST AND HYDRAULIC ACTUATOR	10
1-6	LOCATION OF STRAIN GAUGES ON BRIDGE.	11
1-7	DEFLECTION GAUGE LOCATIONS ON BRIDGE	13
1-8	ACCELEROMETER STATIONS ON BRIDGE	18
3-1	DYNAMIC STRAINS AT SECTION 2.2A vs. FATIGUE CYCLES .	28
3-2	DYNAMIC STRAINS AT SECTION 2.2B vs. FATIGUE CYCLES .	29
3-3	DYNAMIC STRAINS AT SECTION 4.1B vs. FATIGUE CYCLES .	30
3-4	DYNAMIC STRAINS AT SECTION 4.1B vs. FATIGUE CYCLES .	31
3-5	DYNAMIC STRAINS AT SECTION 6.2A vs. FATIGUE CYCLES .	32
3-6	DYNAMIC STRAINS AT SECTION 6.2B vs. FATIGUE CYCLES .	33
3-7	MID-CENTER SPAN DEFLECTION OF NORTH AND SOUTH EXTERIOR GIRDERS vs. NUMBER OF FATIGUE CYCLES. . . .	35
3-8		
3-8	AVERAGE MIDSPAN DEFLECTION vs. NUMBER OF FATIGUE CYCLES	36
3-9	DAMPING RATIO vs. NUMBER OF FATIGUE CYCLES	37
3-10A	BRIDGE DECK CRACKING	43
3-10B	BRIDGE DECK CRACKING	43
3-11	CRUSHING IN CONCRETE CURB.	44
3-12	CRACK INITIATION AT HEEL OF WELD	46

FIGURE		PAGE
3-13	CRACK PROPAGATION.	47
3-14	CROSS SECTION SHOWING TWO FATIGUE CRACKS	47
3-15	TOP CRITICAL SECTION DETAIL.	50
3-16	FATIGUE CRACK INITIATED BY HEAT NUMBER STAMP	51
3-17	SOIL LOG DATA.	53
4-1	ULTRASONIC INSPECTION OF TOP FLANGE.	60
4-2	LOCATIONS AND NUMBERING SCHEME FOR ACOUSTIC EMISSION SENSORS	65
4-3	ACOUSTIC EMISSION AMPLITUDE COUNT DURING BRIDGE FATIGUE TEST.	67
4-4	TRANSDUCER STATIONS.	69
4-5	MECHANICAL IMPEDANCE, STATION 15, TEST 1 AND 2 . . .	79
4-6	MECHANICAL IMPEDANCE, STATION 15, TEST 2 AND 3 . . .	80
4-7	MECHANICAL IMPEDANCE, STATION 15, TEST 3 AND 4 . . .	81
4-8	SPECTRUM OF RESPONSE - B13	86
4-9	MODE SHAPE - B23	87
4-10	CHANGES IN STIFFNESS AND DAMPING, 22 DOF MODEL . . .	88
5-1	FATIGUE FAILURE OF SHEAR CONNECTOR	91
5-2	FATIGUE CRACK IN SHEAR CONNECTOR	91
5-3	DYE PENETRANT CRACK DETECTION AT SECTION 2.2A . . .	92
5-4	DYE PENETRANT CRACK DETECTION AT SECTION 2.3A . . .	92
5-5	DYE PENETRANT CRACK DETECTION AT SECTION 6.1A . . .	93
5-6	FAILURE AT SECTION 2.1A	93
5-7	FAILURE AT SECTION 2.2A	94

FIGURE		PAGE
A-1	ACCELERATION RESPONSE FOR TRANSIENT VIBRATIONS . . .	A 3
A-2	SEMI-LOG PLOT OF RELATIVE ACCELERATION vs. CYCLES OF TRANSIENT VIBRATION	A 3
A-3	PLOT OF FOURIER TRANSFORM OF A TRANSIENT RESPONSE. .	A 7
A-4	FREQUENCY RESPONSE CURVE OF LINEAR SYSTEM.	A 11
A-5	TYPICAL MECHANICAL IMPEDANCE PLOT.	A 15
A-6	DAMPING RATIO, ζ, vs. NUMBER OF FREE VIBRATION CYCLES FOR FIRST BENDING MODE, POSITIVE PEAKS, STATION 17, TESTS 1 AND 2.	A 19
A-7	DAMPING RATIO, ζ, vs. NUMBER OF FREE VIBRATION CYCLES FOR FIRST TORSIONAL, POSITIVE PEAKS, STATION 16, TESTS 1 AND 2.	A 20
A-8	DAMPING RATIO, ζ, vs. NUMBER OF FREE VIBRATION CYCLES FOR SECOND BENDING MODE, POSITIVE PEAKS, STATION 5, TESTS 1 AND 2	A 21
A-9	FREQUENCY RESPONSE CURVE, STATION 17, B11.	A 28
A-10	FREQUENCY RESPONSE CURVE, STATION 17, B13.	A 29
A-11	FREQUENCY RESPONSE CURVE, STATION 17, B14.	A 30
A-12	MECHANICAL IMPEDANCE, STATION 4, TESTS 1 AND 2 . . .	A 34
A-13	MECHANICAL IMPEDANCE, STATION 4, TESTS 2 AND 3 . . .	A 35
A-14	MECHANICAL IMPEDANCE, STATION 4, TESTS 3 AND 4 . . .	A 36
A-15	MECHANICAL IMPEDANCE, STATION 9, TESTS 1 AND 2 . . .	A 37
A-16	MECHANICAL IMPEDANCE, STATION 9, TESTS 2 AND 3 . . .	A 38
A-17	MECHANICAL IMPEDANCE, STATION 9, TESTS 3 AND 4 . . .	A 39
A-18	MECHANICAL IMPEDANCE, STATION 30, TESTS 1 AND 2. . .	A 40
A-19	MECHANICAL IMPEDANCE, STATION 30, TESTS 2 AND 3. . .	A 41
A-20	MECHANICAL IMPEDANCE, STATION 30, TESTS 3 AND 4. . .	A 42

FIGURE		PAGE
B-1	MODE SHAPES.	B 4
B-2a	PLOT OF RAW DATA - B11	B 18
B-2b	PLOT OF RAW DATA - B13	B 19
B-2c	PLOT OF RAW DATA - B14	B 20
B-2d	PLOT OF RAW DATA - T14	B 21
B-2e	PLOT OF RAW DATA - B24	B 22
B-3a	SPECTRUM OF RESPONSE - B11	B 23
B-3b	SPECTRUM OF RESPONSE - B13	B 24
B-3c	SPECTRUM OF RESPONSE - B14	B 25
B-3d	SPECTRUM OF RESPONSE - T14	B 26
B-3e	SPECTRUM OF RESPONSE - B24	B 27
B-4	SPECTRUM OF EXCITING FORCE - B11	B 28
B-5a	MODE SHAPE - B11	B 30
B-5b	MODE SHAPE - B13	B 31
B-5c	MODE SHAPE - B14	B 32
B-5d	MODE SHAPE - T11	B 33
B-5e	MODE SHAPE - T13	B 34
B-5f	MODE SHAPE - T14	B 35
B-5g	MODE SHAPE - B21	B 36
B-5h	MODE SHAPE - B23	B 37
B-5i	MODE SHAPE - B24	B 38
B-6a	MODE SHAPE - RESPONSE vs. (SOUTH SIDE ONLY) - B11. .	B 41
B-6b	MODE SHAPE - RESPONSE vs. (SOUTH SIDE ONLY) - B13. .	B 42
B-6c	MODE SHAPE - RESPONSE vs. (SOUTH SIDE ONLY) - B14. .	B 43
B-6d	MODE SHAPE - RESPONSE vs. (SOUTH SIDE ONLY) - T11. .	B 44

FIGURE		PAGE
B-6e	MODE SHAPE - RESPONSE vs. (SOUTH SIDE ONLY) - T13 .	B 45
B-6f	MODE SHAPE - RESPONSE vs. (SOUTH SIDE ONLY) - T14 .	B 46
B-7	COUPLING FOR 22 DOF	B 47
B-8	NONZERO COEFFICIENT OF 22 DOF MATRIX	B 47
B-9	CHANGES IN DIAGONAL COEFFICIENTS OF STIFFNESS MATRIX - 22 DOF	B 49
B-10	COUPLING FOR SIX DOF	B 50
B-11	CHANGE IN DIAGONAL COEFFICIENTS OF DAMPING MATRIX - 22 DOF	B 53
C-1	DIAGRAM OF PULSE-ECHO A-SCAN EQUIPMENT	C 3
C-2	SPLIT CRYSTAL NORMAL PROBE	C 4
C-3	ANGLE PROBE	C 4
C-4	GRAPHICAL REPRESENTATION OF SNELL'S LAW	C 7
C-5	ANGLE PROBE BEAM PATH AND SKIP DISTANCE IN TEST MATERIAL	C 8
C-6	COMPONENTS OF BEAM PATH (SECTION A-A)	C 10
C-6 (cont)	COMPONENTS OF BEAM PATH (SECTION A-A)	C 11
C-7	ANGLE PROBE CALIBRATION	C 12
C-8	STEPPED CALIBRATION BLOCK	C 13
C-9	SCAN AREA FOR 45° ANGLE PROBE	C 15
C-10	SCAN AREA FOR 70° ANGLE PROBE	C 16
C-11	SOUND PATH WHEN EXAMINING FROM HEEL SIDE OF FILLET WELD.	C 18
C-12	SUSPECTED FLAW ORIGIN IN TOP CRITICAL SECTIONS. . .	C 20
C-13	SOUND PATH AFTER INITIAL FILLET WELD-COVER PLATE SEPARATION.	C 24
C-14	EARLY CRACK GROWTH IN TRANSVERSE FILLET WELD. . . .	C 25
C-15	CRACK AT JUNCTION OF FILLET WELD AND COVER PLATE, SECTION 6.1B	C 25

FIGURE		PAGE
C-16	ADVANCED CRACK GROWTH IN FILLET WELD	C 26
C-17	FILLET WELD CRACK ALONG TAPERED PORTION OF COVER PLATE, SECTION 6.1B	C 26
C-18	SECTION 2.2B AT 337,500 CYCLES	C 28
C-19	SECTION 2.2B AT CONCLUSION OF FATIGUE TEST	C 28
C-20	SECTION 6.1B AT 321,000 CYCLES	C 29
C-21	SECTION 6.1B AT 337,500 CYCLES	C 29
C-22	SECTION 6.1B AT 402,000 CYCLES	C 30
C-23	SECTION 6.1B AT CONCLUSION OF FATIGUE TEST.	C 30
C-24	SECTION 6.2B AT 337,500 CYCLES.	C 31
C-25	SECTION 6.2B AT 402,000 CYCLES.	C 31
C-26	SECTION 6.2B AT CONCLUSION OF FATIGUE TEST.	C 33
C-27	FATIGUE CRACKING AT SECTION 6.2A.	C 34
C-28	FATIGUE CRACKING AT SECTION 2.1A.	C 34
C-29	FATIGUE CRACK INITIATION AT SECTION 4.2B.	C 36
C-30	FATIGUE CRACK INITIATION 36 INCHES WEST OF SECTION 4.2B.	C 36
D-1	HYDRAULIC ACTUATOR AND LOAD DISTRIBUTION FRAME	D 2
D-2	SCHEMATIC OF VIBRATION EXCITATION SYSTEM DURING FATIGUE TEST	D 4
D-3	SCHEMATIC OF VIBRATION EXCITATION SYSTEM USED DURING DYNAMIC TESTS.	D 5
D-4	DEFLECTION GAUGE INSTALLATION	D 8
D-5	LOCATION OF DCDT'S ON BRIDGE.	D 10
D-6	ATTACHMENT OF DCDT TO BRIDGE.	D 10
D-7	DATA ACQUISITION SYSTEM	D 11
D-8	DATA ACQUISITION SYSTEM SCHEMATIC FOR ACCELEROMETERS DURING SWEEP TEST.	D 13

FIGURE		PAGE
D-9	DATA ACQUISITION SYSTEM SCHEMATIC FOR DYNAMIC TESTS	D 14
D-10	DATA ACQUISITION SYSTEM SCHEMATIC FOR STRAIN AND DEFLECTION GAUGES	D 15
D-11	FHWA SIGNAL CONDITIONING AND DIGITAL RECORDING SYSTEMS	D 17
D-12	RESONANCE MONITORING SYSTEM	D 20
E-1	BLOCK DIAGRAM OF ACOUSTIC EMISSION SETUP	E 3
E-2a	ACOUSTIC EMISSION AMPLITUDE COUNT DURING FATIGUE TEST.	E 5
E-2b	ACOUSTIC EMISSION AMPLITUDE COUNT DURING FATIGUE TEST.	E 6
E-2c	ACOUSTIC EMISSION AMPLITUDE COUNT DURING FATIGUE TEST.	E 7
E-2d	ACOUSTIC EMISSION AMPLITUDE COUNT DURING FATIGUE TEST.	E 8
F-1	MOMENT COMPONENTS	F 3
G-1	ELLIPTICAL FATIGUE CRACK.	G 2
G-2	CLOSE UP OF FRACTURE SURFACE, SECTION 2.2B.	G 2
G-3	BEACH MARKS, SECTION 2.2B	G 3
G-4	BEACH MARKS, SECTION 6.1B	G 3
G-5	FATIGUE STRESS AT SECTION 2.1A.	G 5
G-6	FATIGUE STRESS AT SECTION 2.2B.	G 6
G-7	FATIGUE STRESS AT SECTION 6.1B.	G 7
G-8	FATIGUE STRESS AT SECTION 6.2A.	G 8
G-9	FATIGUE STRESS AT SECTION 6.2B.	G 9
G-10	FATIGUE STRENGTH OF END WELDED COVER PLATES	G 14
G-11	TOP CRITICAL SECTION DETAIL	G 16

LIST OF TABLES

TABLE		PAGE
3-1	MOMENTS OF INERTIA.	39
3-2	PILE LOADS DURING FATIGUE TEST.	55
4-1	COMPARISON OF DAMPING RATIO'S AS OBTAINED FROM FOUR DIFFERENT CALCULATING METHODS.	74
4-2	EXPERIMENTAL RESONANT FREQUENCIES	77
4-3	PREDICTED AND MEASURED FREQUENCIES.	B4
A-1	EXPERIMENTAL DAMPING RATIOS BASED ON LOGARITHMIC DECREMENT METHOD (DETERMINED FROM POSITIVE PEAK). . .	A 23
A-1	EXPERIMENTAL DAMPING RATIOS BASED ON LOGARITHMIC DECREMENT METHOD (DETERMINED FROM NEGATIVE PEAKS. . .	A 24
A-2	EXPERIMENTAL VISCOUS DAMPING RATIOS & FREQUENCIES DETERMINED FROM FOURIER TRANSFORM DECAY METHOD . . .	A 26
A-3a	EXPERIMENTAL DAMPING RATIO DETERMINED BY THE BANDWIDTH METHOD (TESTS 1-3).	A 31
A-3b	EXPERIMENTAL DAMPING RATIO DETERMINED BY THE BANDWIDTH METHOD (TEST 4)	A 32
B-1	EXPERIMENTAL RESULTS - FATIGUE TEST	B 7
B-2	EXPERIMENTAL RESULTS - NORMAL MODE TESTS.	B 8
B-3	PREDICTED AND EXPERIMENTAL FREQUENCIES - FATIGUE TEST.	B 10
B-4	PREDICTED AND EXPERIMENTAL FREQUENCIES - NORMAL MODE TESTS	B 11
B-5	PREDICTED AND EXPERIMENTAL DEFLECTION RANGES - FATIGUE TESTS	B 12
B-6	PREDICTED AND EXPERIMENTAL DEFLECTION RANGES - NORMAL MODE TESTS	B 13
B-7	PREDICTED AND EXPERIMENTAL STRESS RANGES - FATIGUE TEST.	B 14

TABLE		PAGE
B-8	PREDICTED AND EXPERIMENTAL STRESS RANGES - NORMAL MODE TESTS.	B 15
B-9	NORMAL MODE DAMPING RATIOS	B 39
B-10	CHANGE IN DIAGONAL COEFFICIENTS IN STIFFNESS MATRIX - SIX DOF	B 51
C-1	FIELD TEST CONSTANTS FOR ANGLE PROBES.	C 10
C-2	ULTRASONIC CRACK MEASUREMENTS AT BOTTOM CRITICAL SECTIONS.	C 21
C-2(cont)	ULTRASONIC CRACK MEASUREMENTS AT BOTTOM CRITICAL SECTIONS.	C 22
C-3	ULTRASONIC CRACK MEASUREMENTS AT TOP CRITICAL SECTIONS.	C 32
C-4	ULTRASONIC FLAW SIZE vs. ACTUAL FLAW SIZE.	C 37
F-1	MOMENTS OF INERTIA	F 9
G-1	AVERAGE FATIGUE STRESS OVER TEST RANGE FOR TOP CRITICAL SECTIONS.	G 10
G-2	AVERAGE FATIGUE STRESS OVER TEST RANGE FOR BOTTOM CRITICAL SECTIONS	G 11

CHAPTER I

INTROOUCTION

1.1 PREFACE

Within the past decade, a considerable amount of research effort has been focused on the fatigue performance of welded steel highway bridges[1]*. Many of today's modern highway bridges have a myriad of welded connections and details. These weldments give rise to microscopic flaws that may propagate under repeated loading into macroscopic cracks. Under certain conditions the cracks progress throughout the entire cross section of the structural member involved. Fatigue fractures were noted in the bridges in the AASHO Road Tests[2]. From time to time fatigue cracks have been reported in freeway bridge girders subjected to heavy truck traffic.

In 1967 the ASCE Subcommittee on Cover Plates[3] reviewed pertinent tests to that date and recommended an extensive research study of the fatigue life of cover-plated beams with various configurations. A substantial test program was subsequently undertaken by Fisher et.al.,[1] the outcome of which was a set of design recommendations for consideration by AASHTO. The most recent recommendations[4] concerning allowable stresses in the vicinity of weldments are currently under review by AASHTO. These design criteria are based on the performance of laboratory models of the components that are prone to fatigue.

As a result of flood control work in the St. Francis River Basin, a relatively new (1963) three-span continuous composite girder highway

*Numbers in parentheses refer to entries in the list of references.

bridge in Butler County, Mo. (MSHD Bridge No. R317), was scheduled for removal. The bridge, shown in Fig. 1-1, was seen as an uncommon opportunity to perform a fatigue test on a full scale structure. Because of the cost, full scale bridges are rarely constructed for the exclusive purpose of testing to destruction. Nevertheless, tests of this nature are needed to provide some validation of the design criteria, which are based on laboratory data.

Phase I of the overall project, which was completed in 1972, consisted of analytical and laboratory studies to verify the feasibility of conducting the fatigue test. The analysis indicated that the critical fatigue regions occurred in the base metal of the girders in the end spans between the end of a cover plate and the field splice. In view of the fact that the bridge had four girders and two end spans, the field test involved 16 critical fatigue regions including both top and bottom flanges.

The test scheme that was adopted provided for the resonant excitation of the bridge in its first bending mode by an electro-hydraulic actuator with a weight of approximately 10 kips attached to the piston.

Detailed results of the Phase I study are contained in a report by Salane et. al.[5]. This report presents the findings of Phase II of the project, which was primarily concerned with the field test that was conducted in the months of August, September and October of 1975. In the preliminary planning, the field test was scheduled for the summer of 1973. However, the not-to-be-denied element of weather and the consequential delay in the flood control work resulted in a postponement of the field test.

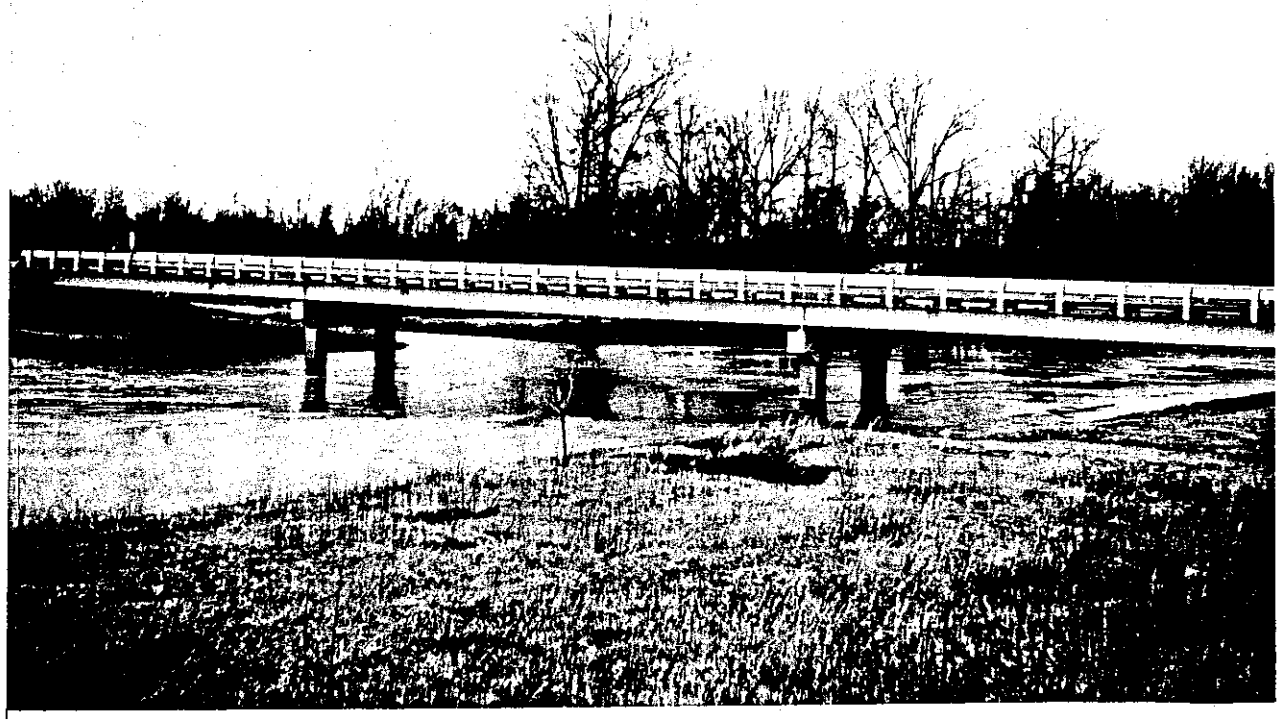

FIGURE 1-1. TEST BRIDGE (MSHD BRIDGE NO. R317)

1.2 PURPOSE AND SCOPE

The fundamental objective of this study was to conduct an in situ fatigue test of the full scale bridge in order to document its fatigue behavior. To achieve the most meaningful data, the level of stress for combined dead and dynamic loading in the critical fatigue regions exceeded the allowable stress for 500,000 cycles as calculated from the AASHTO formulas for fatigue. The applicable formulas were contained in the 1969 AASHTO Standard Specifications and the 1970 and 1971 Interim Specifications. In retrospect, the bridge was designed in 1962 prior to the introduction of fatigue constraints in the specifications.

A second aspect of the study was to use several crack detection techniques in periodic inspections of the bridge during the course of the fatigue test. By so doing, some insight could be gained as to the utility of these techniques. In addition to visual inspection the techniques comprised the following devices and procedures:

1. Ultrasonic inspection of the fatigue regions with a hand-held probe and transceiver.
2. Application of dye penetrant to the cracks.
3. Radiography of the fatigue regions.
4. Inspection of girders with FHWA, ACD and MCD instruments.
5. Determination of the vibration signature by Randomdec Analysis.
6. Measurement of acoustic emission by sensors located in the fatigue regions.

7. Transient, steady-state and sweep tests for one degree-of-freedom dynamic properties.
8. Steady-state tests for multi degree-of-freedom dynamic properties.

1.3 DESCRIPTION OF TEST BRIDGE

The two-lane, three span (72'-93'-72'), continuous composite girder bridge crossed a levee ditch parallel to the St. Francis River, 19.1 miles S.E. of Poplar Bluff, on Route U in Butler County, Missouri. The bridge was designed in early 1962, according to 1961 AASHO specifications[6], for one lane loaded with H15-44.

The principal features of this bridge are shown in Fig. 1-2. Section details are described in the Phase I Report[5]. Four 30-in. wide flange girders of ASTM A36 steel, cover-plated over the main piers (13 ft.-6 in. each side of piers), carried a six in. slab designed for composite action in the positive moment regions. Bolted field splices in the girders were located 18 ft. from the main piers in the end spans and 22 ft. from these piers in the center span.

Unshored construction was used during placing of the slab. The 22 ft. wide roadway had a parabolic crown. Concrete used in the slab had a 28 day compressive strength of 5270 psi. Over the girders a varying concrete haunch was used to ensure a roadway parallel to grade. Slab reinforcing consisted of transverse #5 bars at 6 1/2 in. top and bottom, and longitudinal #4 and #5 bars at various spacings top and bottom. An independently cast reinforced concrete curb anchored a steel guard rail. Shear connectors were C4x5.4, 6 1/4 in. long, fillet

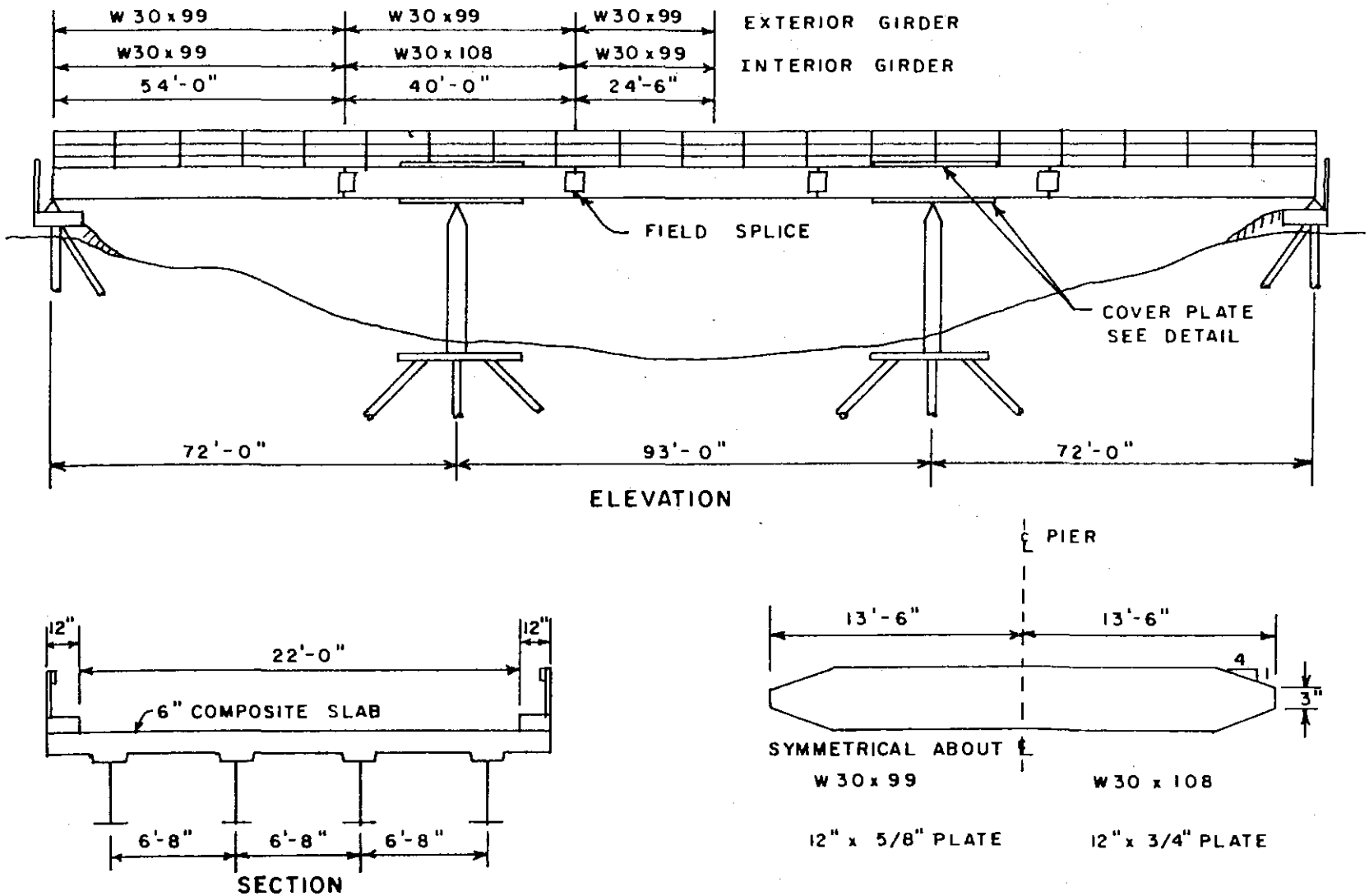

FIGURE 1-2. ELEVATION AND SECTION VIEWS OF TEST BRIDGE

welded to the top flange of the girders at varying spacing except in the regions 12 ft.-6 in. from the piers in the end span to 14 ft.-9 in. from the piers in the center span.

The abutments and piers were supported by precast concrete piles driven to a minimum of 32 ton capacity in sand.

1.4 DESCRIPTION OF FIELD TEST

In order to conduct the field test, alterations to the test site were necessary such as the construction of a bypass road on the north side of the bridge. Also the area under the bridge was backfilled to within approximately 10' of the girders so that scaffolding could be installed. Figure 1-3 shows the physical layout of the test site.

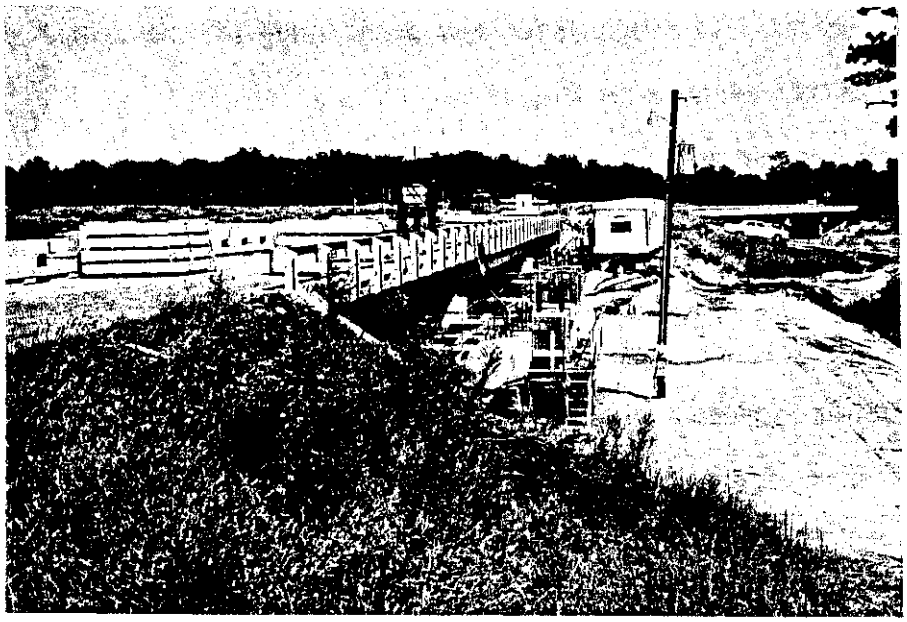

FIGURE 1-3. PHYSICAL LAYOUT OF TEST SITE

1.4.1 Fatigue Loading

The primary aspect of the field test was the application of a fatigue loading to the bridge until major fatigue failures occurred in the critical fatigue regions outlined in Art. 1.1. This criteria resulted in a total of 471,000 fatigue cycles being applied to the bridge. The fatigue loading was applied in intervals of between approximately 20,000 and 60,000 cycles with some of the various crack detection tests being conducted after each loading interval.

Dynamic strain ranges needed for the fatigue test were achieved by exciting the bridge at its first bending mode resonant frequency with a closed-loop electrohydraulic structural vibration system. The vibrator was constructed by attaching weights to the piston rod of a servo-controlled hydraulic actuator. The hydraulic actuator with attached weights was mounted in the center of a load distribution frame (see Fig. 1-4) and this loading system was positioned at the center of the main span as illustrated in Fig. 1-5.

During the fatigue loading each span of the bridge was loaded with approximately 40 kips of ballast consisting of four 10 kip concrete modules arranged on the spans as indicated in Fig. 1-5. The ballast was placed in each span to reduce tensile strains in central regions of the concrete deck. These tensile strains occurred at the center of each of the spans when they were at their uppermost position during a fatigue cycle.

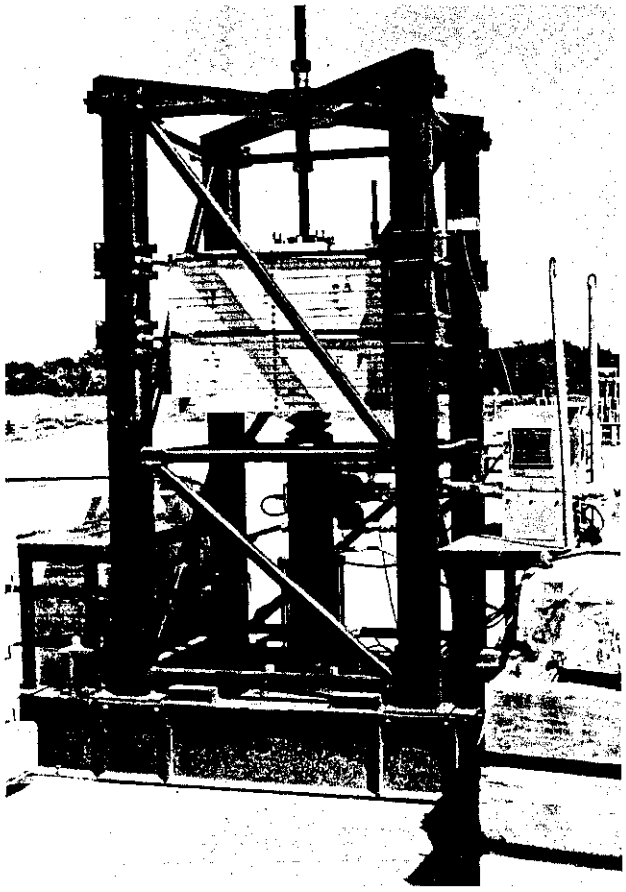

FIGURE 1-4. HYDRAULIC ACTUATOR AND LOAD DISTRIBUTION FRAME

The dynamic strains and deflections of the bridge were recorded periodically throughout the fatigue loading. A strain gauge was located on the top and bottom flanges of each of the girders at seven different sections along the bridge as illustrated in Fig. 1-6. The locations of the strain gauges are designated for this report according to the following scheme. Sections were numbered 1 through 7, beginning at the west end of the bridge. Girders were numbered 1 through 4, starting from the south side of the bridge. The top flange was labeled A while the bottom flange was labeled B. A strain gauge location

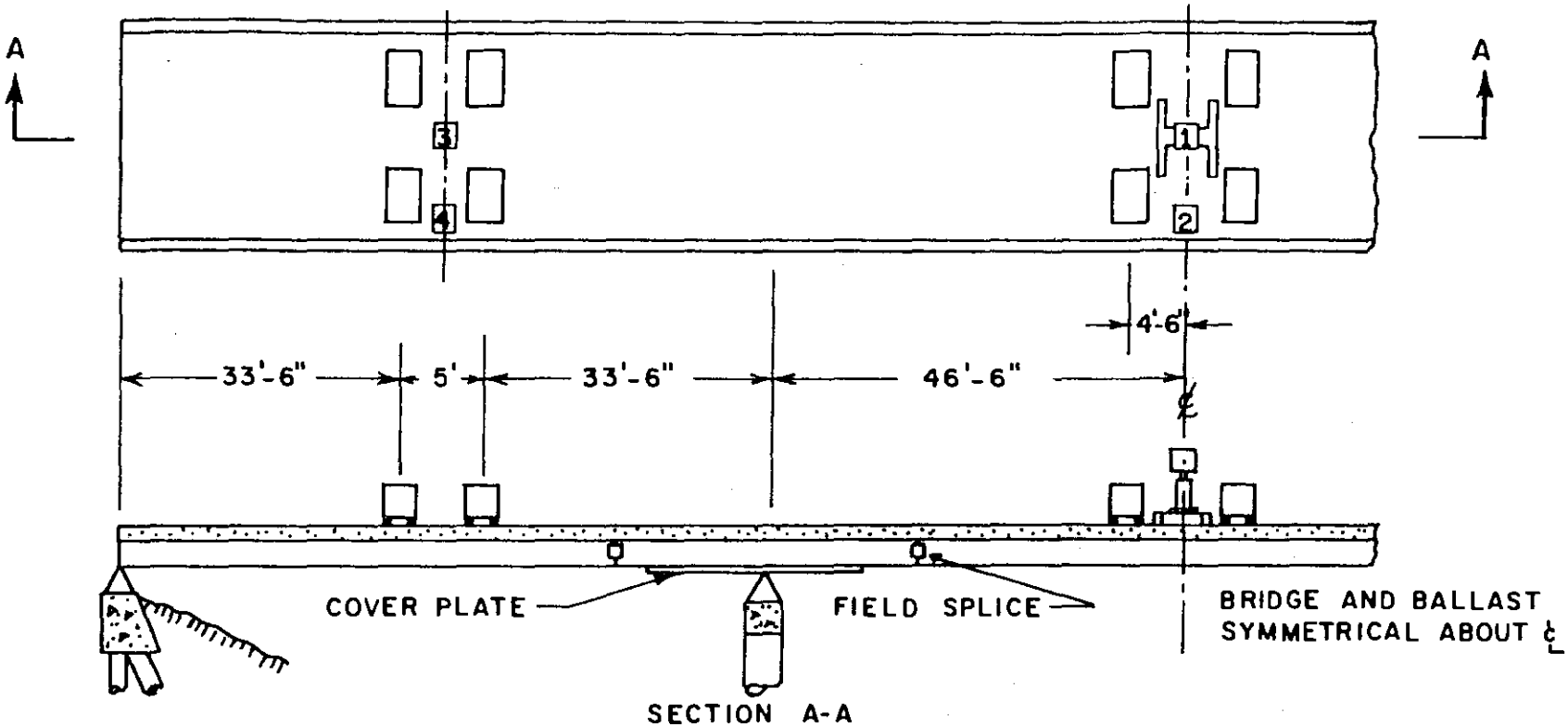

1 LOCATION OF ACTUATOR FOR EXCITATION OF FIRST BENDING MODE

2 LOCATION OF ACTUATOR FOR EXCITATION OF FIRST TORSIONAL MODE

3 LOCATION OF ACTUATOR FOR EXCITATION OF SECOND BENDING MODE.

4 LOCATION OF ACTUATOR SWEEP TEST

FIGURE 1-5. LOCATION OF BALLAST AND HYDRAULIC ACTUATOR

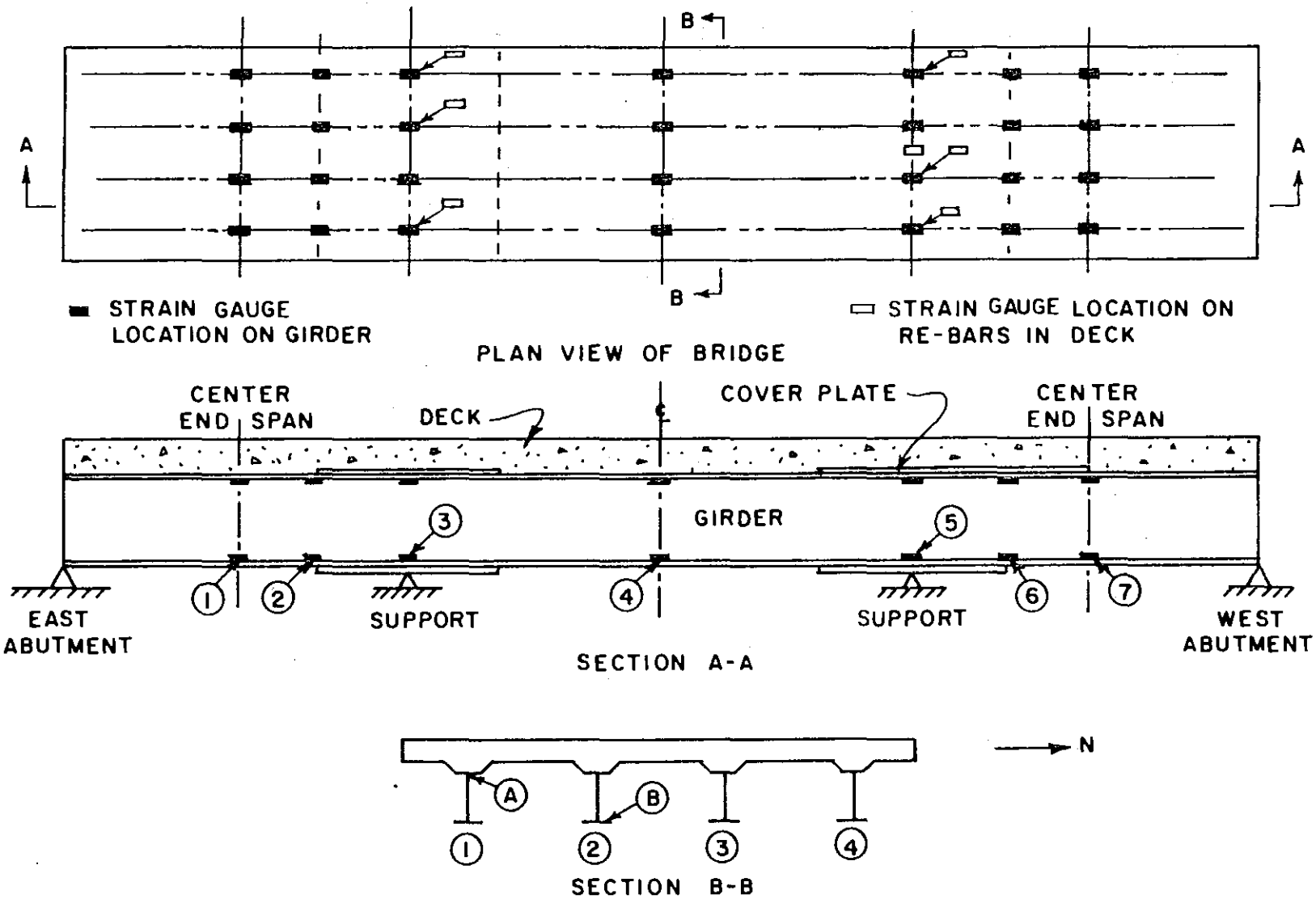

FIGURE 1-6. LOCATION OF STRAIN GAUGES ON BRIDGE

denoted 2.4B implies a strain gauge positioned at section 2, north exterior girder, bottom flange. Strain gauges were also placed on longitudinal reinforcing bars in the concrete deck at sections 3 and 5.

Cantilever beam type deflection gauges with a double amplitude range of 8.0 in. were designed specifically for this study. The deflection gauges were attached to the underside of the bottom flange of the bridge girders at 10 locations as shown in Fig. 1-7.

The fatigue test was commenced by bringing the bridge into resonance such that a 90° phase relationship existed between the stroke of the actuator rod and the deflection of the bridge at mid-center span. The phase relationship was detected and monitored by means of a Lissajous diagram. After the bridge was at resonance, the stroke of the actuator rod was adjusted (which in effect adjusted the total force applied to the bridge) until the required dynamic strain range of approximately 780 μ in/in was reached in the critical fatigue regions. Hand adjustment of the actuator stroke was necessary throughout the fatigue loading to maintain the required dynamic strain range.

A complete description of the experimental setup for the fatigue test is contained in App. D.

1.4.2 Crack Detection Techniques

The second aspect of this study was the application of the various crack detection techniques at selected intervals during the fatigue loading.

During the course of the field test a total of 17 ultrasonic inspections were conducted with a conventional pulse-echo unit. The initial ultrasonic inspection was conducted before the start of the

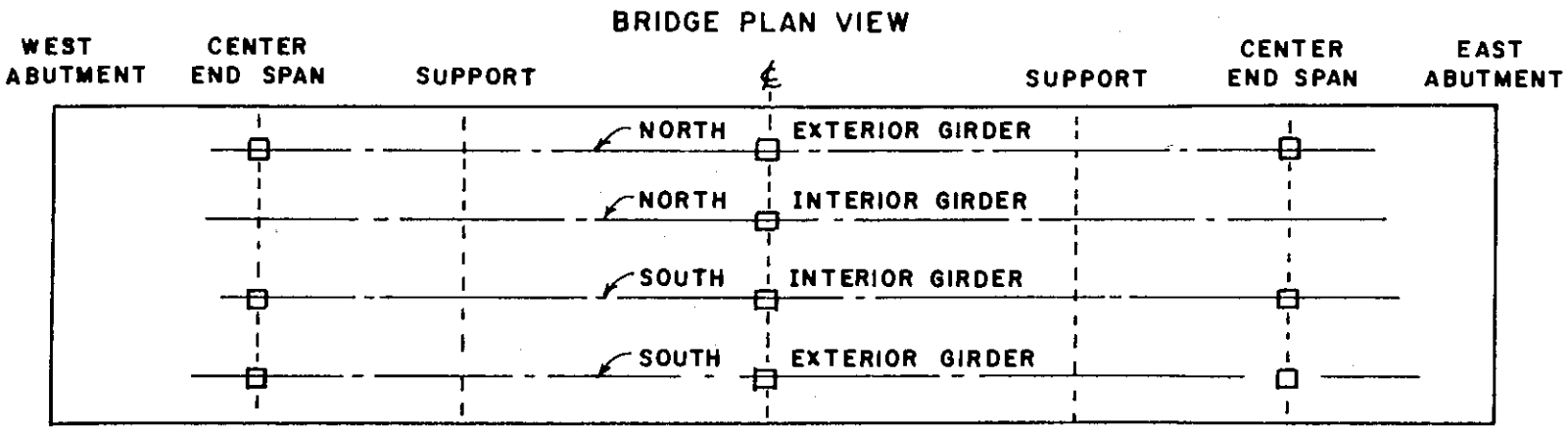

FIGURE 1-7. DEFLECTION GAUGE LOCATIONS ON BRIDGE

fatigue loading and included a complete inspection of both the top and bottom flanges at the ends of the cover plates in the critical fatigue regions.

Once the ultrasonic inspections indicated that the fatigue cracks were 1/2 in. or more in length, a dye penetrant was introduced to enhance the visibility of these cracks at the surface. The dye penetrant was periodically reapplied to trace and record the progress of the crack growth throughout the remainder of the field test.

Four sets of radiographs were taken by a commercial testing laboratory at 0, 98,000, 215,000 and 370,000 fatigue cycles. Radiographs were taken in the bottom flange critical fatigue regions during all four sets while radiographs of the top flange were taken only during the first two sets.

Acoustic emission measurements were periodically recorded at the eight critical fatigue regions as a means of monitoring crack growth during the actual fatigue loading of the bridge. The eight acoustic emission sensors consisted of a piezoelectric element connected in a differential mode to a common amplifier so that data from each sensor could be recorded sequentially on an x-y plotter.

The FHWA provided ACD and MCD units to be used periodically during the field test to detect cracks in the bridge girders. The Acoustic Crack Detector, ACD, is an acoustic device which is designed for the detection of internal flaws in steel members at some distance from the ACD unit. The Magnetic Crack Definer, MCD, is a magnetic field and eddy current device which defines the perpendicular direction of the crack and is used in conjunction with the ACD unit.

Nielsen Engineering and Research, Inc., developers of the "randomdec crack detection technique" employed this technique to analyze vibrational responses of the bridge. Records were periodically recorded during the fatigue loading at locations adjacent to the critical fatigue region. The vibration responses of the bridge were obtained using two different methods of excitation. The first excitation method employed a steel-wheeled dolly which was towed across the bridge at periodic intervals during the field test. The second excitation method was the actual fatigue loading. However, this excitation method was not employed until midway through the field test.

The final crack detection technique centered around whether or not structural damage could be determined by monitoring changes in the dynamic properties of the bridge. In order to determine the dynamic properties, a set of four dynamic tests was performed on the bridge at 0, 95,000, 215,000 and 377,000 fatigue cycles. The four dynamic tests were:

1. Transient Response
2. Normal Mode
3. Frequency Response
4. Sweep.

The first three dynamic tests were conducted using the first three vibrational modes of the bridge which were first bending, first torsion, and second bending. The locations of the hydraulic actuator on the bridge for purpose of exciting each of these three modes independently is shown in Fig. 1-5.

The Transient Response Test was conducted by exciting the bridge at resonance in one of the test modes using the structural vibrational system but employing a much smaller attached weight. Hydraulic power to the actuator was then shut off to allow the bridge to undergo a decaying free vibration which was recorded.

The Normal Mode Test was conducted by exciting the bridge at resonance in one of the test modes. The method of establishing resonance was the same as employed for the fatigue loading. Steady state response of the bridge was then measured at 22 stations on the underside of deck surface to establish the corresponding modal configuration of the bridge.

The Frequency Response Test consisted of a sequence of steady state excitations of the bridge over a frequency interval which centered about one of the first three resonant frequencies. Steady state excitations of the bridge were achieved with the vibration excitation system. By measuring the response of the bridge at selected locations and by including approximately 30 frequencies within the frequency interval, it was possible to establish the frequency response curve for each of the test modes.

The Sweep Test was conducted for the purpose of obtaining vibration signatures of the bridge over a frequency interval which included the first five resonant frequencies. This test was conducted by slowly but continuously varying the excitation frequency applied to the bridge while maintaining the peak force level as constant as possible with the experimental setup. The location of the hydraulic actuator for the sweep test is shown in Fig. 1-5.

During each of the four dynamic tests the vibrational response of the bridge was recorded at various locations with accelerometers. These locations on the underside of the bridge deck are referred to as stations in this report and are shown in Fig. 1-8. Additional details on the experimental setup for the dynamic test are contained in App. D.

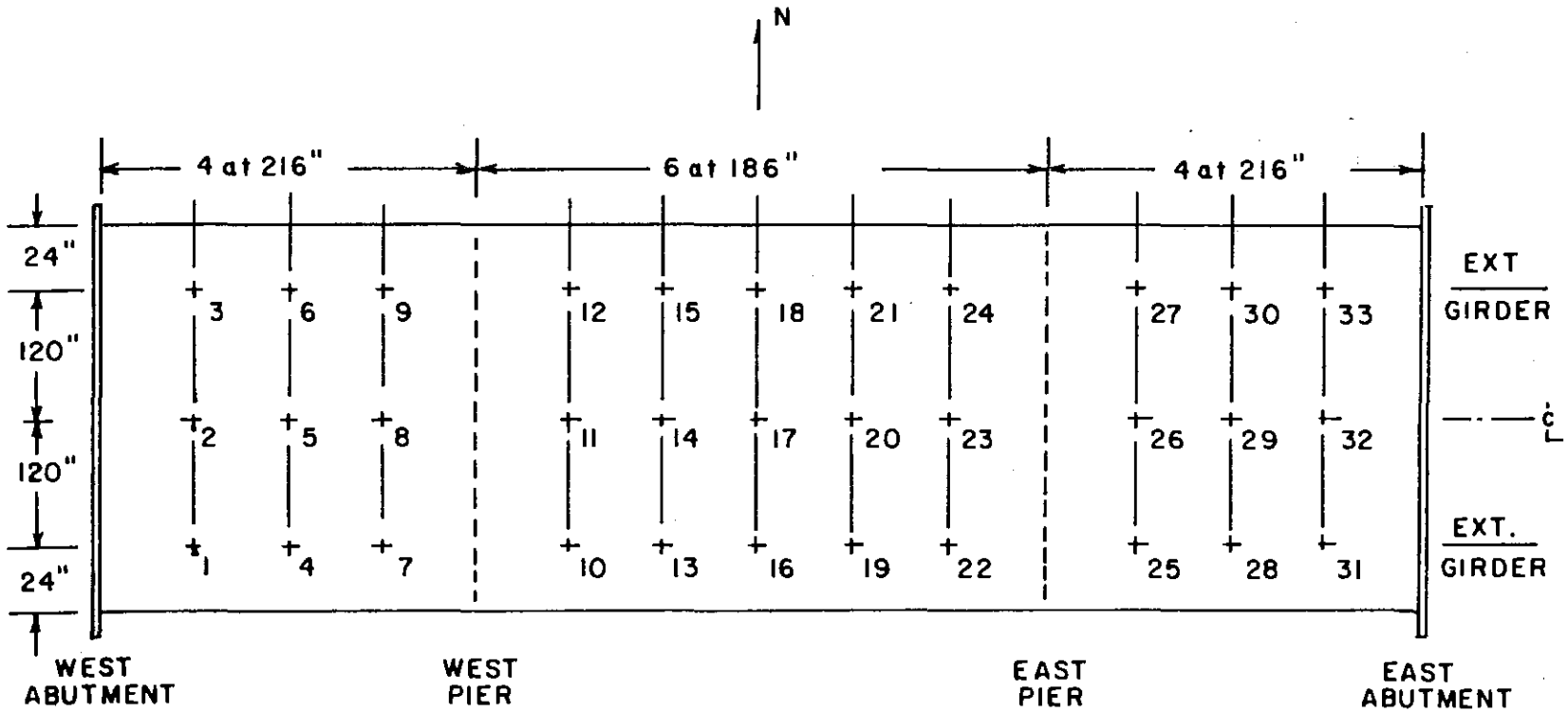

FIGURE 1-8. ACCELEROMETER STATIONS ON BRIDGE

CHAPTER 2

SUMMARY, CONCLUSIONS AND RECOMMENDATIONS

The observed behavior of the bridge during the fatigue test and the static and dynamic analyses of the experimental data are presented in Chapters 3 and 4. This chapter contains the conclusion based on the experimental and analytical results of the study.

2.1 RESPONSE

Use of a closed-loop servo-controlled electro-hydraulic shaker is a feasible method of producing service level repeated stresses in full scale highway bridges.

Multi degree-of-freedom finite element analyses based on fully composite and cracked-slab composite stiffnesses provided reliable upper and lower bounds for the response of the bridge during the fatigue and resonance tests.

Under high amplitude loading overall damping of the bridge was approximately 1.5 percent of critical and the fundamental bending frequency for the ballasted bridge decreased steadily from an initial value of 2.32 Hz to 1.93 Hz at the end of the test.

In the positive moment regions which were designed for composite action the effective moments of inertia under large numbers of cycles of high moment were greater than design values and approximately 10 percent less than those predicted by a fully composite analysis. Effective moments of inertia in the negative moment regions were from 35

to 300 percent greater than design values. Even though there were no shear connectors in these regions the effective moments of inertia were always equal to or greater than the cracked-slab composite moment of inertia.

2.2 FATIGUE

There were eight critical regions at the ends of welded coverplates where the nominal stress range was approximately 22.5 ksi and the predicted fatigue life was approximately 140,000 cycles. One or more fatigue cracks developed at every one of these critical regions, but there was only one failure in 471,000 cycles of loading.

There were eight critical regions at the ends of welded coverplates where the nominal stress range was approximately 8.7 ksi and the predicted fatigue life was approximately 2,000,000 cycles. Two of these regions failed respectively at 453,000 and 462,000 cycles of loading.

The primary differences between these two sets of critical regions were stress range, weld detail, and algebraically-maximum stress.

It may be concluded from this study that under fatigue loading the algebraically-maximum stress is significant at least to the extent that there is a threshold for this stress below which fatigue cracks do not propagate. For A-36 steel this threshold is near zero. Although inconclusive there is some evidence that above this threshold value the algebraically-maximum stress may have an influence on crack-growth rate.

Crack initiation, crack growth, and fracture are distinctly different phases of fatigue failure and a given set of conditions may have significantly different effects on the initiation and growth phases. Thus it may not be possible to accurately predict total fatigue life on the basis of a simple relationship involving only stress range and type of detail.

There were regions of four girders where the stress range in base metal was approximately 32.3 ksi. Although there were no welds in these regions heat numbers had been stamped in the bottom flanges of three of these girders. These heat numbers initiated failures at two separate locations in one of these girders while no cracks were detected in the other girders which were from a different heat of steel. There is evidence that differences in material properties between heats of steel in this bridge were great enough to have a significant influence on fatigue cracking.

2.3 CRACK DETECTION

Three of the crack detection techniques used in this study were effective to some degree in detecting the specific locations of individual cracks. The remainder were effective to varying degrees in the detection of structural deterioration in certain regions of the bridge. None of the techniques could be considered foolproof.

2.3.1 Ultrasonic Inspection

A conventional pulse-echo ultrasonic unit was the most reliable of the inspection methods. In those regions which were monitored

regularly no cracks are known to have grown to a length greater than 1.5 in. without ultrasonic detection. An attempt to evaluate the FHWA-MCD was unsuccessful because there was a malfunction in the only unit available at the time of the test.

2.3.2 Visual Inspection

Visual inspection appeared to be the second most reliable method of detection. Of course, cracks must penetrate the observed surface in order to be detected visually. Use of a dye penetrant significantly reduced the size of crack which could be detected visually.

2.3.3 Radiography

Radiography was nearly as reliable as ultrasonic inspection in the regions where it could be used, but more than half of the material to be inspected was inaccessible to radiography.

2.3.4 Dynamic Properties - Equivalent Single Degree of Freedom Analysis

The damping ratios and resonant frequencies associated with the modes in the lower order frequency region of the bridge were affected by the structural damage which was sustained by the bridge. However, the results show that changes in the damping ratios and resonant frequencies of the bridge do not provide information with regard to the location of the structural damage.

2.3.5 Dynamic Properties Multi Degree-of-Freedom Damping

Changes in modal damping due to structural degradation of the bridge during the fatigue test were discernible. However, there was no way to distinguish between the deterioration of the concrete deck and the fatigue crack growth in the steel girders.

2.3.6 Dynamic Properties - Multi Degree-of-Freedom Stiffness

Changes in the calculated stiffness matrices based on experimental data revealed reductions up to 40 percent in the stiffness of the entire structure during the fatigue test. However, the reductions were not significantly larger in the vicinity of the cracks in the steel girders.

2.3.7 Mechanical Impedance

Indications of the general location of structural damage were provided by changes in the vibration signatures of the bridge which were expressed in the form of mechanical impedance plots. Structural damage to the reinforced bridge deck appeared as an overall significant change in the mechanical impedance plots. However, structural damage to the girders appeared as a noticeable change only in the values of mechanical impedance at resonance and anti-resonance in the higher order frequency range of the mechanical impedance plots.

2.3.8 Randomdec

In some of the critical fatigue zones the Randomdec method of detecting cracks produced crack predictions consistent with the ultrasonic results. However, the findings indicate that the two methods of excitation employed in this study to generate the vibration signatures needed for the Randomdec analysis are not completely adequate for reliable crack detection.

2.3.9 Acoustic Emission

The acoustic emission rate monitored with eight sensors attached to the steel girders in the critical fatigue regions was quite low. Consequently, crack growth in these regions was not evident in the emission rate. There was one exceptionally high emission rate recorded from all sensors approximately 30 minutes (3500 cycles) prior to a fracture of the entire cross section of the south interior girder at midspan.

2.4 Recommendations

The following are specific recommendations based on the findings of this study.

2.4.1 Composite Action

Serious consideration should be given to designing bridges of this type for composite action in the negative moment regions. Considerable economy in the steel section should be realized at the relatively low cost of adding a little extra longitudinal slab reinforcement and some shear connectors. The results of this test indicate that these

shear connectors could be concentrated toward the ends of the negative moment region so as to avoid creating a fatigue problem in the highly stressed region of the top flange directly over the support.

2.4.2 Stenciling

The premature failure of girder number 2 at midspan, points out the potential for fatigue crack initiation resulting from the stamping of heat numbers in the flanges. Although this practice has largely been discontinued for rolled sections, it is still common practice to stamp identification numbers in plates during fabrication. If the final location of a stamped identification number is one of high repeated tensile stress, there is certainly a potential for fatigue crack initiation. Consideration should be given to controlling the use of such identification stamps. The depth and sharpness of the stamp as well as its location are important factors.

2.4.3 Fatigue Stresses

Additional research is needed to determine the exact stress conditions under which fatigue cracks initiate as well as the conditions under which they propagate. In previous studies, these two phases of of fatigue failure have been combined and this may have tended to mask the effects of certain variables.

Parameters to be studied include the maximum stress as well as the stress range. The current AASHTO code is based on tests which indicated that only the stress range was important. Results of the current test suggest the possibility that the maximum stress (in the algebraic sense) may also be significant. It is possible that in the previous tests high tensile residual stresses (near yielding) masked

the significance of this variable. If this is in fact an important parameter, there are procedures through which residual stresses in fabricated structures can be relieved. Material toughness should also be included as a significant parameter in future fatigue research.

2.4.4 Detection Methods

The reliability of conventional ultrasonic techniques and radiography is sufficient to warrant the continued development of inspection programs utilizing these techniques along with visual inspection. However, it must be recognized that in the vicinity of complex connections some cracks may become very large before they can be detected.

There should be continued research into the applicability of acoustic emission for initial screening of bridge structures. The ability of this technique to detect the presence of crack growth even when the transducers are a great distance from the crack shows considerable promise for its use in conjunction with some type of test loading. It may be possible to detect the presence of cracking in a general region of the bridge with acoustic emission and then use ultrasonic techniques to locate the crack more accurately.

Monitoring of just the lower order natural frequencies of a bridge and its damping properties does not appear to hold much promise as a dynamic inspection technique to determine crack locations. The study did show that structural degradation can be detected by use of mechanical impedance and changes-in-stiffness techniques. These techniques also show promise as a comparison method for locating crack zones. Additional research is needed to refine and further develop these techniques as a dynamic inspection method.

CHAPTER 3

BEHAVIOR UNDER FATIGUE LOADING

3.1 DYNAMIC RESPONSE

The dynamic strains were measured by electrical strain gauges located on the inner flange surfaces at various locations along the bridge. The locations of the strain gauges are given in Fig. 1-6. The recorded data were the peak maximum and minimum values of the dynamic strains. Tensile strains were taken as positive values and compressive strains were taken as negative values. In the following discussion the word maximum implies algebraically maximum values.

Figures 3-1 through 3-6 show representative plots of the maximum and minimum dynamic strains at the ends of the cover plates in the west and east end spans and at midspan of the center span. The results shown in Figs. 3-1 through 3-6 reveal that there was fluctuation in the maximum and minimum dynamic strains during the fatigue test. However, the dynamic strain range at all sections remained relatively constant throughout the fatigue test except at those sections where a fatigue failure occurred.

Figure 3-5 shows the dynamic strain history at a section where a fatigue fracture occurred. The results reveal that the dynamic strain range at section 6.2A incurred a steady decrease from 438,000 cycles to 470,400 cycles. During this interval the dynamic strain range at unfailed sections remained nearly constant. The implications of the strain history on the fatigue behavior of the bridge are discussed in the remainder of this chapter and in App. G.

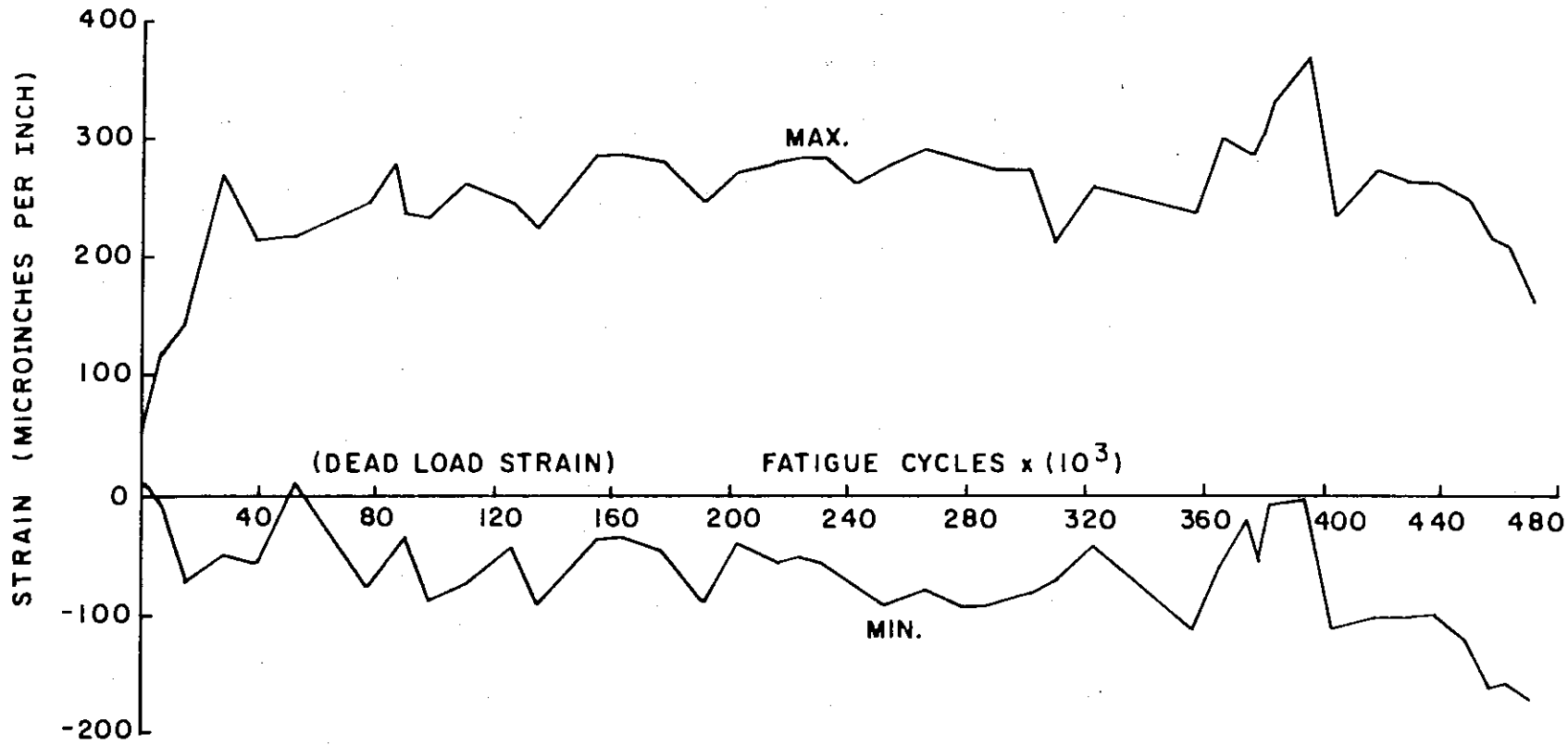

FIGURE 3-1. DYNAMIC STRAINS AT SECTION 2.2A vs. FATIGUE CYCLES

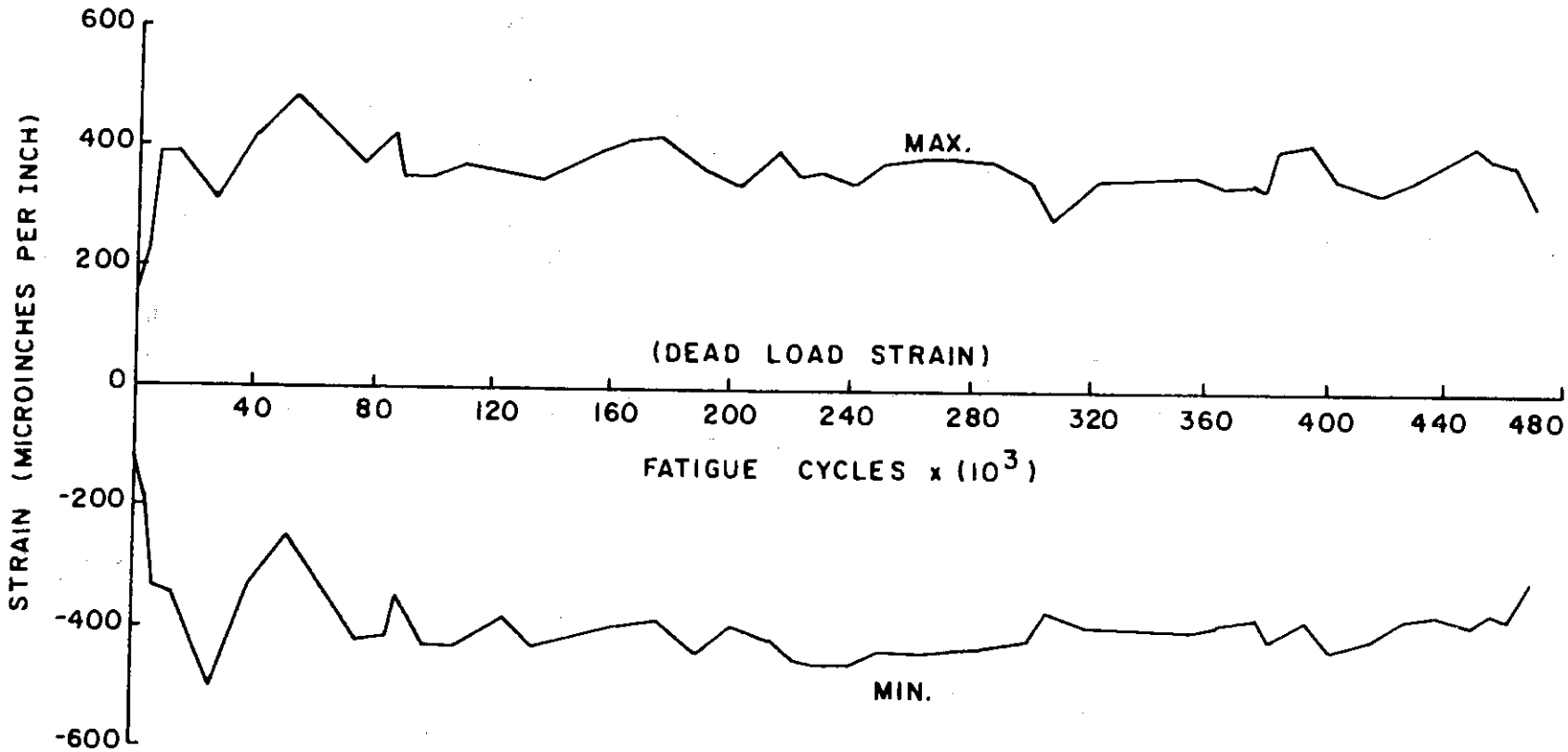

FIGURE 3-2. DYNAMIC STRAINS AT SECTION 2.2B vs. FATIGUE CYCLES

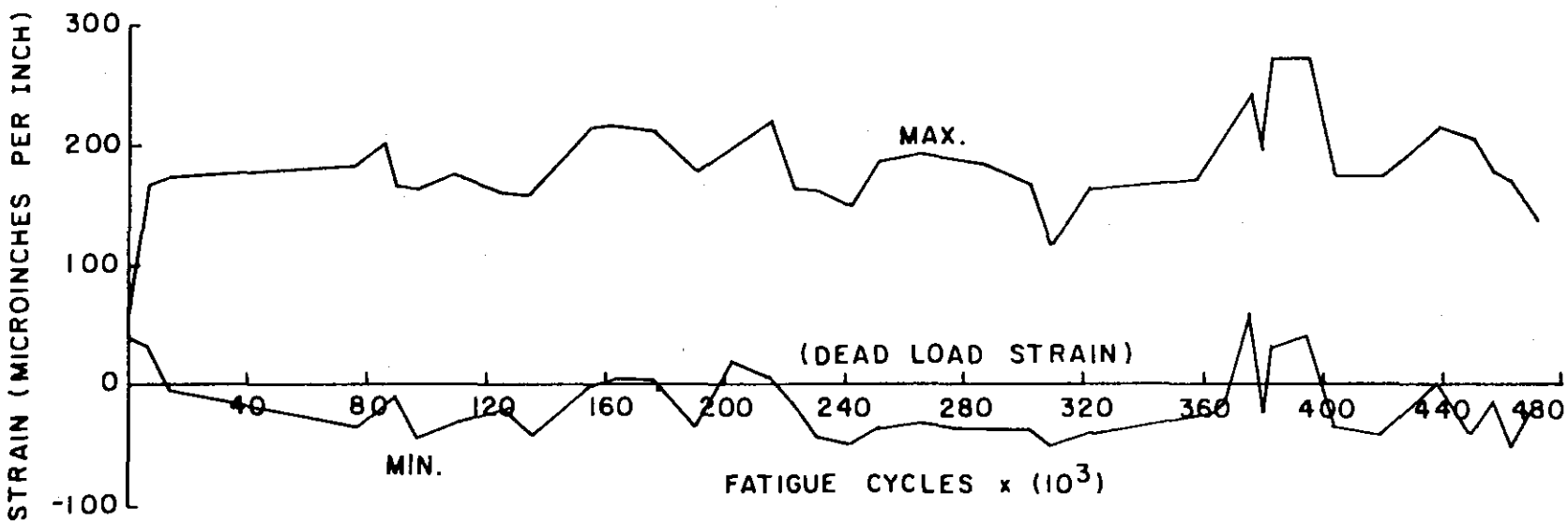

FIGURE 3-3. DYNAMIC STRAINS AT SECTION 4.1A vs. FATIGUE CYCLES

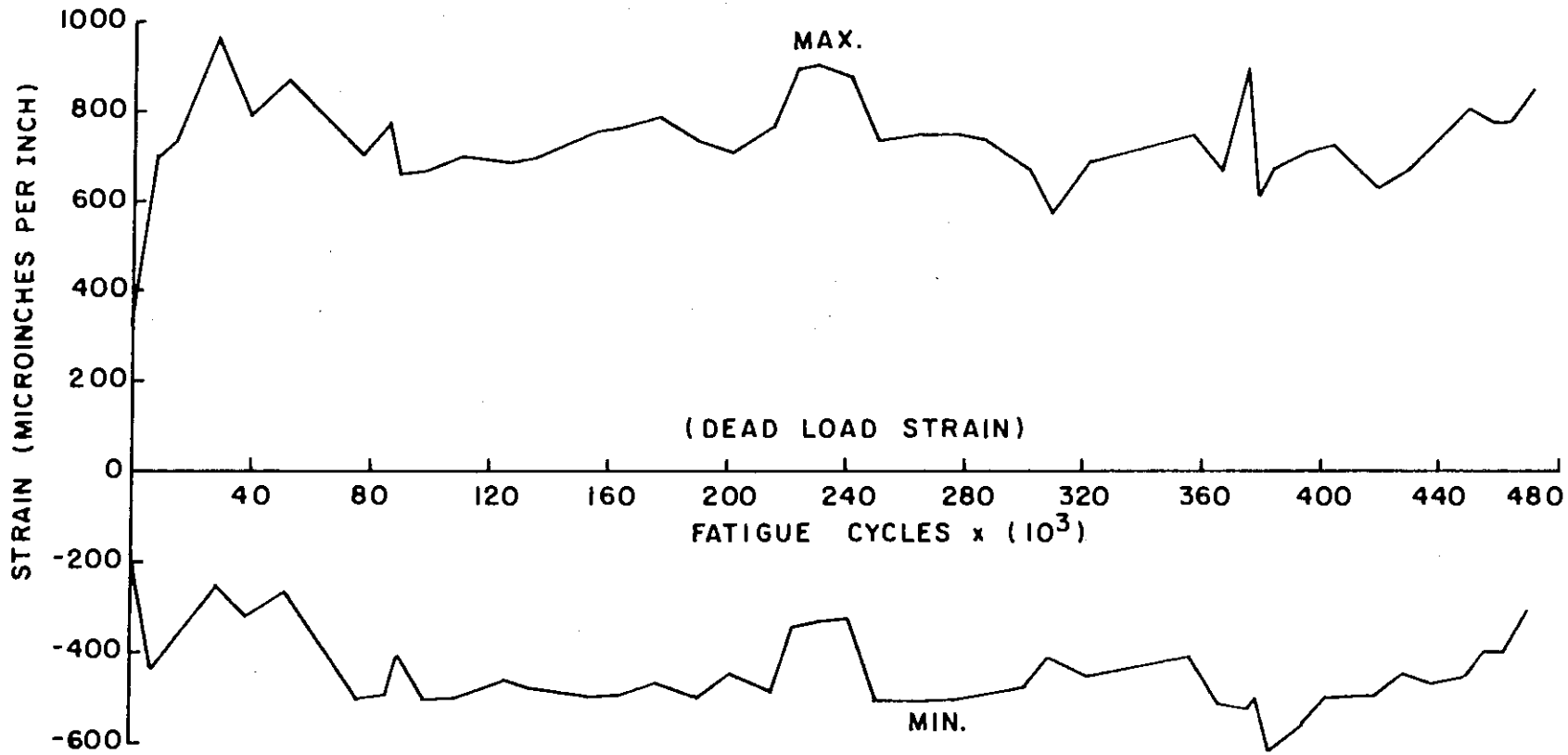

FIGURE 3-4. DYNAMIC STRAINS AT SECTION 4.1B vs. FATIGUE CYCLES

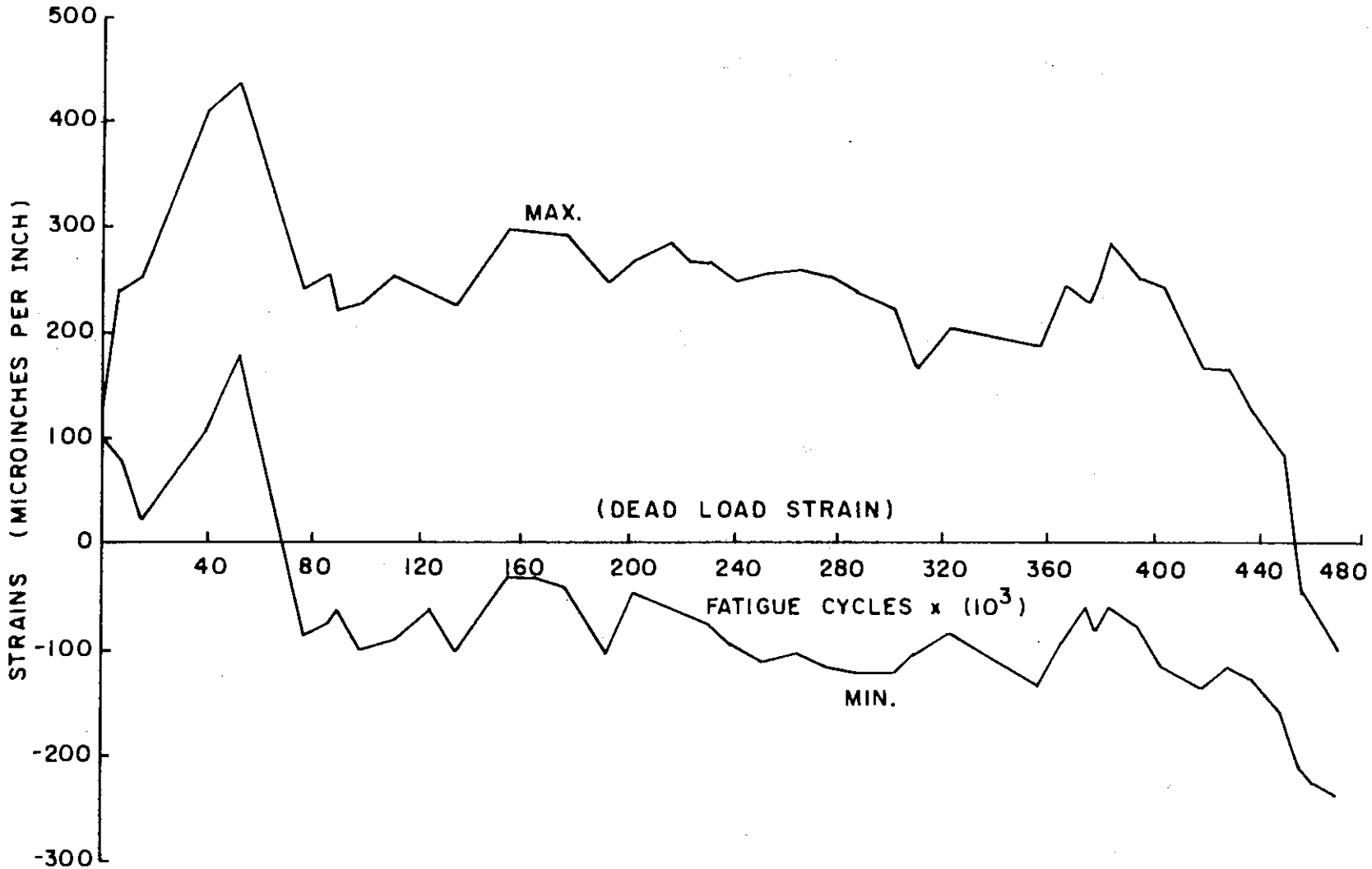

FIGURE 3-5. DYNAMIC STRAINS AT SECTION 6.2A vs. FATIGUE CYCLES

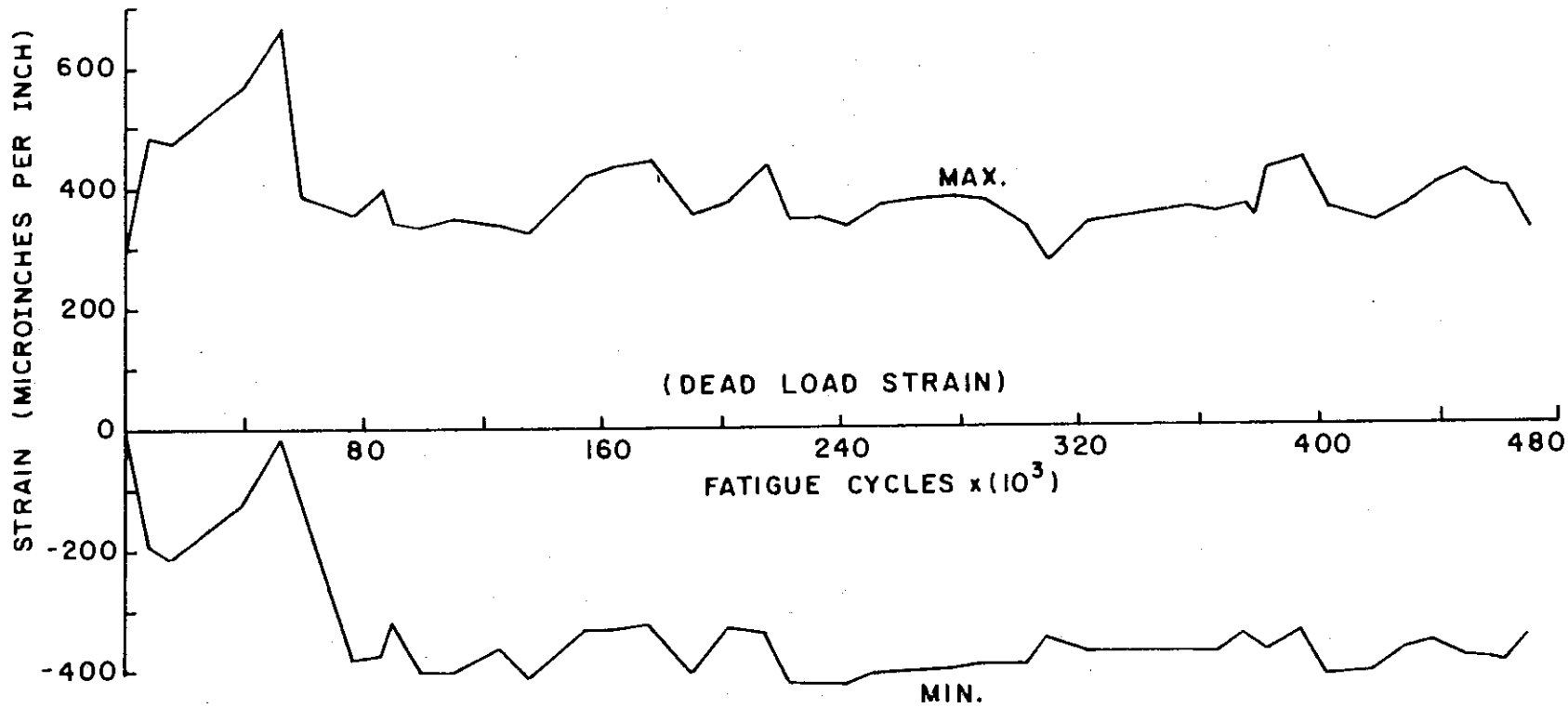

FIGURE 3-6. DYNAMIC STRAINS AT SECTION 6.2B vs. FATIGUE CYCLES

Dynamic deflections were measured at the center of each span by means of electrical deflection gauges. The locations of the deflection gauges are shown in Fig. 1-7.

Figure 3-7 shows the dynamic deflection range at midspan for the north and south exterior girders of the center span. The dynamic deflection range for the south exterior girder varied between 4.45 in. and 5.4 in., while the dynamic deflection range for the north exterior girder varied between 3.75 in. and 4.4 in. during the course of the fatigue test. The difference in the dynamic deflection ranges for the two girders was greater after a fatigue failure and field repair at 377,000 cycles.

Figure 3-8 shows the average deflection range at midspan for the west, center, and east spans. The average deflection range for the center span varied between 4.15 in. and 4.9 in. The average dynamic deflection range for the west end span varied between 2.0 in. and 2.35 in., while the average dynamic deflection range for the east end span varied between 2.20 in. and 2.5 in.

The damping present in the bridge during the fatigue test was determined by the peak amplitude method which is discussed in App. A. A plot of the damping ratio, ζ, vs. number of fatigue cycles is illustrated in Fig. 3-9. The damping ratio varied between 1.25 percent to 1.6 percent over most of the fatigue test. However, after the initial fatigue failure in the center span the damping ratio generally increased until it was 1.82 percent at the termination of the testing program.

3.2 COMPOSITE ACTION

The original bridge design was for composite action in the positive moment regions and non-composite action in the negative moment

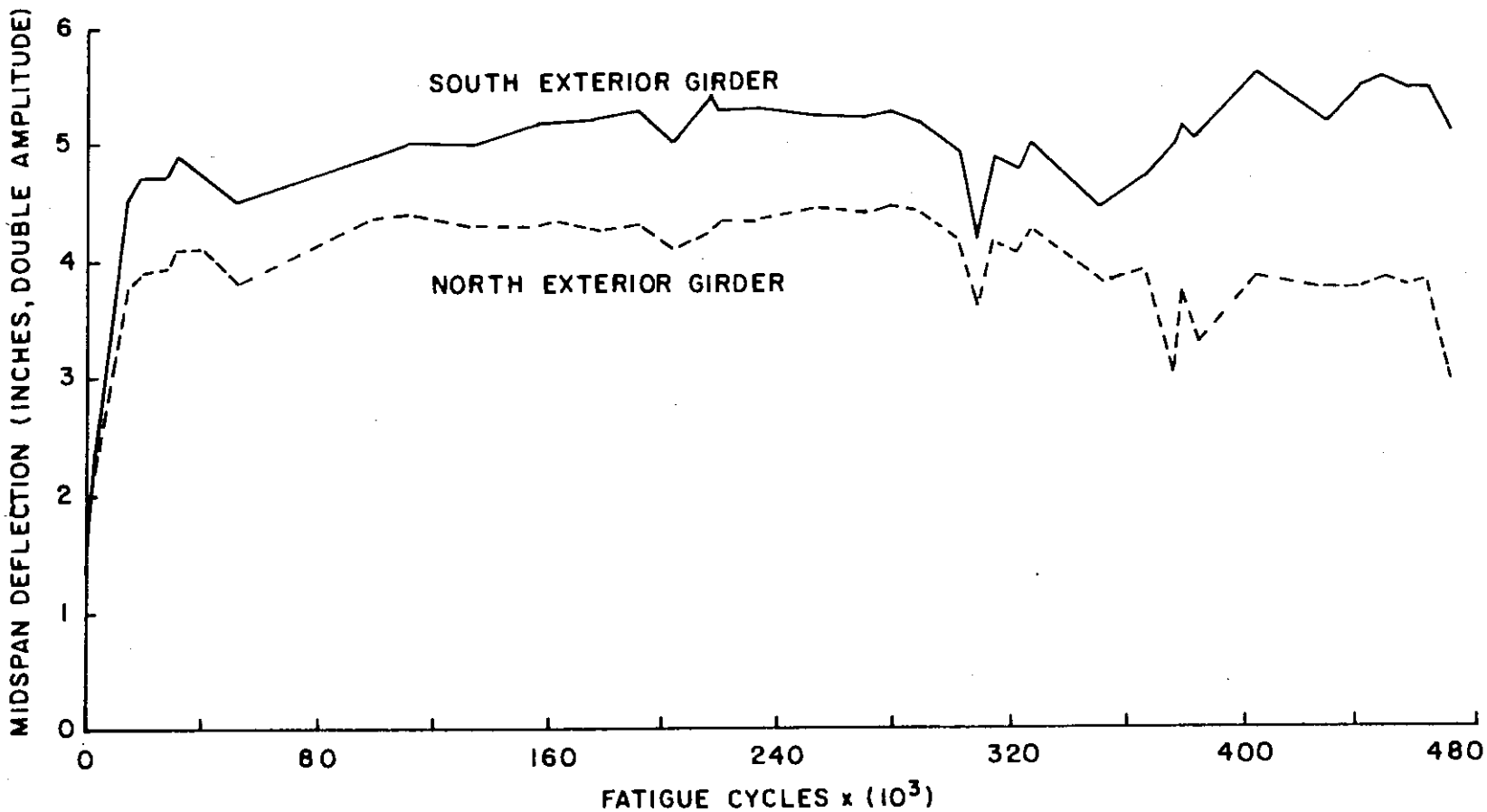

FIGURE 3-7. MID CENTER SPAN DEFLECTION OF NORTH AND SOUTH EXTERIOR GIRDERS vs. NUMBER OF FATIGUE CYCLES

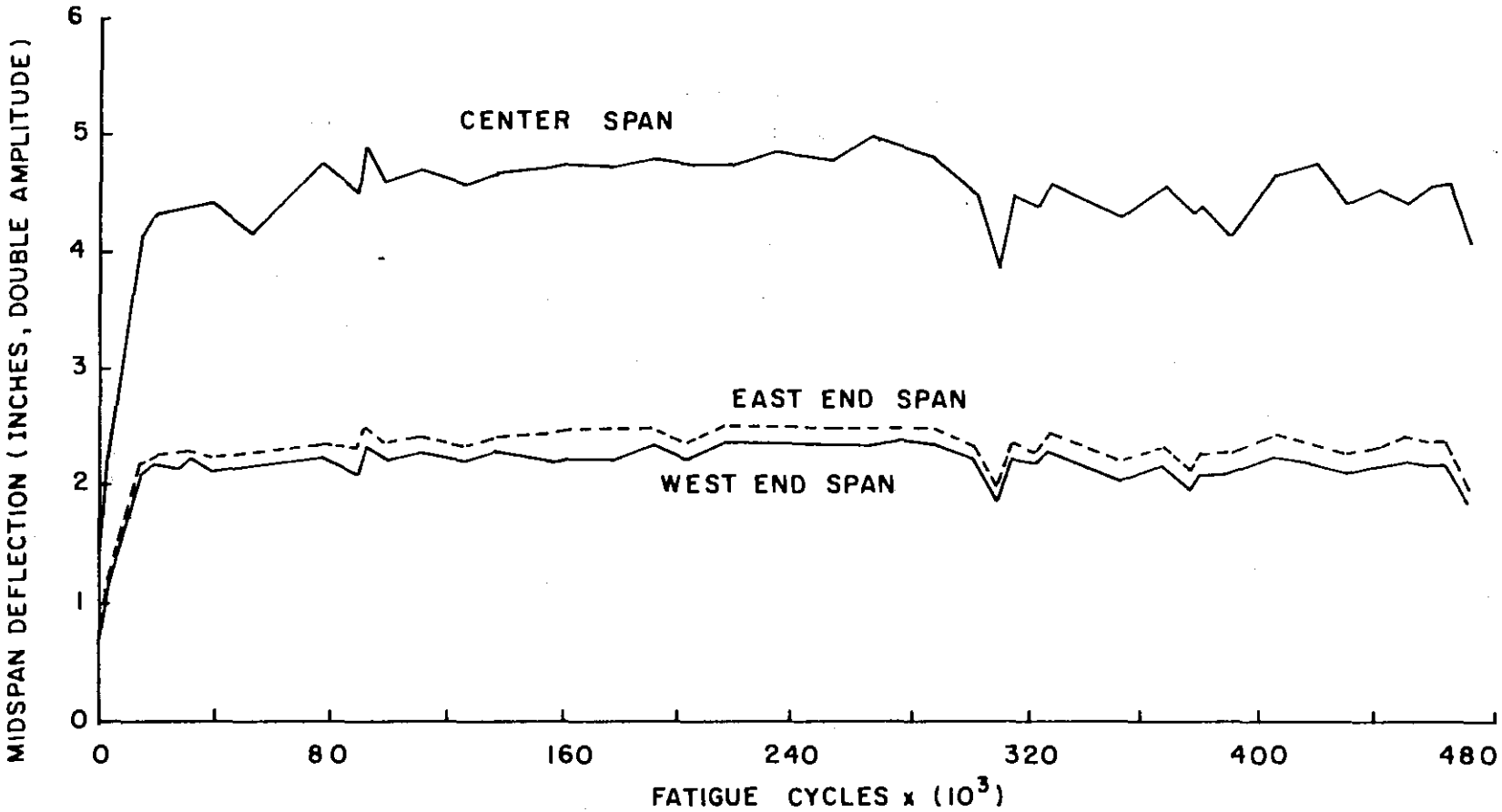

FIGURE 3-8. AVERAGE MIDSPAN DEFLECTION vs. NUMBER OF FATIGUE CYCLES

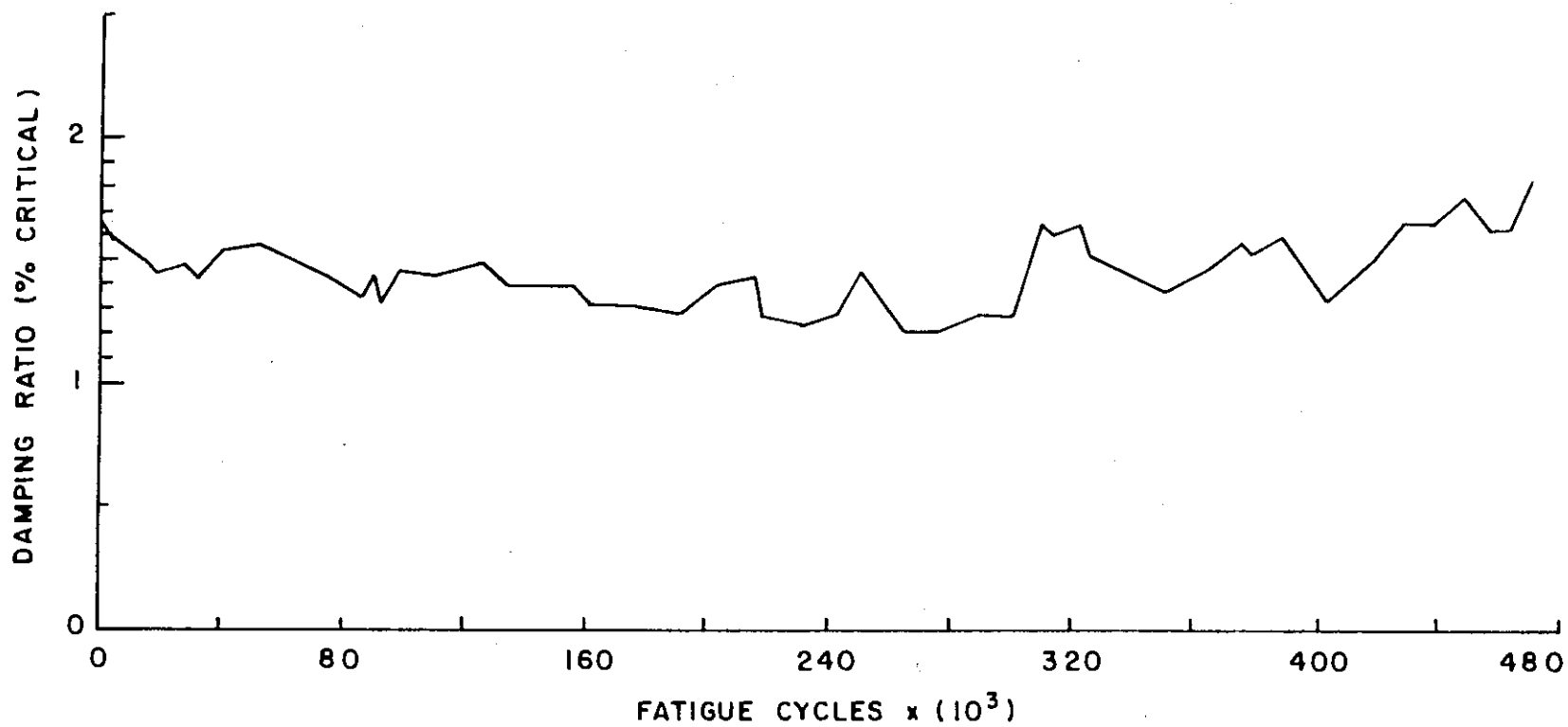

FIGURE 3-9. DAMPING RATIO vs. NUMBER OF FATIGUE CYCLES

regions. Although there were no shear connectors in the negative moment regions the concrete deck slab and its reinforcement were continuous from one positive moment region over the support and into the next positive moment region. For this type of construction there has been considerable controversy as to just how much, if any, composite action is developed over the support.

From strain measurements in the top and bottom flanges of the steel girders it was possible to calculate the effective moment of inertia during the test for each girder at each of the seven instrumented sections. These calculations were based on the assumption that plane sections in the steel girder remain plane and plane sections in the slab remain plane but slip does occur at the joint between the slab and steel beam. Average values of these effective moments of inertia during the test are presented in Table 3-1 along with values calculated for fully composite, cracked slab composite, non-composite, and design conditions. In the cracked-slab composite condition there are no stresses in the slab concrete, but the longitudinal slab steel is fully effective.

For the positive moment regions there are differences between the calculated fully composite moments of inertia and the design moments of inertia because of two factors. First, the design values are based on anticipated haunch depth while the fully composite calculated values are based on haunch depths actually measured in the field. Second, design calculations do not include effects of the curb for exterior girders while the fully composite calculated values include the curbs as a fully effective part of the composite section.

During fatigue loading all of the instrumented sections except those directly over the piers were subjected to alternate cycles of positive

TABLE 3-1. MOMENTS OF INERTIA (in.^{4})

	Calculated				Effective	
	Fully Composite	Cracked Slab Composite	Non Composite	Design	Positive Bending	Negative Bending
Mid-End Spans						
Exterior Girders	16600.	5870	3990	10400	15100	9800
Interior Girders	12800.	5290	3990	11800	12600	9300
End Span Critical Sections						
Exterior Girders	15900.	5760	3990	3990	12000	6670
Interior Girders	13000	5660	4460	4460	10400	6830
Over Piers						
Exterior Girders	23000	9930	7430	7430	*12400	10200
Interior Girders	20000	10800	8670	8670	*14700	11700
Mid-Interior Span						
Exterior Girders	17700	6050	3990	11600	15900	8800
Interior Girders	13600	5400	3990	12200	12800	8100

*Positive bending half of repeated loading cycle. The total moment was always negative at this section.

and negative bending. In each case the magnitude of the negative bending moment was sufficient to cause extensive cracking of the slab. As a result, the effective moments of inertia were substantially higher when the section was subjected to positive bending than when it was subjected to negative bending. Even over the supports where the bending moment was negative at all times the effective moment of inertia was somewhat lower when the moment was at its minimum negative level. This was probably due to a higher degree of intergranular interference during closing of the cracks than during opening of the cracks.

In all cases the effective moment of inertia was higher than the design value. At sections which were designed compositely for positive bending the effective moments of inertia were approximately 10 percent less than the values calculated for fully composite action. This is in agreement with previous experimental and analytical studies[7] and is the result of a small amount of slip which is permitted at the interface by the flexible nature of the shear connectors. The effective moment of inertia for exterior girders at these sections was approximately 40 percent greater than the design value because the design calculations do not account for the curb. Effective moments of inertia for the interior girders at these sections were slightly greater than the design values and this was only because the actual haunches were somewhat deeper than those assumed for the design.

Sections at the ends of the coverplates in the end spans were designed for non-composite action because under service load conditions moments are always negative at these sections. In every case the effective moment of inertia under test conditions was greater than

the cracked slab composite moment of inertia and for positive bending the effective values were approximately 75 percent of the fully composite values or from two to three times the design values. Even for negative bending the effective moments of inertia were between 50 and 70 percent greater than the design values.

The sections over the piers were designed non-compositely for negative moment and were always subjected to negative moment during the test. Again the effective moments of inertia were always at least equal to the cracked slab composite moments of inertia and approximately 35 percent greater than the design moments of inertia. During the positive bending half of the repeated load cycle effective moments of inertia were approximately 67 percent greater than the design values.

It should be emphasized that these effective moments of inertia which were substantially greater than the design values were not static single-cycle laboratory tests but were steady-state values during nearly a half million cycles of very severe loading on a full scale structure. For the top flanges where fatigue is a problem in the negative moment regions the effective section moduli show an even greater overcapacity because the composite action also raises the neutral axis. Details of the composite analysis are presented in App. F.

*

3.3 CONCRETE DECK

A visual examination of the surface of the deck before testing indicated that the deck was in excellent condition. During its twelve year service life the deck had suffered very little spalling and there were only a few noticeable cracks. Extensive transverse cracking of the

*See Addendum, page 89.

deck began to develop almost immediately after full amplitude fatigue loading was applied. This cracking occurred near the centers of the spans as well as over the supports because dynamic deflections were large enough to cause some negative moment even in the mid-span regions. The only uncracked regions were zones approximately 35 ft. in length at each end of the bridge and zones about 18 ft. in length near each end of the center span. The cracking pattern was relatively uniform with crack spacing varying from 5 to 18 in. When the deck was wet from rain during fatigue loading these cracks pumped a slurry of finely ground concrete particles onto the surface of the deck making it very easy to see the cracking pattern, Fig. 3-10.

This cracking had fairly well stabilized by the time 20,000 cycles of load had been applied and there was very little additional deterioration of the deck during the remainder of the test. There was a small amount of noticeable deterioration directly over girder 2 at midspan which occurred immediately after the fracture of girder 2.

Although the curb was cast separately from the deck it was anchored to the deck with Number 5 stirrups and acted compositely with the deck. Since the top of the curb was more than twice as far from the neutral axis of the beam as the surface of the deck, stresses in the curb were very large and there was some crushing of concrete in the curb, Fig. 3-11.

The steel guardrails which were anchored to the deck were designed with slipjoints to accommodate deflection of the bridge. These slip-joints seemed to work very well. However the extremely large deflections of the bridge (nearly 6 in. peak to peak) during the fatigue tests caused the

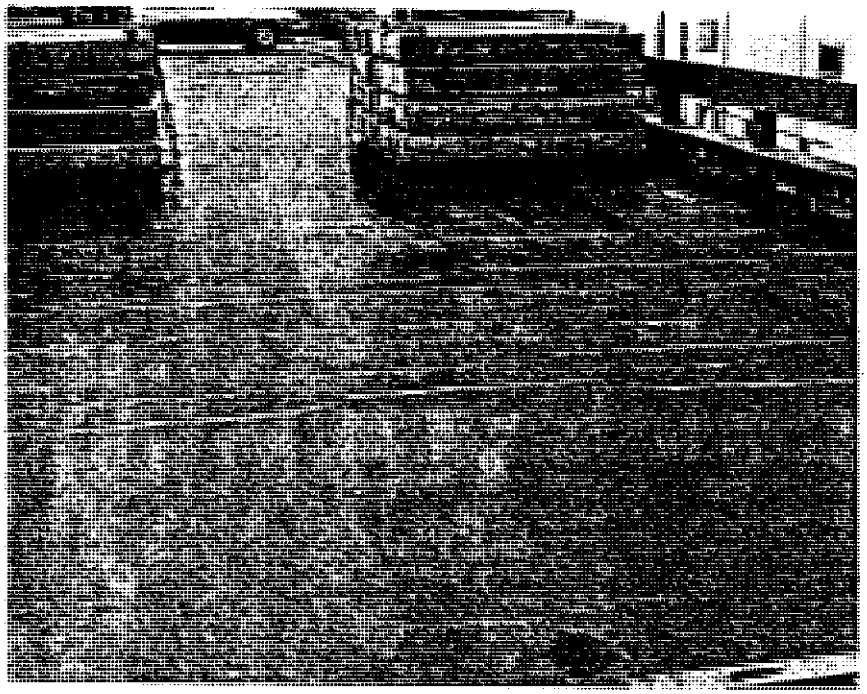

FIGURE 3-10A. BRIDGE DECK CRACKING

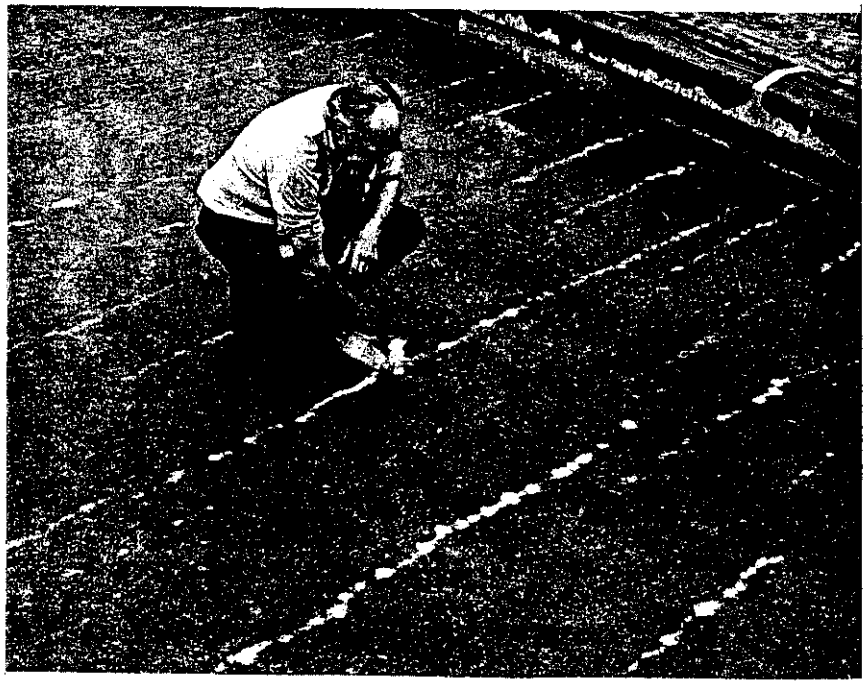

FIGURE 3-10B. BRIDGE DECK CRACKING

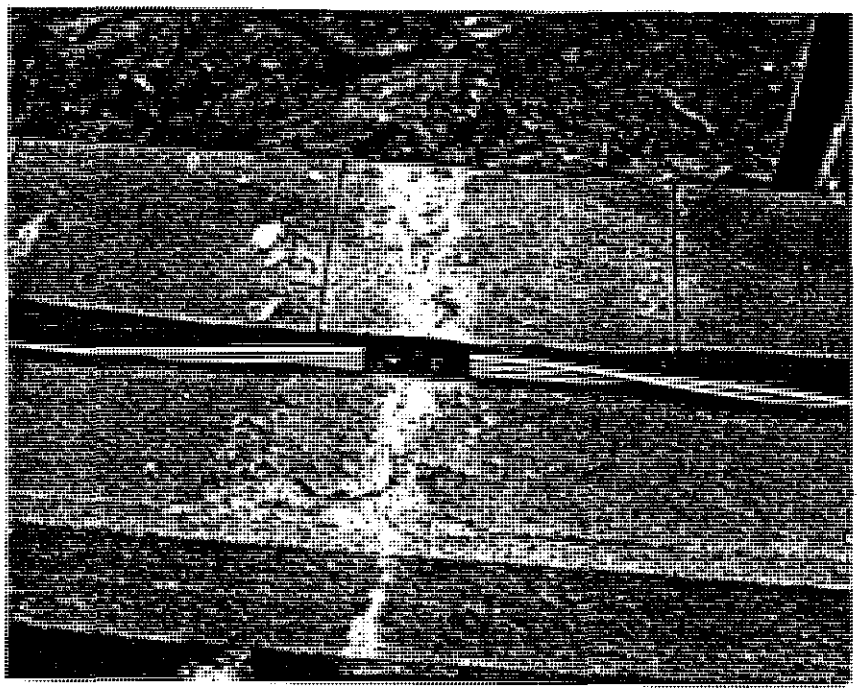

FIGURE 3-11. CRUSHING IN CONCRETE CURB

joints to be overdriven and a number of the bolts were sheared off.

At the end of the test the deck appeared to be in relatively good condition and sustained the traffic of a forklift removing the ballast without difficulty. However, the extensive cracking would no doubt have increased its susceptibility to environmental attack.

3.4 STEEL GIRDERS

Prior to loading the steel girders were given a thorough inspection both visually and ultrasonically. This inspection revealed only one detectable flaw and follow-up inspections during the test indicated that this flaw did not develop into a crack. The feasibility study for the project indicated that the critical regions for fatigue cracking would be at the ends of the bottom flange cover plates in the end spans, gauge sections 2 and 6.

Nominal stresses at these sections including dead load, ballast, and dynamic load were from approximately 20 ksi compression to 2.5 ksi tension or a stress range of 22.5 ksi. Variations from girder to girder were approximately ± 10 percent from these values. Residual stresses which were not measured would have had no effect on the magnitudes of stress ranges but probably shifted all stresses at the points of crack initiation in the tensile direction by several ksi.

During the inspection at the end of 19,500 cycles of load, cracks on the order of 0.25 in. in length were detected ultrasonically in five of the eight critical flange regions. After 287,000 fatigue cycles, cracks had been detected in all eight of these critical regions. These cracks did not initiate at the toe of the weld as might have been expected but started at the heel of the weld at some point across the end of the cover plate as shown in Fig. 3-12. These cracks propagated to the surface of the weld and across the end of the cover plates. In most cases they turned the corner and proceeded along the beveled edge of the cover plate until at some point the crack turned into the weld metal propagating perpendicular to the axis of the beam, Fig. 3-13. Once the cracks entered the weld material they continued through the weld material into the base material of the bottom flange and continued to grow in the typical semi-elliptical pattern. In five of the eight critical flange regions the cracks propagated into the base metal on both sides of the cover plate resulting in two separate cracks in the base metal, Fig. 3-14.

In all there were thirteen separate cracks which entered the base material of the bottom flanges at the ends of cover plates. Two of

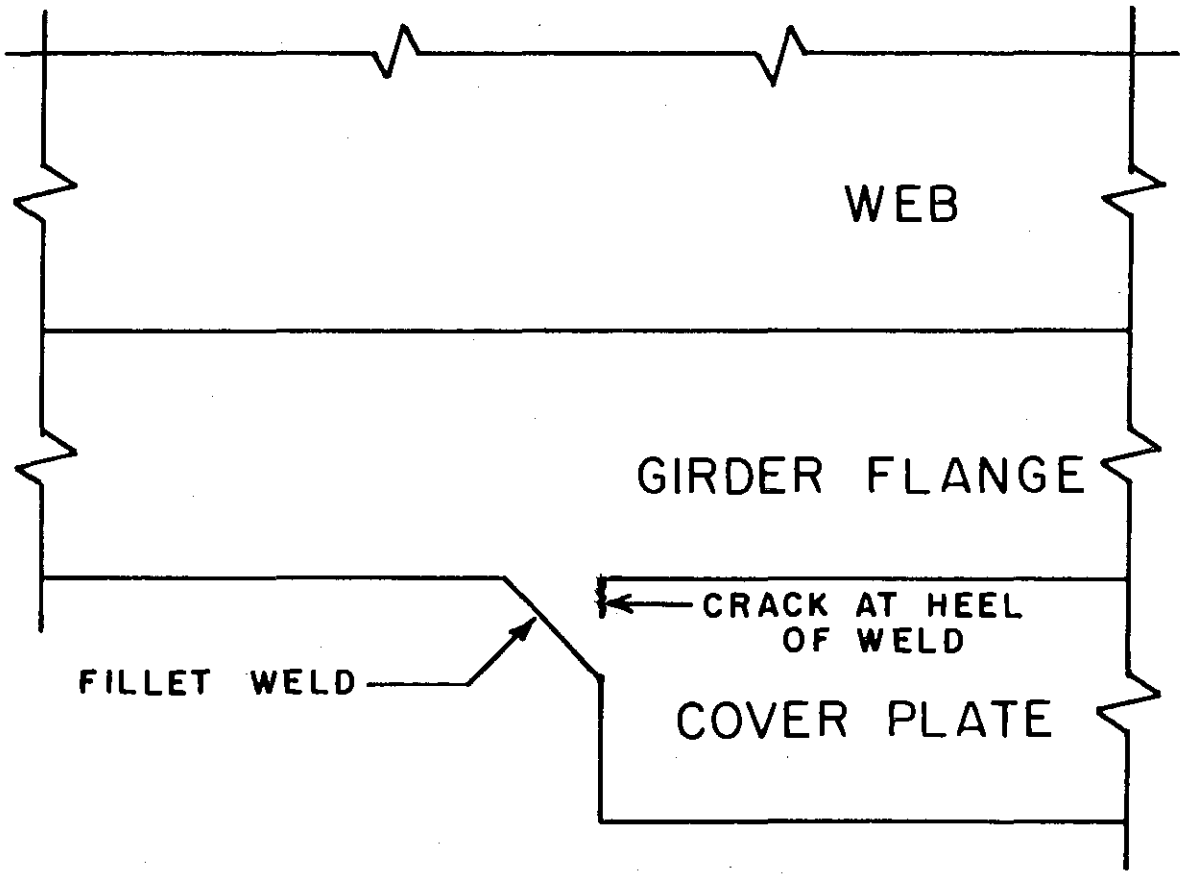

FIGURE 3-12. CRACK INITIATION AT HEEL OF WELD

FIGURE 3-13. CRACK PROPAGATION

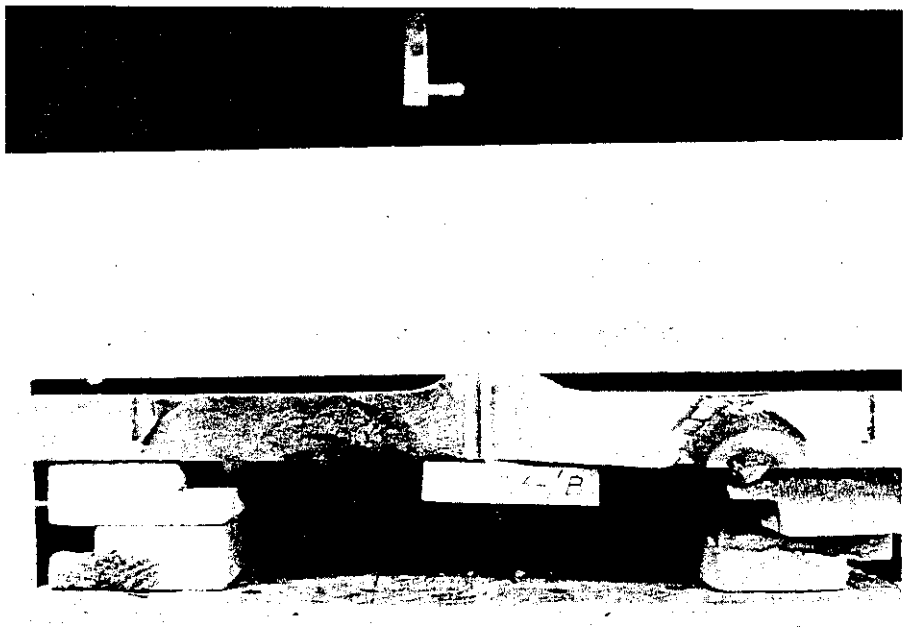

FIGURE 3-14. CROSS SECTION SHOWING TWO FATIGUE CRACKS

these cracks located at section 6.1 propagated to failure completely severing the bottom flange at 455,000 fatigue cycles. The crack on the south side at section 2.2B propagated to a total length of 3.5 in. at 438,000 cycles but showed no perceptible additional growth beyond that point, Fig. 3-14. No growth was observed in any of the other ten cracks beyond approximately 415,000 fatigue cycles.

These observations seem to indicate that the algebraic maximum stress, including residual stress, is significant at least to the extent that there is a threshold for this stress below which fatigue cracks do not propagate. This threshold appears to lie between approximately -2 and +8 ksi but because residual stresses were not measured its exact value cannot be determined from this test. In the one case where the algebraic maximum stress was above the threshold level the cycles to failure were more than three times as great as the number predicted for an equivalent stress range from previous observations by Fisher[1] on beams with much higher algebraic maximum stresses. Calculations during the feasibility study indicated that stress ranges at the ends of the top flange cover plates in the end spans, gauge sections 2 and 6, would be 13 or 14 ksi with the possibility of failure before 500,000 cycles. The initial test plan, therefore, called for continuous ultrasonic monitoring of these regions.

Once the test loading was underway, strain measurements indicated that there was considerably more composite action at these critical sections than had been assumed during the feasibility study. Nominal stresses under test loading were from approximately 6.0 ksi tension to 14.7 ksi tension producing an average stress range of only 8.7 ksi. Both the AASHTO specifications and previous research results presented

by Fisher indicated a fatigue life of nearly 2,000,000 cycles under this low stress range. Because of this and the fact that ultrasonic testing was the critical activity in a very tight testing schedule, ultrasonic monitoring of the top flanges was discontinued.

However at 415,000 fatigue cycles, a routine visual inspection of the bridge revealed that cracks of approximately six in. in length had developed in the top flanges of girder 1 at section 2 and girder 2 at section 6. Ultrasonic monitoring of the top flanges at sections 2 and 6 was immediately reinstated, but no additional cracks in top flanges were detected during the tests.* The cracks in girder 1 at section 2, and girder 2 at section 6, propagated to failure completely severing the flanges at 453,000 and 462,000 cycles respectively.

The fact that two of the eight sections subjected to essentially the same loading failed at less than 25 percent of the cycles permitted by the current code, is reason for concern. In addition to the magnitude of stress range, there were two primary differences between these top flange critical sections and the bottom flanges immediately below them. In the top flanges, the stress range was entirely in the tension region with a maximum tensile stress of 14.7 ksi, while the stress range in the bottom flanges was primarily in the compression region with a maximum tensile stress of only 2.5 ksi. The other difference was the particularly severe weld detail in the top flange.* A channel shear connector had been fillet welded to the base metal of the top flange adjacent to the end of the cover plate such that the two fillet welds were almost toe to toe, Fig. 3-15.

Although Fisher's data would indicate that the maximum tensile stress

*See addendum, page 89.

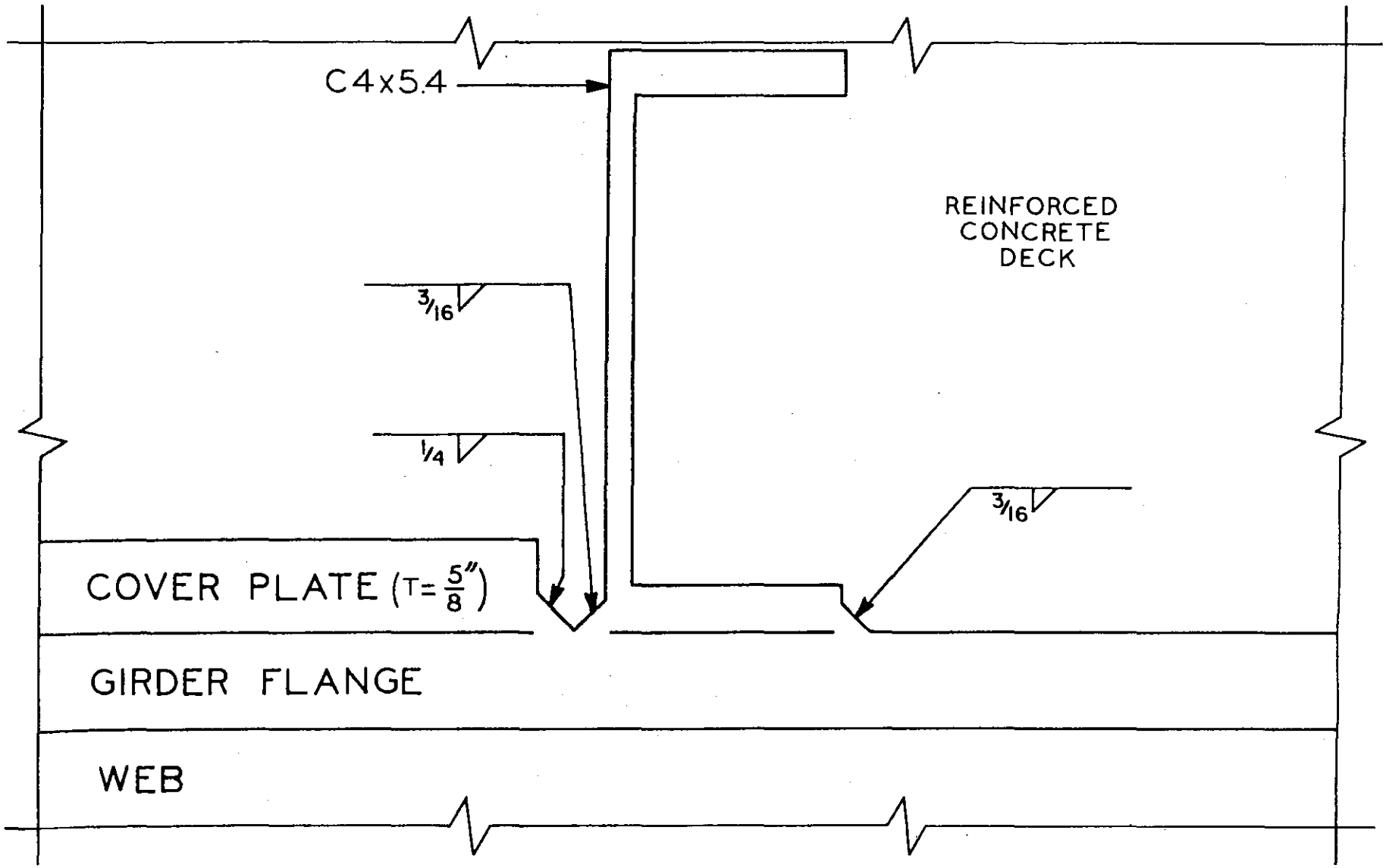

FIGURE 3-15. TOP CRITICAL SECTION DETAIL

was not important and therefore, the severe detail must be responsible for these early failures, there is insufficient evidence in the current investigation to determine which of these two factors precipitated the failures. If it is assumed that the detail was responsible, then it must be recognized that it is possible to have details which are much more severe than category F of the AASHTO code. If it is assumed that the high maximum tensile stress was responsible for the premature failures, then modifications of the code to account for this variable are in order.

At 373,500 fatigue cycles girder 2 failed with a loud bang at the center of the center span. Although the stress cycles at this section were from essentially 0 to 32.3 ksi there were no welds on the flange and base metal at a stress range of 32.3 ksi would not be expected to fail until more than 1.25 million fatigue cycles had been applied. Examination of the fracture revealed that a fatigue crack had initiated at a heat number stamped in the face of the bottom flange, Fig. 3-16.

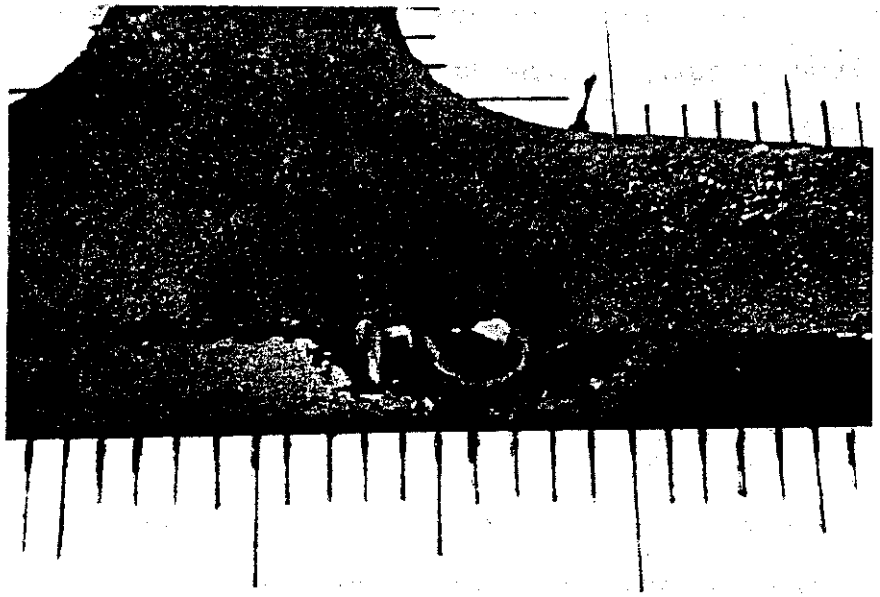

FIGURE 3-16. FATIGUE CRACK INITIATED BY HEAT NUMBER STAMP

A piece of the beam around the fracture was cut out for laboratory examination and a bolted splice applied so that the test could continue. At 470,700 fatigue cycles this girder fractured again at another heat number about 4 in. from the end of the splice. More significant than the effectiveness of the heat stamp as a stress raiser is the fact that girder 2 suffered two fractures while no cracks were detected in the girders on either side of this girder even though they were both subjected to the same stress conditions and were also heat stamped in the face of the bottom flange. Girder 2 was from a different heat of steel than the girders on either side and there was apparently a significant difference in the fatigue resistance of these two heats. A detailed study of these materials is planned for a future project.

A more detailed discussion of the fatigue behavior is presented in App. G.

3.5 SUPPORTING STRUCTURE

The soil under the bridge consisted of a thin layer of clay over a deep layer of sand, as shown in Fig. 3-17. Since saturated sands have a tendency to compact and to liquify when subjected to vibratory loading a study of the pile behavior was undertaken.

The piles were precast concrete, cast with an 8 in. tip diameter and a 16 in. butt diameter. The average length of the piles under the end abutments was about 37 ft., and for those under the main piers about 20 ft. They were driven into the coarse sand until their bearing capacity was reached. The bearing was obviously not firm bedrock and it was anticipated that settlement might occur during testing.

Prior to the testing program the channel was backfilled to about

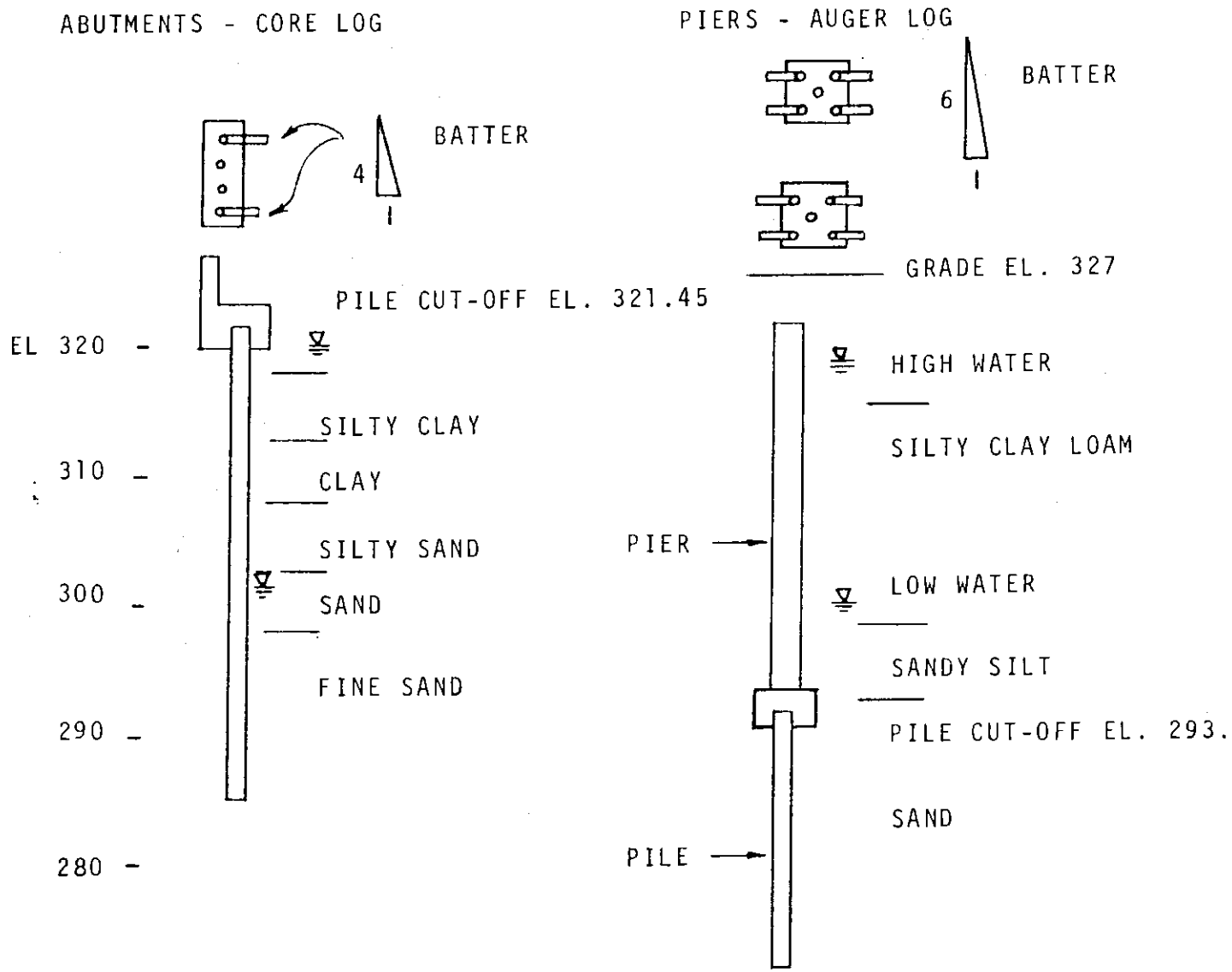

FIGURE 3-17. SOIL LOG DATA

El. 320. This fill added a substantial load to the piles under the main piers. The position of the water table was probably not changed significantly.

The test conditions produced the footing loads given in Table 3-2. At a pile under the end abutments the axial force varied between 23 and 47 kips at about 2.2 Hz. The pile force under the main piers oscillated between 57 and 71 kips. Pile driving data furnished by the Missouri State Highway Department indicated that the average allowable bearing capacity per pile in the end abutments was 114 kips and the corresponding capacity of a pile in the main piers was 83 kips. These values were based on the Engineering News Record formula which presupposes a factor of safety of six.

It was concluded from a study of the meager data available that settlement of the bridge foundations would not be a serious problem so long as the prime loading frequency was substantially less than 10 cps. Nevertheless, a set of level readings was taken on top of each end of each pier and each abutment prior to the start of the testing. These level readings were repeated three times during the test period and after the test was completed. The maximum observed settlement was 0.03 ft. and at most locations the settlement was less than 0.01 ft., which was the resolution of the measurements.

TABLE 3-2. PILE LOADS DURING FATIGUE TEST

	Abutment	Main Pier
No. of piles in footing	4	10
Static Load on Footing		
DL Superstructure	67^k	257^k
DL Substructure	59^k	108^k
DL Earth Fill	0	225^k
DL Ballast	14^k	46^k
Total Static Load	140^k	636^k
Dynamic Load on Footing	$\pm 46^k$	$\pm 70^k$
Maximum Load	186^k	706^k
Minimum Load	94^k	566^k
Resultant Load per Pile		
Static Load	35^k	64^k
Maximum Load	47^k	71^k
Minimum Load	23^k	57^k

CHAPTER 4

CRACK DETECTION METHODS

4.1 ULTRASONICS

During the course of the fatigue test a total of 17 inspections were conducted with a conventional pulse-echo ultrasonic unit. For crack detection the transducer was a 5 MHz 45 degree transceiver probe. During the initial inspection a 5 MHz 90 degree split crystal probe was used to locate the channel shear connectors which were welded to the top of the top flange and embedded in the slab.

The initial inspection was conducted before testing started and included complete inspection of both the top and bottom flanges at the ends of the cover plates in both the end and center spans. This initial inspection also included locating and marking the ends of the cover plates and shear connectors on the top flanges. The only flaw detected during this inspection was in the fillet weld at the end of the top flange cover plate on girder 3 at section 6. However, this flaw did not develop into a crack and there was no noticeable change in the flaw during the entire test.

Because bad weather had forced a very condensed testing schedule and ultrasonic inspection proved to be quite time consuming, subsequent inspections were in general limited to the critical regions of the bottom flanges around the ends of the cover plates in the end spans. The second inspection was conducted after 19,530 fatigue cycles. A total of six cracks each approximately 0.25 in. in length were discovered during this inspection. In every case the ultrasonics clearly

indicated that the crack was not at the toe of the weld as might be expected but rather at the heel of the weld as discussed in Art. 3.4.

At 95,000 cycles a total of ten cracks had been detected ultrasonically but it was not until 202,000 fatigue cycles that any of these cracks were seen visually at the surface. Even then they could be seen only with the aid of a dye penetrant (see Art. 4.2). Visual observations with the aid of the dye penetrant indicated that in some cases the crack in the weld was considerably longer than indicated by the ultrasonic measurement. This was at least in part due to the fact that without special techniques there is an ultrasonic blind spot directly below the web of the beam. In many cases where two cracks were recorded, one on either side of the web, they were actually connected through this blind spot forming a single crack.

All of these cracks were monitored for the remainder of the test and a complete record of crack lengths is presented in App. C. In those cases where the cracks propagated across the entire width of the flange it was possible to trace their growth ultrasonically to within approximately 0.1 in. of the edge before the crack became visible on the edge.

After completion of the test, two sections each containing two cracks which had arrested during the test were cut from the bridge and separated in the laboratory. It was then possible to compare the actual length of these cracks with the lengths indicated by ultrasonic measurements. For two of the cracks the ultrasonic measurements

were essentially correct. One ultrasonic measurement was in error by 0.25 in. and the other in error by 0.4 in.

For the critical regions at the ends of the coverplates on the bottom flanges, the conventional pulse-echo ultrasonic unit proved to be quite reliable in finding fatigue cracks under field conditions. All cracks which grew large enough to be detected visually had previously been detected ultrasonically when they were less than 1.5 in. in length and 60 percent of them were detected at a length of 0.25 in. Estimates of crack length based on ultrasonic inspection were reasonably accurate.

Ultrasonic inspection of the critical regions at the ends of cover plates on the top flanges was not so successful. Because stress ranges were low in the top flanges ultrasonic inspection was discontinued early in the test and was not resumed until two cracks had been observed visually. Of course, the failure to detect these two cracks ultrasonically cannot be interpreted as an adverse reflection on the capability of the ultrasonic inspection because no attempt was made to detect them. However, subsequent ultrasonic inspections of the other six critical top flange regions which were subjected to essentially the same stress histories, revealed no additional cracking. At the time of this writing the deck has not been removed from these girders and it is, therefore, not known whether or not cracks actually exist in these regions.* However, examination of the geometry

*See addendum, page 89.

of the detail at this joint indicates that it would be very difficult to detect cracking if it were to develop at the toe of the fillet weld as shown in Fig. 4-1. Under ideal conditions the surface of the crack is sometimes rough enough to reflect a signal directly back to the transducer, but under field conditions where the transducer must be acoustically coupled to a painted surface which tends to be rough and irregular, it is almost essential that the signal be reflected by doubling a corner if it is to be strong enough for detection. Thus, there is serious doubt about the reliability of conventional ultrasonic inspection to detect cracks in a detail of this type.

Two undetected cracks developed and grew to complete failure in girder 2 near the center line of the bridge. Since cracking was not expected in this region, there had been no ultrasonic inspection prior to development of the first crack. Immediately after the first crack developed the entire area was scanned ultrasonically but no additional cracks were detected. Although there was frequent monitoring of this region during the remaining 93,000 cycles of the test, no additional cracks were detected ultrasonically and the final failure was by sudden fracture of girder 2 approximately 3 ft. from the first fracture. The cracks leading to both of these fractures had initiated at heat numbers stamped into the flange. After the test loading was stopped, these regions were again examined very carefully with the ultrasonic probe but no cracks were detected.

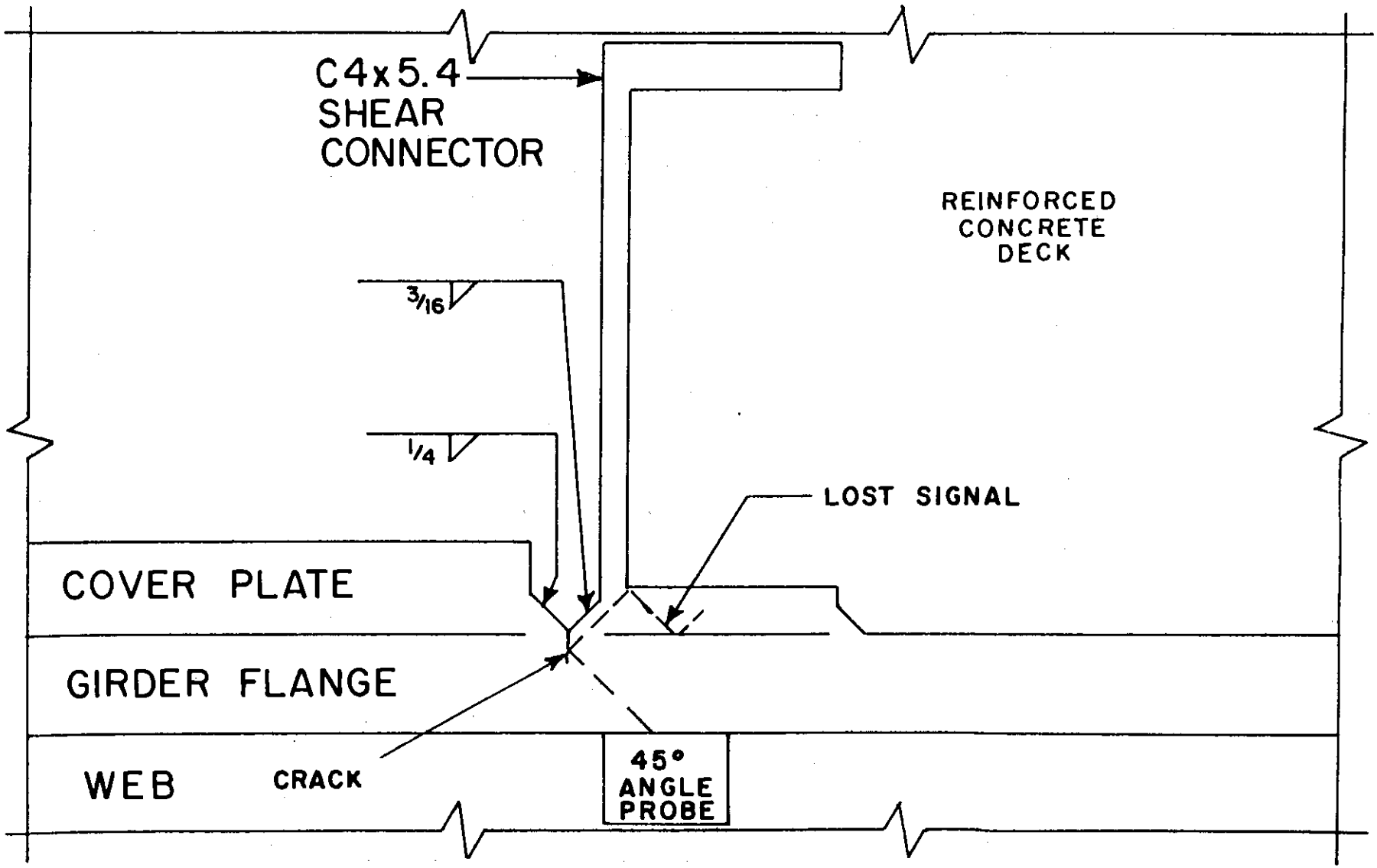

FIGURE 4-1. ULTRASONIC INSPECTION OF TOP FLANGE

4.2 DYE PENETRANT

Once the ultrasonic inspection indicated that cracks in the weld were 0.5 in. or more in length, repeated attempts were made to observe these cracks visually at the surface. When these attempts failed, a dye penetrant was introduced to enhance the visibility of the cracks. These attempts were also unsuccessful until the paint was removed from the area to be inspected. However, once the surface was free of paint, the dye penetrant gave a vivid indication of cracks which were previously invisible to the unaided eye. By reapplying the dye penetrant periodically, it was quite easy to trace the progress of crack growth during the remainder of the test.

Since the dye penetrant is quite easy to apply, and interpretation of the results requires no special training or skill, it would seem to be an excellent field inspection tool. However, for routine bridge inspection, the removal of paint in all of the areas to be inspected would be both difficult and expensive. It is quite likely that once the cracks open up enough to crack the paint, the dye penetrant could be used without removal of the paint. During this test, the paint was removed from all areas soon after the cracks were detected ultrasonically, and no data were recorded which would indicate how large the crack in the base metal must be before it penetrates the paint layer.

4.3 RADIOGRAPHY

Four sets of radiographs were taken by a commercial testing laboratory at 0, 98, 215, and 377 thousand cycles of load. A set of radiographs included one 7 in. by 17 in. film on each side of the bottom flange of each girder at sections 2 and 6. At 0 and 95,000 cycles, the set also included an identical series for the top flanges at sections 2 and 6. Of course, it was necessary to expose films of the top flanges through the six in. thick reinforced concrete deck slab and after two attempts it was concluded that interference from aggregate particles and reinforcing bars in the slab would obscure and prevent detection of any cracks which might be present in the top flange. Radiographs of the top flanges were discontinued after the second set. At 377,000 cycles, three additional films were shot along each side of each bottom flange at the centerline of span 2.

All exposures were made with a 90 curie source of iridium 192 at a distance of 16 in. Exposure times for the bottom flanges were 30 seconds and exposure times for the top flanges were 15 minutes.

At 95,000 cycles, no cracks were indicated on the radiographic examination report, while the ultrasonic inspection indicated ten cracks varying from 0.25 in. to 0.75 in. in length. At 215,000 cycles, the radiographic examination report indicated five cracks across the ends of the cover plates at the heel of the weld, while the ultrasonic inspection still indicated ten cracks two of which were 1 in. in length. However, four of the cracks which were detected radiographically, were indicated to be only 0.25 in. in length by the

ultrasonic inspection and had shown no growth since the previous ultrasonic inspection. The fifth crack had not been detected ultrasonically and the radiograph showed that it had already penetrated the base metal of the bottom flange.

At 377,000 cycles, the radiographic examination report indicated 12 cracks in the critical regions of the bottom flanges while the ultrasonic inspection indicated a total of 16 cracks. Again there was no general trend in comparing the crack lengths as indicated by the two methods. For some cracks, the radiograph indicated the greater length, while for others the ultrasonic inspection indicated the greater length. The largest crack, which had been observed both ultrasonically and visually with the aid of a dye penetrant to be in excess of 2.5 in. in length, was not detected radiographically.

The special films exposed in the center span covered a region of the bottom flanges approximately two feet on either side of the center line of the bridge. No cracks were detected other than the one complete fracture of girder 2. Unfortunately, the region covered by these films was not quite long enough to cover the section where the final fracture occurred approximately 93,000 cycles after these films were exposed.

Radiographic inspection suffers from some of the same shortcomings as ultrasonic inspection. There tends to be a blind spot in the center of the flange directly opposite the web. It is also much easier to detect cracks which are exactly perpendicular to the face of the

flange. This is because detection depends on the existence of a significant reduction in the density of material along a straight line through and perpendicular to the flange at the location of the crack. Thus, if the crack is not perpendicular to the face of the flange, the line intersects the crack for only a short length and there is little change in the total density of material along the line. It is also much easier to detect cracks which are open than those which are tightly closed.

4.4 ACOUSTIC EMISSION

During the fatigue test, acoustic emission measurements were made at eight locations on the bridge as a means of monitoring crack growth. Acoustic emission sensors were attached to the bottom flanges of the steel girders in the end spans where the welded cover plates over the piers terminated. These locations were in the critical fatigue regions that were subjected to periodic ultrasonic inspections during the fatigue test. The locations of the sensors are shown in Fig. 4-2.

Each sensor consisted of a piezoelectric element connected in a differential mode. The resonant frequency of a sensor was 230 KHz. and the electronic filters in the instrumentation setup provided a frequency bandpass from 100 KHz to 400 KHz.

Acoustic emissions data were recorded as an amplitude count per second of time. A one second interval was tantamount to approximately two fatigue cycles for the bridge. An emission count at each location

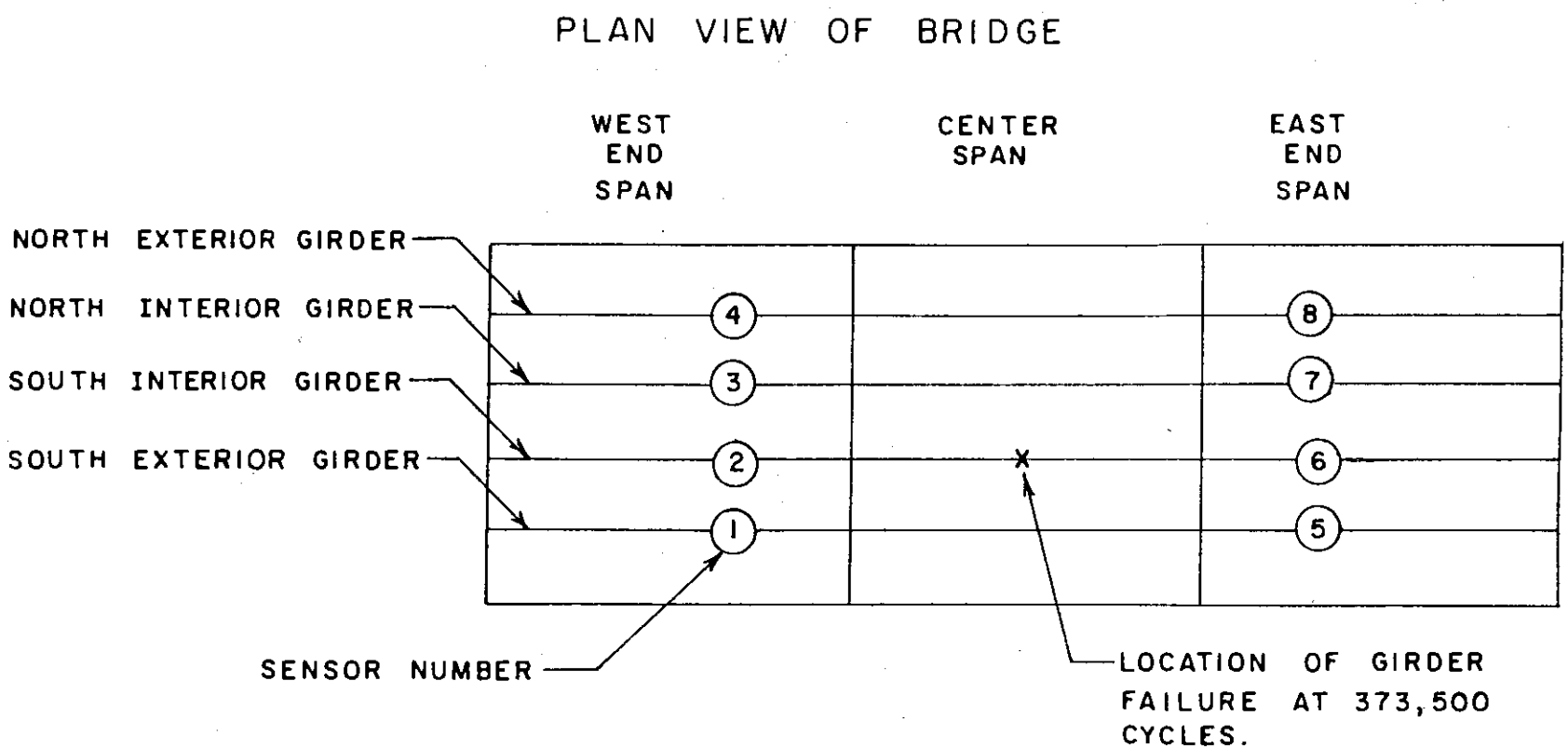

FIGURE 4-2. LOCATION AND NUMBERING SCHEME FOR ACOUSTIC EMISSION SENSORS

was taken over a 150 second interval. The eight sensors were coupled to a common amplifier so that data from each sensor could be recorded serially on an x-y plotter.

The fatigue test was initiated prior to installation of the sensors. Consequently, the first set of data was taken at 56,000 fatigue cycles. Fourteen sets of data were obtained during the fatigue test. At the outset of the emission monitoring there appeared to be a repetitive noise in the sensor output signal during a portion of the bridge fatigue cycle. Therefore, the emission count was inhibited over that portion of the cycle. The inhibit circuitry was subsequently disconnected after the seventh data set was recorded at 281,000 cycles.

Figure 4-3 illustrates the mean value of the emission amplitude count per second for each of the 14 data sets for sensors 1 and 8. Failures occurred in the girder flanges within three feet of sensors 1, 5 and 6. Ultrasonic inspections (see Art. 3.4) revealed these failures after 462,000, 455,000 and 453,000 fatigue cycles respectively. The maximum nominal tensile stress due to dead, ballast and inertial loading was 15 ksi at the locations of sensors 1 and 6. The corresponding tensile stress at the location of sensor 5 was 2 ksi. At these stress levels the acoustic emission rate is normally quite low. Consequently the growth of fatigue cracks at these locations is not discernible in the recorded emission count.

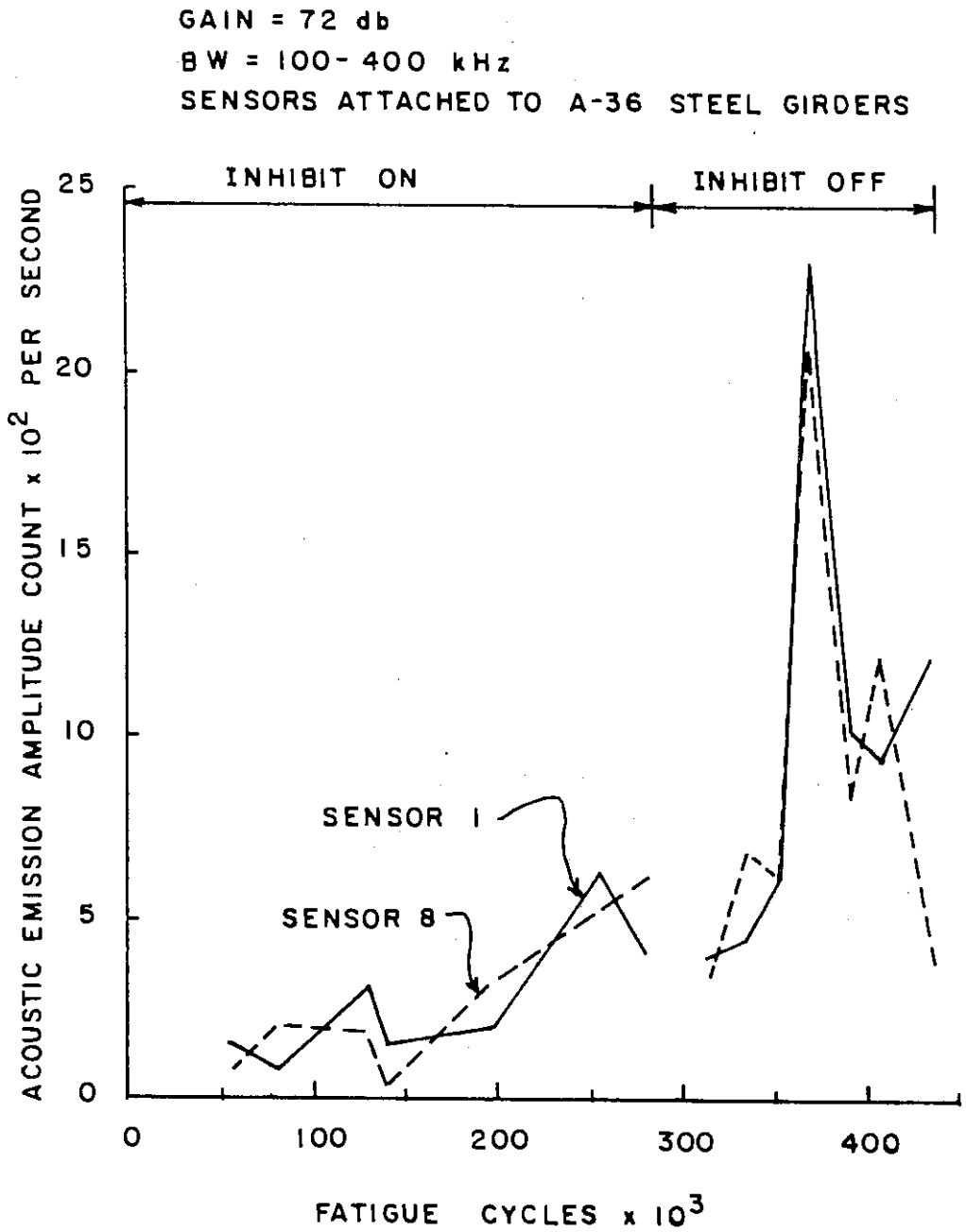

FIGURE 4-3. ACOUSTIC EMISSION AMPLITUDE COUNT DURING BRIDGE FATIGUE TEST

However, one notable failure of an entire cross section of a girder did occur at the midspan of the south interior girder at 373,500 cycles. In this section the maximum nominal tensile stress was 27 ksi. The emission count recorded at 370,000 cycles was unusually high for all sensors. Figure 4-3 illustrates this for sensors 1 and 8. The failure occurred approximately 25 minutes after the data were obtained.

Appendix E of this report contains a more detailed description of the test procedures and results.

4.5 RANDOMDEC

The Randomdec technique of analyzing high frequency vibration signatures was employed as an inspection method by instrumenting the bridge with accelerometers at 24 stations as shown in Fig. 4-4. These stations were at the ends of the cover plates located on the top and bottom flanges of the girders in the two end spans. Two accelerometer stations were positioned in each bottom flange region and one accelerometer station was positioned in each top flange region.

Two means of excitation of the bridge were employed for this study. The first method of excitation was a high frequency excitation in the form of a steel-wheel dolly towed across the unballasted bridge by a fork lift truck. The second method of excitation was the fatigue loading of the ballasted bridge. The use of the second method of excitation permitted a greater number of acceleration records to be recorded during the fatigue test than was possible with the first

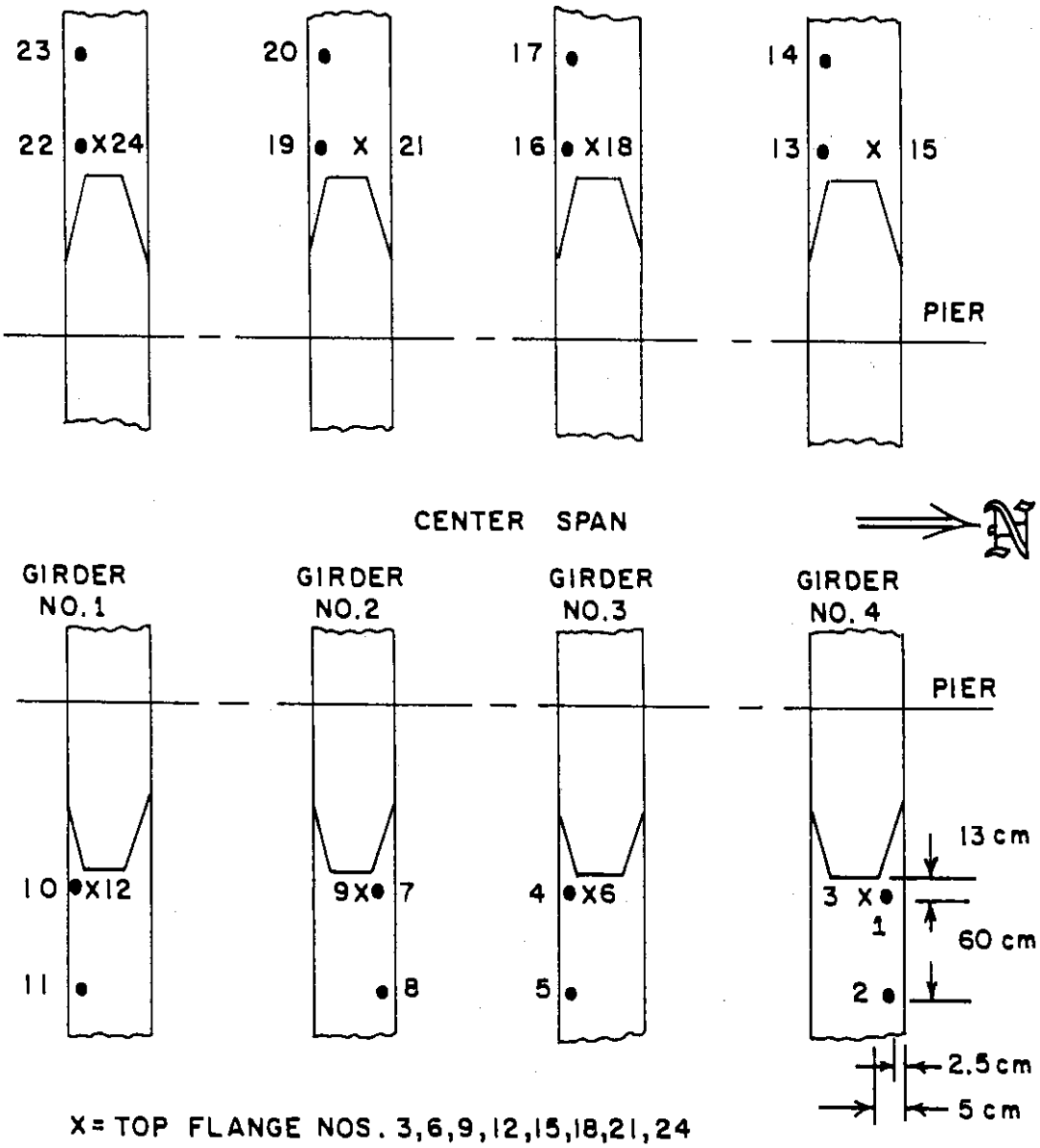

X = TOP FLANGE NOS. 3,6,9,12,15,18,21,24

● = BOTTOM FLANGE

PLAN VIEW (LOOKING DOWN ON GIRDERS)

FIGURE 4-4. TRANSDUCER STATIONS

method. However, the decision to employ the second method of excitation was made approximately midway through the fatigue test.

Detailed results of the Randomdec analysis of the accelerometer records are presented in reference[8]. However, some of the significant results obtained from this study are presented below.

Changes in the structural characteristics of the bridge were detected using both the dolly loading and the fatigue loading. Results obtained from the fatigue loading of the bridge will be discussed first. The Randomdec analysis of the acceleration records at station 10 (Section 6.1B) revealed that a large change in the vibration signature took place between 250,000 and 314,000 cycles. However, the amount of change in the vibration signature decreased between 314,000 and 360,000 cycles with very little change occurring after 365,000 cycles. This result is consistent with the findings of the ultrasonic inspection (see section 6.1B in Table C-2) which showed very little growth of the cracks in this zone between inspections at 360,870 and 380,000 cycles. The analysis of the acceleration records associated with station 19 (section 2.2B) showed that a drastic change occurred in the vibration signature between 278,000 and 320,000 cycles. This sudden change in the vibration signature correlates with the ultrasonic inspections of this zone (see section 2.2B in Table C-2) in which no cracks were detected at 215,000 cycles, but large cracks were observed at the next ultrasonic inspection which occurred at 287,000 cycles.

No changes in the vibration signature were observed in the bottom flanges of the girders as a result of the dolly loading. It is felt that this is due to the fact that the dolly loading was not sufficient to open up the cracks which were initially in compression due to the dead load of the bridge. However, both the dolly and the fatigue loading produced results which show changes in the vibration characteristics at some of the top flange locations. The analysis of the accelerometer records at station 21 (section 2.2A) indicated that a severe change in the vibration signature occurred between 270,000 and 302,000 cycles. This result suggests that this drastic change in the vibration signature is an indication of a sudden fracture in the top flange in the vicinity of section 2.2A. However, no fatigue fracture was observed visually at this location.

Finally, the failure which occurred in one of the interior girders in the center span was not predicted during this aspect of the study since none of the accelerometer stations were anywhere near the center of the midspan. The closest accelerometer station was 75 ft. from the failure and this distance was too large for a change in the vibration signature to be detected from the accelerometer records which were recorded only over a high frequency range of the response.

4.6 FHWA ACOUSTIC AND MAGNETIC CRACK DETECTOR UNITS

The Acoustic Crack Detector, ACD, unit is designed for the detection of internal flaws in steel members at some distance from the unit. This device emits acoustic waves which are passed through

a couplant to the steel member. The reflection of the acoustic wave off of a flaw or discontinuity in the steel is used to estimate electronically the presence and location of a crack or edge of the member.

The Magnetic Crack Definer, MCD, unit was designed to be used in conjunction with the ACD. The MCD is a magnetic field and eddy current device which has a very limited operating range and thus is not employed until a crack or discontinuity has been detected by the ACD. The MCD is used to essentially define the perpendicular direction of a flaw or discontinuity.

During the checkout of the ACD with a test block, it was observed that proper readout could not be obtained because of a failure of some of the LED's (Light Emitting Diodes) in the probe-readout head. However, an attempt was made to use this probe to detect cracks in a test bar and to locate the edge discontinuities of a girder flange. Neither of these tests produced positive indications of flaws or discontinuities.

A new probe for the ACD unit was obtained from the FHWA. A checkout of this probe indicated that a major malfunction had occurred. An examination of the probe in consultation with FHWA technicians showed that the malfunction was in the plug. When this problem was corrected, a probe readout and battery check indicated that the unit was operable. However, the new probe would not give the proper indications when coupled to the calibration block on the ACD pack. No further efforts were made to use the ACD unit.

4.7 DAMPING RATIOS, RESONANT FREQUENCIES AND VIBRATION SIGNATURES

The dynamic tests were performed for the purpose of evaluating changes in the dynamic properties of the bridge. Three of the dynamic tests performed on the bridge were

1. Transient Response Test,
2. Frequency Response Test, and
3. Sweep Test.

The objectives of the first two dynamic tests were to determine the equivalent linear viscous damping of three different modes and to evaluate the usefulness of damping in detecting structural damage. The purpose of the sweep test was to obtain vibration signatures of the bridge in the form of mechanical impedance plots and to evaluate whether or not changes in the mechanical impedance signify the presence of structural deterioration. This section presents the significant results from these tests. A detailed discussion of the analysis technique and a more comprehensive presentation of the results is contained in App. A.

Damping ratios were calculated from the transient response of the first three modes of the bridge by the logarithmic decrement and Fourier transform decay methods. The bandwidth method was used to determine the damping ratios for the first three modes from the frequency response curves associated with both up and down sweeps of a quasi-steady forced excitation of the bridge.

Table 4-1 presents a summary of the damping ratios associated with the first three modes of the bridge as determined from the experi-

TABLE 4-1 COMPARISON OF DAMPING RATIO'S AS OBTAINED FROM FOUR DIFFERENT CALCULATION METHODS

First Bending Mode Damping Ratio's (% Critical)						
Dynamic Test No.	Transient Response(1)			Frequency Response(1)		Normal Mode
	Log Decrement		Transform	Up Sweep	Dn. Sweep	
1	1.1*	1.2**	1.1	1.3	1.8	1.3
2	1.6	1.7	2.5	1.0	1.4	2.0
3			2.2	1.0	1.7	1.7
4			2.7	1.8	2.1	1.9

(1) From data taken at Station 17
* Based on linear curve fit to data
** Based on quadratic curve fit to data

First Torsional Mode Damping Ratio's (% Critical)						
Dynamic Test No.	Transient Response(2)			Frequency Response(2)		Normal Mode
	Log Decrement		Transform	Up Sweep	Dn. Sweep	
1	.9	.6	1.6	1.7	1.9	1.3
2	1.4	2.2	3.3	.8	2.9	2.2
3			3.1	.8	2.0	2.0
4			2.7	1.6	2.1	1.7

(2) From data taken at Station 16

Second Bending Mode Damping Ratio (% Critical)						
Dynamic Test No.	Transient Response(3)			Frequency Response(3)		Normal Mode
	Log Decrement		Transform	Up Sweep	Dn. Sweep	
1	1.0	1.4	1.2	1.3	1.6	1.3
2	1.6	2.3	2.8	1.5	1.6	1.9
3			2.2	1.4	1.7	1.6
4			2.1	1.3	1.4	1.5

(3) From data taken at Station 29

mental data by the various damping ratio calculation methods employed during this study. The damping ratios, as determined by the logarithmic decrement method, are presented only for the first two tests in Table 4-1 because it was not possible to use this method in Tests 3 and 4 due to the presence of multi-frequency components in the transient response. The normal mode results presented in Table 4-1 are discussed in more detail in Art. 4.8 and App. B.

The damping ratios obtained by the various methods show some differences in the magnitude of the results for a given test. However, all of the various methods predict the same overall trends in the damping ratios between the different tests and the three modes.

The cumulative damage to the bridge had a considerable influence on the damping ratios associated with each of the three modes over the course of the fatigue test. In general, there is a considerable increase in the damping ratio for each of the modes between Test 1 and 2. This increase in the damping ratio can be accounted for by (1) slippage which developed between the deck and the girders; and (2) working of the cracked surfaces in the reinforced concrete deck. This latter influence on the damping of the bridge was very evident during a rainstorm in which a lime slurry was pumped from the cracks. All three modes show a general but moderate decrease in the damping ratios between Tests 2 and 3. This decrease is probably due to a decrease in the working of the cracked surfaces in the reinforced concrete deck. Although

there is a change in the damping ratios for all three modes between Tests 3 and 4, there is no definite trend. However, the damping present in the bridge is still higher in Test 4 for each of the modes than it was in Test 1.

Although the damping ratio as a dynamic property is affected by the cumulative fatigue damage, there is no indication from the results found in this part of the study that changes in the damping ratio will provide information on the location of the damage. However, the monitoring of changes in the damping ratio over the service life of the bridge may provide information that changes are taking place in the structural integrity of the bridge.

Table 4-2 presents the resonant frequencies of the bridge as determined from the frequency response curves associated with the first three modes. All of the results are for a forced excitation level of 0.7 g's peak single amplitude relative acceleration of the moving mass.

The results show that the first three resonant frequencies of the bridge decreased continuously from Test 1 to Test 4 with one exception. The exception occurred in the second bending mode where there was an increase in the resonant frequency from Test 2 to Test 3 Thus, the resonant frequencies of the bridge are definitely affected by the structural damage to the bridge and are an indicator that some change is taking place in the dynamic characteristics of the bridge.

TABLE 4-2 EXPERIMENTAL RESONANT FREQUENCIES

DYNAMIC TEST NO.	TEST 1		TEST 2		TEST 3		TEST 4	
MODE	UP	DOWN	UP	DOWN	UP	DOWN	UP	DOWN
First Bending	2.828	2.813	2.640	2.640	2.596	2.581	2.446	2.448
First Torsion	3.540	3.536	3.259	3.238	3.174	3.185	2.995	2.980
Second Bending	4.520	4.526	4.134	4.150	4.175	4.175	4.070	4.086

However, changes in the resonant frequencies give no indication as to the location of the damage.

The most significant indications of change in the dynamic properties of the bridge are provided by the vibration signatures in the form of mechanical impedance plots. These plots, which included the lowest five resonant frequencies of the bridge, indicate the deterioration in the reinforced concrete deck between Tests 1 and 2 and the failure and fatigue damage in the girders which occurred between Tests 3 and 4. Figures 4-5 through 4-7 show a set of overlays of the mechanical impedance plots for Tests 1 and 2, Tests 2 and 3, and Tests 3 and 4, associated with station 15.

The structural damage to the reinforced concrete deck which mainly occurred between Tests 1 and 2 appears as an overall significant change in the mechanical impedance plots, as illustrated in Fig. 4-5. The greatest change in the mechanical impedance plots between Tests 3 and 4 occurred at stations 9 and 15, which were the closest stations to points of fatigue damage and failure in the bridge girders. The change in the mechanical impedance plots between Tests 3 and 4, as shown in Fig. 4-7, suggests that structural damage to the girders appears as a change in the values of mechanical impedance at resonance and anti-resonance in the higher order frequency range.

The use of vibration signatures in the form of mechanical impedance plots shows promise as a means of detection of fatigue damage and thus, may have future potential as an inspection technique. However, further study is needed to fully evaluate this method as an inspection technique.

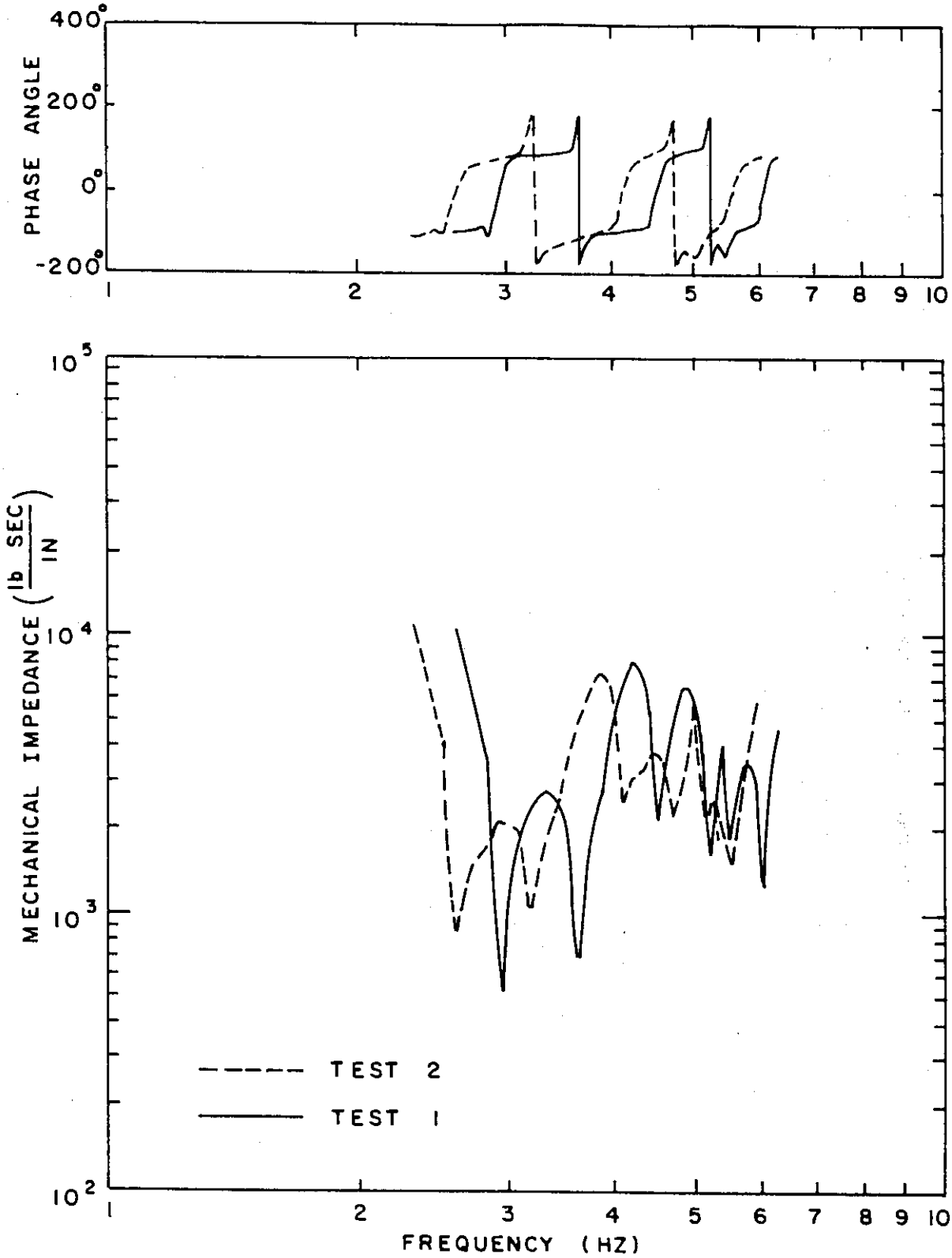

FIGURE 4-5. MECHANICAL IMPEDANCE, STATION 15, TEST 1 AND 2

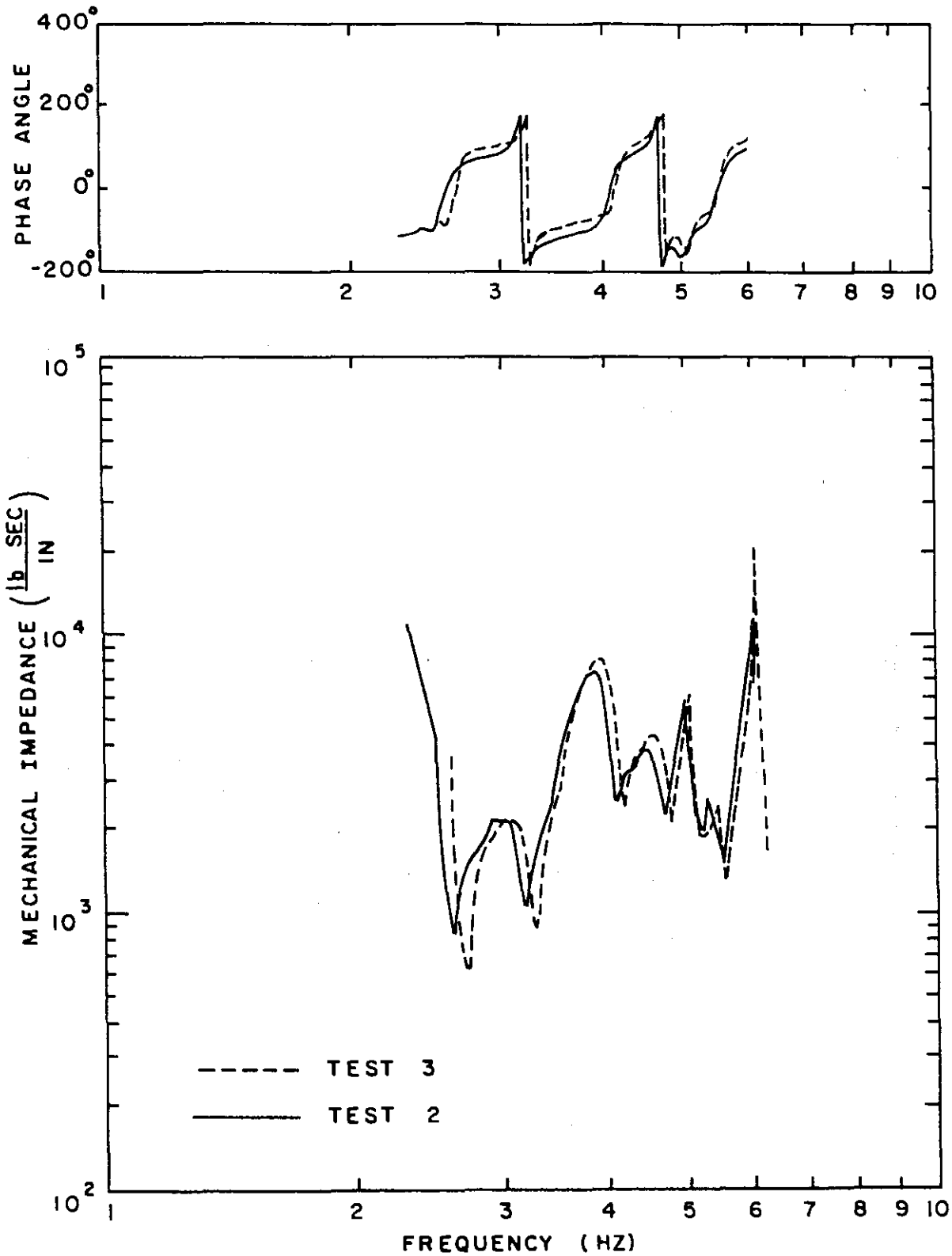

FIGURE 4-6. MECHANICAL IMPEDANCE, STATION 15, TEST 2 AND 3

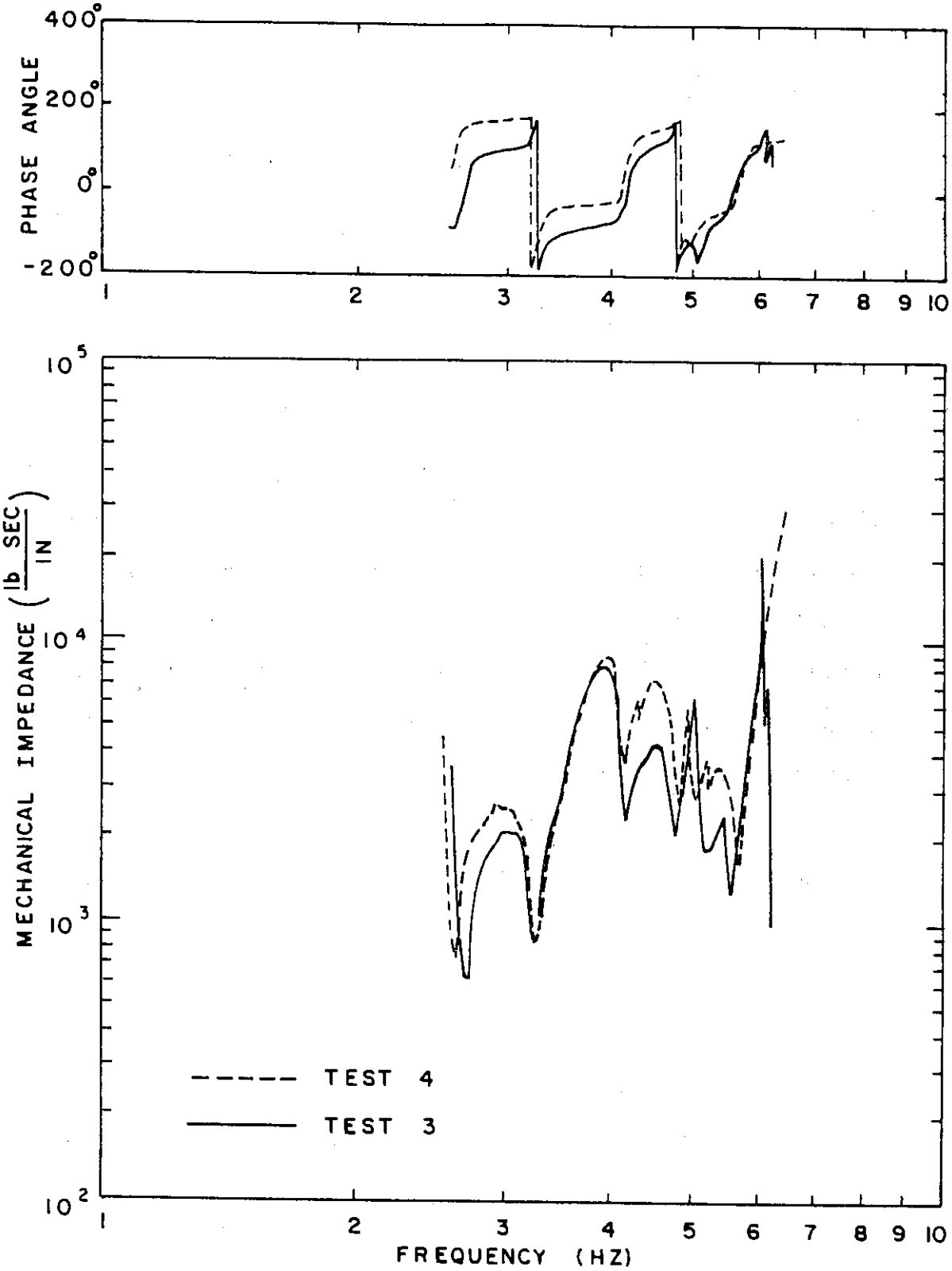

FIGURE 4-7. MECHANICAL IMPEDANCE, STATION 15, TEST 3 AND 4

4.8 MULTI DEGREE-OF-FREEDOM

Prior to the field test, an extensive series of dynamic analyses was performed to predict the force requirements and response (deflections and stresses) of the bridge. Both ballasted and unballasted cases were considered in the finite-element analysis. Three states of deterioration of the bridge deck were included in the analyses. These states were fully composite, composite and cracked slab composite. The fully composite state assumed that the deck over the entire length of the bridge was acting compositely with the girders. In the composite state, the deck was assumed to be acting compositely with the girders in the positive dead load moment regions. In the negative moment regions, only the reinforcement acted compositely with the girders; whereas, in the cracked slab composite state, only the deck reinforcement acted compositely with the girders over the entire length of the bridge. The fully composite and cracked slab composite states provided upper and lower bounds respectively for the anticipated behavior.

One aspect of this study was to evaluate the dynamic properties of the bridge. To accomplish this task, a series of forced vibration normal mode resonance tests was conducted prior to initiating the fatigue test and during interruptions in the fatigue test. Each series of normal mode tests consisted of exciting the unballasted bridge in its first bending mode, second bending mode and first torsional mode. The level of excitation during these tests was approximately 1/8 of the excitation applied in the fatigue test. Accelerations were measured at 22 locations (stations) on the underside of the

bridge deck in order to establish the mode shapes. These mode shapes were subsequently used in the calculations for the dynamic properties of the bridge.

Table 4-3 presents the calculated frequencies for the three states and the measured frequencies during the fatigue test and normal mode tests. A comparison of the tabulated frequencies reveals that the changes in frequency during the fatigue test were small. For the normal mode tests, the frequencies increased slightly in some instances in the third and fourth tests. It should be noted that Test 4 was conducted with the fracture in the flange and web of the south interior girder at midspan.

Plots of the measured accelerations at arbitrary stations revealed that the bridge response was symmetric in all modes in Test 1. However, in Test 3, the negative portion of the response in the first bending mode was not symmetric with respect to the positive portion of the response. The lack of symmetry was more pronounced in Test 4. The torsional and second bending modes appeared to be symmetric in all four tests.

A spectral analysis was performed on all of the acceleration data. This analysis displayed the presence of a harmonic component in the response in only the first bending mode in Tests 3 and 4. The harmonic in Test 4 was expected in view of the fracture in the girder at midspan. However, the harmonic was also present in Test 3 which was conducted 62,000 fatigue cycles prior to the fracture. A

TABLE 4-3. PREDICTED AND MEASURED FREQUENCIES

FATIGUE TEST

Predicted		Measured	
State	Hz	Fatigue Cycles (k)	Hz
Fully Composite	2.600	0	2.32
Composite	2.480	31.3	2.067
Cracked Slab Composite	1.600	91.5	2.066
		190.2	2.025
		241.0	2.032
		470.4	1.932

NORMAL MODE TESTS

Predicted (Hz)

State	First Bending	First Torsion	Second Bending
Fully Composite	2.908	3.104	4.633
Composite	2.530	2.769	4.420
Cracked Slab Composite	1.892	--	3.020

Measured (Hz)

	Test 1	Test 2	Test 3	Test 4
First Bending	2.869	2.507	2.638	2.385
First Torsion	3.507	3.270	3.047	3.136
Second Bending	4.507	4.120	4.177	3.987

spectrum of the response in the first bending mode in Test 3 is shown in Fig. 4-8.

Lack of symmetry and the harmonics in the response of the bridge in the first bending mode in Tests 3 and 4 were indications that the structure had deteriorated.

The mode shapes for the two exterior girders obtained from a spectral analysis of the acceleration data were also plotted. These plots disclosed that the shapes for the two girders differed. This was evident in all the normal mode tests. Figure 4-9 depicts the second bending shape in Test 3. The difference in shapes increased as the fatigue tests progressed.

Damping ratios calculated for each of normal mode tests ranged from 1.3 to 2.2 percent. The ratios increased from Test 1 to Test 3 and then decreased in Test 4. This trend was also observed in the Phase I[5] study.

Stiffness and damping coefficients based on a lumped parameter system analysis were computed for the exterior girders. Changes in these coefficients between Tests 1 and 3 ($\Delta K_{(3-1)}$, $\Delta C_{(3-1)}$) and Tests 1 and 4, ($\Delta K_{(4-1)}$, $\Delta C_{(4-1)}$) are shown for the south girder in Fig. 4-10.

The stiffness plots demonstrate that the bridge was deteriorating. However, the fracture in the interior girder adjacent to Station 11 is not evident from an examination of Fig. 4-10.

A detailed description of the test procedures and the results is contained in App. B.

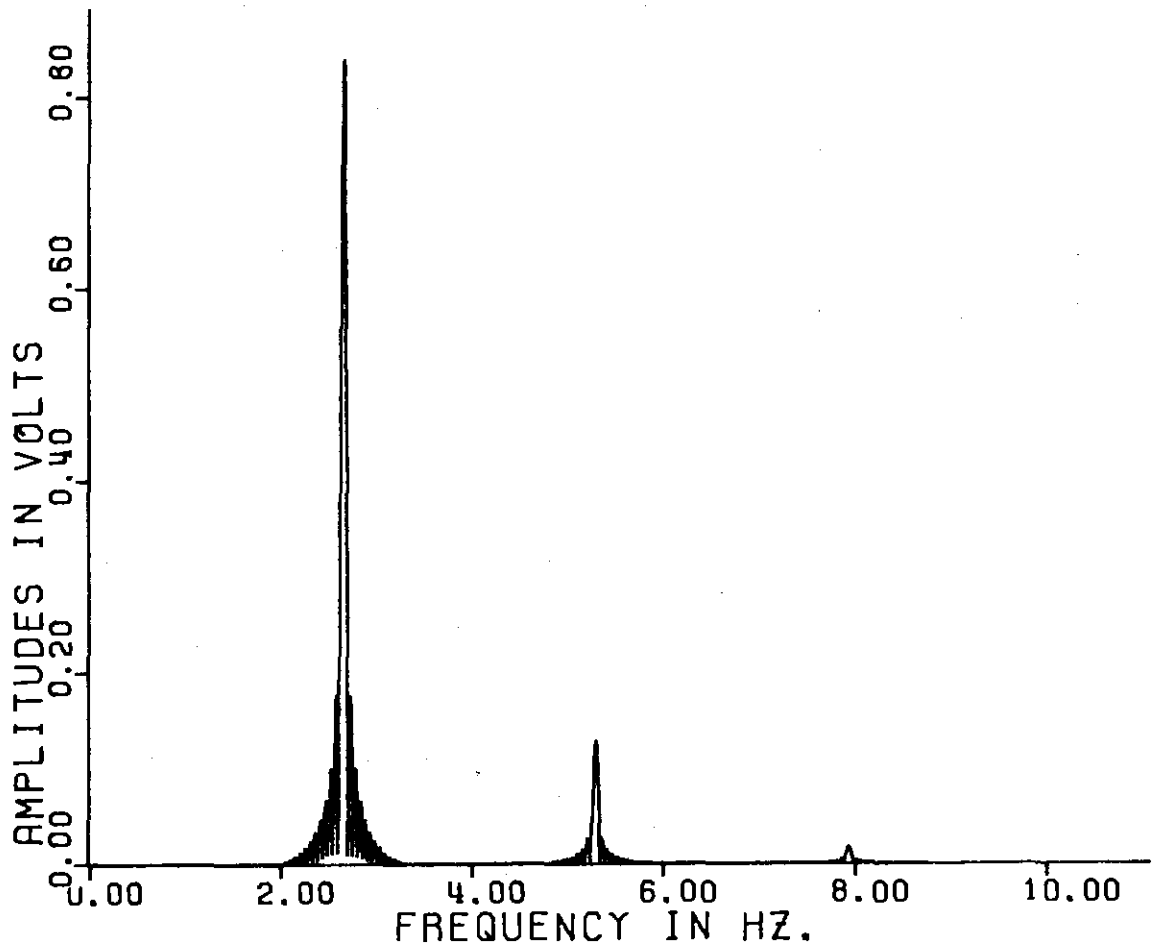

FIGURE 4-8. SPECTRUM OF RESPONSE - B13

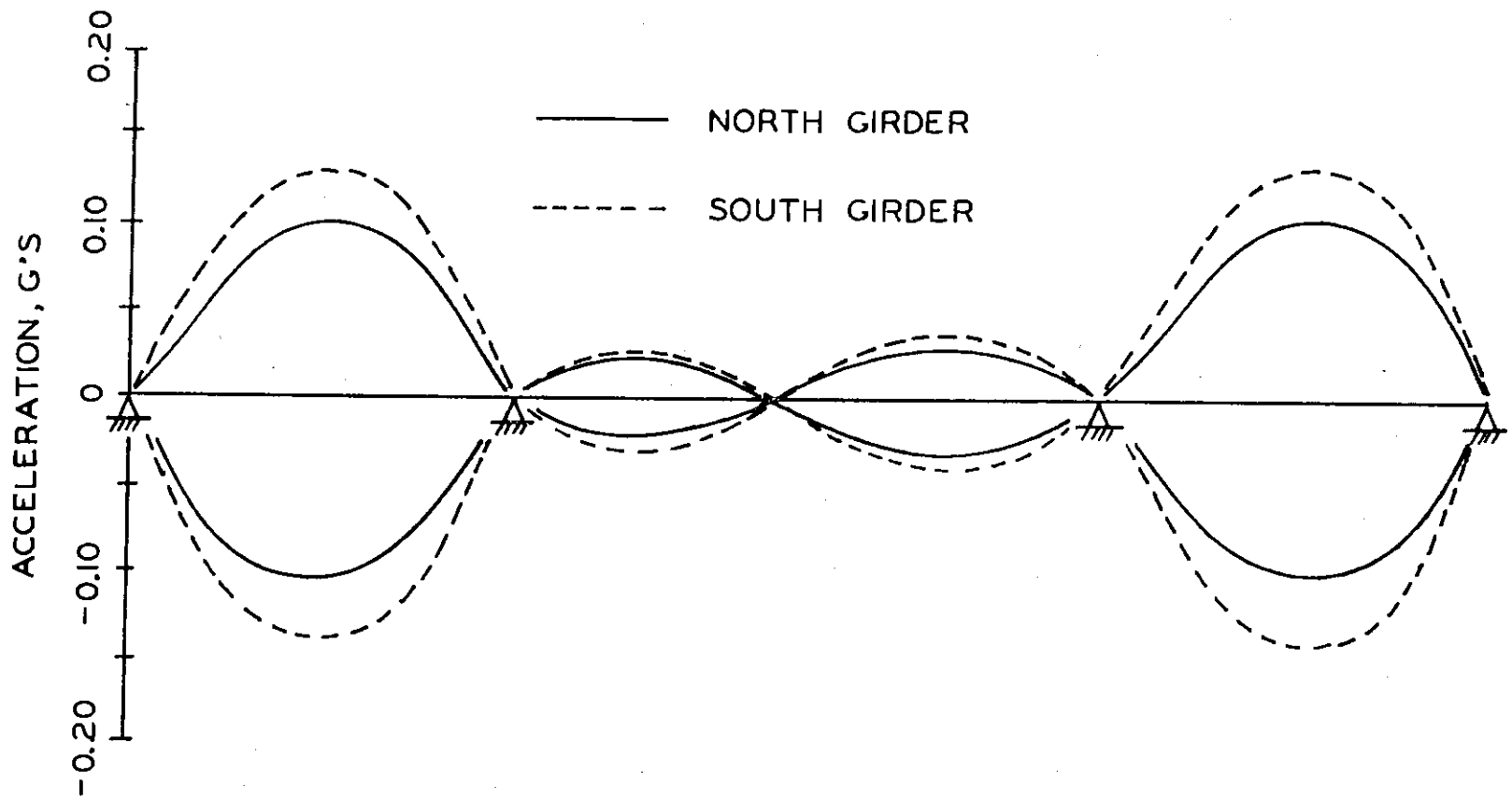

FIGURE 4-9. MODE SHAPE - B23

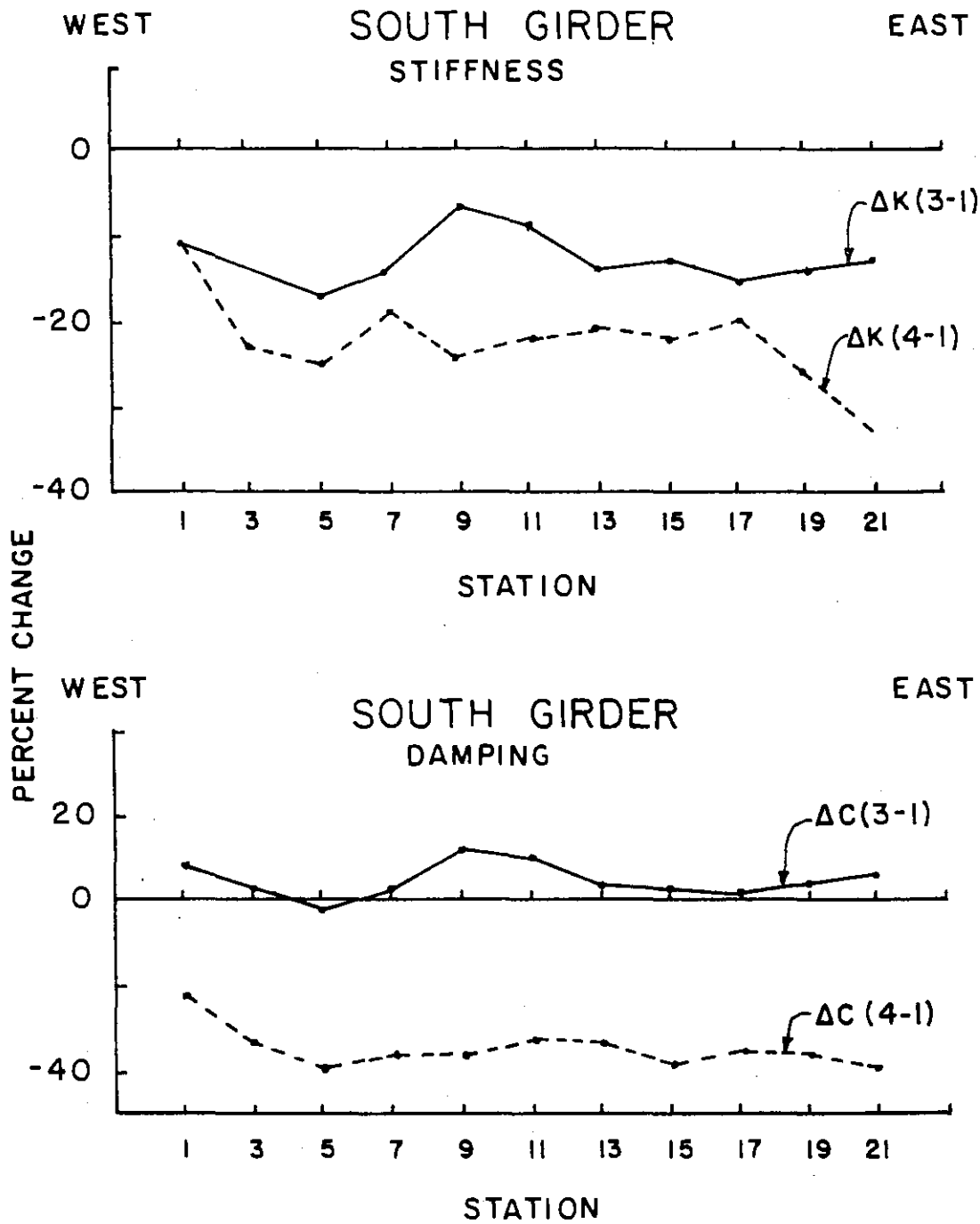

FIGURE 4-10. CHANGES IN STIFFNESS AND DAMPING
22 DOF MODEL

ADDENDUM

Subsequent to the initial writing of this report and just prior to its publication, the contract for demolition of the bridge was completed, making it possible to examine the top girder flanges which had previously been embedded in the concrete deck. The following is a brief summary of observations made at that time.

During demolition, the concrete was quite easily broken away from the reinforcing bars and shear connectors, indicating that damage to the concrete during the test had been extensive. It was clear that on many of the bars, especially the transverse reinforcement, bond had been broken by the prolonged high amplitude fatigue loading.

A total of five shear connectors had failed by fatigue. Four of the failures were at the east end of the center-span positive-moment region of girder number 1. The other failure was the end connector at the west or opposite end of the center-span positive-moment region of girder no. 1. All of these failures were by fatigue of the channel web with the exception that in one case a small region of the channel flange was also broken out, Fig. 5-1. A few additional shear connectors had also developed fatigue cracks, Fig. 5-2.

In addition to sections 2.1A and 6.2A where the top flanges were completely severed by fatigue cracking, cracks in the welds at the ends of the cover plates were detected with dye penetrant at sections 2.2A, 2.3A, and 6.1A, Figs. 5-3 through 5-5. Details of the welds between the shear connectors and the ends of the cover plates at these locations were not exactly as indicated by the drawings, Fig. 3-15, in that the two fillet welds tended to overlap forming a shallow trough rather than a deep sharply-defined V notch, Fig. 5-6.

These welds which were made in 1962 were probably done with a stick welder and there is evidence that the weld beads were restarted in the region of overlap. Thus, although the general geometry of the joint is not sharp it is quite possible that cold laps or even shrinkage cracking existed at the weld intersection. If in fact such defects were present they could account for the relatively low number of cycles to failure of sections 2.1A and 6.2A.

In all cases the cracks did initiate at the intersection of the two welds. In the case of section 2.1, this intersection was very near the end face of the cover plate. Unfortunately, the nearly two years which elapsed between the end of the fatigue test and demolition of the bridge permitted severe corrosion of the fracture surfaces and so far it has not been possible to determine the exact point of crack initiation at section 2.1. At section 6.2 there was a three-sixteenths inch slag inclusion, Fig. 5-7, at the weld intersection, and it is highly likely that the fatigue crack initiated from this point. None of these cracks in the top flanges were detected ultrasonically prior to visual observation.

FIGURE 5-1. FATIGUE FAILURE OF SHEAR CONNECTOR

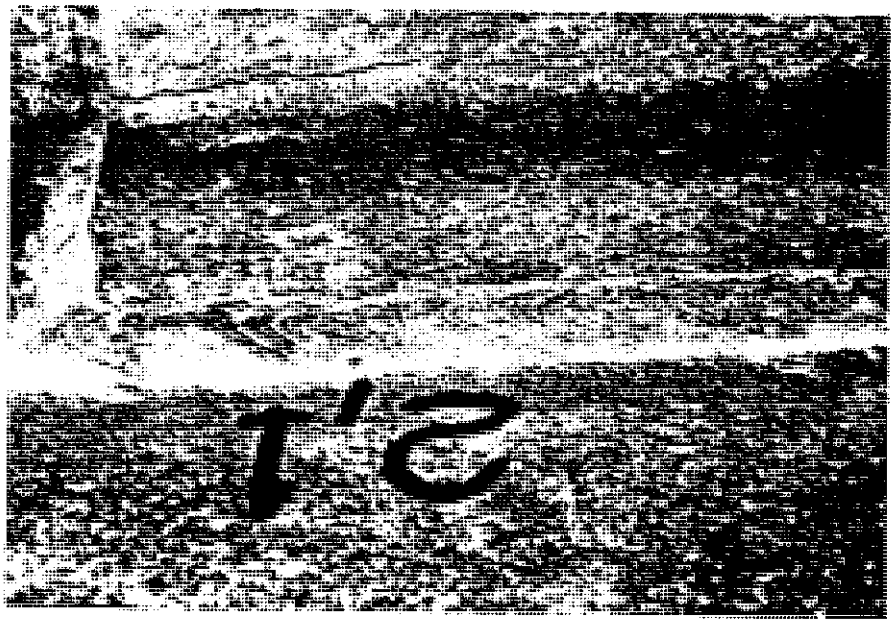

FIGURE 5-2. FATIGUE CRACK IN SHEAR CONNECTOR

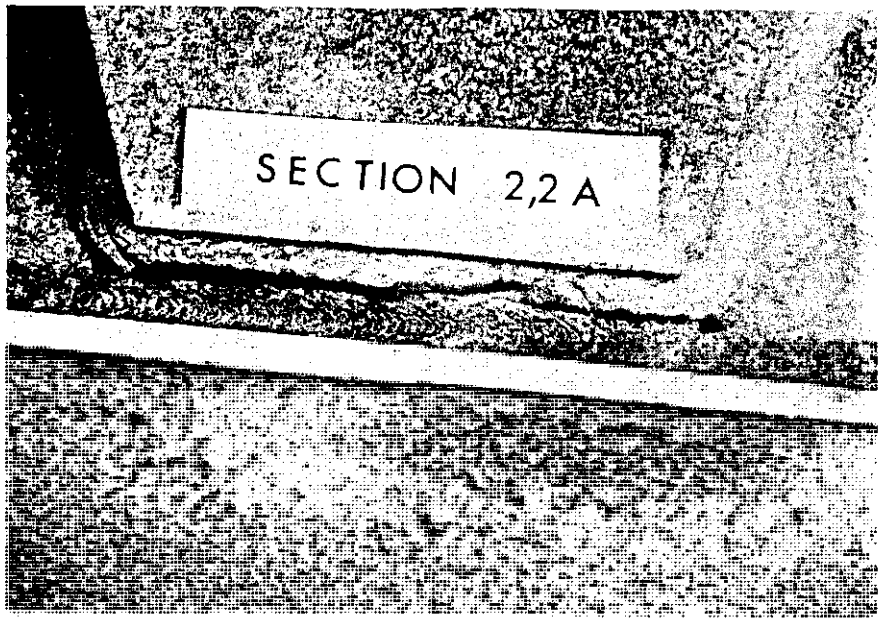

FIGURE 5-3. DYE PENETRANT CRACK DETECTION AT SECTION 2.2A

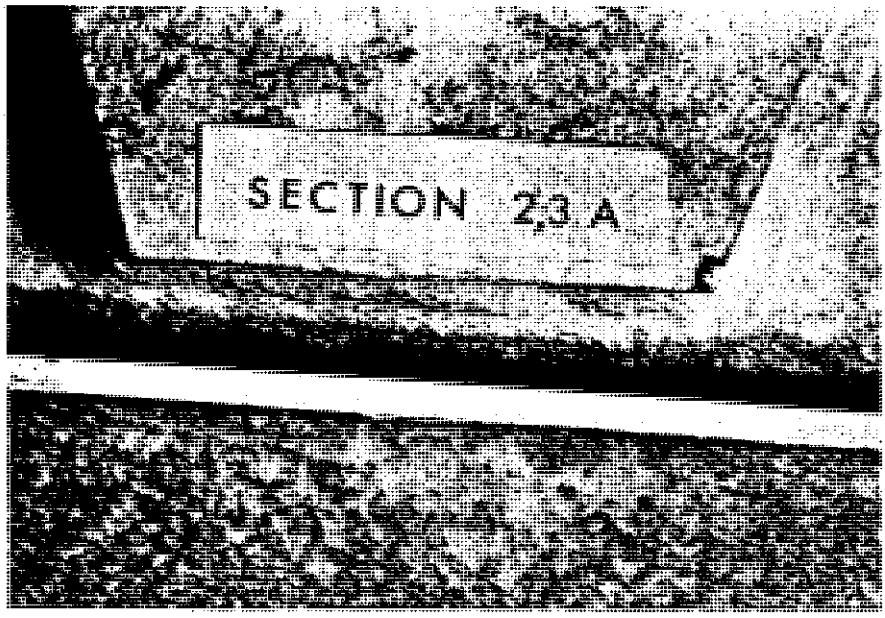

FIGURE 5-4. DYE PENETRANT CRACK DETECTION AT SECTION 2.3A

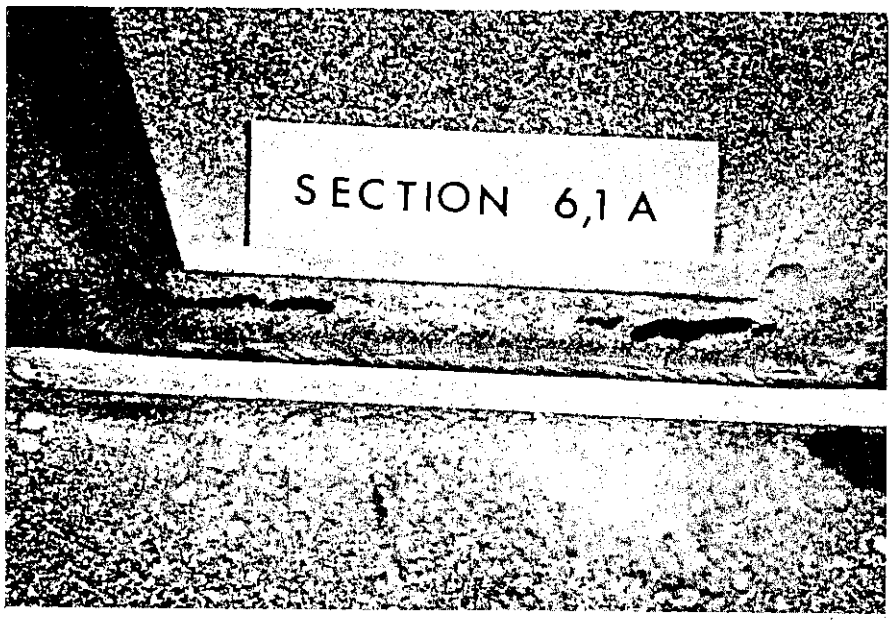

FIGURE 5-5. DYE PENETRANT CRACK DETECTION AT SECTION 6.1A

FIGURE 5-6. FAILURE AT SECTION 2.1A

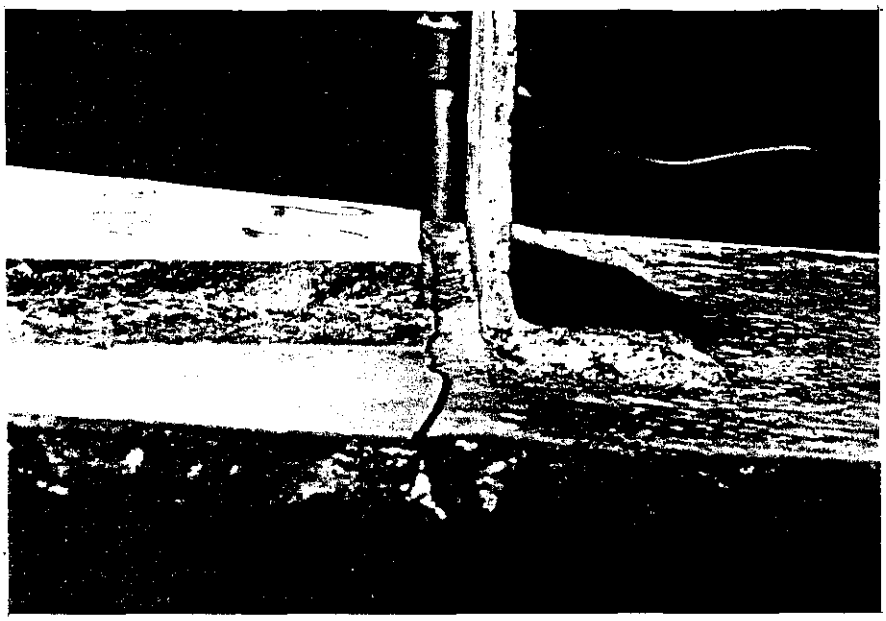

FIGURE 5-7. FAILURE AT SECTION 6.2A

REFERENCES

(1) Fisher, J. W., Frank, K. H., Hirt, M.A., and McNamee, B. M., "Effect of Weldments on the Fatigue Strength of Steel Beams," NCHRP Report 102, Highway Research Board, 1970.

(2) Highway Research Board, "The AASHO Road Test, Report 4, Bridge Research," Special Report No. 6117, National Academy of Sciences National Research Council, Washington, D.C., 1962.

(3) American Society of Civil Engineers, Subcommittee on Cover Plates of the Task Committee on Flexural Members, J. W. Fisher, Chairman, Commentary on Welded Cover-Plated Beams," Journal of the Structural Division," ASCE, Vol. 93 No. ST4, Aug. 1967, pp. 95-122.

(4) Fisher, J. W., "AISC Guide to 1974 AASATO Fatigue Specifications," Draft Copy.

(5) Salane, H. J., Duffield, R. C., McBean, R. P., Baldwin, J. W., and Galambos, T. V., "An Investigation of the Behavior of a Three-Span Composite Highway Bridge," Report 71-5 Missouri Cooperative Highway Research Project, University of Missouri-Columbia, Nov. 1971.

(6) American Association of State Highway Officials, Standard Specifications for Highway Bridges, Washington, D.C., Eighth Edition, 1961.

(7) McGarraugh, J. B. and Baldwin, J. W., "Lightweight Concrete-on-Steel Composite Beams," AISC Engineering Journal, July 1971.

(8) Reed, R. E., Jr. and Cole, H. A., Jr., "Randomdec: Mathematic Background and Application to Detection of Structural Deterioration in Bridges," FHWA-RD-76-181.

APPENDIX A

SINGLE DEGREE OF FREEDOM DYNAMIC PROPERTIES

A.1 ANALYSIS TECHNIQUES AND EXPERIMENTAL PROCEDURES

A.1.1 Transient Vibration Test

The transient vibration test is one of several types of dynamic tests which can be performed as a means of determining the equivalent viscous damping ratio ζ. The most common method of determining the damping ratio ζ from a transient vibration test is the logarithmic decrement method. This method of measuring damping is valid for a multi-degree-of-freedom system provided that the system vibrates in a single mode. The logarithmic decrement method is fairly easy to apply provided the transient response is completely isolated to a single mode of vibration or if the influence of other frequency components on the transient response is negligible.

When significant multifrequency components are present in the transient response of a structure another method of determining the damping ratio must generally be used since it is very difficult to filter-out the unwanted frequency components using analog or digital techniques without distorting the modal component of interest. In this investigation, the damping ratio ζ was determined from the Fourier Transform of the transient response when multifrequency components were present in the response signal.

A.1.1.1 The Logarithmic Decrement Method

The expression for the determination of the damping ratio ζ from the transient response can be derived from the transient solution of the equation of motion for a single-degree of freedom system or from

the transient modal solution for a multi-degree of freedom system. The logarithmic decrement method [A2] makes use of the natural logarithm of the ratio of an initially selected peak of the transient vibration to the nth successive peak as shown in Fig. A-1 and is expressed by the equation [A2].

$$\zeta = \frac{1}{2\pi n} \text{ Ln } \left(\frac{\ddot{X}_1}{\ddot{X}_{n+1}}\right) \qquad n = 0, 1, 2, \ldots \qquad (A.1)$$

where ζ = linear viscous damping ratio

$\ddot{X}_1$ = selected peak amplitude of acceleration

$\ddot{X}_{n+1}$ = peak amplitude of acceleration after n cycles

n = number of elapsed cycles of vibration

The use of various experimental values of $\ddot{X}_{n+1}$ in Eq. A.1 will usually not yield a unique value for the damping ratio ζ. Because of the experimental variation in ζ, a better evaluation of damping can be obtained from a semi-log plot of $\frac{\ddot{X}_{n+1}}{\ddot{X}_1}$ versus the cycle number n as illustrated in Fig. A-2. In equation form, the curves in Fig. A-2 are represented as

$$\ln \frac{\ddot{X}_{n+1}}{\ddot{X}_1} = -2\pi n\zeta$$

where n = 0, 1, 2, 3, ...

If the type of damping in the structure is equivalent linear viscous damping, then the curve joining the points in the semi-log plot of $\frac{\ddot{X}_{n+1}}{\ddot{X}_n}$ vs. number of cycles will be a straight line as shown in Fig. A-2. When the curve in Fig. A-2 is convex downward this indicates that the damping ratio ζ decreases with decreasing amplitude; while a convex curve indicates that the damping ratio ζ increases with decreasing amplitude.

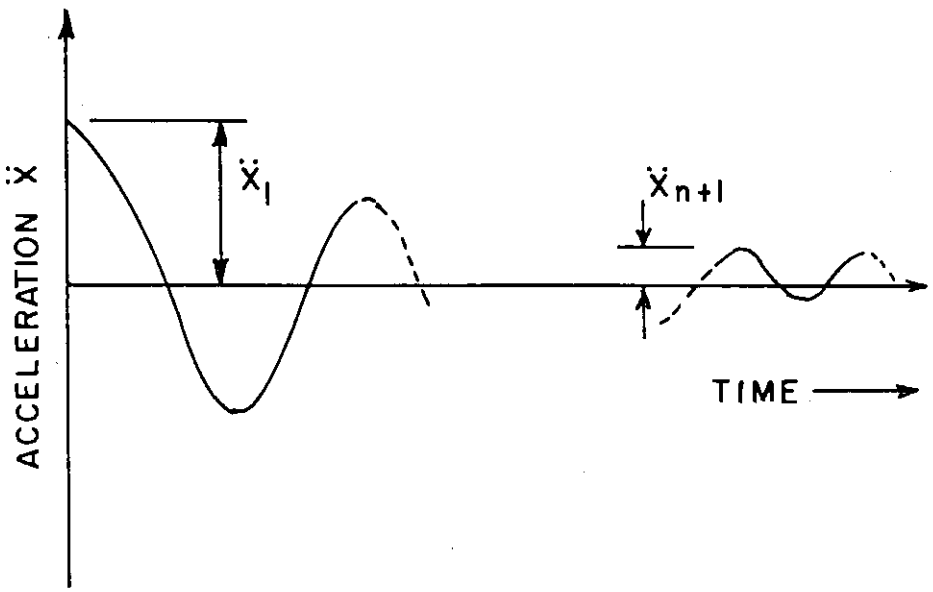

FIGURE A-1. ACCELERATION RESPONSE FOR TRANSIENT VIBRATIONS

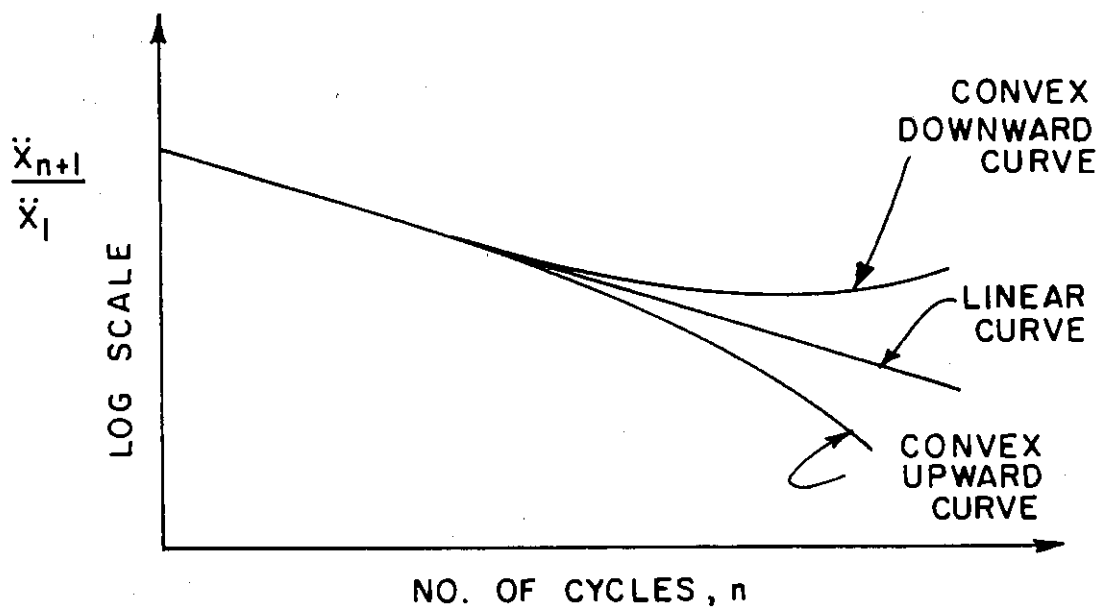

FIGURE A-2. SEMI-LOG PLOT OF RELATIVE ACCELERATION vs. CYCLES OF TRANSIENT VIBRATION

The determination of the damping ratio ζ from the semi-log plots, of the type shown in Fig. A-2, is best accomplished by fitting a polynomial least squares curve to the experimental data. A straight line least square fit to the data will allow the determination of an equivalent linear viscous damping ratio ζ from the slope of the line. From a second or third order polynomial least squares fit to the data, a value of the damping ratio ζ can be determined which is the amount of damping present in the system at the level of vibration associated with the nth elapsed cycle.

A.1.1.2 Transform Decay Methods

The transform decay methods presented in this subsection were developed because of the presence of significant frequency components in the transient response of the bridge as discussed previously. The transform decay method of analysis uses the same transient vibration response signal as was used in the logarithmic decrement method of analysis. The transform method of determination of damping from the experimental data does not appear to be very sensitive to the presence of multi-frequency components because the frequency components are effectively separated in the frequency domain[A1]. The transform decay technique makes use of the properties of Discrete Fourier Transforms (DFT), which are discussed in detail in references[A1, A3, A4].

For a single-degree of freedom system the equation of motion for free vibration[A2] is given by

$$\ddot{X} + 2\,\zeta\,\omega_n\,\dot{X} + \omega_n^{\,2}\,X = 0 \qquad (A.2)$$

where X = displacement of structure at midspan

$\dot{X}$ = velocity

$\ddot{X}$ = acceleration

ω_n^2 = K/M = square of circular natural frequency

K = equivalent stiffness

M = equivalent mass

ζ = C/C_c, damping ratio

C = damping coefficient

C_c = Critical damping = $2M\omega_n$

The transient or homogeneous solution of Eq. A.2 is

$$X(t) = Ae^{-\zeta\omega_n t} \operatorname{Cos} (1 - \zeta^2 \quad \omega_n t + \beta) \tag{A.3}$$

in which A and β are constants to be evaluated from the initial conditions at time $t = 0$.

The continuous time series represented by Eq. A3 can be transformed into the frequency domain by use of the Fourier transform[A5]. The expressions for the transform of a continuous function are determined by the use of the Fourier integral which is expressed by

$$X(\omega) = \int_{-\infty}^{\infty} X(t)\, e^{+i\omega t}\, dt^* \tag{A.4}$$

where $X(\omega)$ = Fourier transform function

$X(t)$ = Time domain function

ω = circular frequency

t = time

$i = \sqrt{-1}$, symbol denoting an imaginary quantity.

*Some authors define the Fourier integral with a negative exponential.

The application of Eq. A.4 to Eq. A.3 when $\beta = 0$ results in a Fourier transform which can be expressed as a complex function in the form

$$X(\omega) = a(\omega) + i[b\ (\omega)] \tag{A.5}$$

where

$$a(\omega) = \mathrm{Re}X(\omega) = A\ \frac{\zeta\omega_n\ (\omega_n^{\ 2} + \omega^2)}{(\omega_n^{\ 2} - \omega^2)^2 + 4\zeta^2\omega_n^{\ 2}\omega^2} \tag{A.6}$$

$$b(\omega) = \mathrm{Im}\ X(\omega) = A\ \frac{\omega(\omega^2 + \omega_n^{\ 2}\ (2\zeta^2 - 1)\ )}{(\omega_n^{\ 2} - \omega^2)^2 + 4\zeta^2\omega_n^{\ 2}\omega^2} \tag{A.7}$$

Plots of Re $X(\omega)$ vs. ω and Im $X(\omega)$ vs. ω are illustrated in Fig. A-3.

The equivalent damping ratio ζ associated with a transient response signal can be calculated from the Fourier transform of the transient response signal by the following method. Figure A-3 indicates that the maximum and minimum values of the imaginary component of the transform are separated along the frequency axis by $2\zeta\omega_n$. The value of ζ can thus be found from the relation

$$\zeta = \frac{\omega_2 - \omega_1}{2\omega_n} = \frac{f_2 - f_1}{2f_n} \tag{A.8}$$

where ω_1 (f_1) and ω_2 (f_2) are the circular frequencies (response frequencies) associated with the maximum and minimum values respectively of the imaginary component of the Fourier transform.

The techniques for using Eq. A.8 for the determination of ζ when phase shifting and multi-frequency components are present in the transient response data, which was the case in this investigation, are presented in reference[A1].

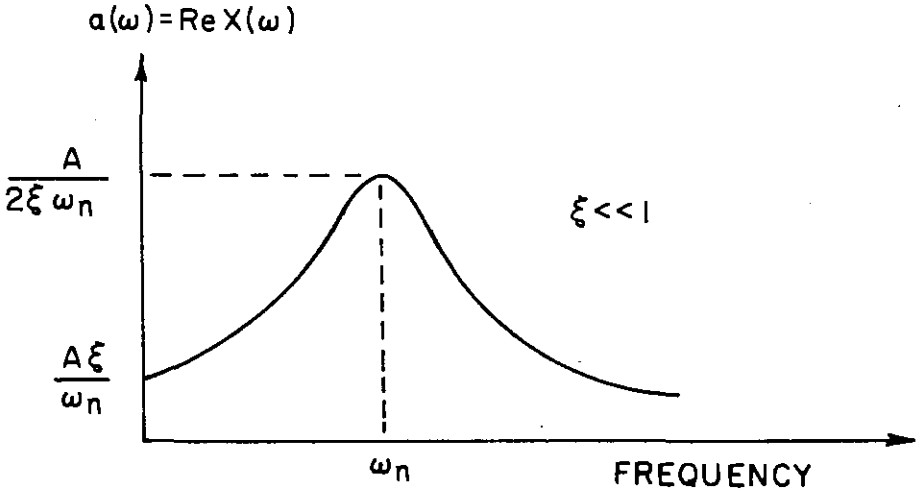

(a) PLOT OF REAL COMPONENT OF X(ω)

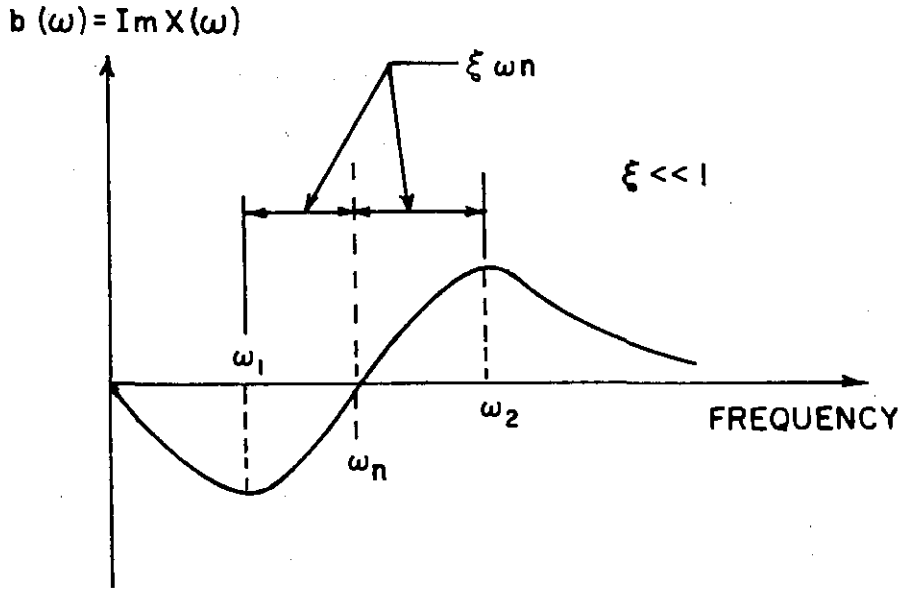

(b) PLOT OF THE IMAGINARY COMPONENT OF X(ω)

FIGURE A-3. PLOT OF FOURIER TRANSFORM OF A TRANSIENT RESPONSE

A.1.1.3 Experimental Procedures for the Transient Test

A transient test was conducted at each of the first three resonant frequencies of the bridge during each of the four sets of dynamic tests. The resonant frequencies were associated with the following vibrational modes:

1. 1st Bending,
2. 1st Torsion and
3. 2nd Bending

The transient test consisted of exciting the bridge with a quasi-steady state excitation, supplied by the hydraulic actuator, until the resonant frequency associated with the selected mode could be detected with the aid of a Lissajous diagram as discussed in App. D. Once the resonant condition was established, accelerometer signals from three locations on the bridge were recorded for an interval of ten seconds. As soon as the ten second steady-state interval of response was achieved, the hydraulics to the actuator were shut down almost instantaneously which placed the bridge in a state of transient decaying response. Thirty seconds of transient response data were recorded for a total of forty seconds of continuous data for the transient test.

A.1.2 Frequency Response Generation Test

A.1.2.1 Dynamic Properties

A frequency response curve describes the response of a structure to a steady state forced excitation over a selected frequency range which generally includes one or more of the structure's natural frequencies. The analysis and examination of the experimental data obtained from a Frequency Response Curve Generation Test can provide

information about dynamic properties such as

1. Resonant frequencies of a structure and,
2. Equivalent linear viscous damping ratios of a structure.

The analysis approach used in this aspect of the study depends on the frequency response curve generated about a resonant frequency of the structure being dependent only on the response due to that mode. In order to precisely obtain the above information from the experimental data several conditions must be met or achieved.

If the forced steady-state excitation is harmonic, then the natural frequencies of the structure must have sufficient separation to minimize the influence of the other modes on the particular mode of interest. It should be recalled that a steady-state harmonic forced vibration excites all modes at the frequency of the excitation[A6]. However, due to the characteristics of resonance, the influence of the other modes on the mode of interest will be minimal, if not negligible, if sufficient separation exists between the natural frequencies.

When the forced vibration is periodic but nonharmonic, that is when the excitation contains multiples of the fundamental excitation frequency, then the conditions exist for the response to have significant multi-frequency components. When the steady-state forced vibrational response contains multi-frequency components, such as occurred in this experimental program, then the response must be subjected to either analog or digital filtering methods.

The experimental data taken during the dynamic tests was filtered prior to recording in digital form with a 10 Hz low-pass analog filter. The digital data was further effectively filtered by the use of Fast Fourier transform techniques as outlined in reference[A1].

When the frequency response curve can be established for a single mode, then an equivalent linear viscous damping ratio ζ can be determined from the frequency response curve provided the response is sufficiently linear. One method that can be used to calculate the damping ratio ζ is the Bandwidth method. This method requires obtaining from the frequency response curve the frequency at resonance f_n and the frequencies f_1 and f_2 associated with amplitude of response equal to 0.707 times the amplitude at resonance as shown in Fig. A-4. These latter two points are referred to as the half-power points. The equivalent linear viscous damping ratio ζ can then be determined from the equation

$$\zeta = \frac{f_2 - f_1}{2f_n} \tag{A.9}$$

The above expression for the determination of the damping ratio ζ can be derived from the steady-state solution for the equation of motion for a single degree of freedom system or from the steady state modal solution for a multi-degree of freedom system. Reference[A7] contains a derivation of Eq. A.9 along with a detailed discussion of the Bandwidth method.

A.1.2.2 Experimental Procedure for the Frequency Response Curve Generation Test

The frequency response curve generation test was conducted three times for each of the four sets of dynamic tests at the first three resonant frequencies, f_r, of the bridge. The test was conducted in two phases which consisted of a primary or set-up phase and the final phase which was the actual experimental generation of the response of the bridge about a resonant frequency. For both phases of the test, the bridge

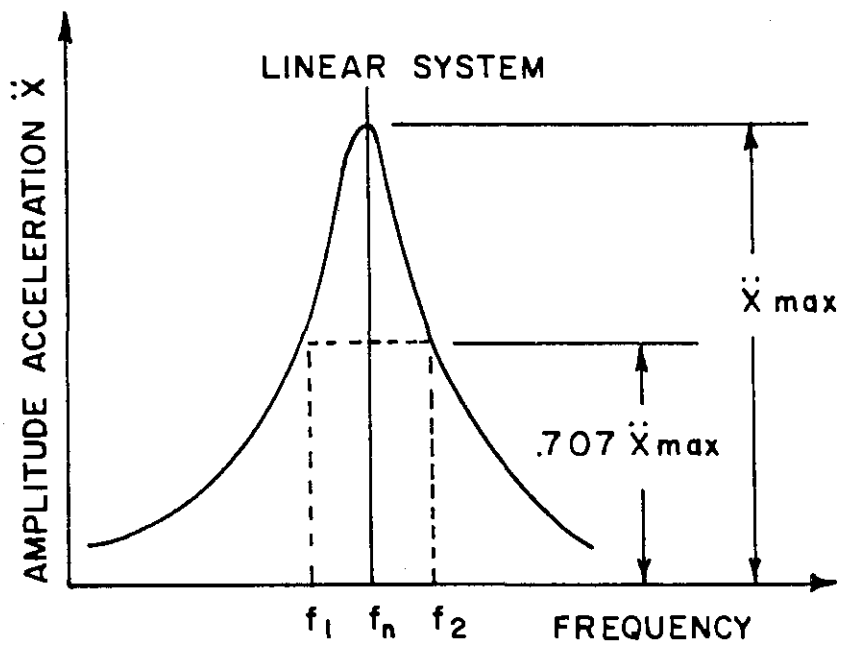

FIGURE A-4. FREQUENCY RESPONSE CURVE OF LINEAR SYSTEM

was subjected to an independent steady state excitation force, of 788 pounds. This level of excitation was necessary to achieve sufficient voltage levels from the transducers. However, the strain levels in the bridge girders were quite low for this level of excitation as compared to the strain levels reached during the fatigue test phase of the study.

The primary phase of the test consisted of bringing the bridge into resonance at one of the selected resonant frequencies with the aid of a Lissajous diagram. After the resonant frequency was determined, a frequency range for the test was established which was equal to $f_r \pm 0.2$ Hz. Approximately 30 points within this frequency range were selected for conducting the test.

The final phase of the tests always commenced at the lower limit of the frequency range. The frequency was then incremented until the upper limit of the frequency range was achieved while always maintaining a constant level of excitation. The bridge was allowed to vibrate at each point within the frequency range long enough for the bridge to reach a steady-state response. When the test from the lower limit to the upper limit of the frequency range was completed the test was repeated. However, the repeated test started at the upper limit of the frequency range and ceased at the lower limit. The purpose of conducting the test over both an increasing and decreasing frequency increment was to establish any existence of the nonlinear jump phenomenon.

A.1.3 Sweep Test

A.1.3.1 Introduction

Sweep tests were conducted on the bridge as a means of obtaining

a vibration signature of the bridge. The resulting experimental data was analyzed to obtain a vibration signature in the form of a mechanical impedance plot. Mechanical impedance is a complex quantity which is expressed in terms of the ratio of the input force to the response velocity at a point on the structure and the phase angle between the force and the velocity.

A.1.3.2 Mechanical Impedance

The response of a multi-degree of freedom system to a point force can be expressed in terms of the convolution integral[A10].

$$X_j(t) = \int_{-\infty}^{\infty} h_{jk}\,(t - \tau)\, f_k\,(\tau)\, d \qquad (A.10)$$

where

$X_j(t)$ = response at the jth point

$h_{jk}(t)$ = response at the jth point due to an impulse at the kth point

and $f_k(t)$ = excitation force applied to the kth point.

In reference[A8] it is shown that the mechanical impedance ratio can be derived from Eq. 10 by taking the Fourier Transform of both sides of the equation and the corresponding result can be expressed as

$$Z_{jk}(\omega) = \frac{F_k\,(\omega)}{V_j\,(\omega)} \qquad (A.11)$$

where

$Z_{jk}(\omega)$ = mechanical impedance of the jth point due to a force at the kth point

$F_k(\omega)$ = Force at the kth point

$V_j(\omega)$ = velocity at the jth point due to the Force at the kth point

The mechanical impedance $Z_{jk}(\omega)$ is a property of a linearly elastic structure and is independent of the excitation force $F_k(t)$ and its corresponding Fourier Transform $F_k(\omega)$. If the structure has a nonlinear stiffness then the mechanical impedance is also a function of the magnitude of the excitation.

When discussing mechanical impedance, the terms point and transfer impedance are used. When the velocity is measured at the point of application of the force, the impedance is referred to as the point impedance, i.e., in Eq. A.11 point impedance occurs when $j = k$. However, if the velocity is measured at a point other than the point of application of the force, the impedance is termed the transfer impedance, i.e. in Eq. A.11 $j \neq k$.

A typical mechanical impedance plot is shown in Fig. A-5 along with the corresponding phase angle diagram which is also illustrated in Fig. A-5. There are several major observations to be made about a mechanical impedance plot.

1. The minimum points in Fig. A-5 are associated with the resonant point of the structure.
2. The phase angle between the force and the velocity at these resonant points is zero as illustrated in Fig. A-5.
3. The maximum points in Fig. A-5 are called the anti-resonant points and occur theoretically when the phase angle between the force and the velocity is again zero as shown in Fig. A-5.
4. The point mechanical impedance provides a measure of the damping in a structure at resonance.

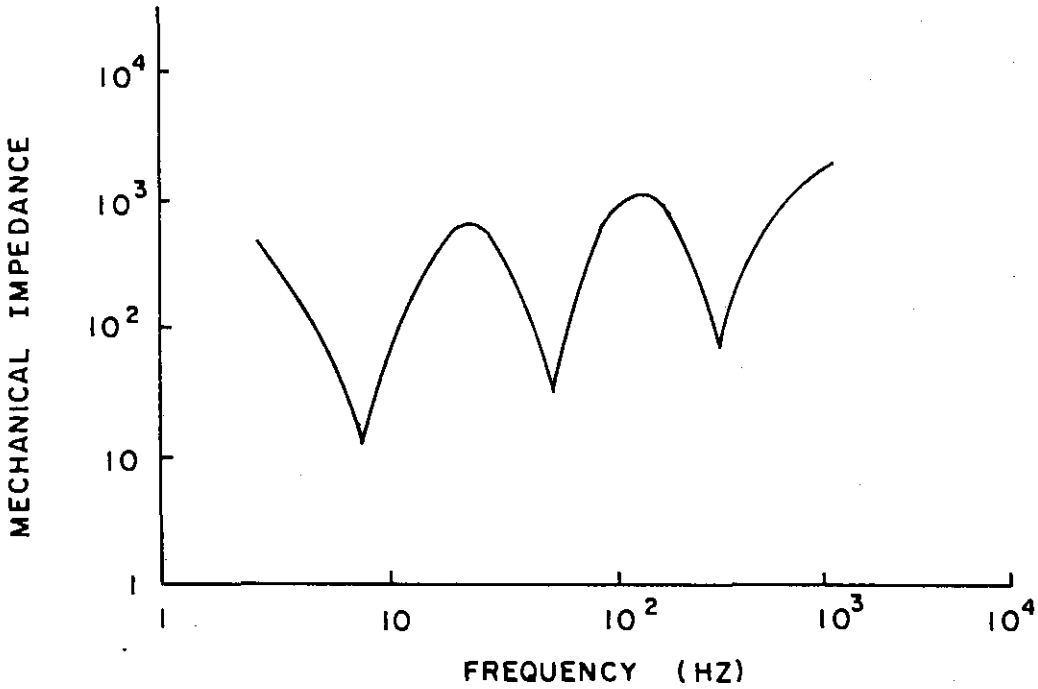

a) AMPLITUDE OF MECHANICAL IMPEDANCE

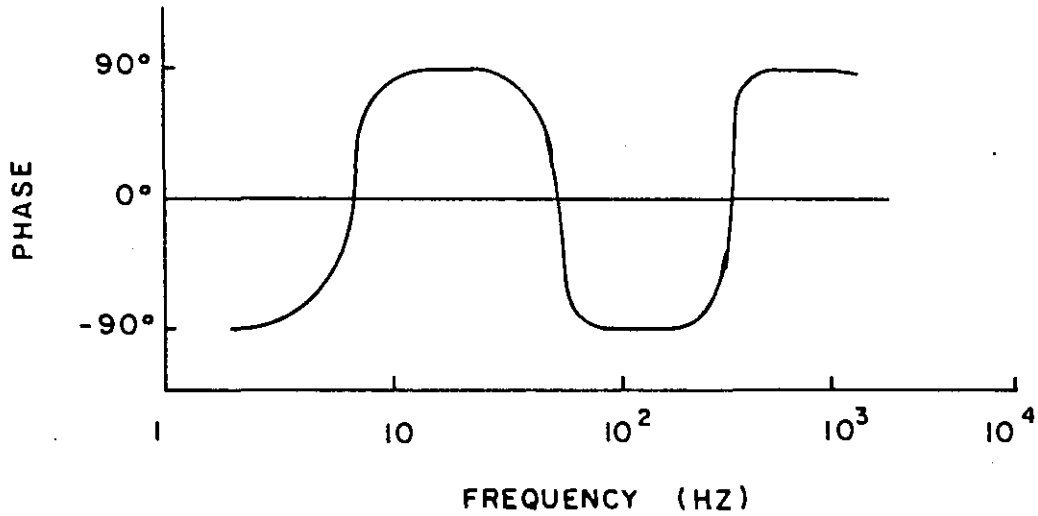

b) PHASE ANGLE OF MECHANICAL IMPEDANCE

FIGURE A-5. TYPICAL MECHANICAL IMPEDANCE PLOT

A.1.3.3 Experimental Procedure for the Sweep Test

The sweep test was performed once during each of the four sets of dynamic tests and was conducted in two phases. In the primary or setup phase the bridge was subjected to a quasi-steady state excitation. The first five resonant frequencies of the bridge were then established with the aid of the Lissajous diagram. A frequency range was then established for the test which had a lower limit of 0.5 Hz below the first resonant frequency. The upper limit of the frequency range was a minimum of 0.5 Hz above the fifth resonant frequency of the bridge.

The second phase of the test was the carrying out of the actual sweep test. One of the goals of this test was to apply by means of the hydraulic actuator a linear swept sinewave excitation to the bridge. However, the establishment of a constant force level is dependent on the compressor speed of the electronic controller for the hydraulic actuator. The amplitude controller used in these tests was able to achieve a constant force level in the laboratory using a single-span bridge model[A7]. However, in the field test the amplitude controller did not have sufficient compressor speed to maintain a constant force level and thus an excitation in the form of a swept sinewave with varying amplitude was applied to the bridge over the chosen frequency ranges of the test. The sweep rate for both the laboratory and the field tests were the same. The actual force versus frequency levels achieved during the field tests are discussed in reference[A1].

The actual sweep test was conducted at a sweep rate of 0.02 Hz/sec. and the test was started at the lower limit of the frequency range. The test ended when the upper limit of the frequency range was reached.

A.1.4 Peak Amplitude Method

The damping ratio ζ was determined from the dynamic response data recorded during the fatigue test by means of the peak amplitude method[A7]. The damping ratio for this method is given by the equation

$$\zeta = \frac{m}{M+m} \frac{Z}{2X} \tag{A.12}$$

Z was the single amplitude stroke of the actuator, and m was the mass of the "moving mass" which was 25.3 lbs-sec^2/in. The effective mass, M, of the bridge was determined from the equation

$$M = \frac{k}{\omega_n^2} \tag{A.13}$$

where k is the effective stiffness of the structure. The effective stiffness of the bridge was obtained by applying a static load at midspan of the center span and measuring the corresponding deflection. The term ω_n was taken as the circular frequency of the bridge at the very beginning of the fatigue test. It was assumed during the calculation of the damping ratio, ζ, by the peak amplitude method that the effective mass, M, was invariant. The effective mass was determined to be 341.4 lbs-sec^2/ in.

A.2 EXPERIMENTAL RESULTS

A.2.1 Transient Response

The analysis of the transient response data for the determination of the amount of equivalent linear viscous damping present in the bridge was achieved by using both the logarithmic decrement and Fourier transform decay methods. However, the logarithmic decrement method was used only to analyze the transient response data from Tests 1 and 2 because of

serious discrepancies introduced by the multifrequency components present in the transient response data obtained in Tests 3 and 4. The contribution of various multifrequency components to the transient response can be observed in a frequency spectrum. The frequency spectrums shown in Figs. B-9a and B-9c were obtained from the steady-state forced vibrational response test conducted for Tests 1 and 4. The frequency spectrums show that the multifrequency components had a much greater influence on the transient response in Test 4 than in Test 1. This is indicated by the greater amplitude of response of the higher order frequency components in Test 4 than in Test 1. The Fourier transform decay method, as discussed in reference[A1], is generally not influenced to a very great extent by the multifrequency components encountered during the transient tests; therefore, it was possible to determine the damping ratios by the Fourier transform method for Tests 1 through 4.

A.2.1.1 Damping Ratio Results (Logarithmic Decrement)

The results of the analysis of the transient response data by the logarithmic decrement method are presented in this section in two forms: selected graphs of the damping ratio, ζ, versus number of free vibration cycles and a tabular summary of selected values of the damping ratio. The graphs of the damping ratio vs. the number of free vibration cycles represent quadratic curve fits to the damping ratios determined from the analyses of the data. A quadratic curve fit was chosen because many of the nonlinear mathematical models for damping[A9] are quadratic in form. Figures A-6 through A-8 illustrate the magnitude of the damping ratio, ζ, versus number of free vibration cycles for the first bending mode at station 17, the first torsion mode at station 16

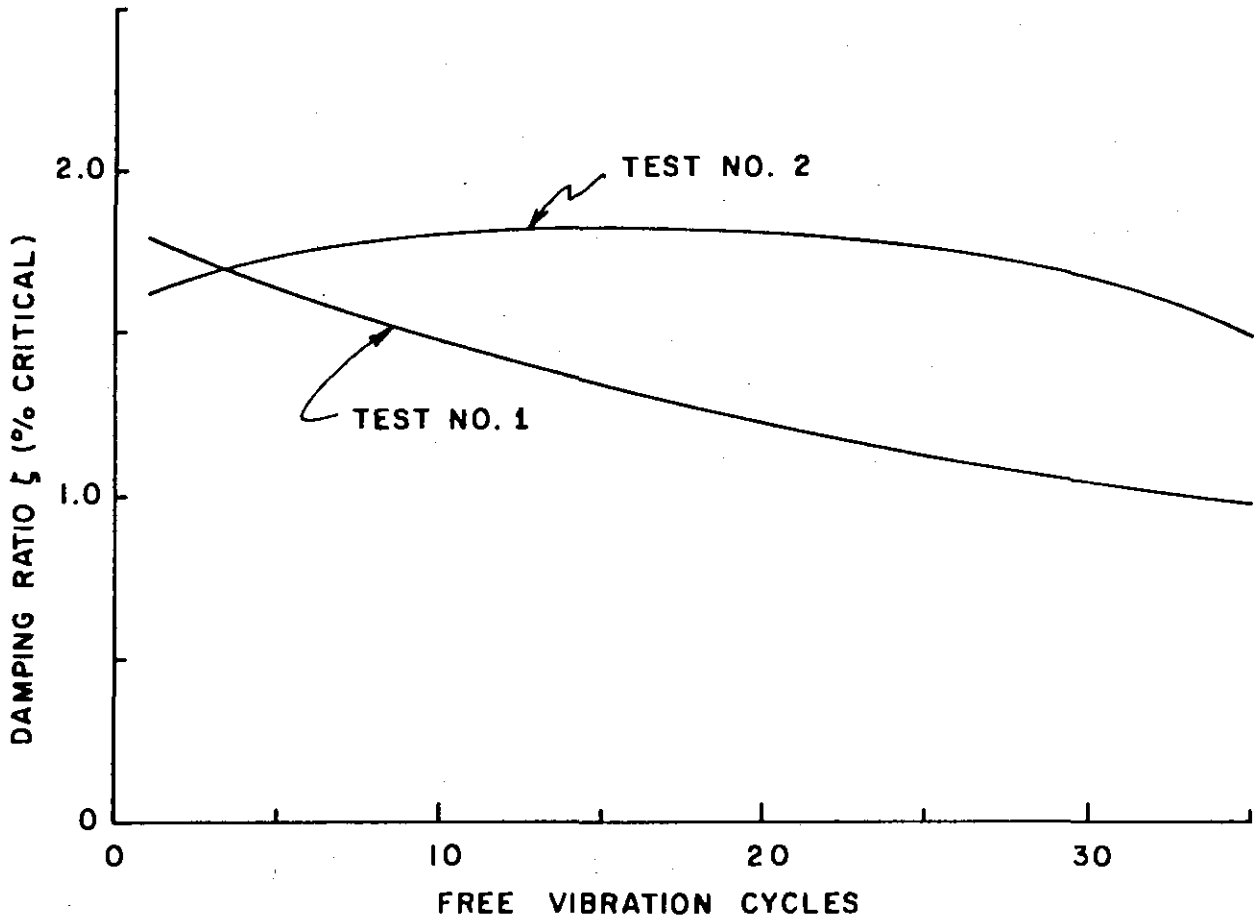

FIGURE A-6. DAMPING RATIO, ζ, VS. NUMBER OF FREE VIBRATION CYCLES FOR FIRST BENDING MODE, POSITIVE PEAKS, STATION 17, TESTS 1 & 2

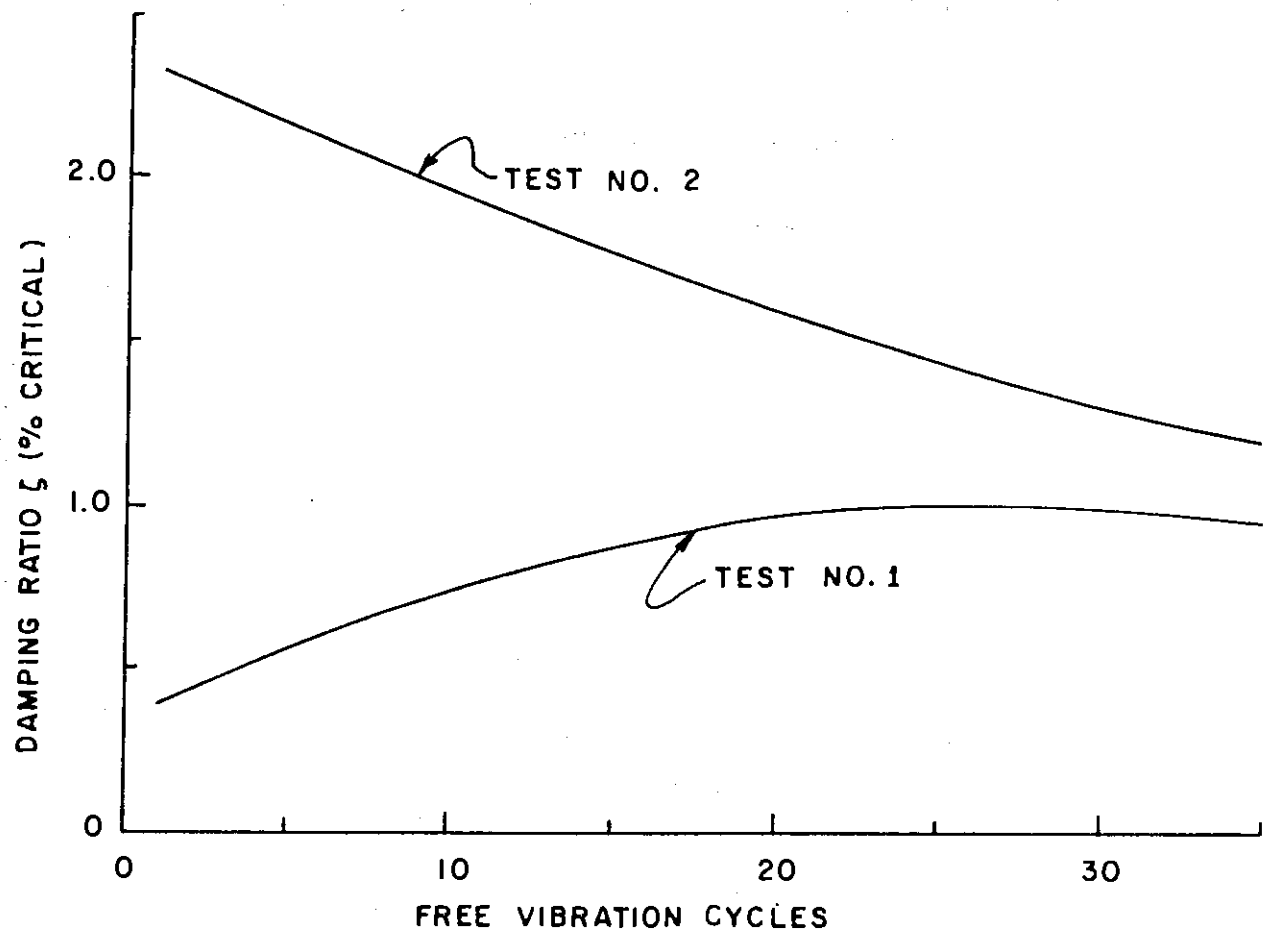

FIGURE A-7. DAMPING RATIO, ζ, VS. NUMBER OF FREE VIBRATION CYCLES FOR FIRST TORSIONAL, POSITIVE PEAKS, STATION 16, TESTS 1 & 2

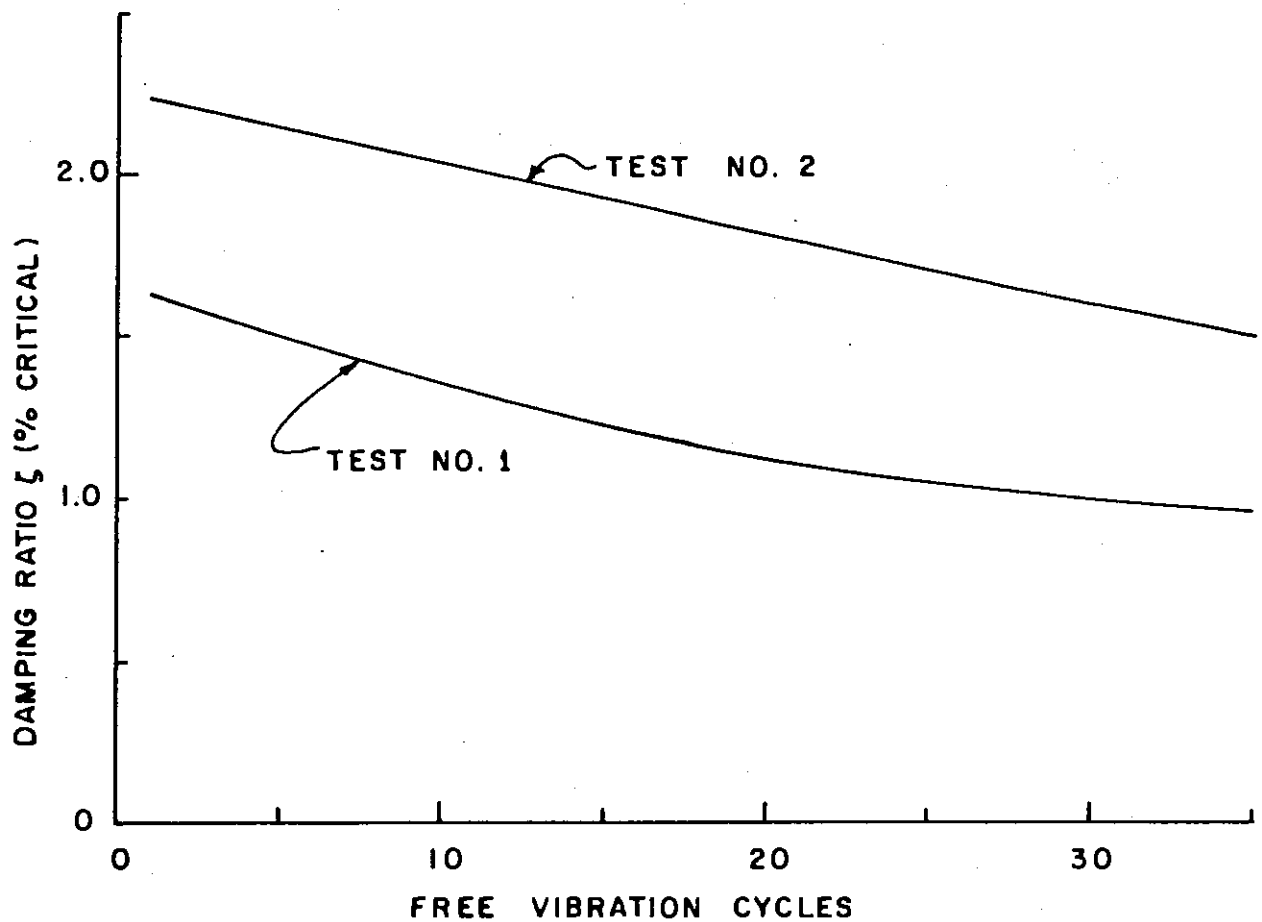

FIGURE A-8. DAMPING RATIO, ζ, VS. NUMBER OF FREE VIBRATION CYCLES FOR SECOND BENDING MODE, POSITIVE PEAKS, STATION 5, TESTS 1 & 2

and the second bending mode at station 5. The location of these various stations on the bridge deck are given in Fig. 1-8. The graphs illustrated in Figs. A-6 through A-8 are generally representative of the damping ratio, ζ, versus the number of free vibration cycles at other stations on the bridge deck.

The graphs indicate that the damping ratio, ζ, for both the first bending and second bending modes in Test 1 decreased as the bridge underwent a decaying vibration; whereas, for the torsional mode, the damping ratio, ζ, for the most part increased as the bridge underwent a decaying motion over the first 35 cycles. The results from Test 2 show that changes have occurred in the damping ratios for each of the three modes. The results clearly indicate that there has been an overall increase in the damping present in the bridge from Test 1 to Test 2 as determined by the logarithmic decrement method. Also, the first torsional and second bending modes now show a decrease in damping as the bridge undergoes a decaying motion up to 35 cycles. The damping associated with the first bending mode has undergone a noticeable change in that the damping ratio, ζ, shows a momentary increase and then decrease during the first 35 cycles of vibration. Since the amplitude of the bridge is decreasing during each cycle of motion, the results given by Figs. A-6 through A-8 indicate that the damping present within the bridge is dependent on a parameter or parameters associated with the amplitude of the oscillatory motion. Although not illustrated in the graphs, the results also show that damping ratios associated with the cycles of oscillation greater than 35 approach a constant magnitude.

Table A-1 presents a selected set of damping ratios. The west, center and east notations given in Table A-1 refer to the spans of the bridge.

TABLE A-1 EXPERIMENTAL DAMPING RATIOS BASED ON LOGARITHMIC DECREMENT METHOD (DETERMINED FROM POSITIVE PEAK)

Positive Peaks (% Critical)

		Linear			2nd Degree Cyc 5			2nd Degree Cyc 30		
		West	Center	East	West	Center	East	West	Center	East
TEST 1	B_{11}	.90	1.06	1.14	1.43	1.64	1.93	.87	1.04	1.10
	T_{11}	.78	.94	.98	.56	.57	.84	.82	.99	1.02
	B_{21}	1.02	1.21	1.03	1.49	2.02	1.41	.99	.95	1.01
TEST 2	B_{12}	1.32	1.61	1.76	1.61	1.72	1.79	1.36	1.66	1.83
	T_{12}	--	1.35	1.27	--	2.15	2.38	--	1.31	1.21
	B_{22}	1.61	--	1.64	2.14	--	2.26	1.59	--	1.63

TABLE A-1 EXPERIMENTAL DAMPING RATIOS BASED ON LOGRAITHMIC DECREMENT METHOD (DETERMINED FROM NEGATIVE PEAKS)

Negative Peaks (% Critical)

		Linear			2nd Degree Cyc 5			2nd Degree Cyc 30		
		West	Center	East	West	Center	East	West	Center	East
TEST 1	B_{11}	.83	.89	.96	1.21	1.02	1.45	.83	.89	.94
	T_{11}	.81	.99	1.02	.37	.66	.96	.87	1.04	1.04
	B_{21}	1.02	.99	.97	1.40	1.35	1.18	.99	1.11	.96
TEST 2	B_{12}	1.21	1.47	1.48	2.11	1.48	1.84	1.16	1.48	1.46
	T_{12}	--	1.26	.94	--	2.23	1.46	--	1.22	.93
	B_{22}	1.59	--	1.66	1.95	--	2.15	1.59	--	1.65

The station location within the span can be obtained from Fig. 1-8. The damping ratios presented in Table A-1 are based on the determination of the damping ratio by the logarithmic decrement method using both the positive side and the negative side of the decaying response. The terms "positive" and "negative" do not refer here to the direction of motion of the bridge but refer to the positive or negative voltage output of the transducer used to measure the decaying response. Table A-1 shows that there is a notable difference between the damping ratios determined from the positive side of the transient response signal as opposed to the damping ratios determined from the negative side. This again indicates a dependence of damping on the amplitude of oscillation.

A.2.1.2 Damping Ratio Results (Fourier Transform Decay Method)

The equivalent linear viscous damping of the bridge determined by the means of the Fourier transform decay method from the transient response data is presented in Table A-2. The table contains the damping ratio determined for each of the three spans of the bridge. The station locations for each of these three spans are shown in Fig. 1-8. In addition, the table also gives the damped natural frequencies of each of the first three vibrational modes of the bridge as predicted by the Fourier transform decay method. A discussion of the damping results based upon the Fourier transform decay method is not presented in this appendix. The discussion is contained in Art. 4.7 where all of the results based on the various methods for determining the damping present in the bridge are compared and the results analyzed. It should be noted, however, that the Fourier transform decay method shows a consistency in the calculation of the damping ratio in each of the three spans for each of the three

TABLE A-2 EXPERIMENTAL VISCOUS DAMPING RATIOS & FREQUENCIES DETERMINED FROM FOURIER TRANSFORM DECAY METHOD

First Bending Damping Ratio (% Critical)				
Test No.	Frequency (Hz)	East	Center	West
1	2.92 (2.90)*	1.0	1.1	1.0
2	2.66 (2.73)	2.6	2.5	2.5
3	2.67	2.2	2.2	2.1
4	2.49	2.9	---	2.5

First Torsion Damping Ratio (% Critical)				
Test No.	Frequency (Hz)	East	Center	West
1	3.62 (3.60)	1.7	1.6	1.7
2	3.34 (3.42)	3.3	3.3	---
3	3.11	3.2	3.1	3.0
4	3.19	2.6	2.7	2.7

Second Bending Damping Ratio (% Critical)				
Test No.	Frequency (Hz)	East	Center	West
1	4.59 (4.57)	1.1	---	1.3
2	4.23 (4.28)	2.8	---	2.7
3	4.29	2.1	2.1	2.2
4	4.14	2.2	2.1	2.1

*Number in parentheses indicate damped natural frequency determined from the time transient response signal.

modes. It should be noted in Table A-2 that the damped natural frequencies which are contained in parentheses are values determined by a computer analysis of the actual time response signal. A comparison of the two sets of damped natural frequencies for Tests 1 and 2 shows a generally good agreement between the values predicted by the Fourier transform approach and those obtained directly from the time response signal.

A.2.2 Results Based on the Frequency Response Curves

This section presents the results obtained from the frequency response curves associated with the bridge. All of the frequency response curves were obtained from response data which was generated at a steady-state single amplitude excitation level of 0.7 g's peak relative acceleration of the "moving mass". The frequency response data were obtained at three different stations on the bridge deck for each of the first three modes of vibration. The frequency response curves shown in Figs. A-9 through A-11 are associated with the first bending mode at station 17 for dynamic tests 1, 3 and 4. Reference[A1] contains the remaining frequency response curves for first torsion and second bending modes at stations 16 and 29, respectively, for all the dynamic tests. A single graph shows both response curves for a quasi-steady up and down sweep of the excitation frequency.

Table A-3 presents the damping ratio, ζ, as determined by the bandwidth method from the frequency response curves associated with both the up and down quasi-steady sweep of the excitation frequency. Table A-3 also gives the magnitude of the damping ratio as determined for each of the three spans of the bridge.

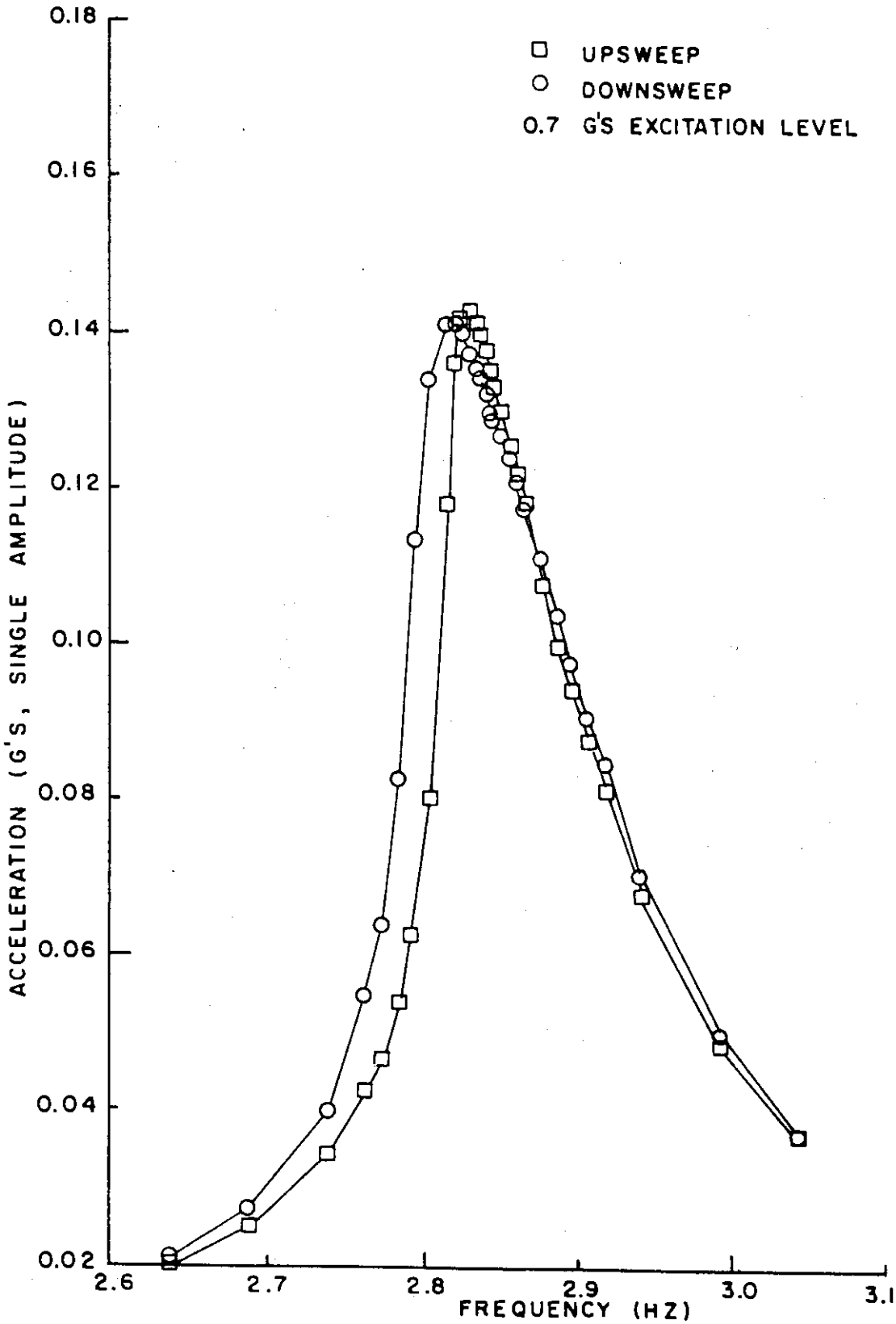

FIGURE A-9. FREQUENCY RESPONSE CURVE, STATION 17, B11

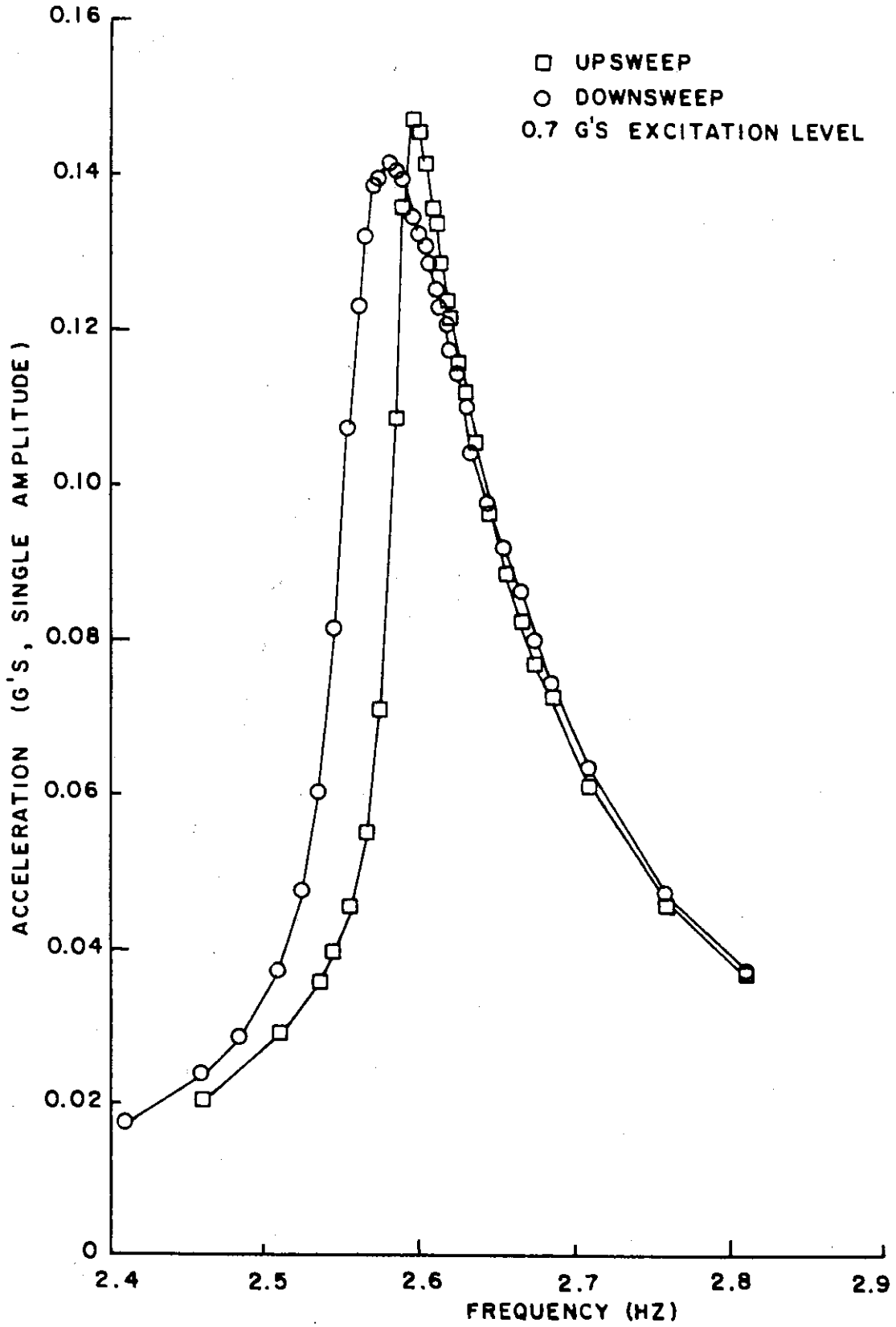

FIGURE A-10. FREQUENCY RESPONSE CURVE, STATION 17, B13

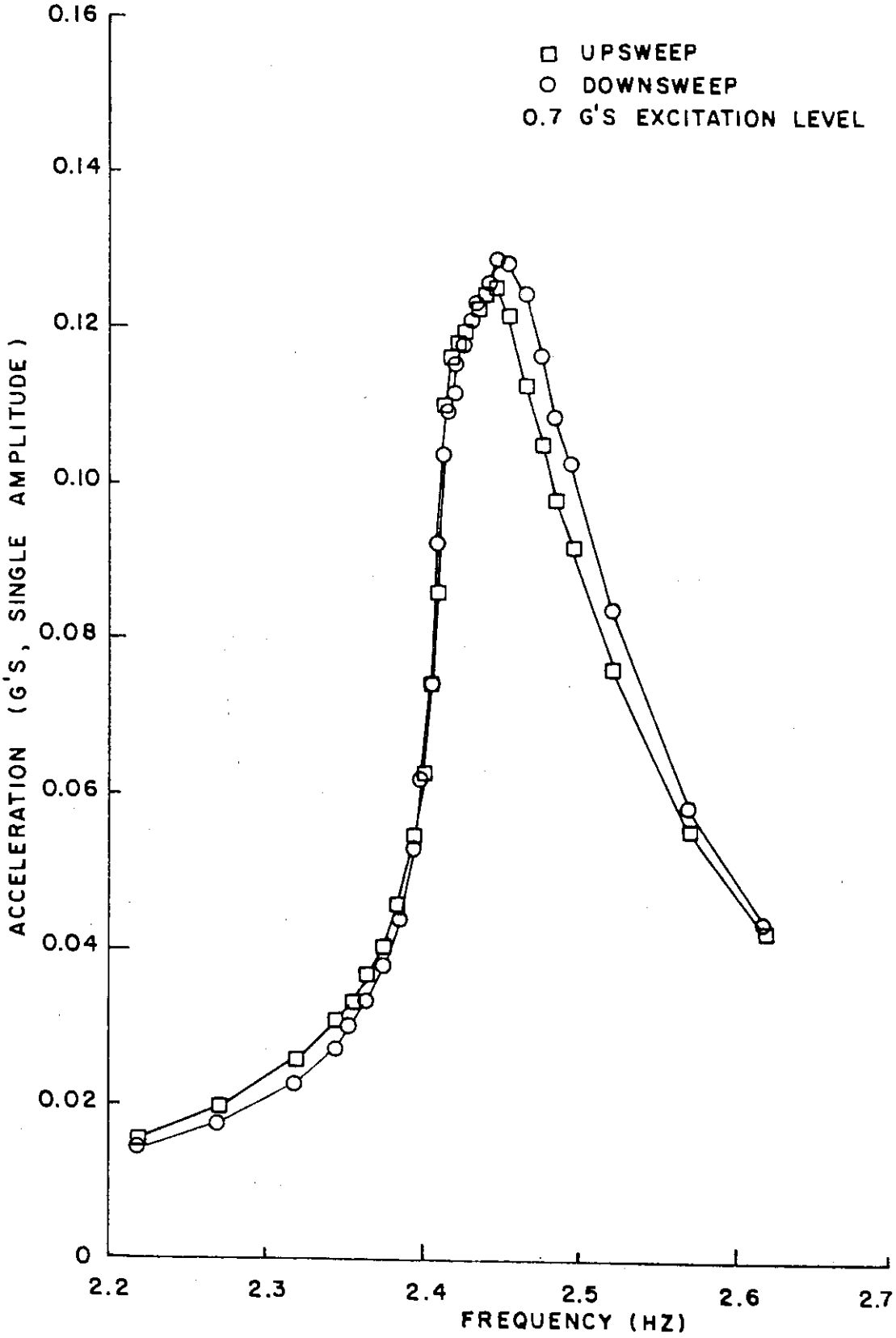

FIGURE A-11. FREQUENCY RESPONSE CURVE, STATION 17, B14

TABLE A-3a EXPERIMENTAL DAMPING RATIO DETERMINED BY THE BANDWIDTH METHOD (TESTS 1-3)

Test No.	Station No.	ρ(up) (%)	ρ(Dn) (%)
B11	5	1.36	1.83
	17	1.30	1.78
	29	1.35	1.82
T11	4	1.83	2.06
	16	1.71	1.93
	28	1.86	2.05
B21	5	1.23	1.41
	14	1.80	1.91
	29	1.33	1.55
B12	5	1.01	1.44
	17	.96	1.40
	29	1.01	1.43
T12	4	.75	3.15
	16	.78	2.85
	28	.80	3.31
B22	5	1.34	1.40
	14	2.35	2.34
	29	1.51	1.60
B13	5	1.08	1.77
	17	1.04	1.71
	29	1.09	1.78
T13	4	.39	2.33
	16	.75	2.03
	28	.38	2.41
B23	5	1.17	1.54
	14	2.59	2.73
	29	1.37	1.68

TABLE A-3b EXPERIMENTAL DAMPING RATIOS DETERMINED BY THE BANDWIDTH METHOD (TEST 4)

Test No.	Station No.	ρ(Up) (%)	ρ(Dn) (%)
	5	1.91	2.13
B14 (.7 g's)*	17	1.84	2.07
	29	1.91	2.12
	4	1.96	2.37
T14 (.7 g's)	16	1.64	2.12
	28	2.14	2.46
	5	--	--
B24 (.7 g's)	14	2.32	2.52
	29	1.26	1.35
	5	1.38	1.57
B14 (.4 g's)	17	1.33	1.55
	29	1.38	1.57
	4	2.46	2.64
T14 (.4 g's)	16	2.07	2.35
	28	2.49	2.72
	5	--	--
B24 (.4 g's)	14	2.57	2.37
	29	1.30	1.29

*Excitation Level

Table 4-2 presents a summary of the resonant frequencies of the bridge as obtained for the first three fundamental modes associated with Tests 1 through 4. The results clearly indicate that the resonant frequencies of the bridge decreased from Test 1 through Test 4 for all three modes with one exception. The exception occurred in the torsional mode where there was an increase in the torsional resonant frequency from Test 2 to Test 3. The decrease in the resonant frequencies of the bridge from Test 1 to Test 4 is a definite indication that the structural damage to the bridge from the fatigue test caused a decrease in the stiffness of the bridge.

A.2.3 Results From The Sweep Test

This section presents the results from the sweep test. Results are presented in the form of mechanical impedance plots. For each test, mechanical impedance was determined from data taken at four different locations on the bridge deck, stations 4, 9, 15 and 30.

A set of mechanical impedance plots for Tests 1 and 2, Tests 2 and 3, and Tests 3 and 4 were constructed from computer generated plots of mechanical impedance for stations 4, 9, 15 and 30. These plots are illustrated in Figs. A-12 through A-20 for stations 4, 9 and 30. The plots for station 15 are given in Figs. 4-5 through 4-7. An examination of the mechanical impedance plots reveals that significant changes occurred in the mechanical impedance of the bridge between Tests 1 and 4.

The greatest change in mechanical impedance occurred between Test 1 and Test 2 as illustrated in Fig.'s A-12, A-15, A-18 and 4-5. These graphs show that there was a significant decrease in all of the five resonance frequencies indicated on the mechanical impedance plots. Also,

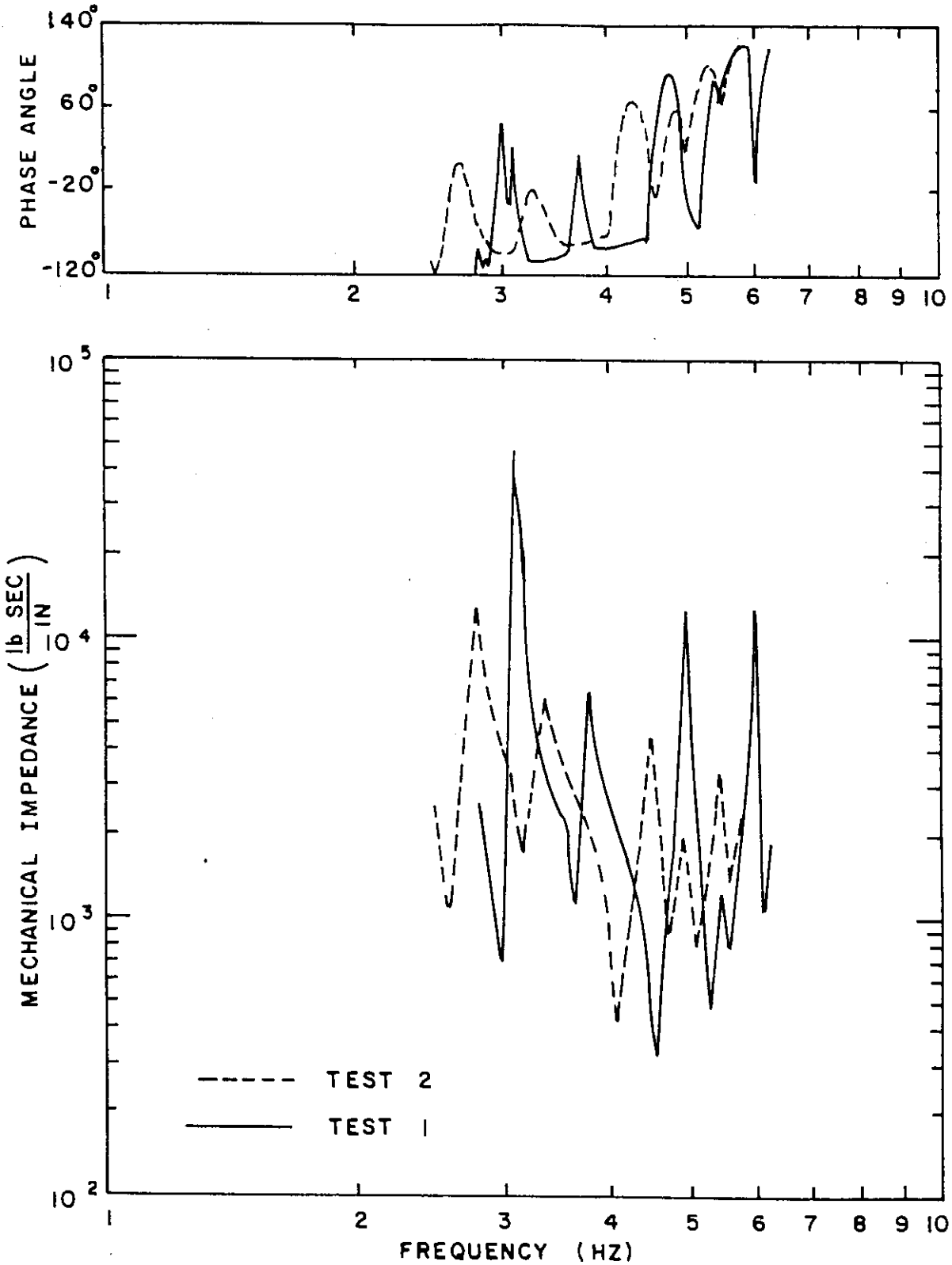

FIGURE A-12. MECHANICAL IMPEDANCE, STATION 4, TEST 1 AND 2

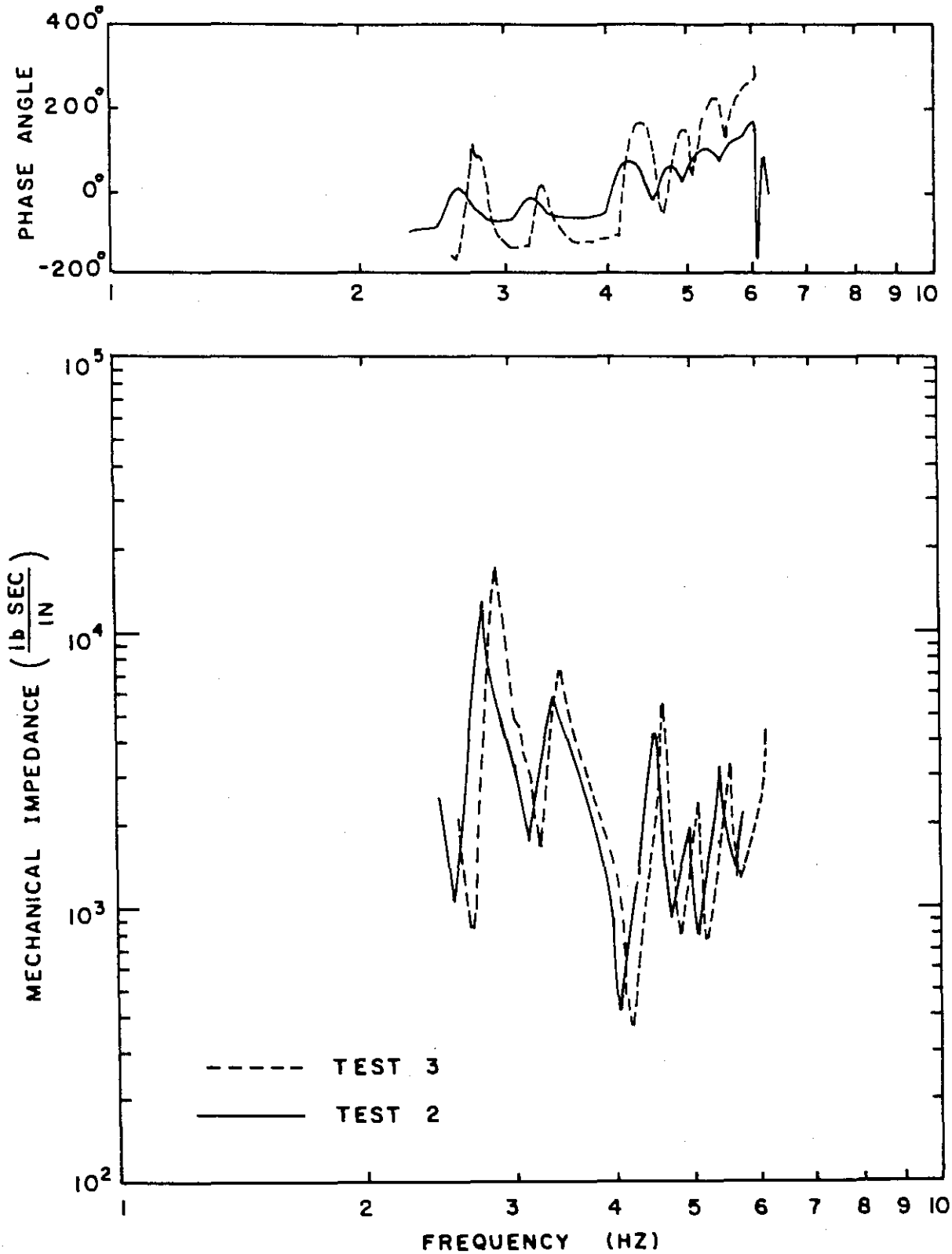

FIGURE A-13. MECHANICAL IMPEDANCE, STATION 4, TEST 2 AND 3

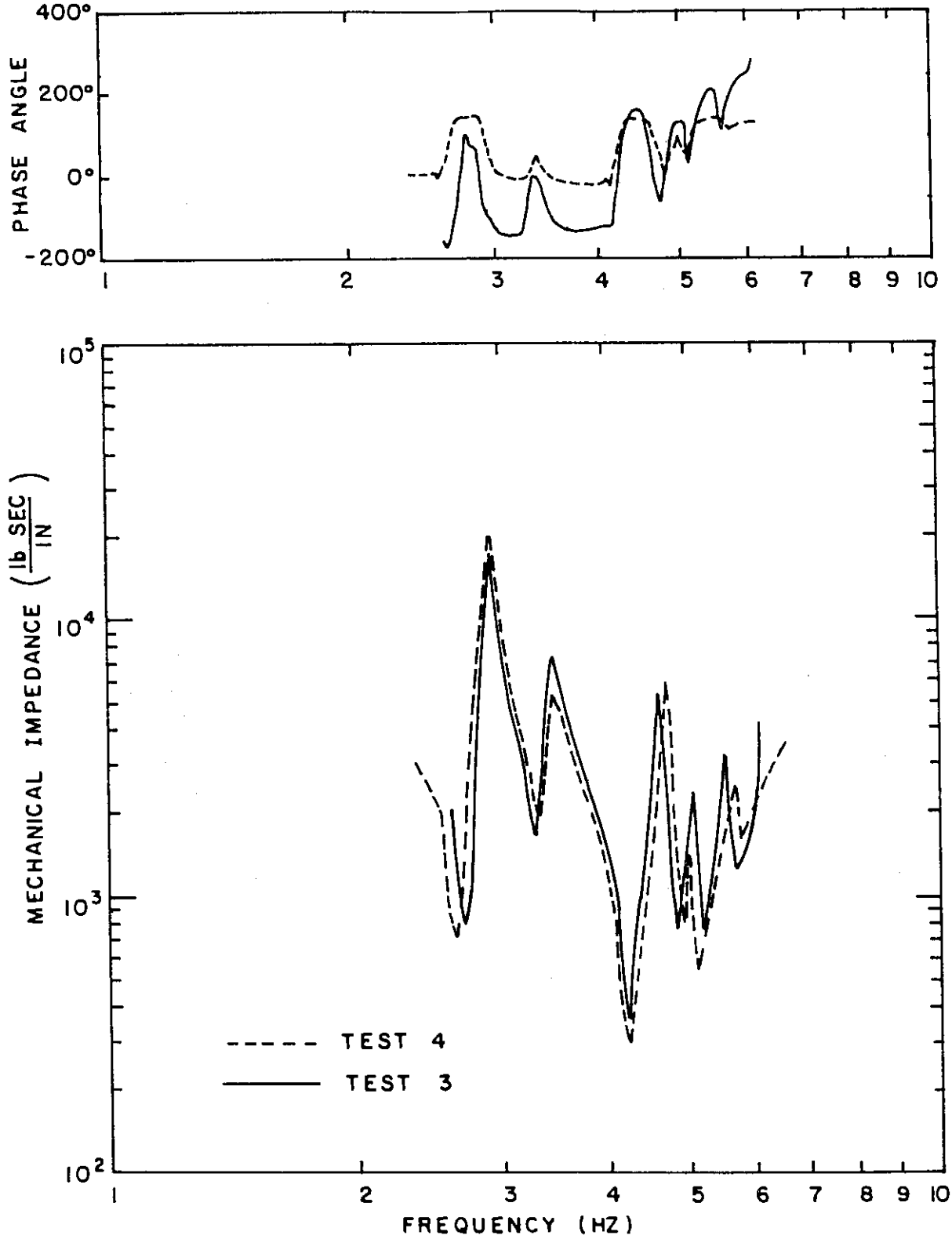

FIGURE A-14. MECHANICAL IMPEDANCE, STATION 4, TEST 3 AND 4

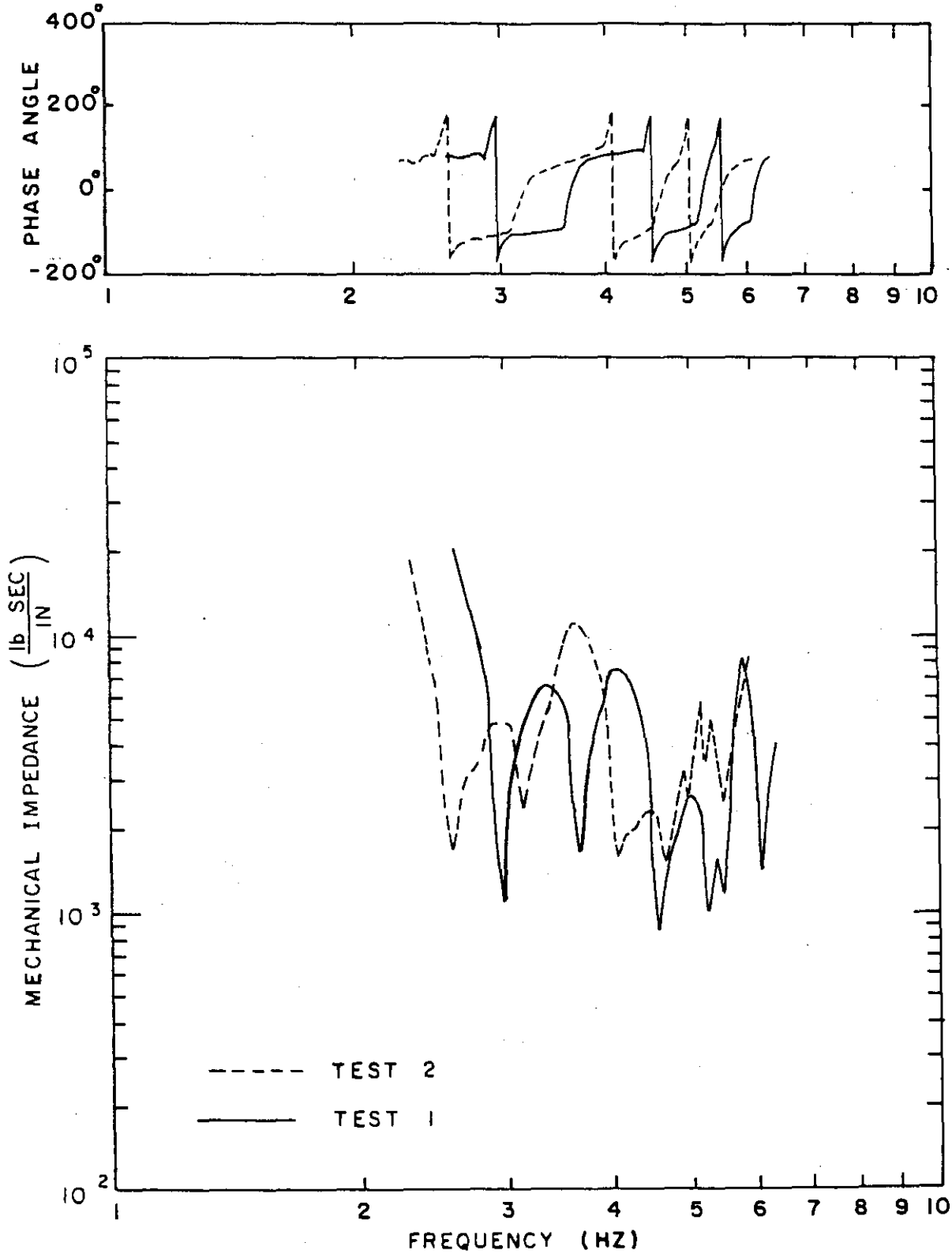

FIGURE A-15. MECHANICAL IMPEDANCE, STATION 9, TEST 1 AND 2

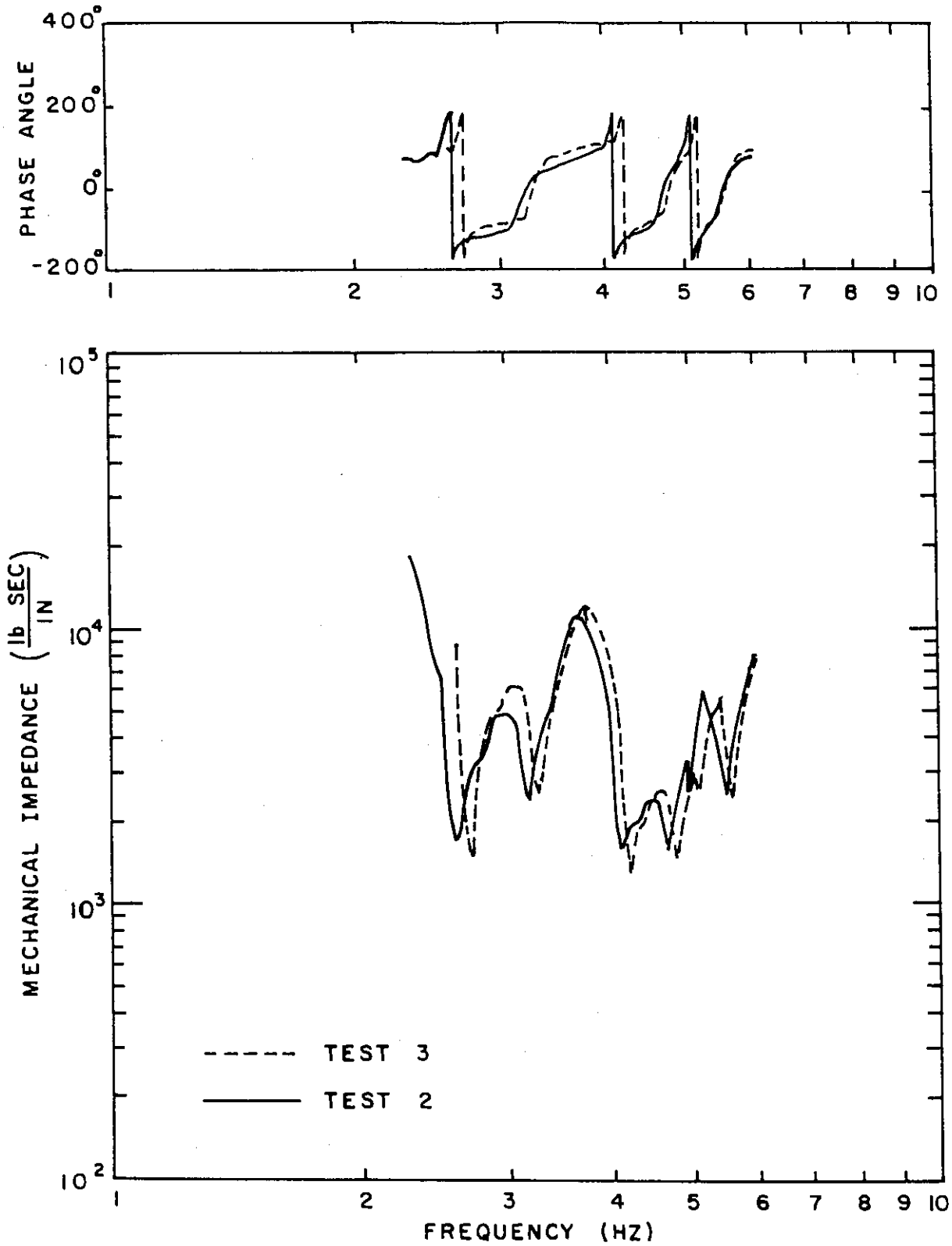

FIGURE A-16. MECHANICAL IMPEDANCE, STATION 9, TEST 2 AND 3

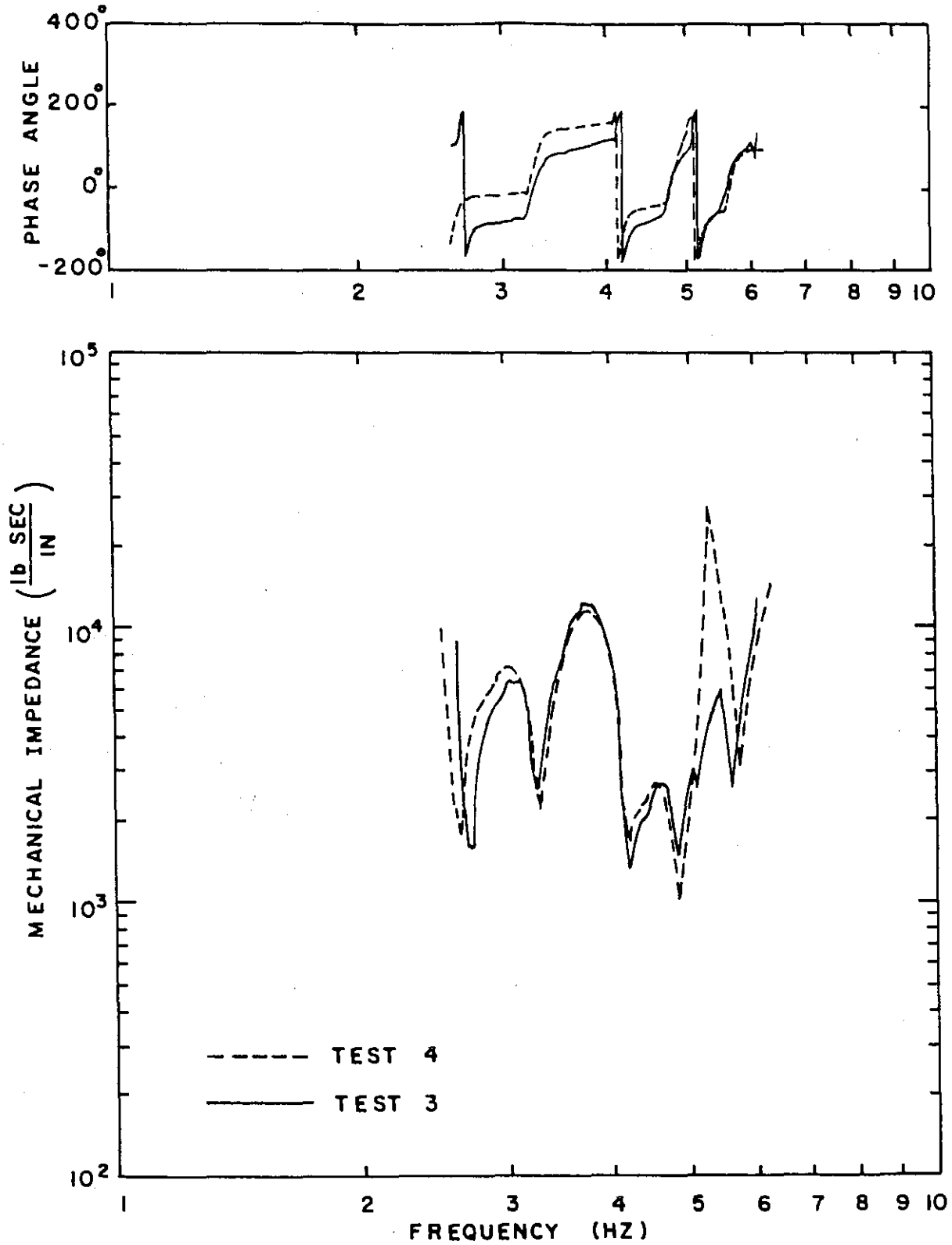

FIGURE A-17. MECHANICAL IMPEDANCE, STATION 9, TEST 3 AND 4

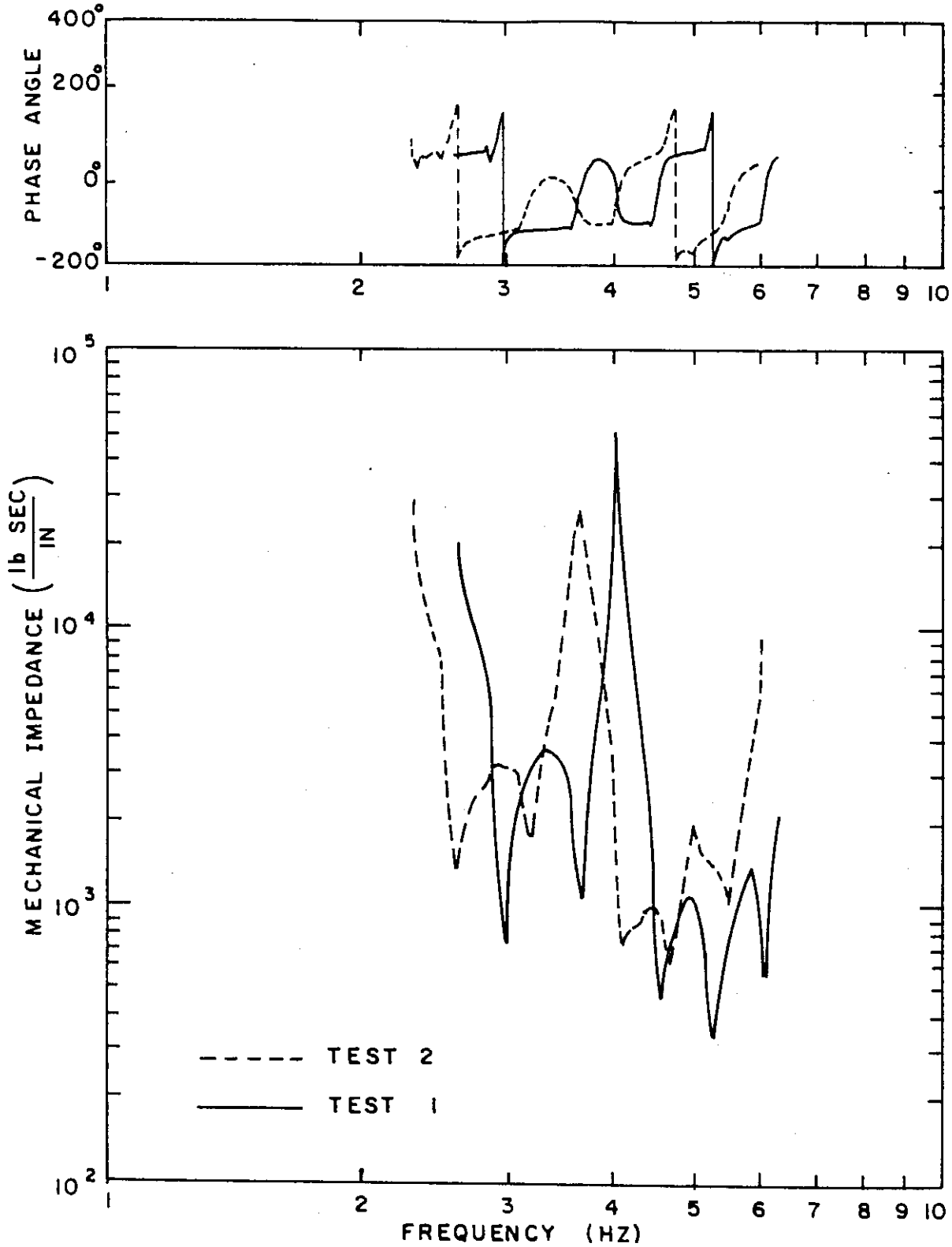

FIGURE A-18. MECHANICAL IMPEDANCE, STATION 30, TEST 1 AND 2

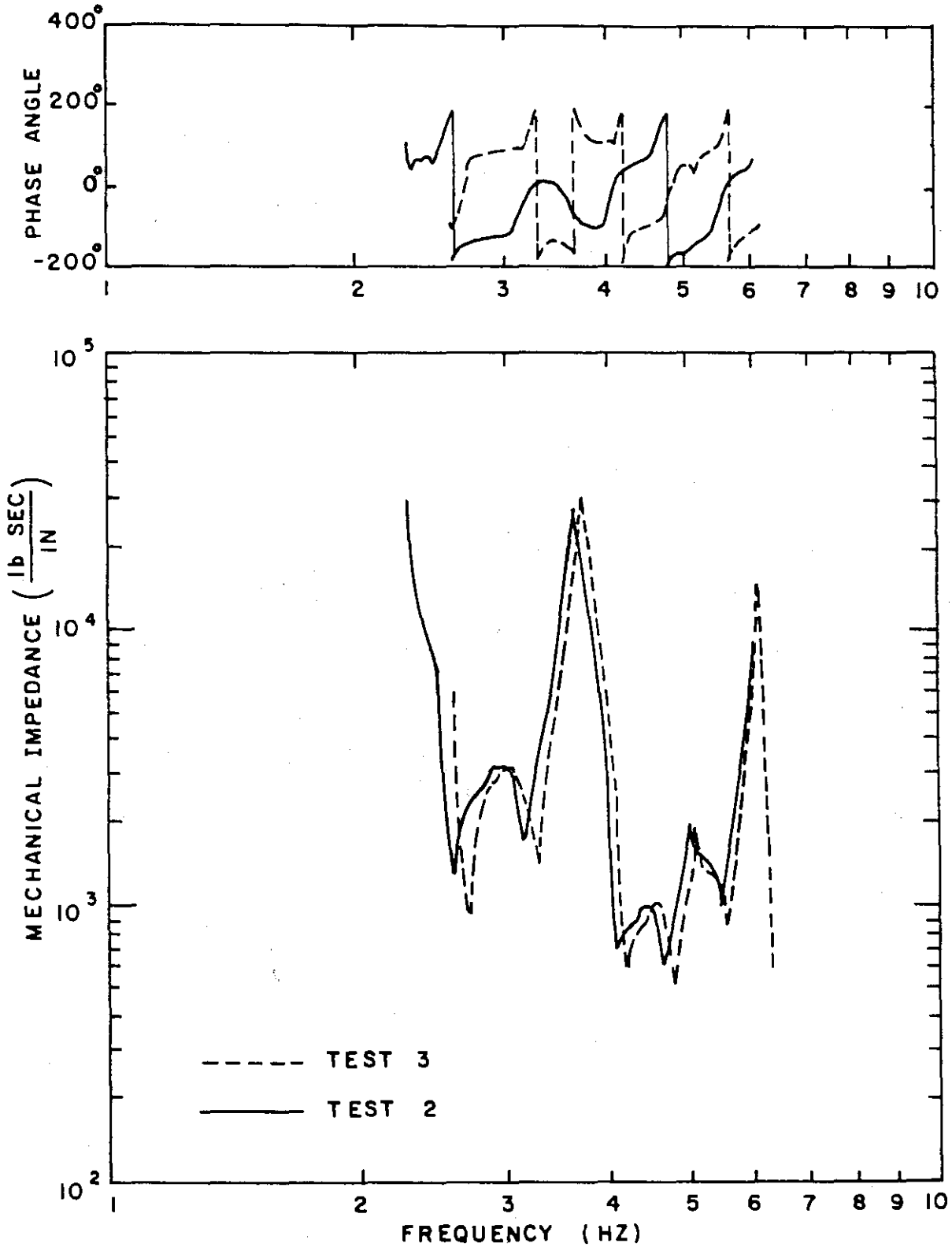

FIGURE A-19. MECHANICAL IMPEDANCE, STATION 30, TEST 2 AND 3

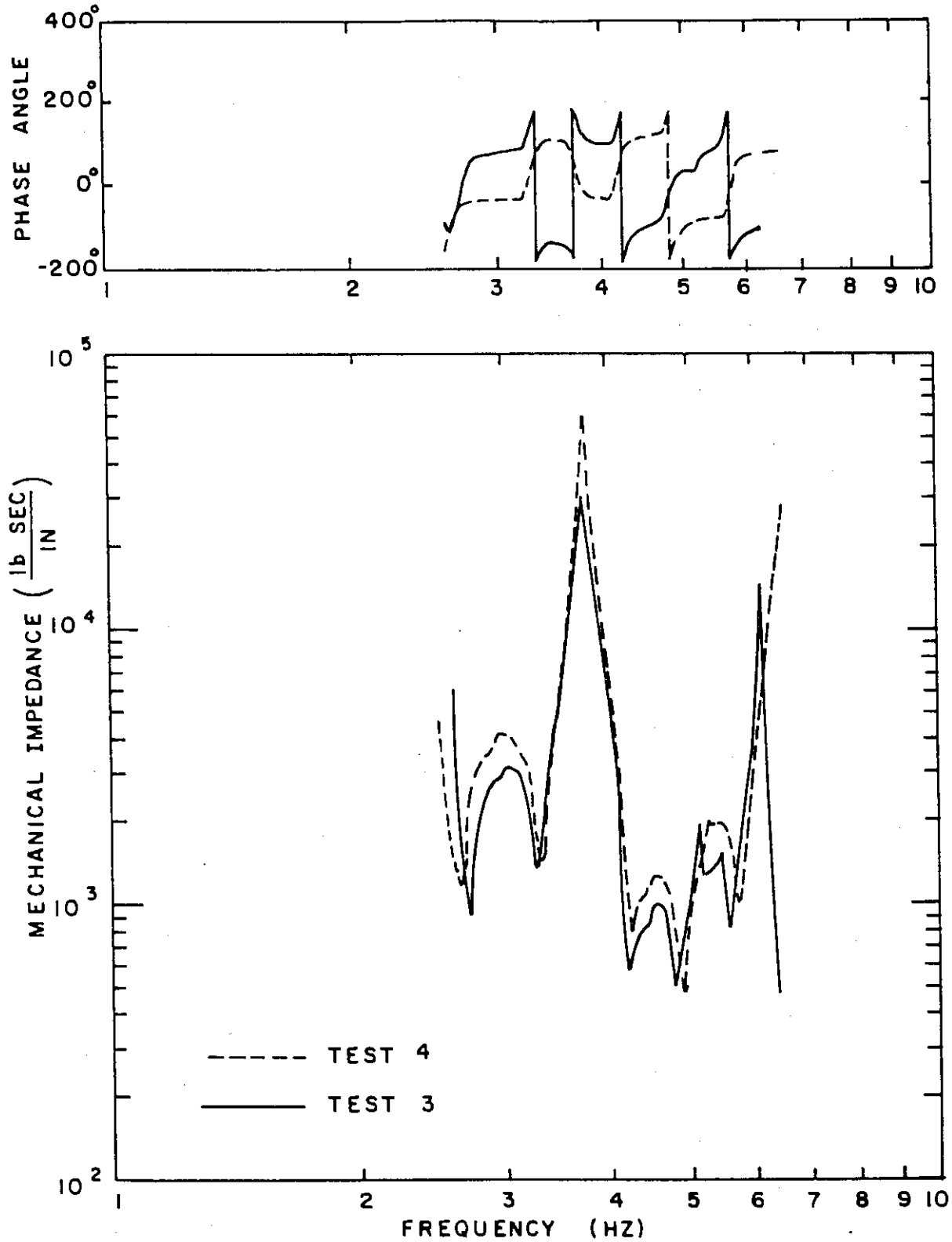

FIGURE A-20. MECHANICAL IMPEDANCE, STATION 30, TEST 3 AND 4

these graphs indicate that there was an increase in the magnitude of the mechanical impedance at all five resonant frequencies. This increase implies an increase in the damping of the bridge between Tests 1 and 2. This finding concurs with the damping results presented in sections A.2.1 and A.2.2. The large change in mechanical impedance between Tests 1 and 2 appears to be associated with the deterioration of the deck of the bridge.

Figures A-13, A-16, A-19 and 4-6 reveal that there was very little change in mechanical impedance of the bridge between Tests 2 and 3. This is indicated by the very small change in the five resonant frequencies and by the small amount of decrease in the magnitude of mechanical impedance at resonance. However, the decrease in mechanical impedance at the resonant frequencies does imply a decrease in the damping of the bridge which is consistent with the damping results presented in Sections A.2.1 and A.2.2. These findings also agree with the fatigue history of the bridge, in which visual observations of the bridge deck indicated minimal fatigue damage between Tests 2 and 3.

Figures A-14, A-17, A-20 and 4-7 illustrate the changes which occurred in mechanical impedance at stations 4, 9, 15 and 30 between Tests 3 and 4. These graphs reveal that there was a greater change in mechanical impedance of the bridge between Tests 3 and 4 than there was between Tests 2 and 3. This is a definite indication of the effect of the cracks and failure in the girders. It is significant to note that Figs. A-17 and 4-7, which represent the plots of mechanical impedance at stations 9 and 15, show the most significant change. Station 15 was located near the center of the bridge where the failure occurred in the south interior girder. It should be noted that the greatest change in mechanical impedance

between Tests 3 and 4 occurs at the higher order frequencies. This is indicated by the changes in the values of the resonant and anti-resonant frequencies and the values of mechanical impedance at both resonance and anti-resonance.

A.2.4 Discussion Of Experimental Results

A summary of the damping ratios obtained from the four dynamic tests by the various damping ratio calculation methods employed during this study are presented in Table 4-1. The damping ratios obtained by the various methods show some disparity in the magnitude of the results. However, all of the various methods predict the same overall trends in the damping ratios between the different dynamic tests and the three modes.

The disparity in the magnitude of the damping ratios for a given dynamic test can be generally accounted for by the fact that each of the methods for determining damping is based on the assumptions that the damping present is linear viscous damping and that the stiffness of the vibratory system is linear. However, the results presented in Art. A.2.1 indicate that the damping present in the bridge is not linear. Deviation from the assumptions associated with the various calculation methods will produce variations in the damping ratios as determined by each of these methods.

The remainder of the discussion of the results is contained in Art. 4.7.

REFERENCES

A1. Brady, R. K., "An Experimental Study of the Dynamic Characteristics of a Composite Highway Bridge," Master's Thesis, University of Missouri-Columbia, August 1977.

A2. Thomson, W. T., "Vibration Theory and Applications," Prentice-Hall, Inc., Englewood Cliffs, N.J., 1965.

A3. Childer, D. G. and Durling, A. E., "Digital Filtering and Signal Processing," West Publishing Co., St. Paul, Minnesota, 1976.

A4. Brigham, O. E., "The Fast Fourier Transform," Prentice-Hall, Inc., Englewood Cliffs, N.J., 1974.

A5. Popoulis, A., "The Fourier Integral and its Applications," McGraw-Hill Book Company, Inc., New York, 1962.

A6. Hurty, W. C. and Rubinstein, M. F., "Dynamics of Structures," Prentice-Hall, Inc., Englewood Cliffs, N.J., 1964.

A7. Salane, H. J., Duffield, R. C., McBean, R. P., Baldwin, Jr., J. W., and Galambos, T. V., "Investigation of the Behavior of a Three-Span Composite Highway Bridge," Report 71-5, Missouri Cooperative Highway Research Program, November 1971.

A8. Amdall, J. K., "Investigation of Mechanical Impedance Techniques," Master's Report, University of Missouri-Columbia, January 1974.

A9. Reed, R. R., "Analysis of Structural Response with Different Forms of Damping," NASA TN D-3861.

A10. Jenkins, G. M. and Watts, D. G., "Spectral Analysis and its Applications," Holden Day, San Francisco, 1968.

APPENDIX B

MULTI-DEGREE OF FREEDOM DYNAMIC PROPERTIES

B.1 INTRODUCTION AND PROBLEM STATEMENT

This appendix contains the results of a study of the dynamic behavior of the aforementioned bridge based on a multi-degree-of-freedom system. One of the objectives of this study was to determine whether the bridge properties are significantly altered by cumulative damage during the service life of a bridge and whether a forced vibration test can be used to detect this damage. The study includes both preliminary analyses and an evaluation of the data obtained from the field testing of the structure. Preliminary analyses were performed for the fatigue and dynamic tests.

Deterioration of the bridge at various stages of the fatigue test was also considered in the preliminary analyses. The results of the preliminary analyses are compared to those obtained experimentally.

B.2 PROCEDURE

In the computations the bridge is presented as a lumped parameter, multi-degree-of-freedom system, with linear, elastic theory being utilized. Damping is assumed to be proportional to stiffness or mass or a linear combination thereof. The number of degrees-of-freedom (DOF) used in the acquisition of test data differed with that

used in the analytical study but those points which were considered critical are included in both cases.

Both dynamic and static responses are obtained from the analytical study. The static responses are used in calculating dead load stresses and deflections. Calculated responses are compared with corresponding experimental results to determine the reliability of analytical predictions.

Changes in the stiffness and damping properties of the bridge are also evaluated from the dynamic tests. The setup for these tests is similar to the fatigue test except all the ballast is removed and three resonant frequencies rather than one are excited. Accelerations are measured at various points on the bridge and then analyzed to evaluate the stiffness and damping properties.

In this report the normal mode tests are identified by B1X for first bending, T1X for torsion, and B2X for second bending where X is the number of the test, (X=1,2,3,4).

B.3 DESCRIPTION OF NORMAL MODE DYNAMIC TESTS

B.3.1 General

Four sets of normal mode tests were performed to determine the changes in the dynamic properties of the bridge at various stages of the fatigue test.

For each normal mode test the bridge was excited at one of its natural frequencies. All ballast was removed for these tests and

the exciting force reduced to the extent that stresses were approximately 12 percent of those induced in the fatigue test. Sketches of the mode shapes are shown in Fig. B-1.

B.4 PRELIMINARY ANALYSES

B.4.1 General

Preliminary dynamic analyses of the test bridge were performed prior to the field test. These analyses were performed so that values could be obtained for the response and forces which would be required in the fatigue and dynamic tests. In this manner parameters such as actuator requirements and transducer ranges could be established before the actual field test began. The results from these analyses also provides a source for comparison between analytical and experimental results.

Two computer programs were used in the preliminary analyses. One program, DYNBM,[B1] was prepared in-house. The second program was STRUDL (Structural Design Language) from the ICES (Integrated Civil Engineering Systems) package prepared by the Massachusetts Institute of Technology. In DYNBM the bridge is modeled as an equivalent one-dimensional beam with 25 DOF, while in the STRUDL analysis the bridge is modeled as a two-dimensional, 74 DOF grid. Both programs are based on linear, elastic theory.

The analyses were performed with and without ballast on the bridge. In this way values were obtained for both the fatigue test and the dynamic tests.

FIRST BENDING

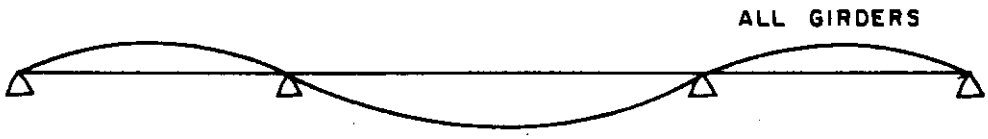

FIRST TORSION

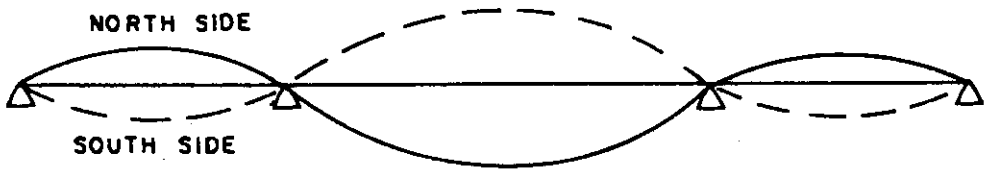

SECOND BENDING

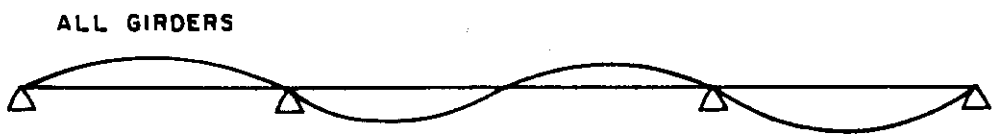

FIGURE B-1. MODE SHAPES

B.4.2 Bridge Properties

The structural properties of the bridge would be changing as the fatigue test progressed due to deterioration of the bridge deck. This presented a problem in the preliminary analyses since the rate of deterioration was unknown. It was decided that three different states of deterioration would be included in the analyses of the structure. These three states are fully composite, composite, and cracked slab composite. In fully composite action, the entire slab is acting compositely with the girders; no deterioration has yet occurred in the slab. In composite action, however, the concrete is assumed to be acting compositely with the girder in the regions of positive dead load moment, while in the regions of negative dead load moment only the slab reinforcement is included in the composite section. Finally in the cracked slab composite state, the deck has deteriorated to such an extent that only the slab reinforcement is acting compositely with the girders along the entire length of the bridge.

The results obtained by using these three states provided an upper and lower bound for the dynamic response and the experimental requirements of the test equipment. Two percent equivalent viscous damping was assumed in all analyses.

A noncomposite action was assumed when determining dead load stresses since the dead load of the slab and structural steel was completely carried by the girders.

B.5 COMPARISON OF PREDICTED AND EXPERIMENTAL RESULTS

B.5.1 General

In this article the analytical results obtained from DYNBM and STRUDL are compared with the experimental results. By comparing the results of the two programs, an evaluation can be made as to whether the additional degrees of freedom used in the STRUDL analysis make a significant difference in predicted response to warrant the additional cost incurred. The STRUDL analysis costs approximately eight times as much as the DYNBM analysis.

Experimental data from the second set of normal mode tests appeared to be erroneous. Therefore, comparison of these data will not be included in this report.

B.5.2 Tabulation of Experimental Results

The experimental results used for comparison are listed in Tables B-1 and B-2. The notation is defined at the end of this article. All values, except damping, were measured directly during the testing. Peak strains and deflections were measured at station 16 (see Fig. 1-8) for all tests except the second bending mode of the normal mode tests in which case station 4 was used. All strains were measured at the top of the bottom flange. Strains are converted and listed in terms of stress using a modulus of elasticity of 29,500 ksi. Only the ranges (double amplitudes) of stresses and deflections are listed since only the ranges will be used for comparison.

TABLE B-1 EXPERIMENTAL RESULTS - FATIGUE TEST

Cycles (K)	Z (in) SA	f (Hz)	X (in) DA	ε (μin/in) DA	ζ (%)
0.0	0.500	2.320	1.53	237	1.5
31.3	1.295	2.067	4.78	684	1.3
76.2	1.350	2.042	4.88	723	1.4
91.5	1.300	2.066	5.09	770	1.3
125.3	1.370	2.045	4.78	702	1.5
154.5	1.325	2.042	5.17	761	1.3
190.2	1.230	2.025	5.11	773	1.2
241.0	1.200	2.032	5.12	761	1.2
313.5	1.450	2.030	4.88	729	1.6
470.4	1.505	1.932	4.89	711	1.8

SA = Single amplitude

DA = Double amplitude

MOVING MASS = 9.76 kips

TABLE B-2 EXPERIMENTAL RESULTS - NORMAL MODE TESTS

Test	Z (in) SA	f (Hz)	X (in) DA	ε (μ in/in) DA	ζ (%)
B11	0.800	2.869	0.200	89	1.3
T11	0.503	3.507	0.144	74	1.3
B21	0.325	4.507	0.075	59	1.3
B12	0.990	2.570	0.202	83	2.0
T12	0.600	3.270	0.150	41	2.2
B22	0.385	4.120	0.076	50	1.9
B13	0.960	2.638	0.250	65	1.7
T13	0.720	3.047	0.115	27	2.0
B23	0.365	4.177	0.080	47	1.6
B14	1.110	2.385	0.266	59	1.9
T14	0.665	3.136	0.101	27	1.7
B24	0.425	3.987	0.074	38	1.5

(moving mass = 1.115 kips)

DA = Double amplitude

SA = Single amplitude

The notation used is defined as follows:

f = frequency (Hz)

σ = stress (Ksi)

ε = strain (in./in.)

ζ = damping ratio (%)

X = peak deflection (in.), double amplitude

Z = stroke of actuator (in.), single amplitude.

The forcing function is sinusoidal for all tests and stroke will be presented here and throughout the report as single amplitude.

B.5.3 Tabulation of Comparisons

Comparisons between the results from the preliminary analysis programs and the experimental results are tabulated in Tables B-3 through B-8. Stress and deflection comparisons are made at station 4 for the second bending mode of the normal mode tests and at station 16 for all other tests. Composite action is assumed when comparing experimental data with results determined by preliminary analysis.

Stresses and deflections from the preliminary analyses are scaled proportionally so that the damping ratios agree with those obtained from experimental data.

B.6 RESULTS OF DYNAMIC ANALYSIS

B.6.1 General

In this article the results of the analysis of the normal mode data are discussed. The objective of the analysis is to determine

TABLE B-3 PREDICTED AND EXPERIMENTAL FREQUENCIES - FATIGUE TEST

Calculated - Hz.

STATE	STRUDL	DYNBM	% DIFF.
Fully Composite	2.60	2.50	3.8
Composite	2.48	2.41	2.9
Cracked Slab Composite	1.595	1.53	4.1

Experimental

Cycles (K)	Frec. (Hz)
0.0	2.320
31.3	2.067
76.2	2.042
91.5	2.066
125.3	2.045
154.5	2.042
190.2	2.025
241.0	2.032
313.5	2.030
470.4	1.932

TABLE B-4 PREDICTED AND EXPERIMENTAL FREQUENCIES
- NORMAL MODE TESTS

Calculated - Hz.

FIRST BENDING	STRUDL	DYNBM	% DIFF.
Fully Composite	2.908	2.780	4.4
Composite	2.530	2.780	2.8
Cracked Slab Composite	1.892	1.790	5.4
SECOND BENDING			
Fully Composite	4.633	4.480	3.3
Composite	4.420	4.320	2.1
Cracked Slab Composite	3.020	2.900	4.0

Experimental - Hz.

TEST	EXPT.	STRUDL	% DIFF	DYNBM	% DIFF
		(F)			
B11	2.869	2.908	-1.4	2.780	3.1
T11	3.507	3.104	11.5	--	--
B21	4.507	4.633	-3.6	4.480	0.6
		(C)		(C)	
B13	2.638	2.530	4.1	2.460	6.7
T13	3.047	2.769	9.1	--	--
B23	4.177	4.420	-5.8	4.320	-3.4
B14	2.385	2.530	-6.1	2.460	-3.1
T14	3.136	2.769	11.7	--	--
B24	3.987	4.420	-10.8	4.320	-8.3

(F) - Fully Composite

(C) - Composite

TABLE B-5 PREDICTED AND EXPERIMENTAL DEFLECTION RANGES - FATIGUE TESTS

DYNBM vs. STRUDL; Center Midspan

STAGE	% DIFF
Fully Composite	5.9
Composite	6.2
Cracked Slab Composite	7.7

$$\% \text{ DIFF} = \frac{\text{STR-DYN}}{\text{STR}} \times 100$$

Experimental Results, Sta. 17

Cycles (k)	Expt. DA	STRUDL DA	% DIFF	DYNBM DA	% DIFF
0.0	1.53	1.57	-2.6	1.47	3.9
31.3	4.78	4.71	1.5	4.40	7.9
76.2	4.88	4.55	6.8	4.25	12.9
91.5	5.09	4.72	7.3	4.42	13.2
125.3	4.78	4.32	9.6	4.04	15.5
154.5	5.17	4.82	6.7	4.51	12.8
190.2	5.11	4.85	5.1	4.53	11.4
241.0	5.12	4.73	7.6	4.43	13.5
313.5	4.88	4.29	12.1	4.02	17.6
470.4	4.89	4.80	1.8	4.50	8.0

DA = Double amplitude (in.)

TABLE B-6 PREDICTED AND EXPERIMENTAL DEFLECTION RANGES - NORMAL MODE TESTS

DYNBM vs. STRUDL

FIRST BENDING Center Midspan	% DIFF
Fully Composite	9.6
Composite	7.0
Cracked Slab Composite	1.9
SECOND BENDING Center End Span	
Fully Composite	3.5
Composite	5.5
Cracked Slab Composite	1.1

Experimental Results, Sta. 16

TEST	EXPT DA	STRUDL DA	% DIFF	DYNBM	% DIFF
B11	0.200	0.237	-18.5	0.211	-5.5
T11	0.144	0.172	-19.4	--	--
*B21	0.075	0.083	-10.7	0.071	5.3
B13	0.250	0.218	12.8	0.193	22.8
T13	0.115	0.153	-33.0	--	--
*B23	0.080	0.076	5.0	0.065	18.8
B14	0.266	0.225	15.4	0.200	24.8
T14	0.101	0.166	-64.4	--	--
*B24	0.074	0.095	-28.4	0.080	-8.1

*Compared at Station 4

DA = Double amplitude (in.)

TABLE B-7 PREDICTED AND EXPERIMENTAL STRESS RANGES - FATIGUE TEST

DYNBM vs. STRUDL, Sta. 7, Top of Bottom Flange

STAGE	% DIFF
Fully Composite	4.6
Composite	8.5
Cracked Slab Composite	8.6

Experimental Results, Sta. 7, Top of Bottom Flange

Cycles	Expt. DA	STRUDL DA	% DIFF	DYNBM DA	% DIFF
0.0	8.0	8.0	-0.0	6.6	17.5
31.3	23.2	24.0	-3.4	19.7	15.1
76.2	24.5	23.3	4.9	19.0	22.4
91.5	26.1	24.2	7.3	19.7	24.5
125.3	23.8	22.0	7.6	18.0	24.4
154.5	25.8	24.6	4.7	20.2	21.7
190.2	26.2	24.7	5.7	20.2	22.9
241.0	25.8	24.2	6.2	19.8	23.3
313.5	24.7	21.9	11.3	17.9	27.5
470.4	24.1	20.2	16.2	16.5	31.5

Comparison based on composite action

DA = Double amplitude (ksi)

TABLE B-8 PREDICTED AND EXPERIMENTAL STRESS RANGES - NORMAL MODE TESTS

DYNBM vs. STRUDL, Sta. 16, Top of Bottom Flange

FIRST BENDING Center Midspan	% DIFF
Fully Composite	11.3
Composite	7.1
Cracked Slab Composite	4.5
SECOND BENDING - Sta. 4	
Fully Composite	6.6
Composite	4.6
Cracked Slab Composite	4.5

Experimental Results, Sta. 16, Top of Bottom Flange

TEST	EXPT. DA	STRUDL DA	% DIFF	DYNBM	% DIFF
B11	3.0	3.7	-23.3	3.4	13.3
T11	2.5	2.5	0.0	--	--
*B21	2.0	1.8	10.0	1.7	15.0
B13	2.2	3.4	-54.5	3.2	-45.0
T13	1.8	2.1	-16.7	--	--
*B23	1.6	1.7	6.3	1.6	0.0
B14	2.0	3.5	-75.0	3.3	-65.0
T14	1.8	2.5	-38.9	--	--
*B24	1.3	2.1	-61.5	2.0	-53.8

*Compared at Station 4

DA = Double amplitude (in.)

the changes in the dynamic properties. The stiffness and damping matrices are compared as the fatigue test progressed.

A study of the raw data signals and mode shapes also reveals deterioration of the bridge. The trends observed in these data indicate what should be expected from the analysis. A discussion of the changes observed in the signals and mode shapes is also included in this Appendix.

The normal mode test data recorded during Test 2 appears to be erroneous and will not be included with these results.

B.6.2 Study of Data

Changes in the structure can be noted by a study of data prior to performing an analysis. This article will illustrate those changes which can be seen by studying raw data signals, mode shapes of the response, and a spectral analysis of the data.

B.6.2.1 Raw Data

By observing plots of the raw data at a station for each mode of the normal mode tests, a definite trend is noticed. As expected the signals from all modes of Test 1 are a smooth sinusoidal curve. However, the signal of the first bending mode of Test 3 shows that the negative portion of the cycle is not symmetric with respect to the positive portion of the cycle. The first bending mode of Test 4 displays an even larger anomaly. This indicates that the bridge is no longer vibrating in a pure first bending mode. The wave shape

of the torsional and second bending modes are smooth in all tests. The presence of the additional frequency in the first bending mode revealed the need for a spectral analysis. A plot of the accelerations at the reference station is shown for various normal mode tests in Figs. B-2a through B-2e.

B.6.2.2 Spectral Analysis

A spectral analysis of the data reveals the presence of a harmonic component in the first bending mode of Tests 3 and 4, with the amplitude of the harmonic becoming larger in Test 4. No significant harmonic is detected in the spectrum of the other modes. Plots of the spectra for several modes are in Figs. B-3a through B-3e. Although the Nyquist frequencies of the first bending and torsional modes are 35 Hz and 50 Hz for the second bending mode, the plots are only valid to 10 Hz. This is due to the analog filter with a low band pass of 10 Hz which was applied to the accelerometer signals.

Spectral analysis of the exciting force for the first bending mode in Test 1 shows a small harmonic component. This is shown in Fig. B-4. None of the other excitations were recorded. The anomaly visible in the first bending mode plot of the raw accelerometer signal is a harmonic and its absence in Test 1 and subsequent growth in Tests 3 and 4 indicate the structure is deteriorating. As it does, it apparently becomes more susceptible to the harmonic component of the exciting force. Since no significant harmonic is visible in the torsional

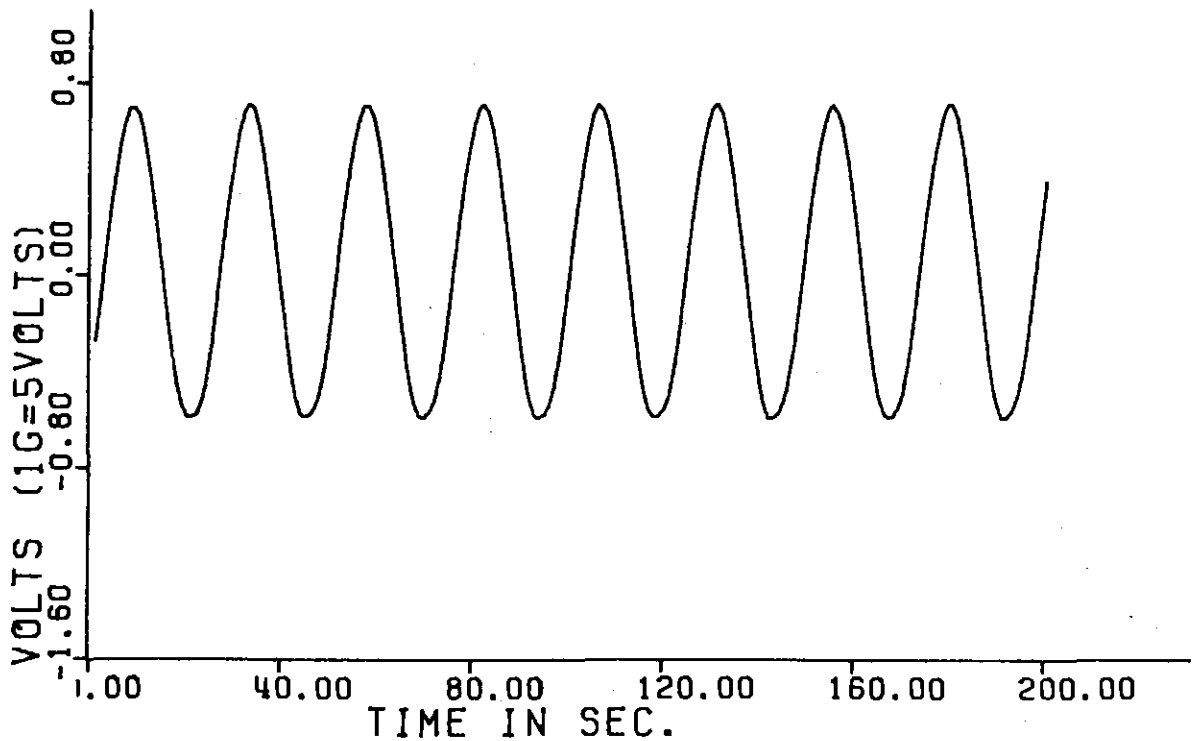

FIGURE B-2a. PLOT OF RAW DATA - B11

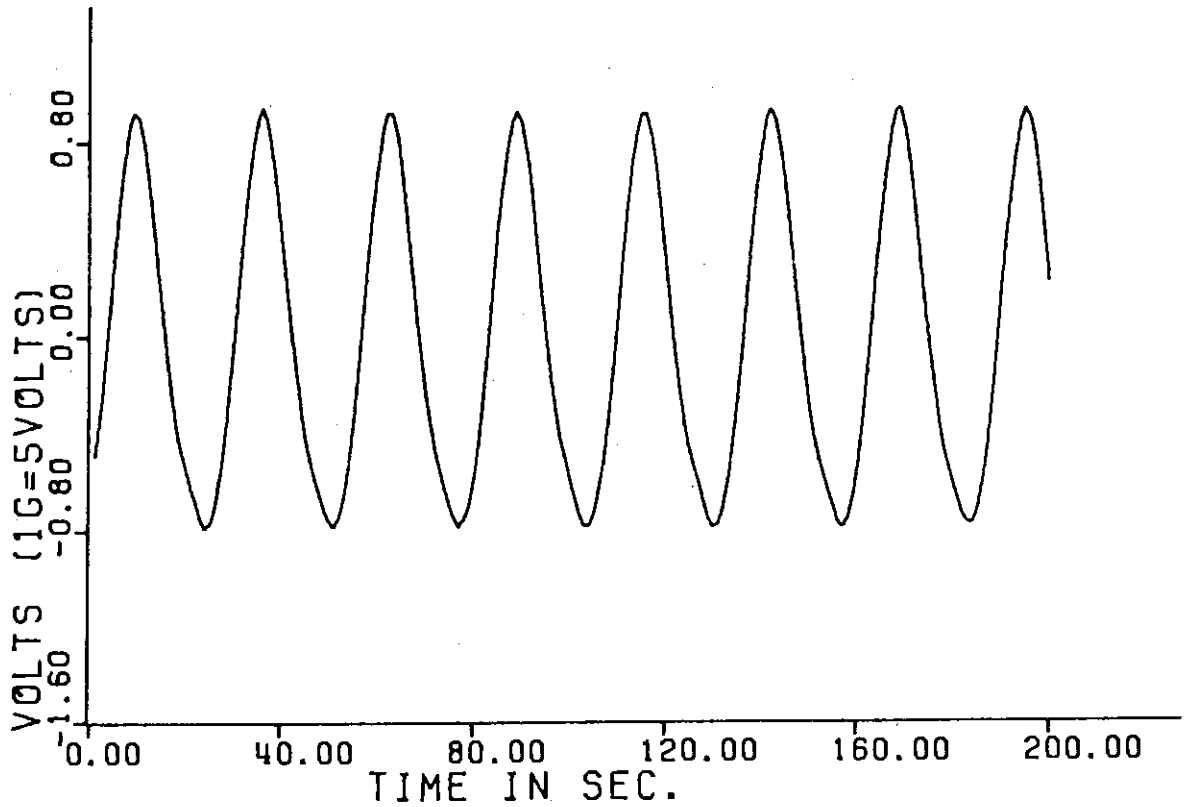

FIGURE B-2b. PLOT OF RAW DATA - B13

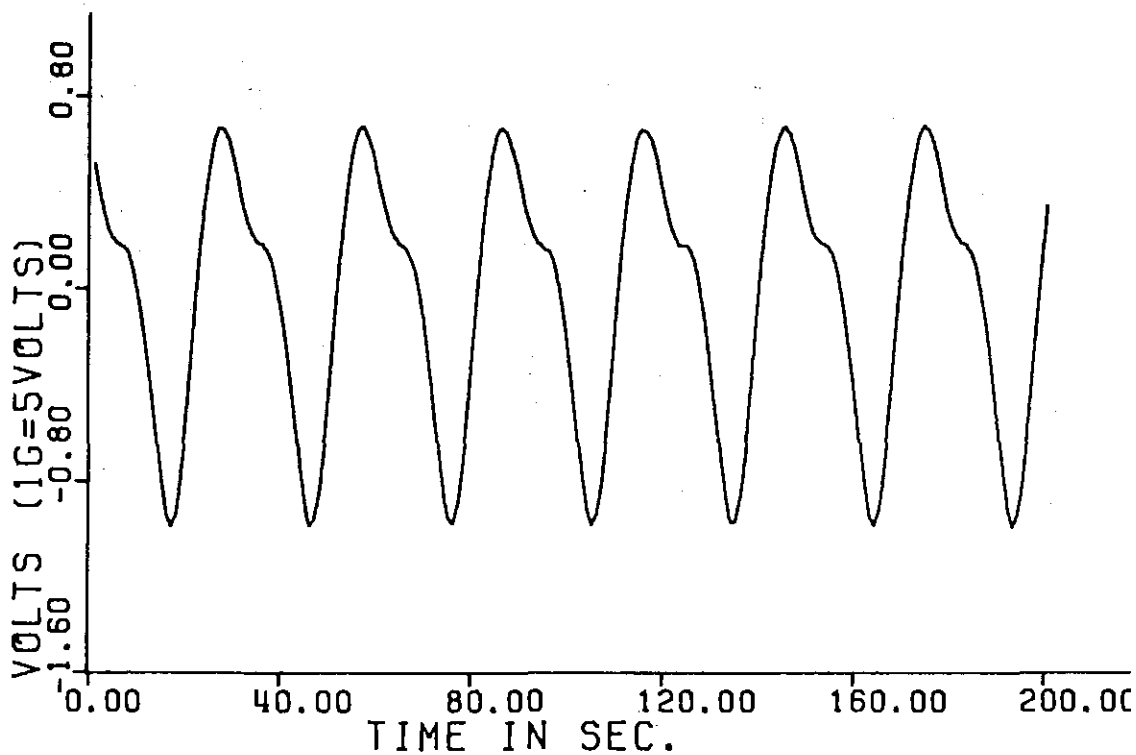

FIGURE B-2c. PLOT OF RAW DATA - B14

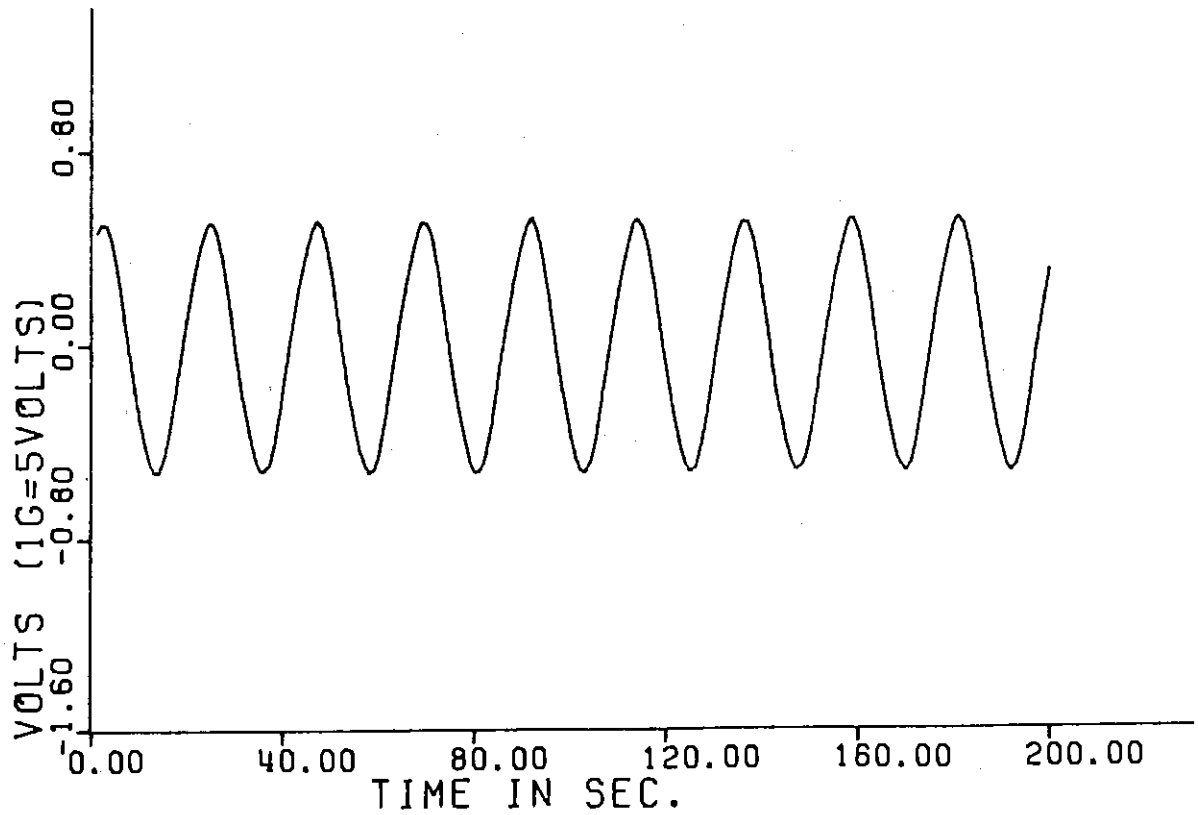

FIGURE B-2d. PLOT OF RAW DATA - T14

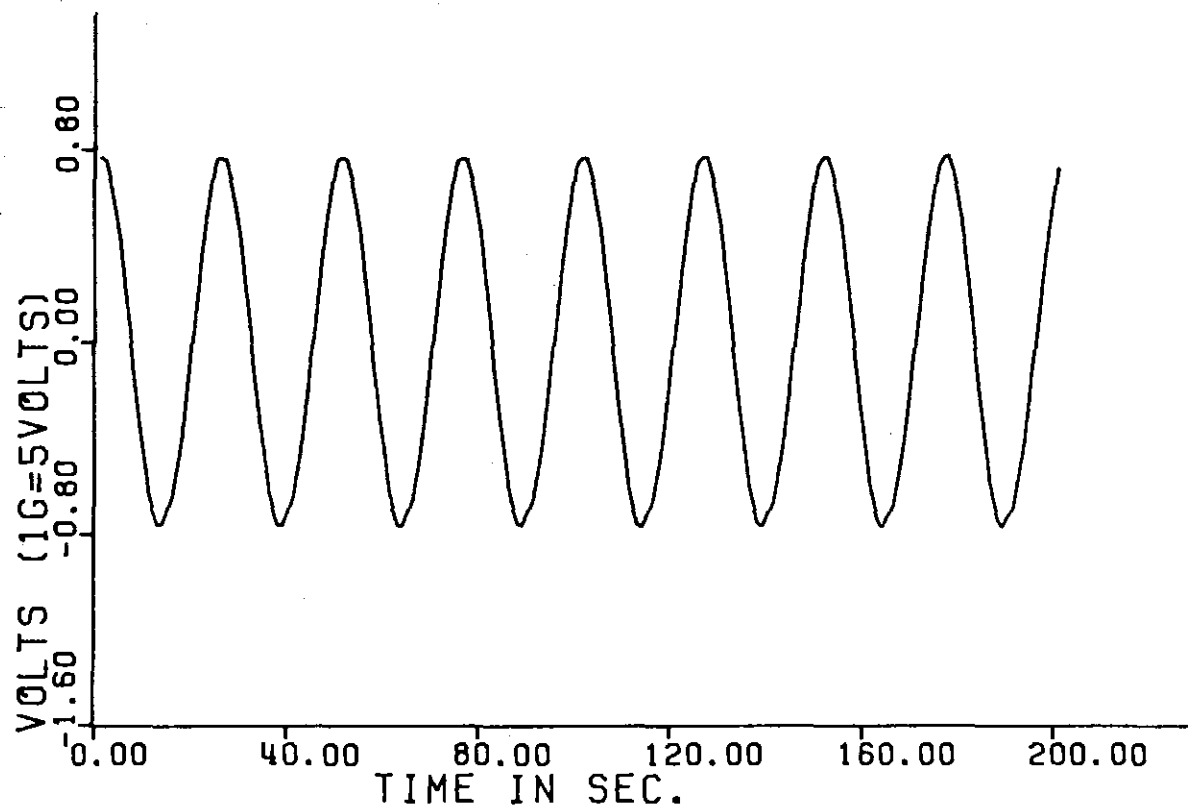

FIGURE B-2e. PLOT OF RAW DATA - B24

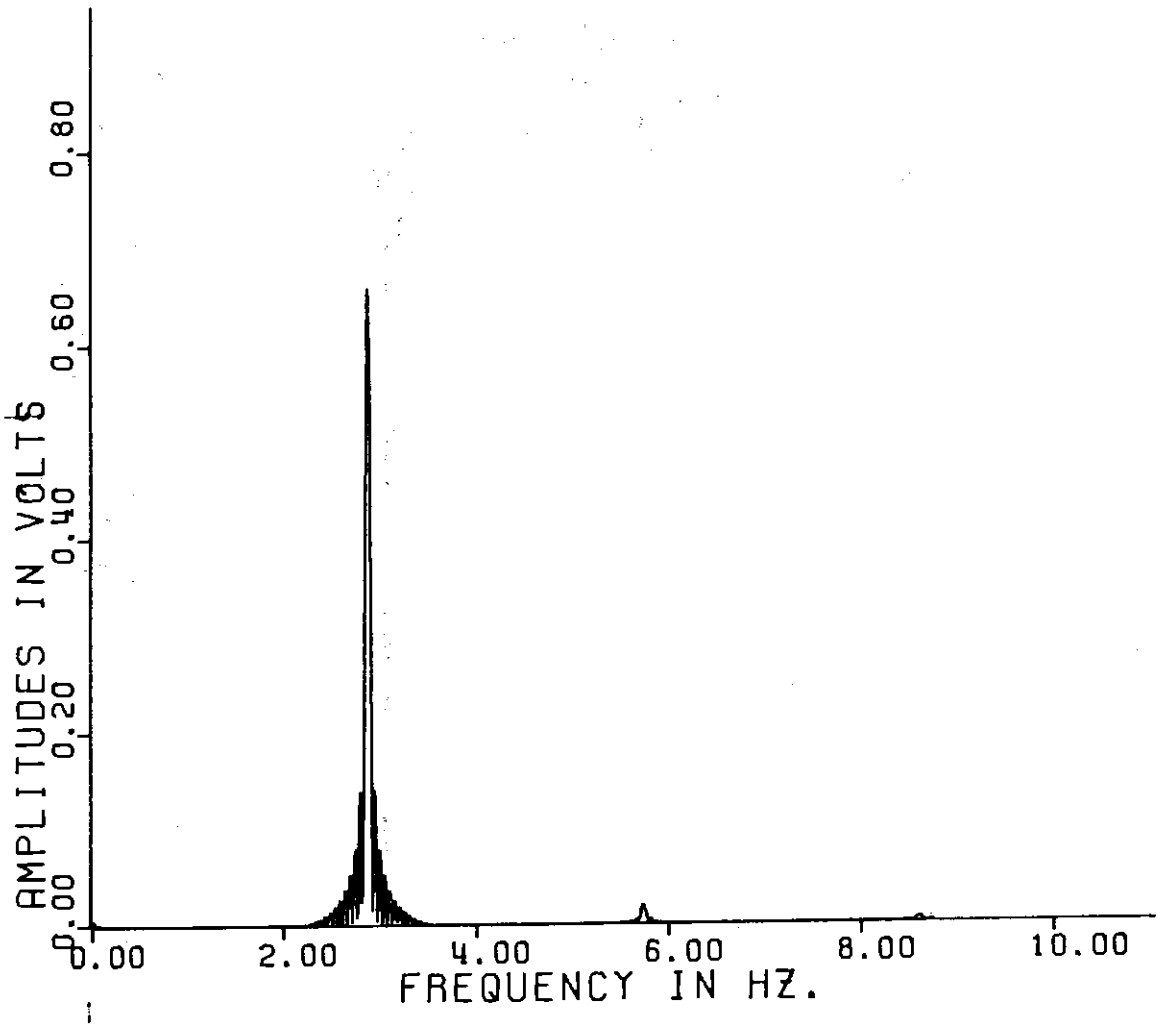

FIGURE B-3a. SPECTRUM OF RESPONSE - B11

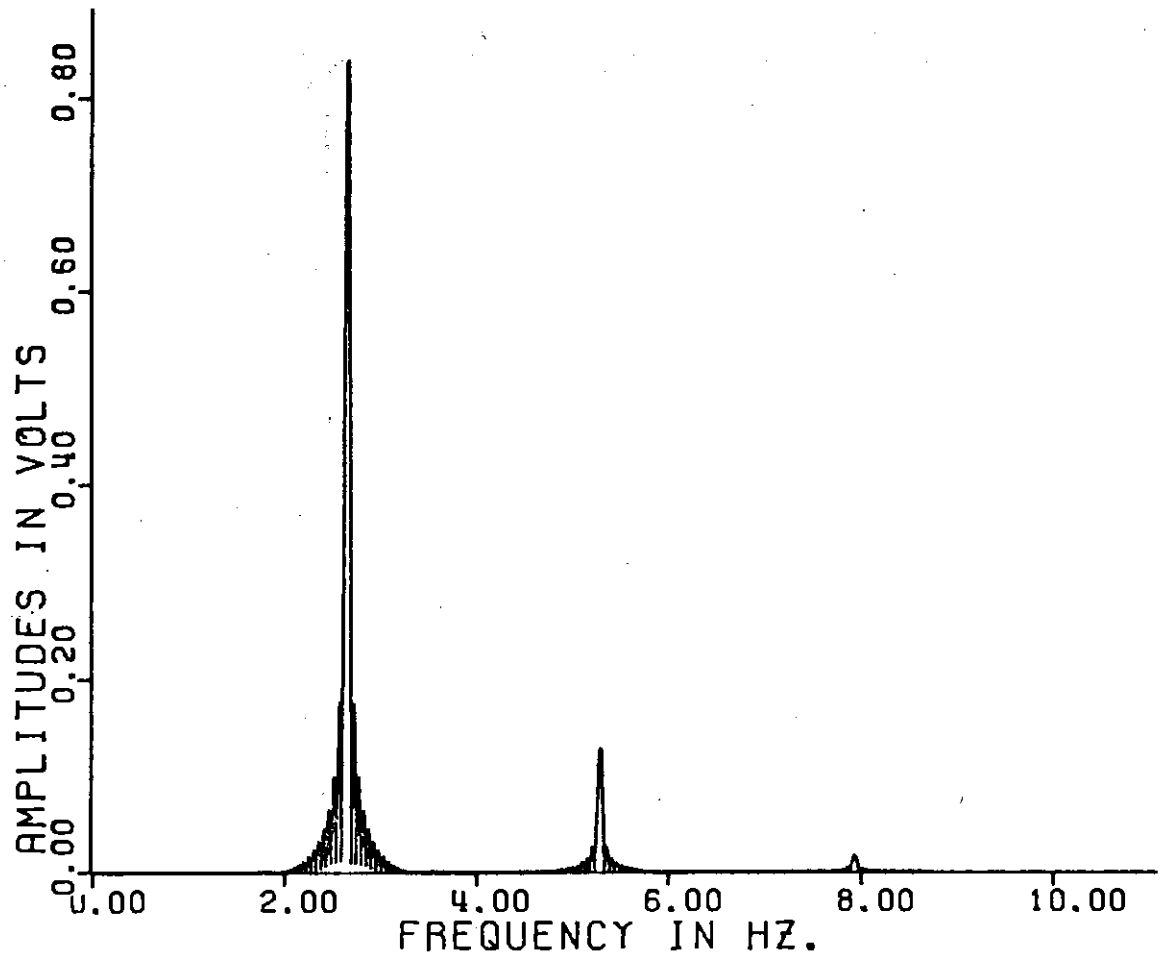

FIGURE B-3b. SPECTRUM OF RESPONSE - B13

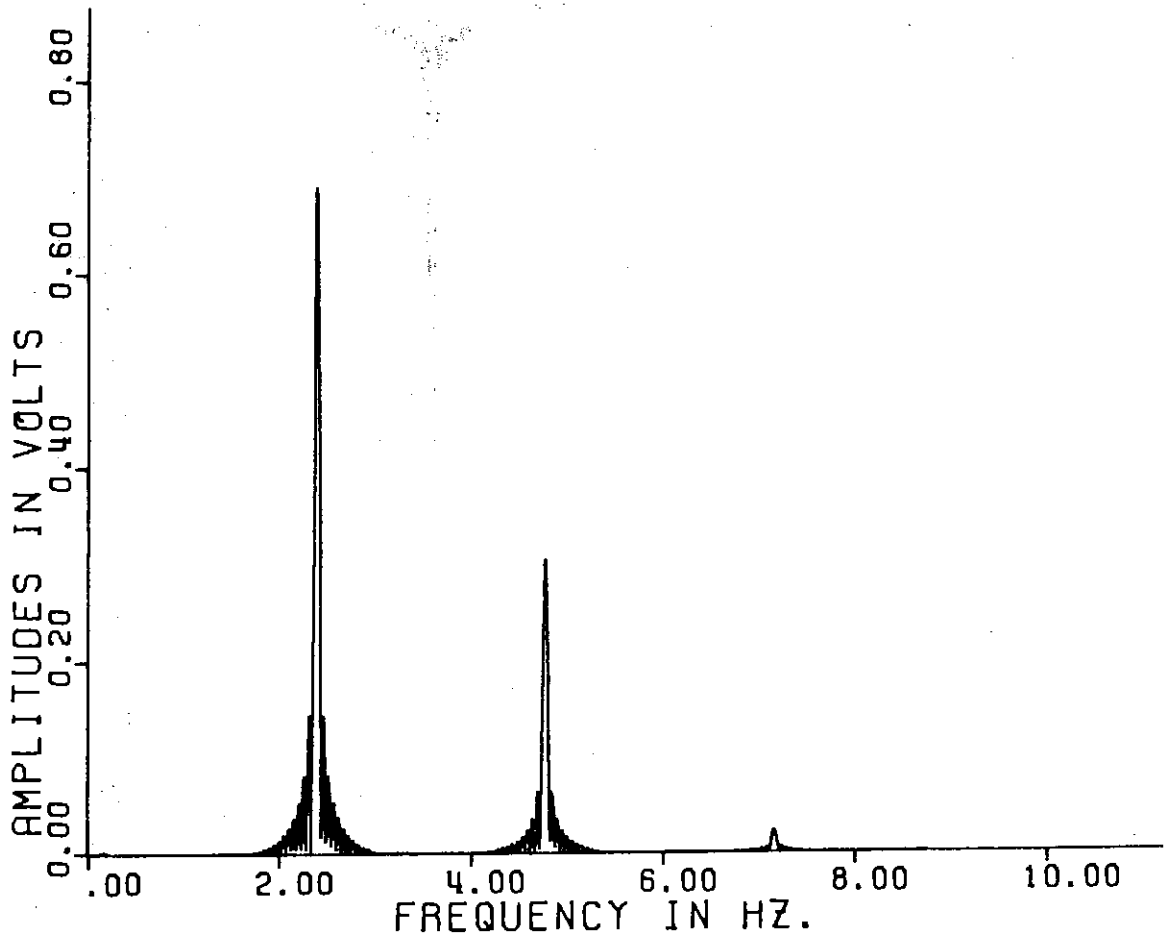

FIGURE B-3c. SPECTRUM OF RESPONSE - B14

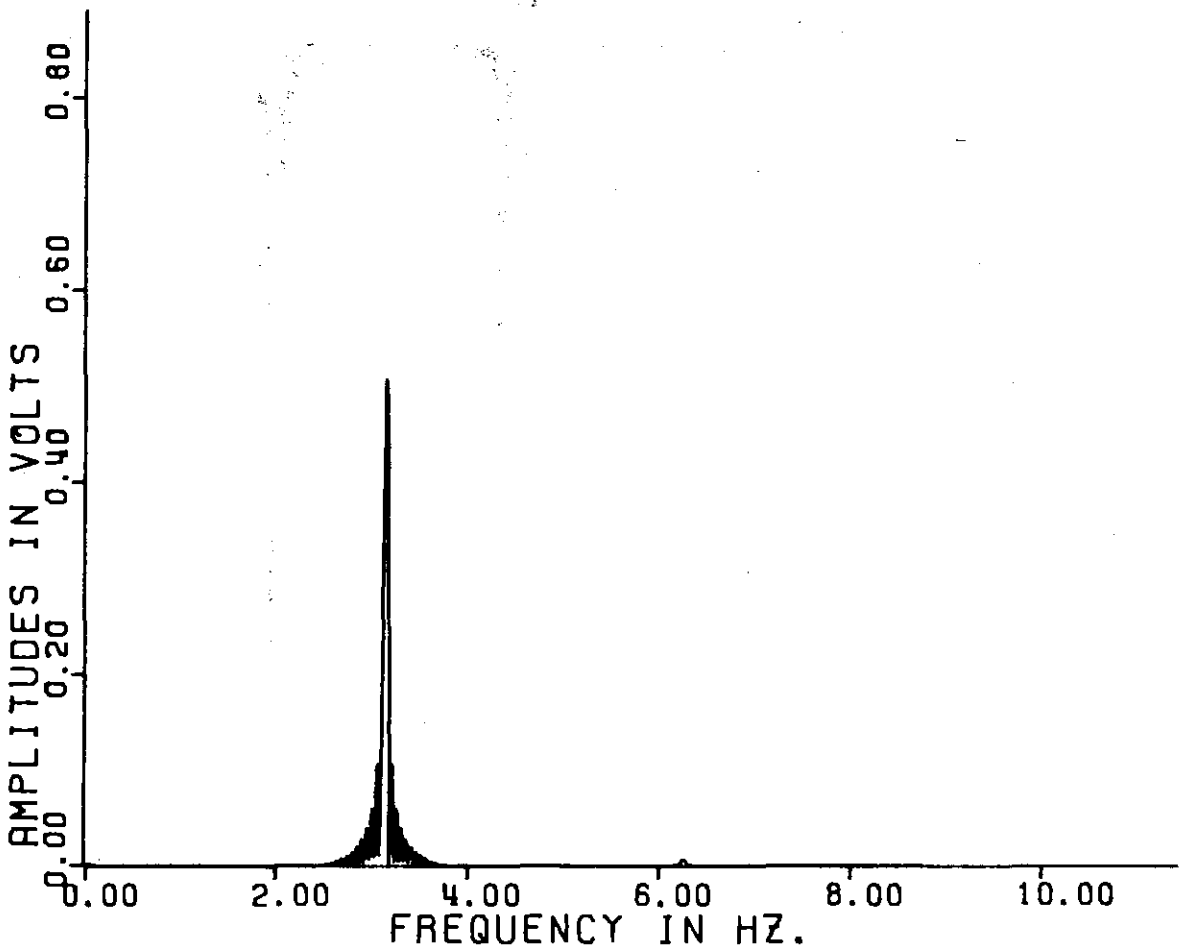

FIGURE B-3d. SPECTRUM OF RESPONSE - T14

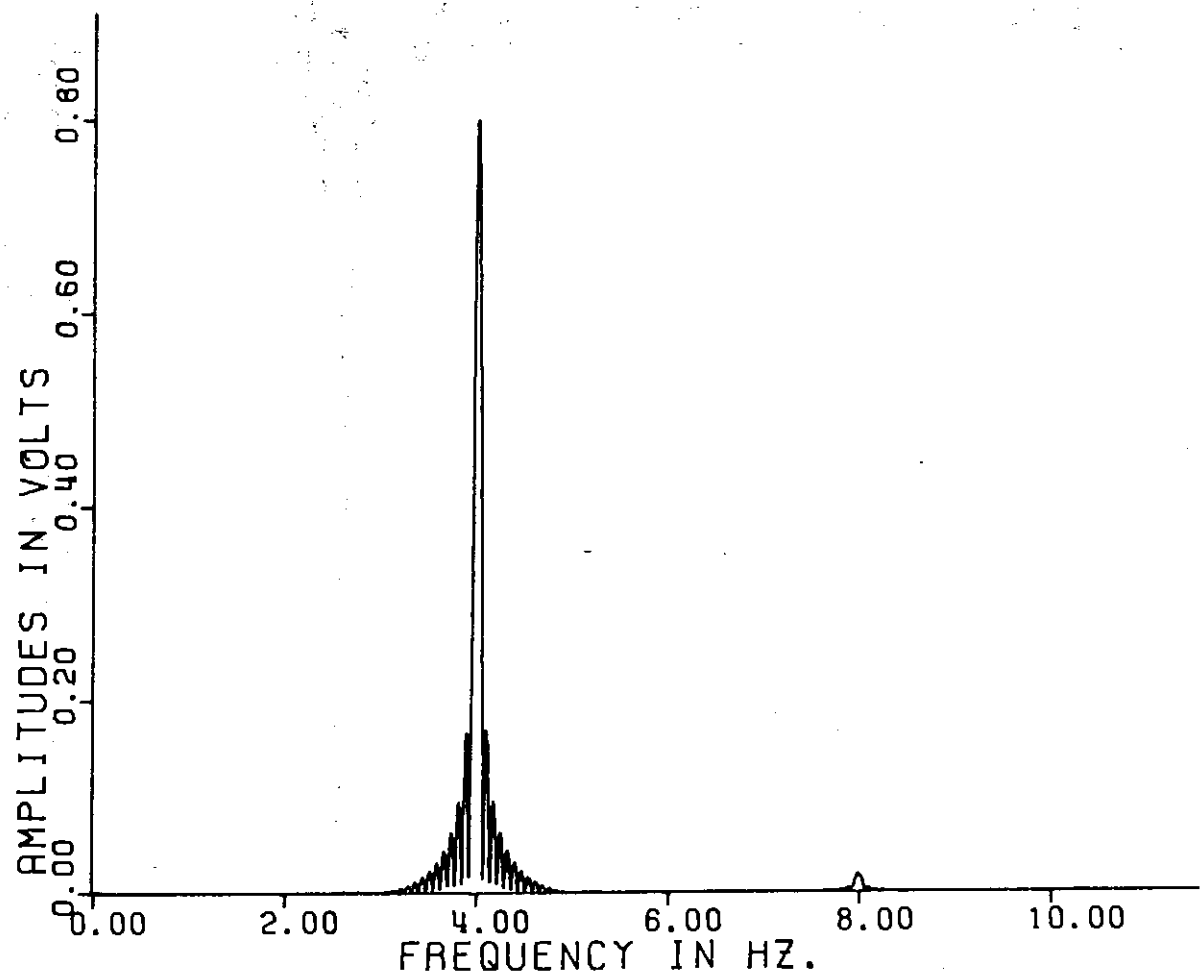

FIGURE B-3e. SPECTRUM OF RESPONSE - B24

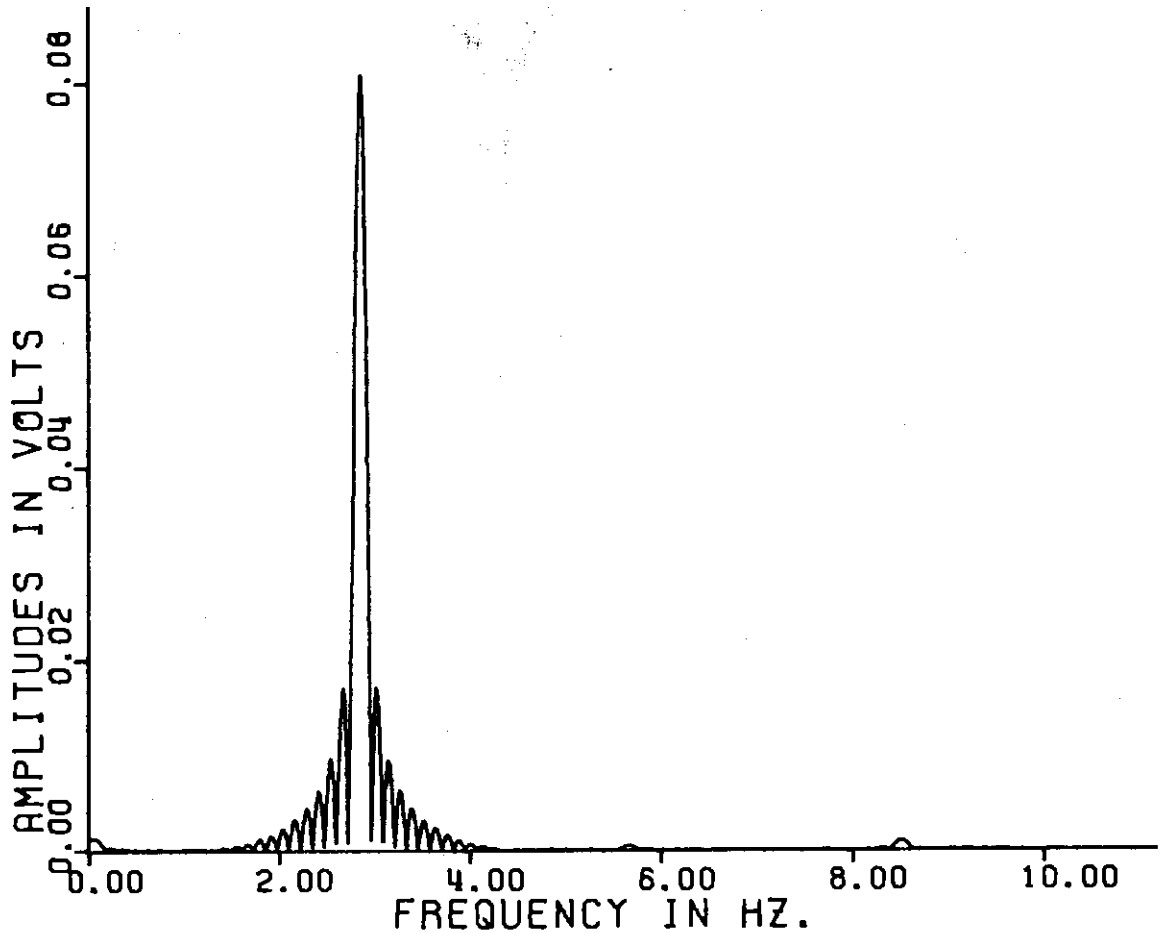

FIGURE B-4. SPECTRUM OF EXCITING FORCE - B11

or second bending response data, it appears that the bridge has not yet deteriorated sufficiently for the higher harmonics of the exciting frequencies to have a noticeable effect. Deterioration is also shown in all modes by the decrease in the natural frequencies from Tests 1 to 4. The modal frequencies for each of the tests are tabulated in Table B-2.

8.6.2.3 Mode Shapes

Mode shapes of the bridge were obtained by plotting the positive and negative peaks at each station. These mode shapes illustrate the response of the bridge with the harmonic included.

A study of these mode shapes shows the south girder has a larger deflection and the difference between the deflections of the north and south sides increased as the fatigue test progressed. This would indicate that the south side of the bridge is deteriorating at a faster rate. It is in agreement with the visual and ultrasonic inspections (B2) which revealed extensive crack growth in the end span of the south exterior girder at the ends of the cover plates and the south interior girder was completely fractured at the center of the mid span when Test 4 was performed.

The mode shapes of the torsional mode appear to contradict the results obtained from the inspections. The torsional mode shows the north side of the bridge deflecting more than the south side. Figures B-5a through B-5i display the plots of the mode shapes for each of the three tests.

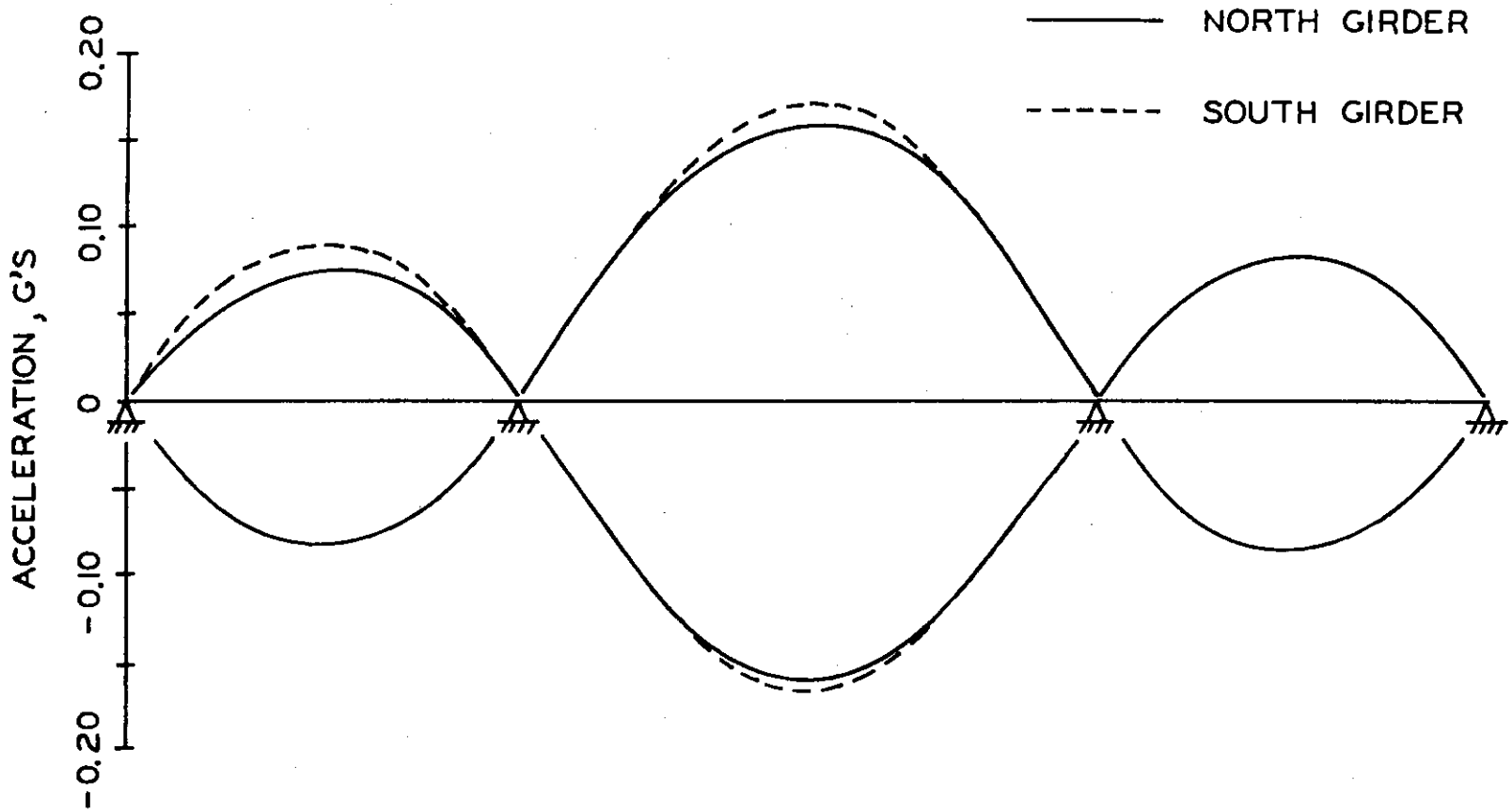

FIGURE B-5a. MODE SHAPE - B11

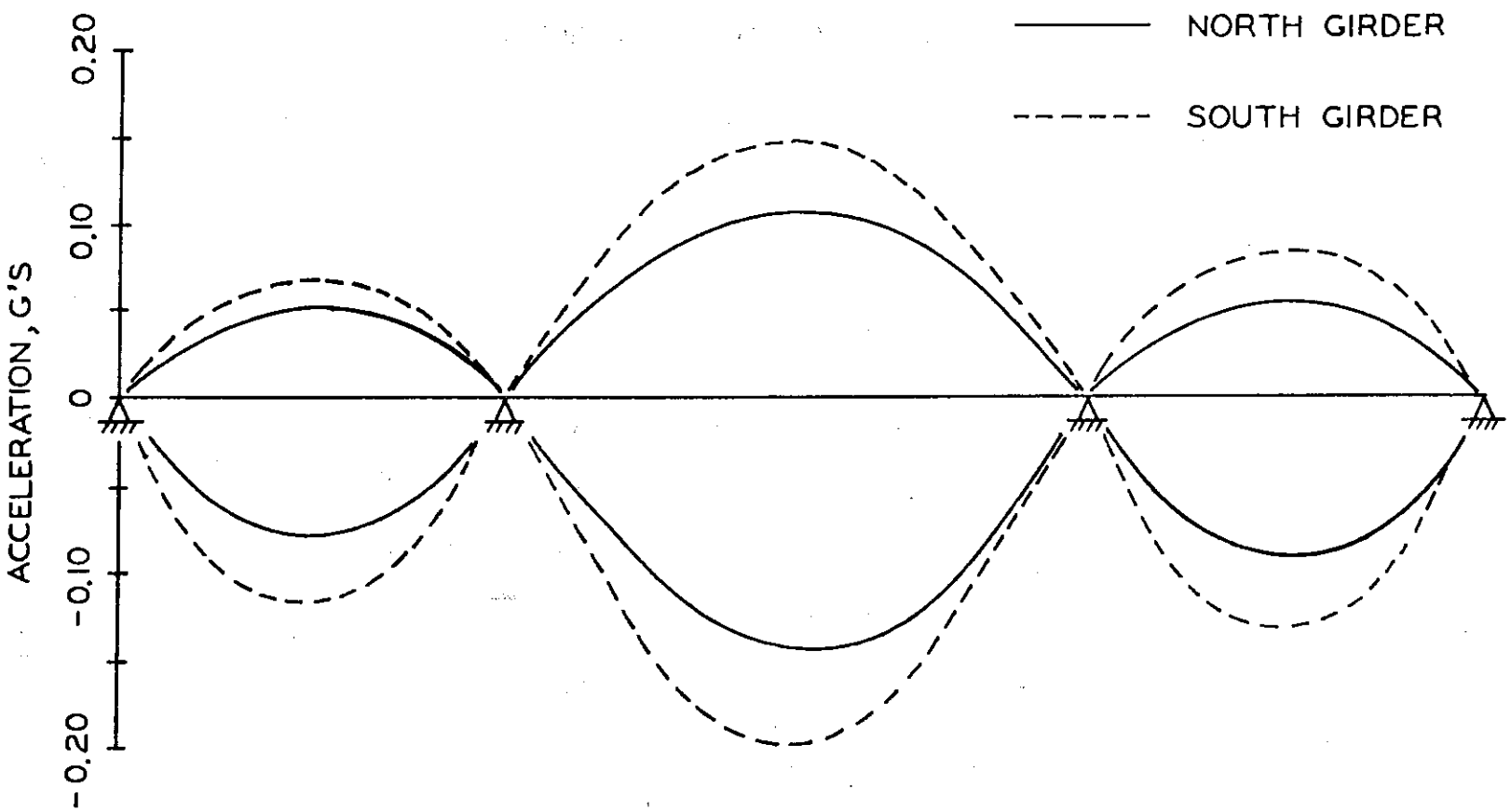

FIGURE B-5b. MODE SHAPE - B13

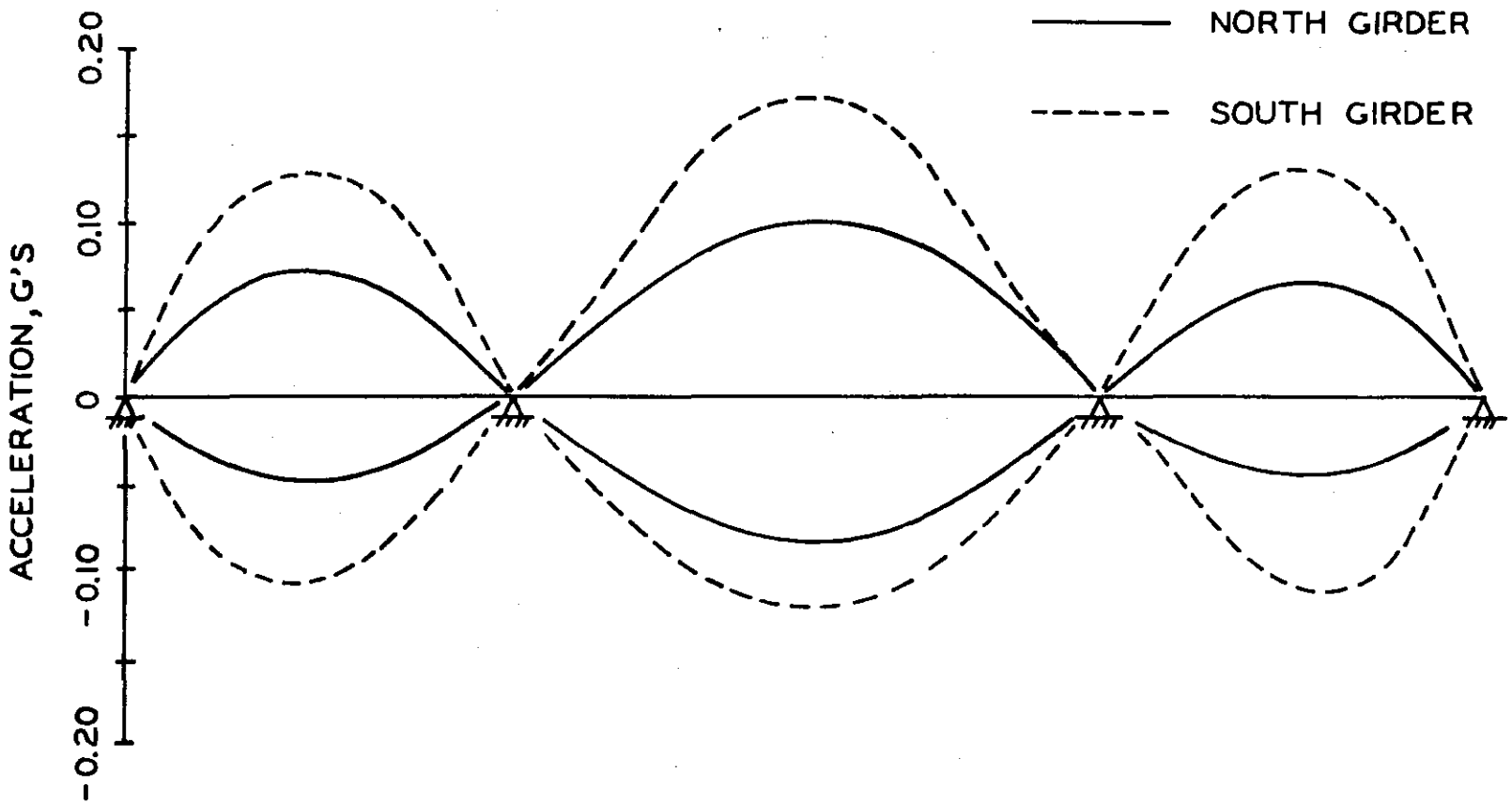

FIGURE B-5c. MODE SHAPE - B14

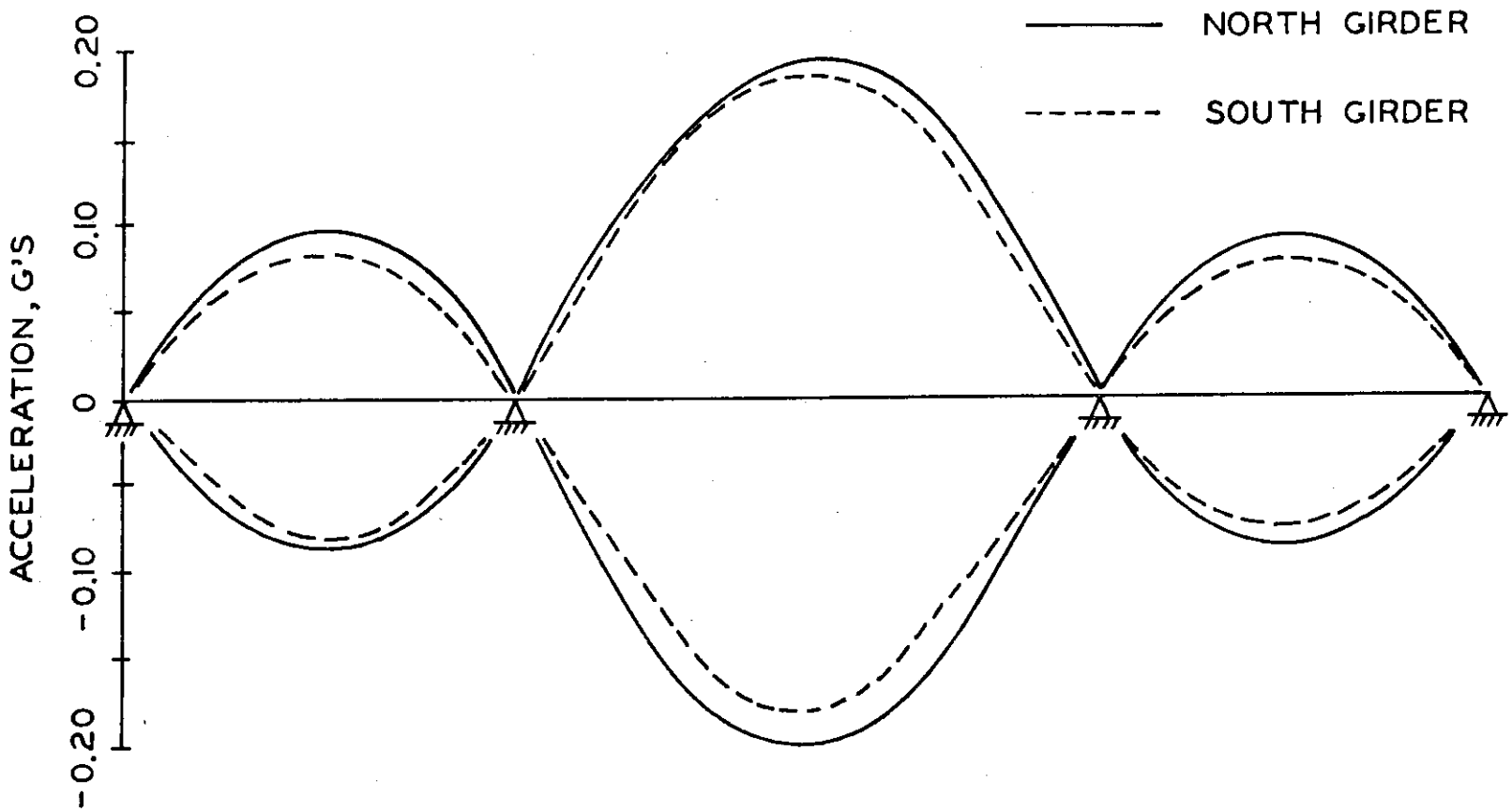

FIGURE B-5d. MODE SHAPE - T11

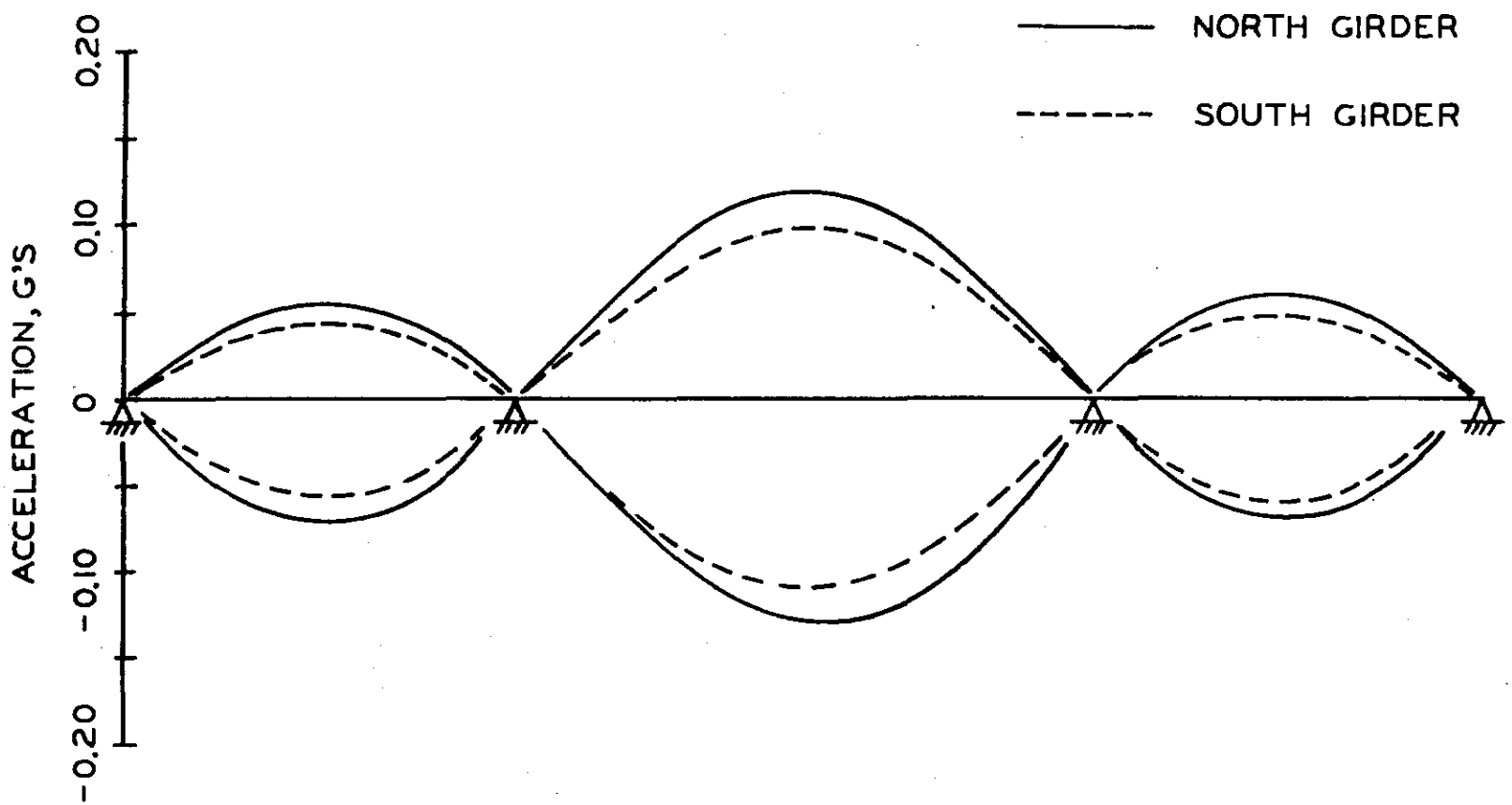

FIGURE B-5e. MODE SHAPE - T13

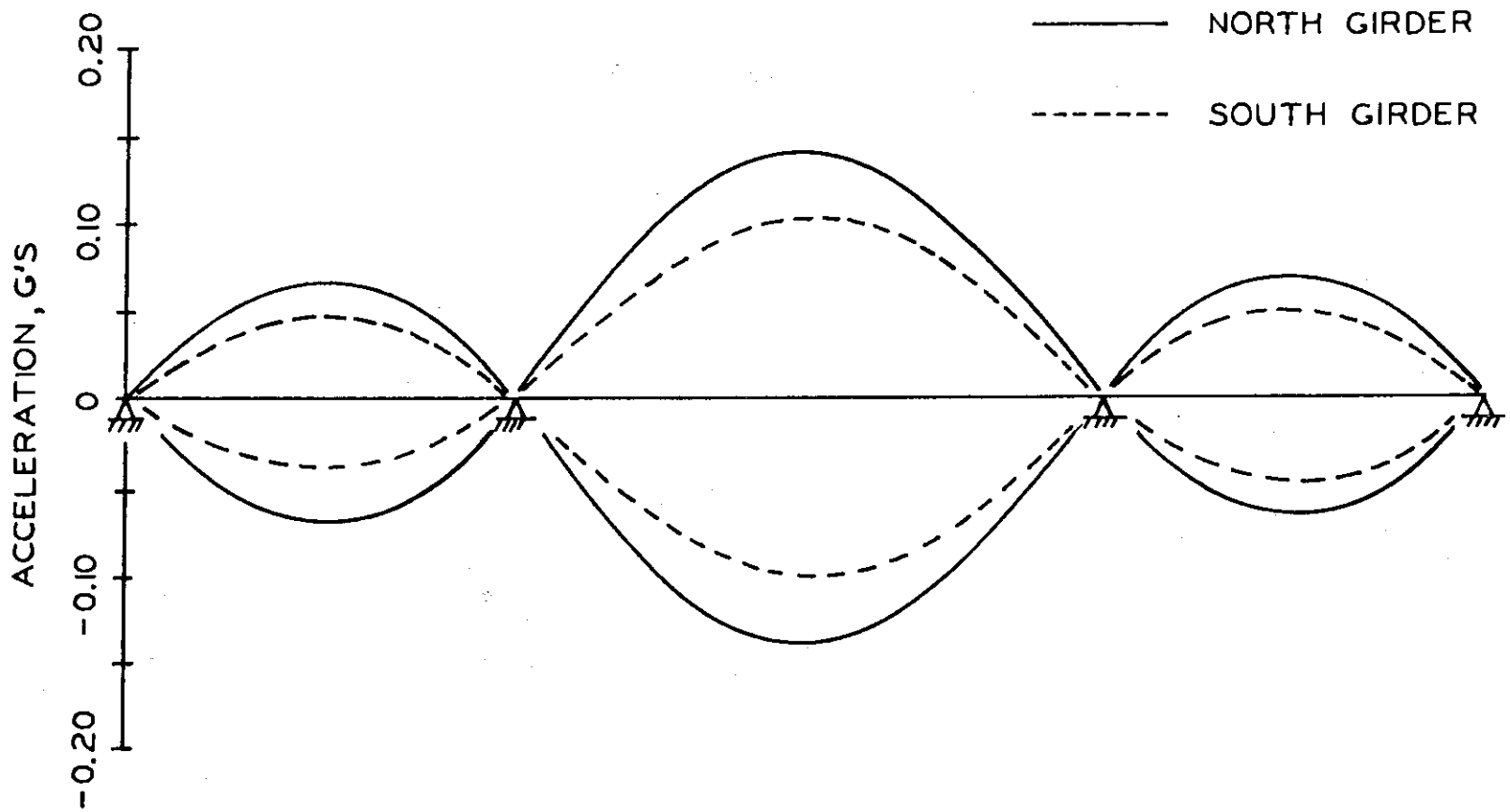

FIGURE B-5f. MODE SHAPE - T14

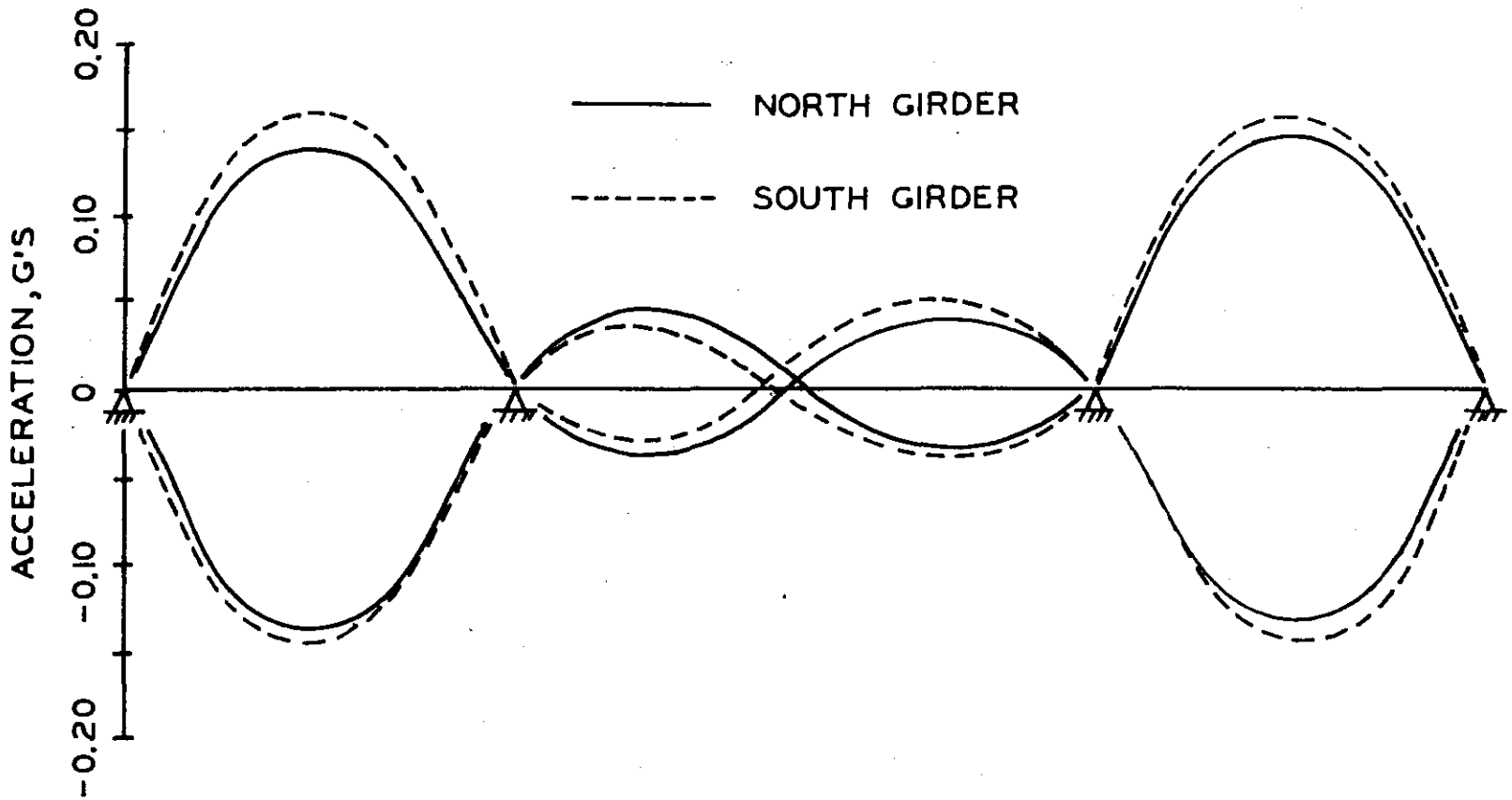

FIGURE B-5g. MODE SHAPE - B21

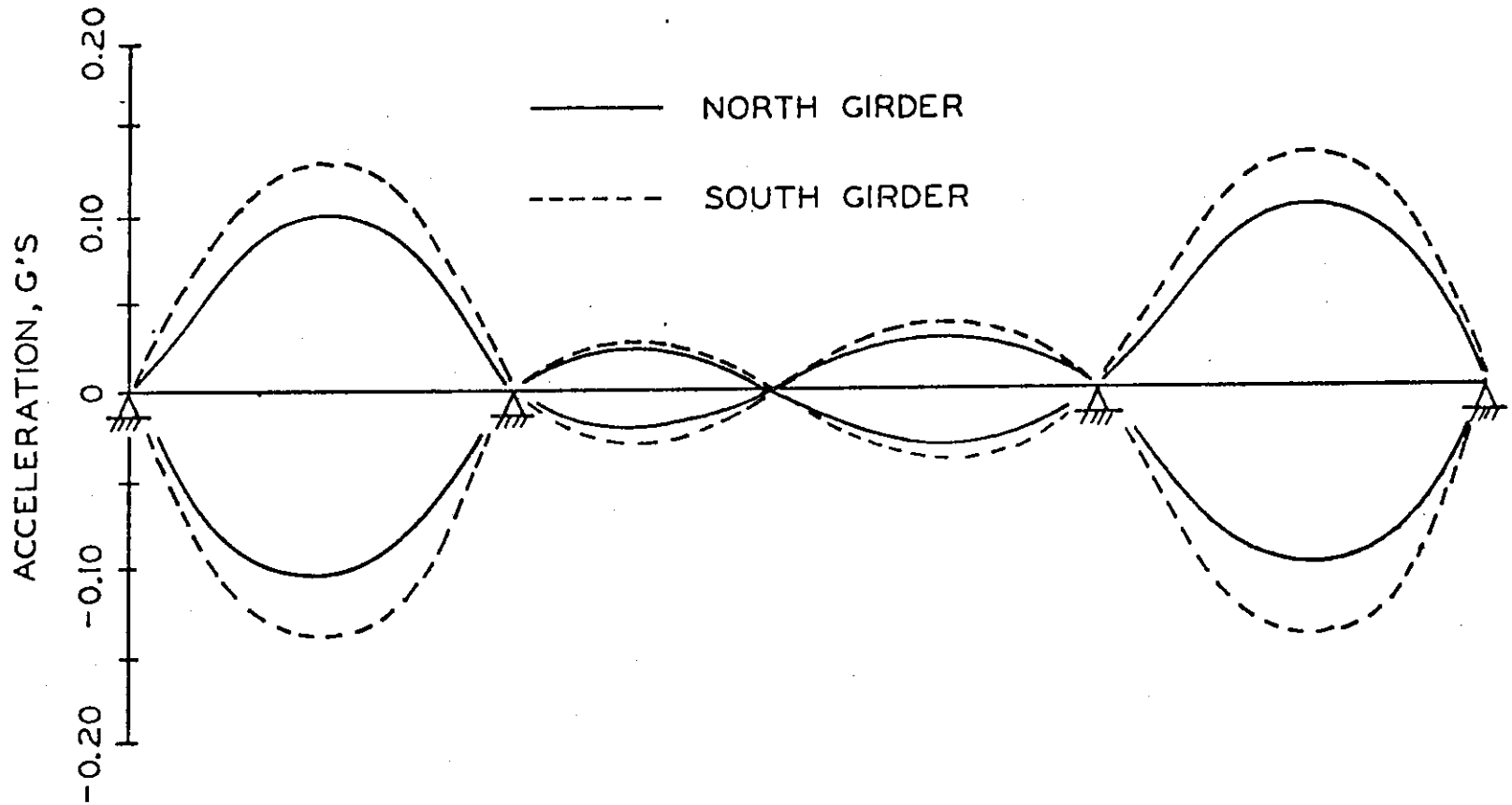

FIGURE B-5h. MODE SHAPE - B23

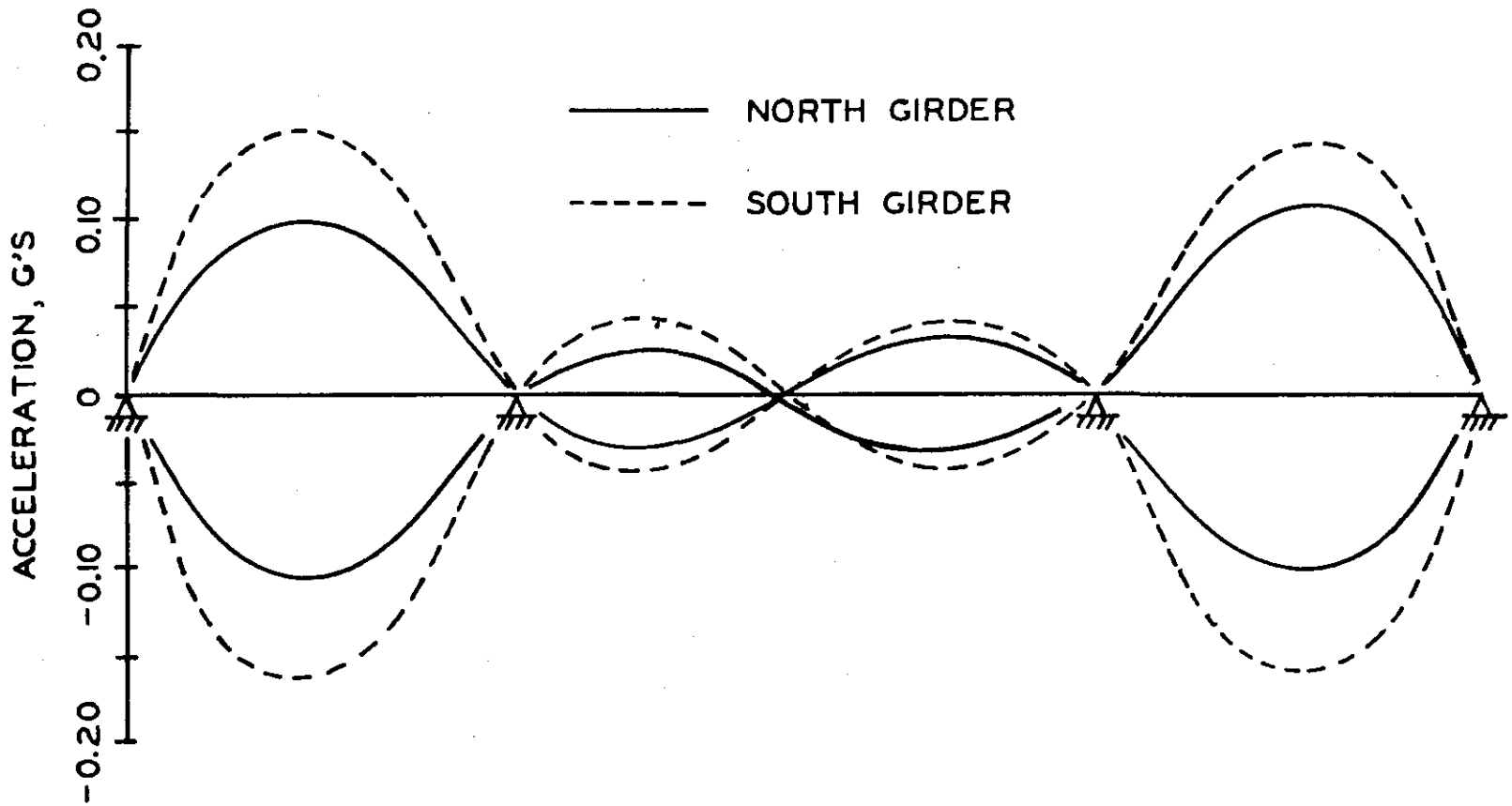

FIGURE B-51. MODE SHAPE - B24

B.6.3 Dynamic Properties

The results obtained from an analysis[B3] of the normal mode test data are presented in this article.

B.6.3.1 Damping Ratio

Damping ratios for the normal mode tests are shown in Table B-9. Very little insight into the location of deterioration can be derived from the damping ratios determined from the experimental data. The damping ratios increased initially and then decreased as the fatigue test progressed. This same trend was observed in the model study in Phase I[B1].

TABLE B-9. NORMAL MODE DAMPING RATIOS

TEST	DAMPING RATIO (ζ) (%)
B11	1.3
T11	1.3
B21	1.3
B13	1.7
T13	2.0
B23	1.6
B14	1.9
T14	1.7
B24	1.5

Due to the harmonic component present in the exciting force, the modal damping ratio for Tests B13 and B14 are too high. The mode shapes are derived from a spectral analysis of the response data, thus

removing any response due to the harmonic component. However, no force data was recorded for Tests 3 and 4 so the harmonic cannot be removed from the exciting force. Therefore, the modal damping ratios are too high because the force $\{F\}$ includes the harmonic component while the mode shapes $\{\phi\}$ do not. Figures B-6a through B-6f show the difference between the mode shapes of the south girder as obtained from the peak response and the values obtained from a spectral analysis.

B.6.3.2 Stiffness Matrix

The stiffness matrix for the bridge is obtained from the normal mode equations. Since the bridge has 22 DOF and three measured modes were determined experimentally, 66 equations are available. Various types of couplings were tried which yielded less than 66 unknowns with the simple cross coupling shown in Fig. B-7 yielding the best results. This type of coupling results in 53 unknowns and forms a matrix with the nonzero coefficients being clustered symmetrically about the diagonal as shown in Fig. B-8. For best results a coupling should be used which has a matrix with nonzero elements clustered as closely as possible about the diagonal.

The diagonal elements are considered to be most significant. Hence, they are used in comparing the stiffness matrices for the different tests. To show how the stiffness varies each test is compared to Test 1. The percent difference used for comparison is calculated

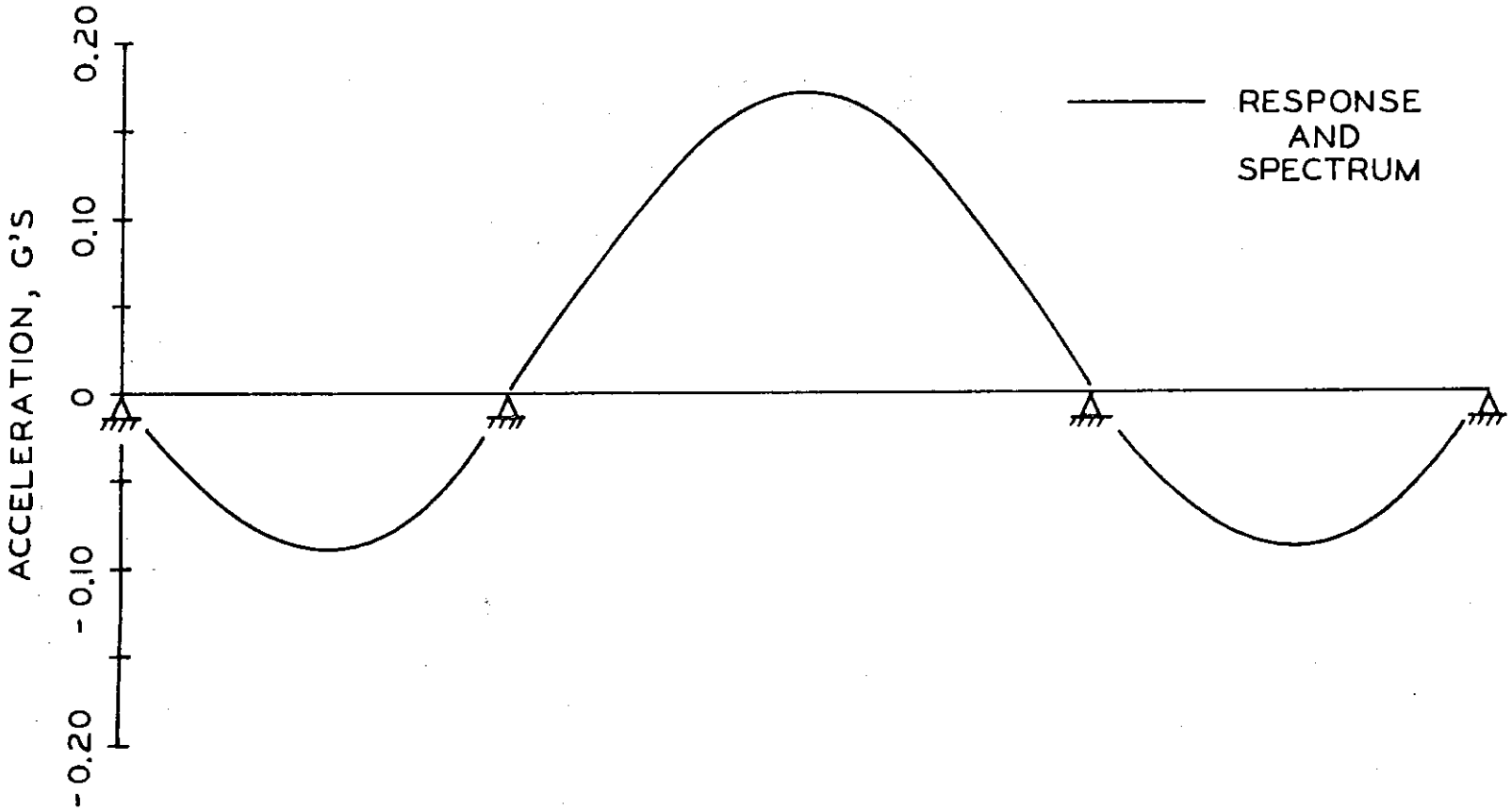

FIGURE B-6a. MODE SHAPE - RESPONSE vs. SPECTRUM
(SOUTH SIDE ONLY) - B11

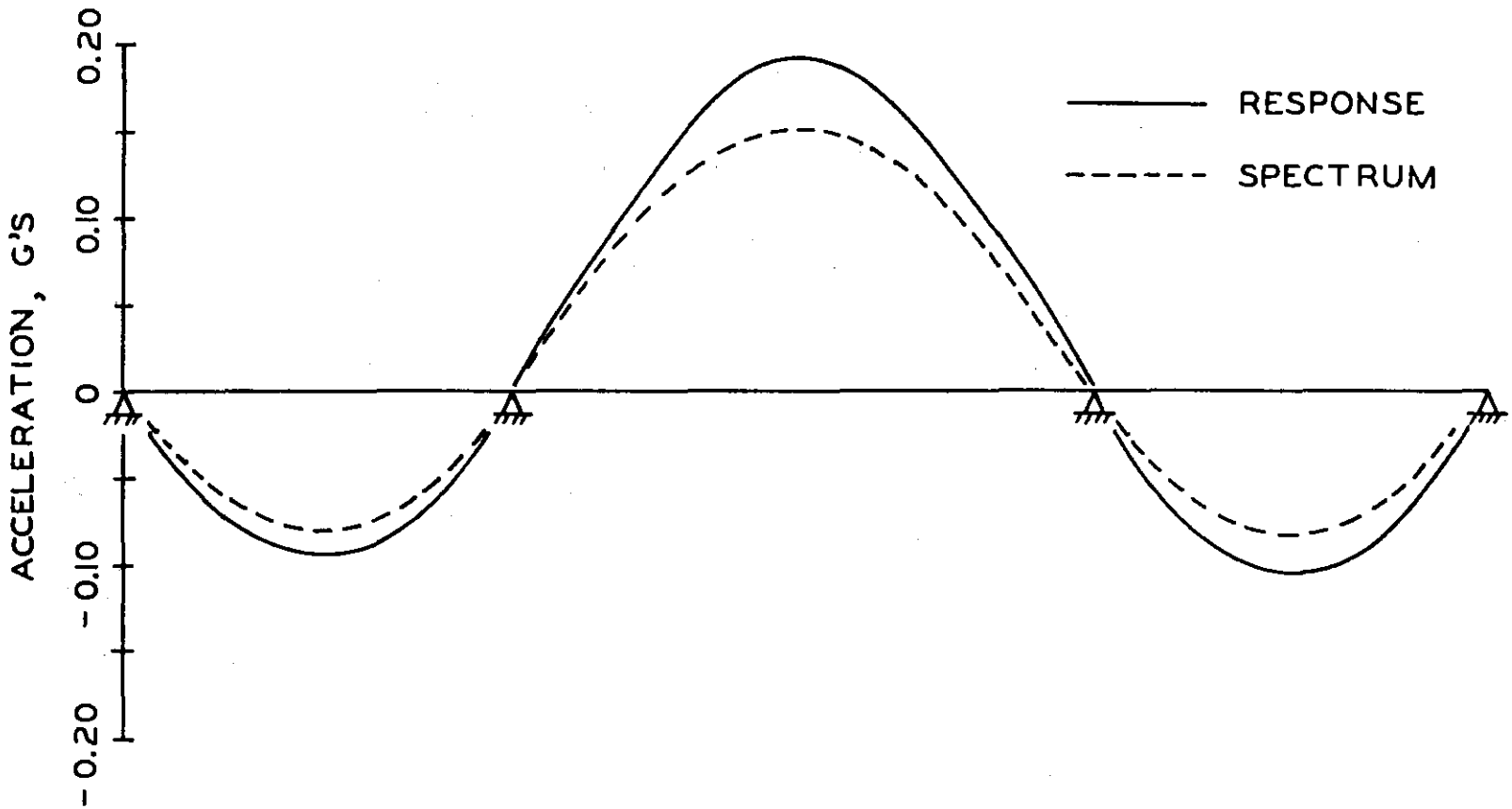

FIGURE B-6b. MODE SHAPE - RESPONSE VS. SPECTRUM
(SOUTH SIDE ONLY) - B13

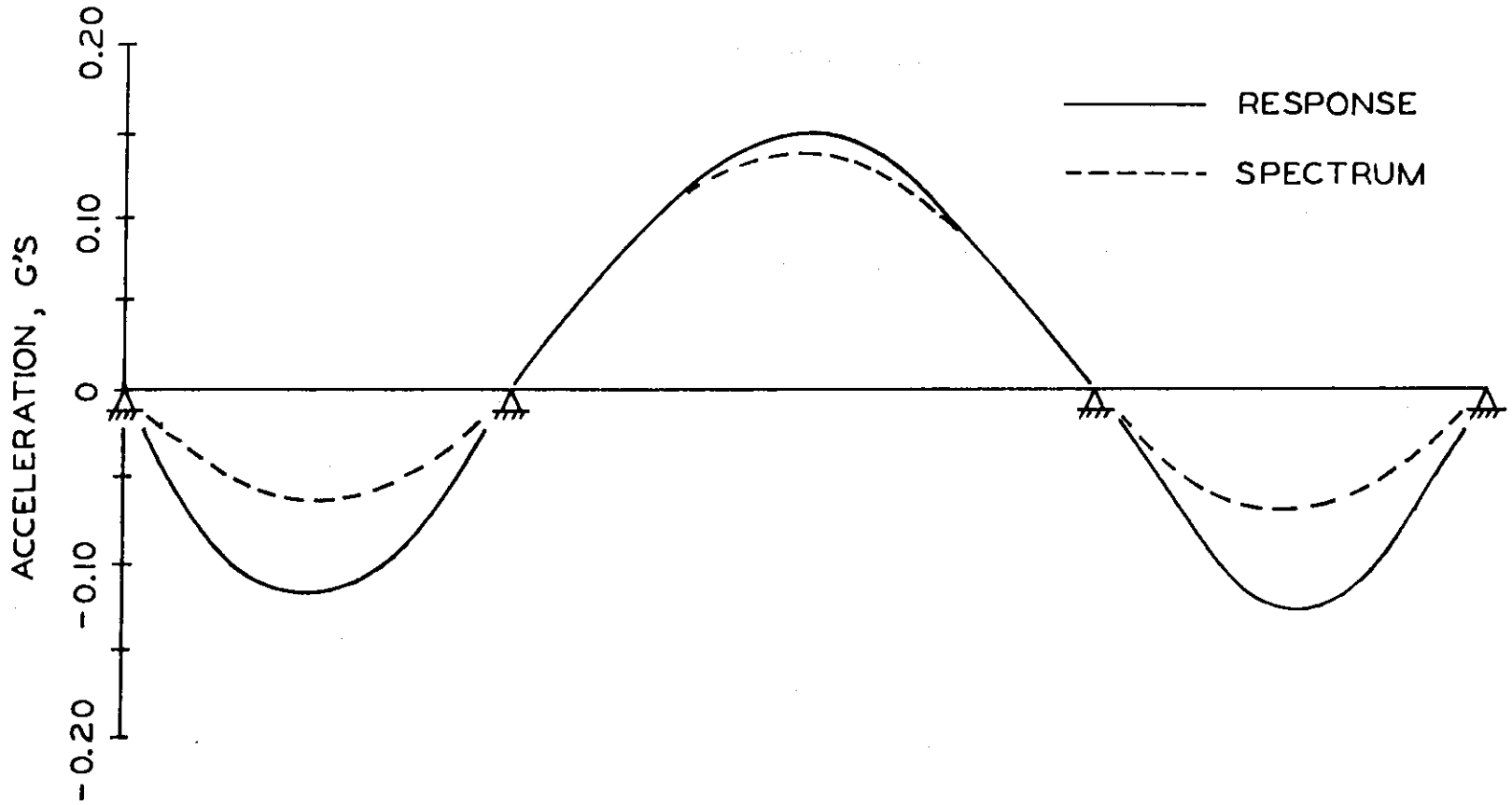

FIGURE B-6c. MODE SHAPE - RESPONSE vs. SPECTRUM
(SOUTH SIDE ONLY) - B14

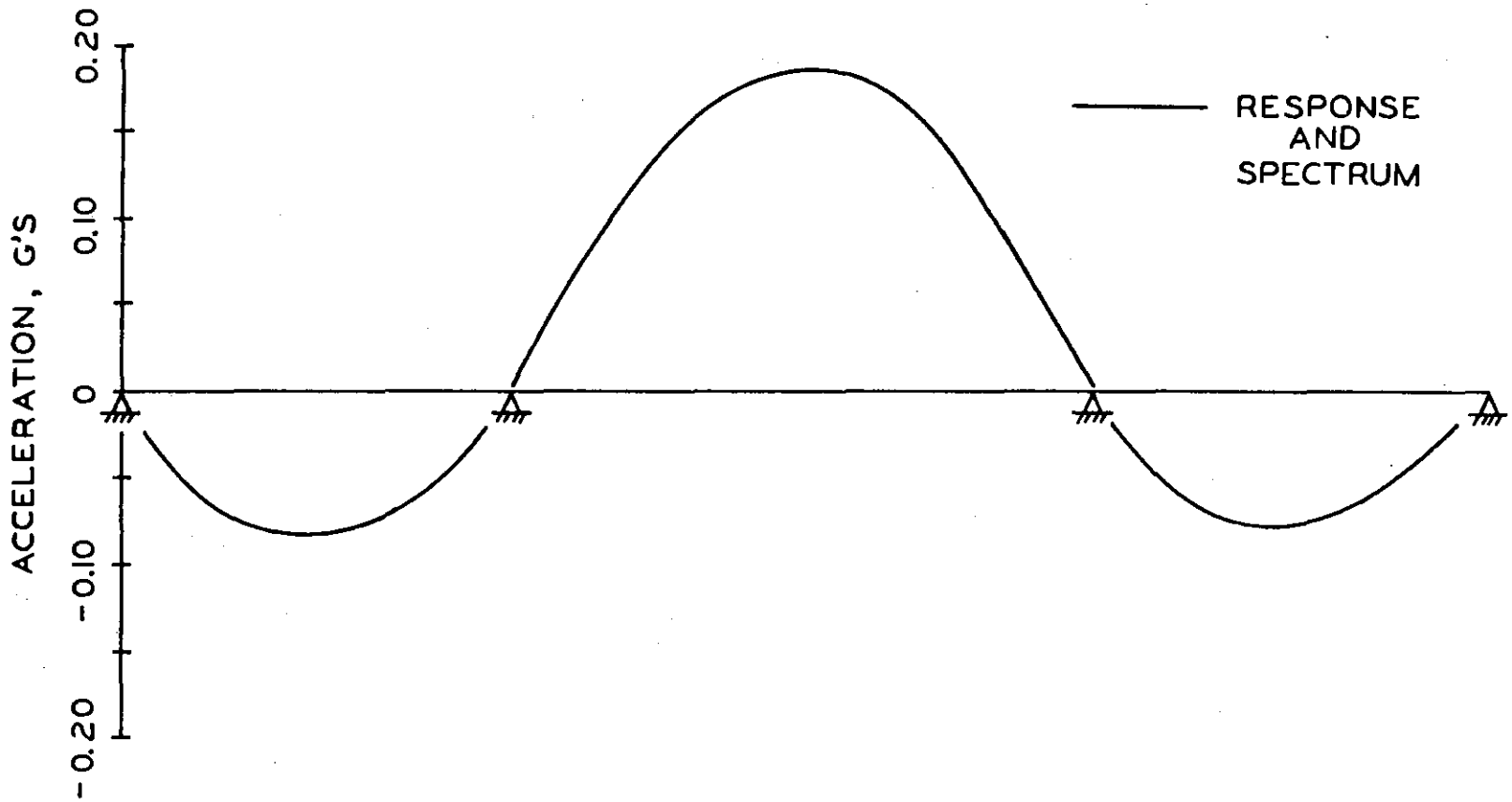

FIGURE B-6d. MODE SHAPE - RESPONSE vs. SPECTRUM
(SOUTH SIDE ONLY) - T11

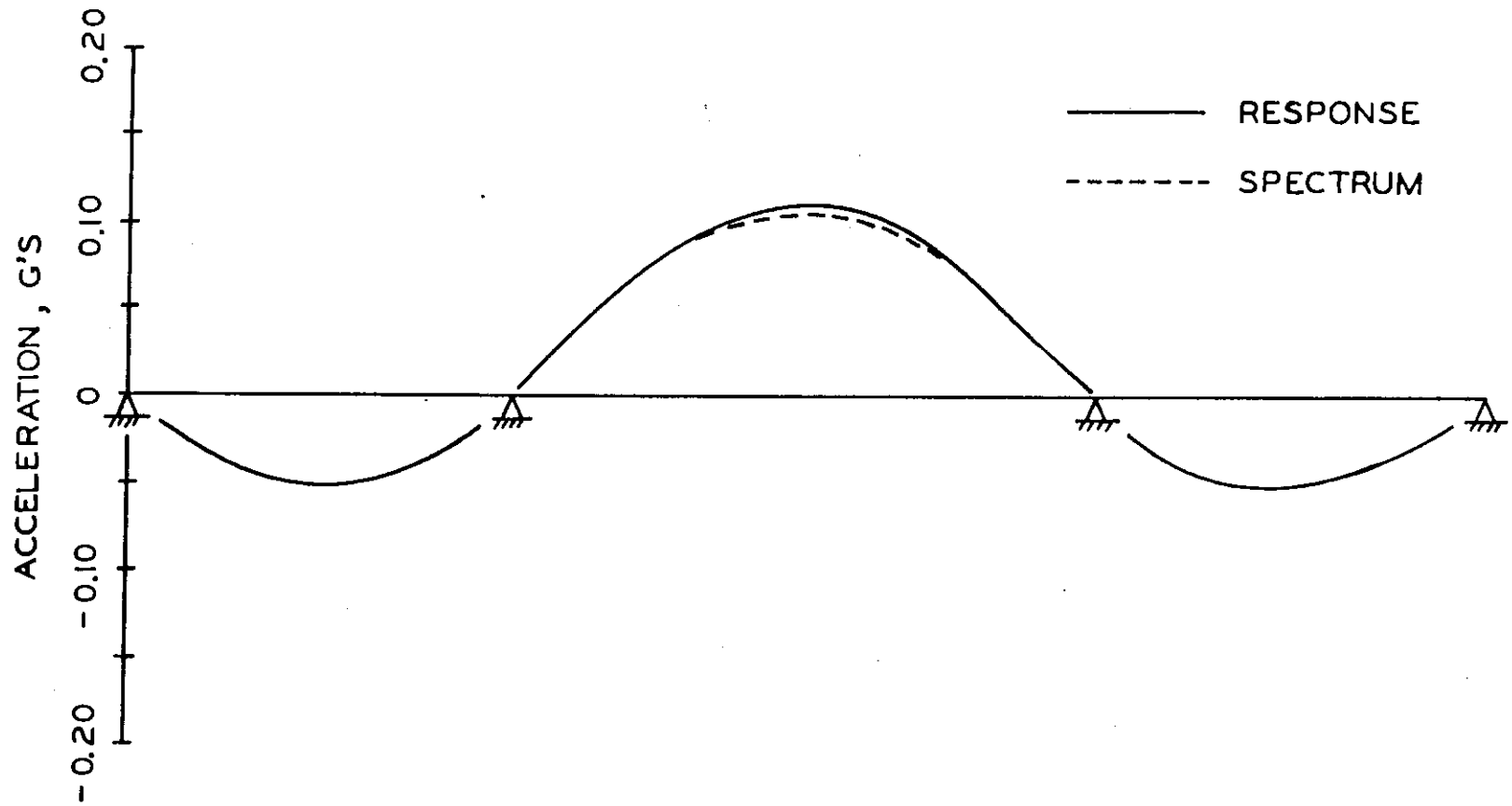

FIGURE B-6e. MODE SHAPE - RESPONSE vs. SPECTRUM
(SOUTH SIDE ONLY) - T13

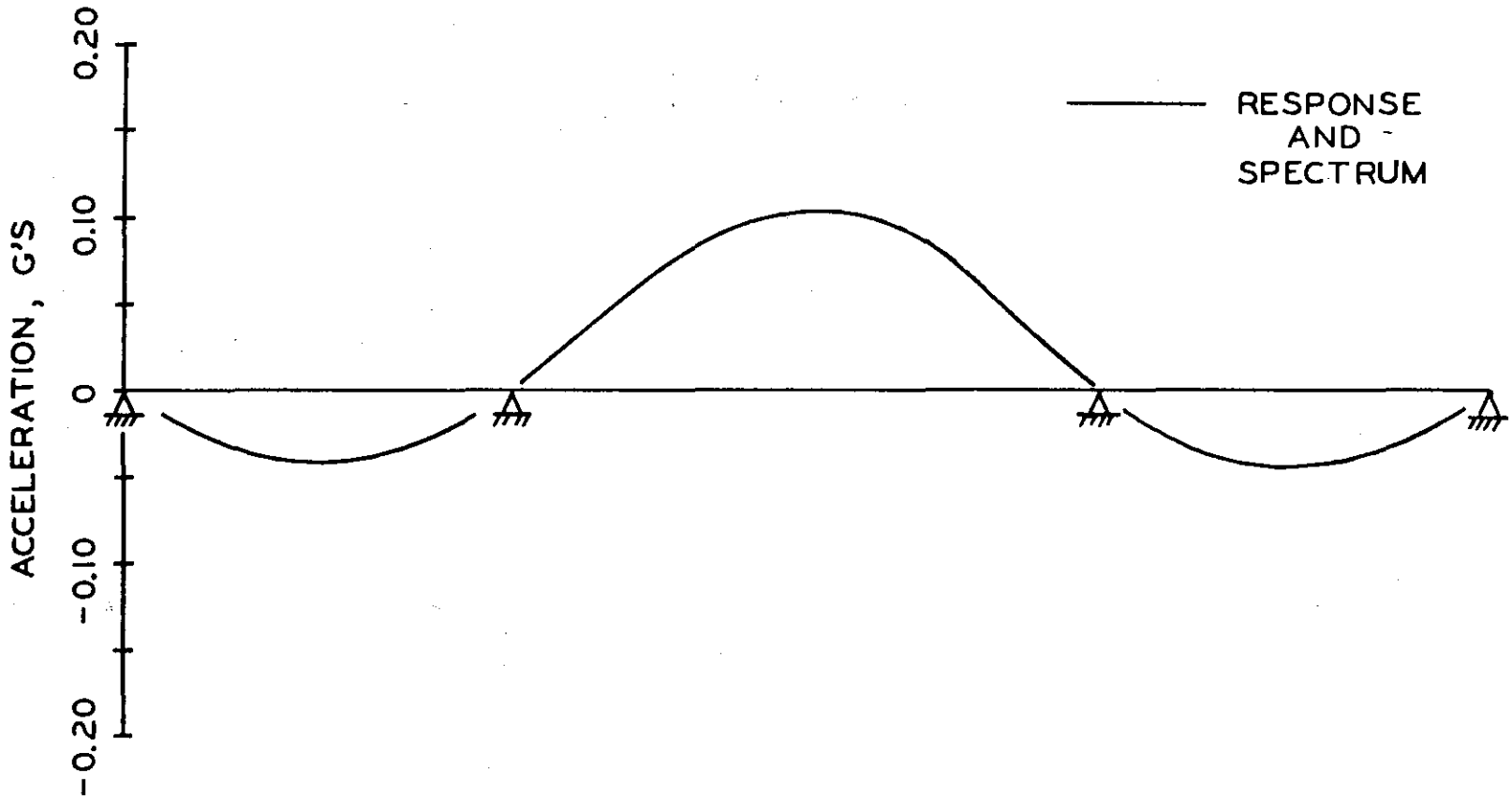

FIGURE B-6f. MODE SHAPE - RESPONSE vs. SPECTRUM
(SOUTH SIDE ONLY) - T14

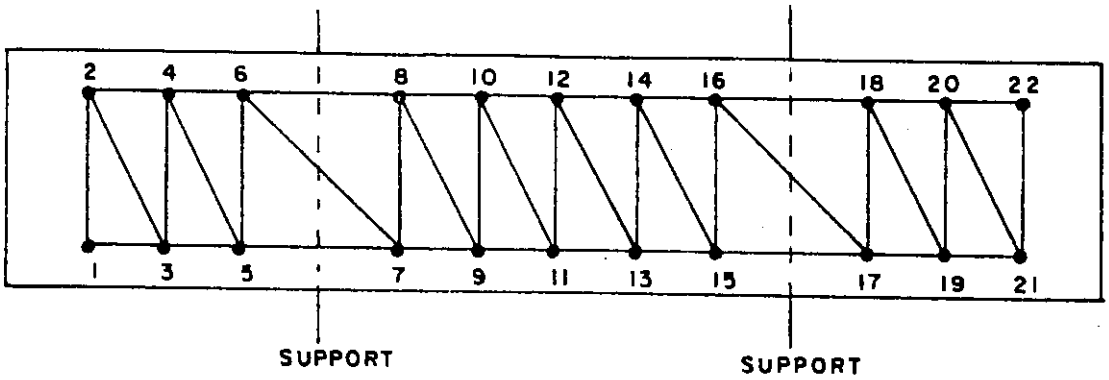

FIGURE B-7. COUPLING FOR 22 DOF

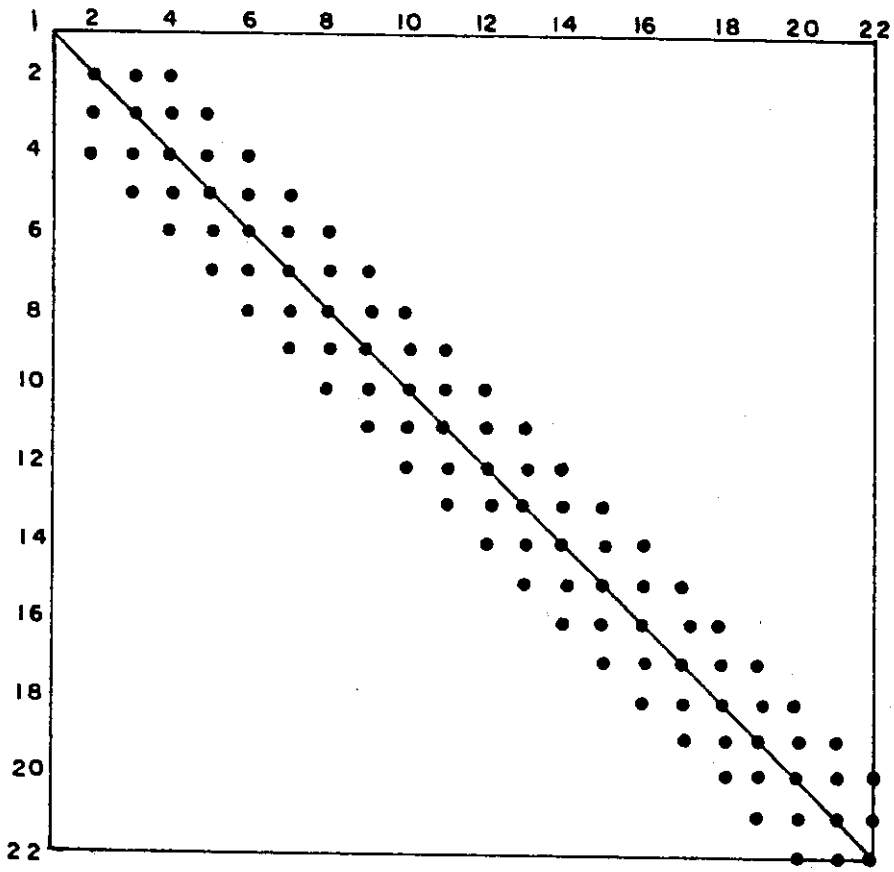

FIGURE B-8. NONZERO COEFFICIENTS OF 22 DOF MATRIX

$$\Delta K_{(i-1)} = \frac{K_i - K_1}{K_1} \times 100 \qquad \text{(B-1)}$$

where

K_i = a diagonal coefficient of the stiffness matrix for Test i, i = 3,4

K_1 = corresponding diagonal coefficient for Test 1.

The percent differences in stiffness calculated for Tests 3 and 4 are shown in Fig. B-9.

While this type of coupling does result in some increases in the calculated stiffness, it does yield significant decreases along the entire south side of the bridge. These decreases focus toward the center of the mid span and the regions at the end of the cover plates in the end spans. This agrees with the results obtained from visual and ultrasonic inspections. The reason for reductions at the 21st and 22nd nodes is not known. However, the stiffness consistently decreases in each test.

The determination of the stiffness matrix is very sensitive to errors in the mode shapes. Because coupling is incomplete, a least squares reduction is used. The solution to the equations is dependent upon the magnitude of the individual mode shapes. Therefore, by scaling any one mode shape the solution is changed. This makes the stiffness susceptible to variations in force level or the presence of a harmonic since either could affect the magnitude of the mode shapes. To establish a consistent set of vectors for each mode, the accelerations for each mode are normalized with respect to the reference accelerations. The normalized accelerations are then checked for orthogonality. Weights inversely proportional to the square of the orthogonality errors are assigned to the vectors.

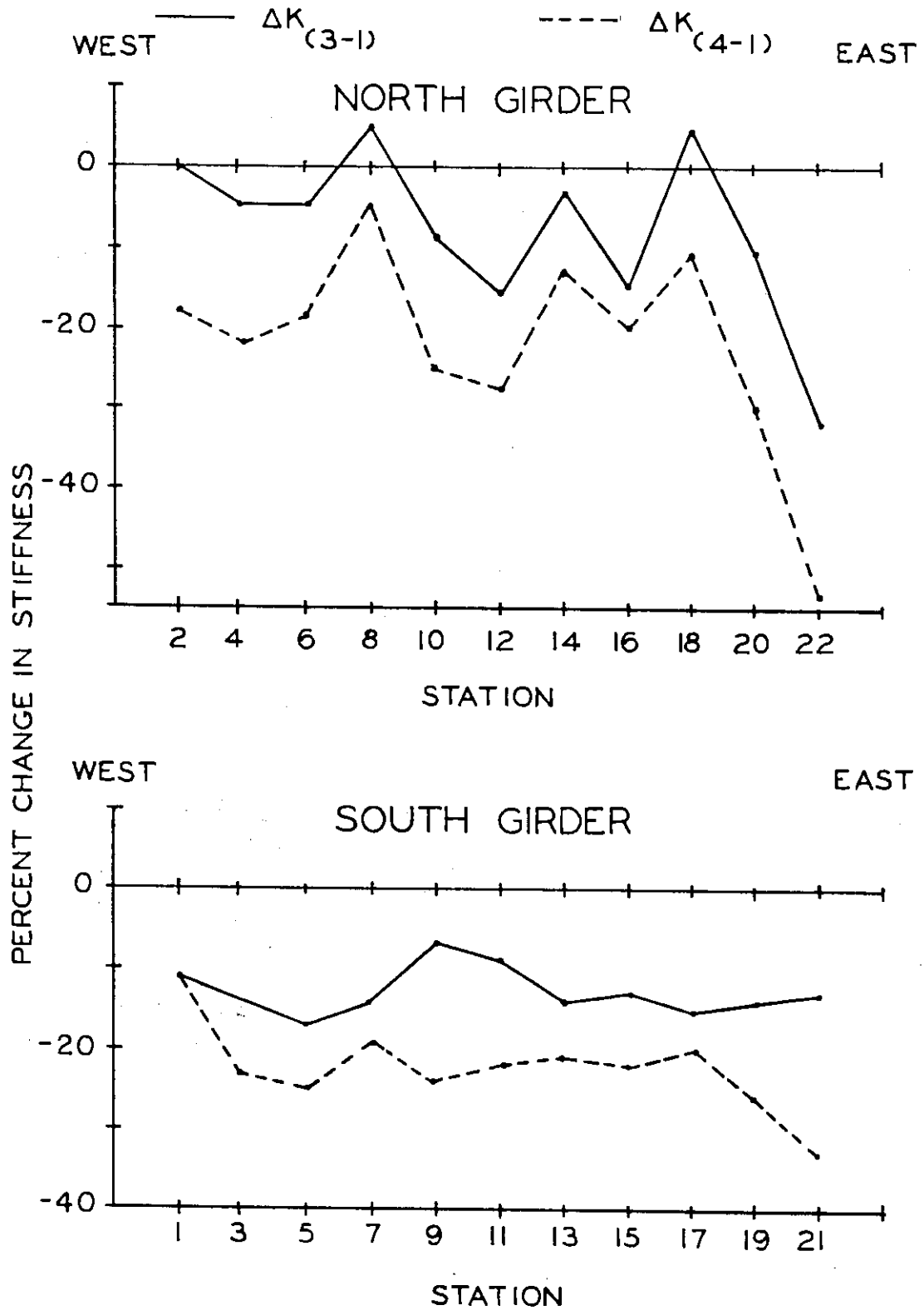

FIGURE B-9. CHANGES IN DIAGONAL COEFFICIENTS OF STIFFNESS MATRIX - 22 DOF

A six DOF system is also applied to the structure as is shown in Fig. B-10. Only Tests 1 and 4 are compared but the results show the same tendencies as those demonstrated by the 22 DOF analysis. Table B-10 shows the percent difference in stiffness obtained in the six DOF analysis.

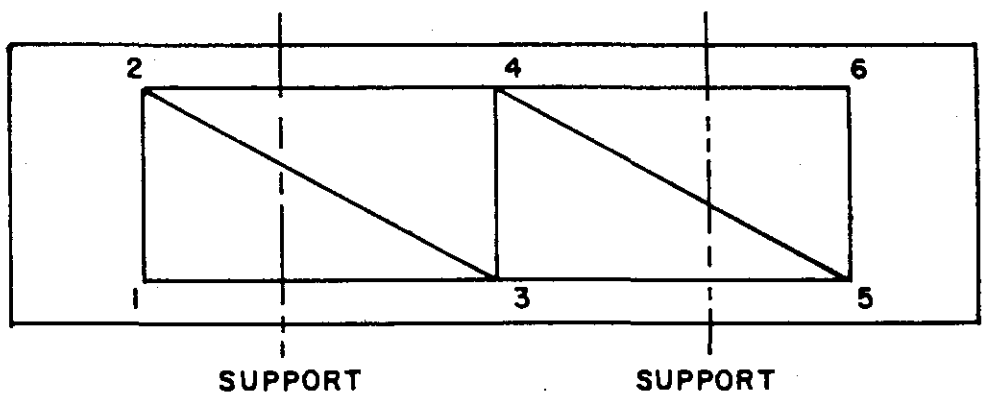

FIGURE B-10. COUPLING FOR SIX DOF

$\Delta K_{(4-1)}$ NODE	-18 % + 2	-12 % + 4	-11 % + 6
$\Delta K_{(4-1)}$ NODE	-24 % + 1	-25 % + 3	-24 % + 5

TABLE B-10. CHANGE IN DIAGONAL COEFFICIENTS IN STIFFNESS MATRIX - SIX DOF

B.6.3.3 Damping Matrix

The damping matrix is obtained from solution procedures similar to those used for the stiffness matrix.

As in the stiffness matrix comparisons, only diagonal coefficients are considered by calculating the percent difference using Test 1 as the reference. Therefore

$$\Delta C_{(i-1)} = \frac{C_i - C_1}{C_1} \times 100 \qquad \text{(B-2)}$$

where

C_i = diagonal coefficient of damping matrix from Test i, i = 3, 4

C_1 = corresponding diagonal coefficient of damping matrix from Test 1.

The differences in damping for the tests are shown in Fig. B-11. The changes in the diagonal coefficients of the damping matrix exhibit an increase followed by a decrease.

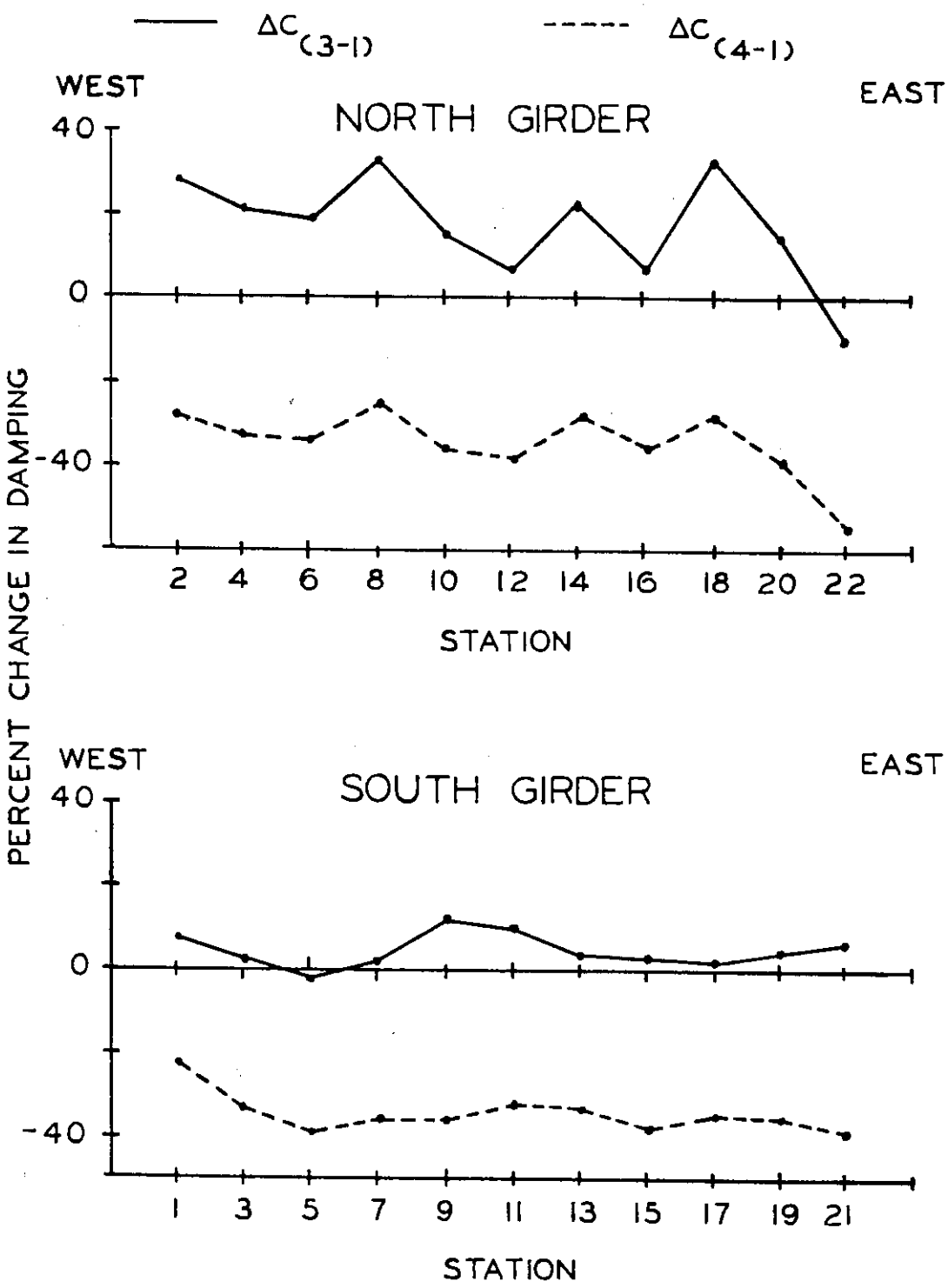

FIGURE B-11. CHANGE IN DIAGONAL COEFFICIENTS OF DAMPING MATRIX - 22 DOF

REFERENCES

B1. Salane, H.J., et al., "An Investigation of the Behavior of a Three-Span Composite Highway Bridge," Final Report - Phase I, Missouri State Highway Dept. - Federal Highway Administration, University of Missouri-Columbia, 1971.

B2. Samborski, Stanley T., III, "An Ultrasonic Study of Fatigue-Crack Growth", M.S. Thesis, University of Missouri-Columbia, December 1976.

B3. Singla, Vishay, PhD Thesis in preparation, University of Missouri, Columbia, 1976.

APPENDIX C

ULTRASONICS

C.1 INTRODUCTION

Ultrasonic inspection is based on the transmission of energy through the test material in the form of a sound wave. As the wave passes through the material it can be reflected by a flaw, a free surface, or a combination of the two. The primary task involved in ultrasonic inspection is that of detection and interpretation of the reflected wave.

The basic components necessary for ultrasonic testing are (1) a unit which will generate an electric signal, (2) a probe (search unit) capable of transmitting energy through a test specimen, (3) a probe (search unit) capable of receiving the transmitted or reflected energy, and (4) a unit which will visually display information concerning the energy as it passes through the test specimen[C2].

C.2 TYPE OF EQUIPMENT

Conditions which surround a field inspection of a full scale highway bridge require that ultrasonic inspection equipment be portable. The unit chosen for the Butler-County bridge test was entirely self contained. The power supply, the probe(s), and the display unit could be carried and operated by one individual.

C.2.1 Scope

The basic unit used for the field inspection was a pulse-time flaw detector. The unit utilized an A-span presentation, Fig. C-1, to visually display flaws.

Briefly, an A-scan presentation makes use of the assumption that the velocity of sound remains constant throughout a homogeneous material[C3]. This assumption neglects mode changes, which do in fact occur, but will suffice to explain the functions of an A-scan presentation. Therefore, if the velocity of sound through a given material is known, the time required for a sound wave to travel a given distance can easily be determined. A-scan presentation converts time directly into distance and visually displays the results on a cathode ray tube (CRT). Distance, in inches, is calibrated on the horizontal scale, and return signal amplitude, in dB, is calibrated on the vertical scale.

C.2.2 Probes

Two types of probes were chosen for the actual field inspection[C4]. The first type was a 5 MHz transmitter-receiver probe, Fig. C-2, containing a split-crystal. One side of the crystal transmitted the sound wave while the other side received the reflected wave. The sound wave was projected into the test specimen at an angle of 90° to the surface upon which the probe was coupled.

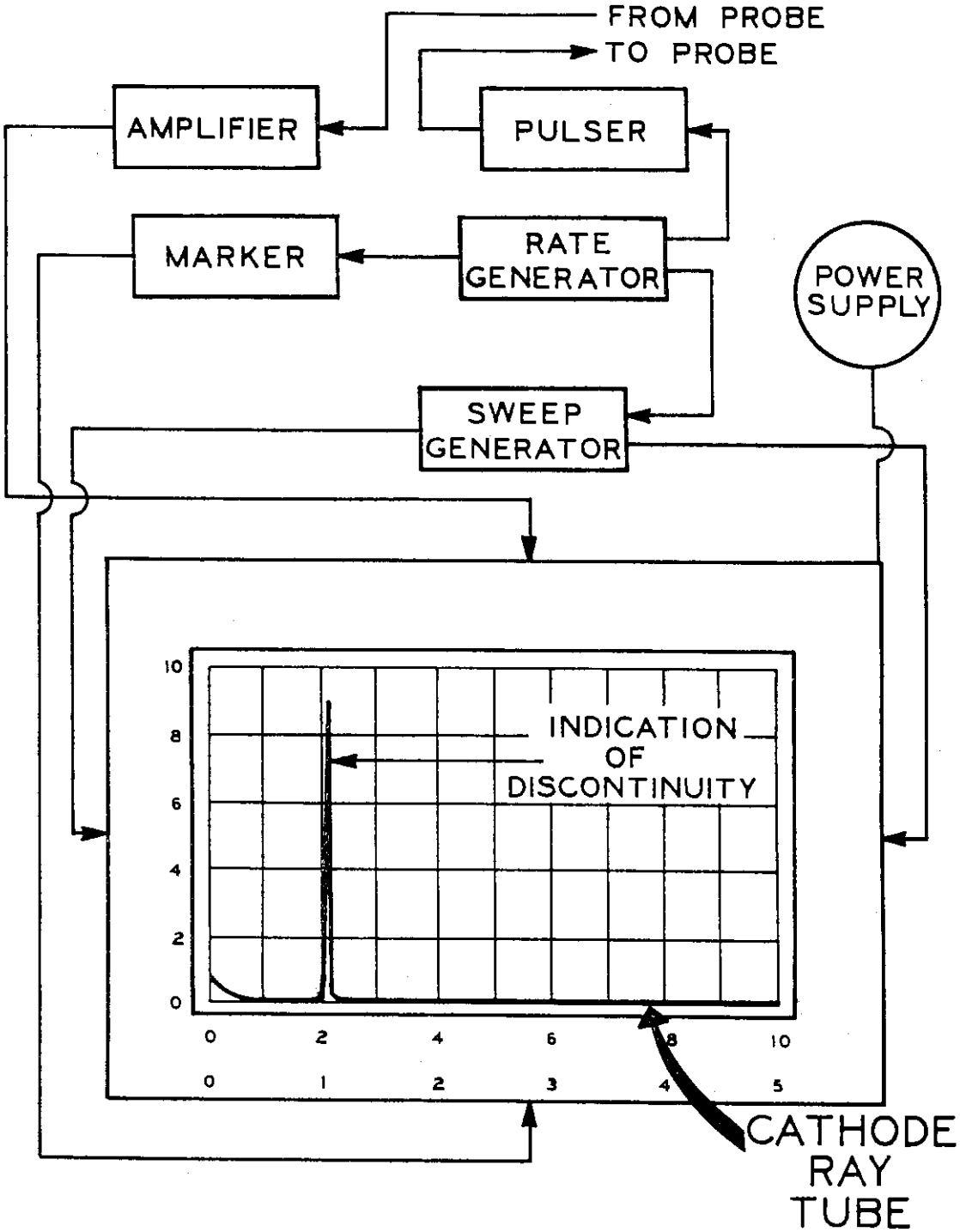

FIGURE C-1. DIAGRAM OF PULSE-ECHO A-SCAN EQUIPMENT

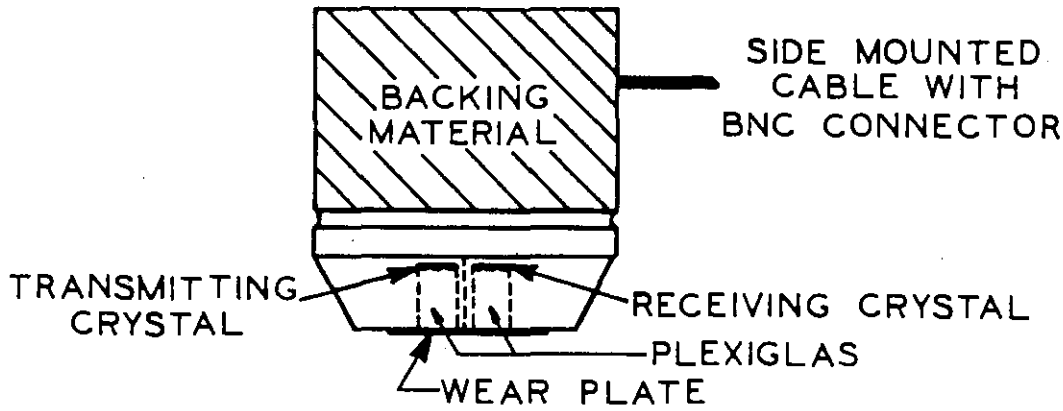

FIGURE C-2. SPLIT CRYSTAL NORMAL PROBE

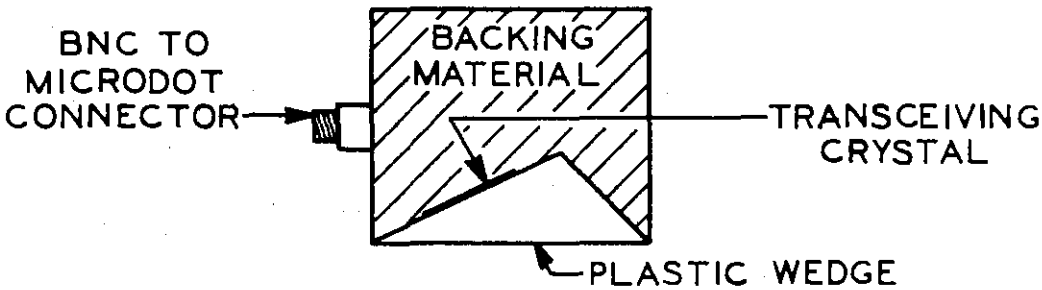

FIGURE C-3. ANGLE PROBE

The second type was a 5 MHz angle beam transceiver probe (Fig. C-3) containing a crystal which was capable of acting as both transmitter and receiver. Two angle beam transceiver probes were chosen for the field test. The angle probes projected sound waves at 45° and 70°, with respect to a vertical axis through the test specimen, respectively.

C.3 MECHANICS OF SOUND WAVES

C.3.1 Piezo-electric Effect

The characteristic which enables the crystals placed within the probes to function as transmitters and receivers of energy is known as the piezo-electric effect. Basically, this is the ability of a material (crystal) to transform electrical impulses into mechanical energy, and mechanical energy into electrical impulses[C5]. This phenomenon is accomplished through the expansion and contraction of the crystal as it is electrically or mechanically stimulated. The type of piezo-electric crystal found within the chosen probes was lead zirconate titanate.

C.3.2 Reflection and Refraction

When an ultrasonic wave strikes the interface between two different materials, part of the wave is reflected and part refracted. The portion that is reflected may be determined from the following equation[C5],

$$\frac{E_r}{E_i} = \frac{\rho_1 V_1 - \rho_2 V_2}{\rho_1 V_1 + \rho_2 V_2} \qquad (C.3.1)$$

where

E_r = reflected energy

E_i = incident energy

ρ_1 = density of first material

ρ_2 = density of second material

V_1 = velocity of wave in first material

V_2 = velocity of wave in second material.

At an air to solid interface, essentially 100 percent of the sound wave is reflected. At a plastic to steel interface, approximately 60 percent of the sound wave is reflected.

Refraction takes place when an ultrasonic wave passes from one medium to another at an angle other than 90°[C2, C3, C5]. A difference in material properties between the two respective surfaces causes a change in velocity, which in turn causes the sound wave to bend. The bending process obeys Snell's Law, which is stated mathematically in Eq. C.3.2, and which is shown graphically in Fig. C-4. The angle of incidence for which the angle of refraction equals 90° is called the critical angle of refraction. At angles greater than the critical angle the sound wave is totally reflected, that is, no energy enters the second material[C2,C3,C5,C6].

$$\frac{\text{Sin } \phi_1}{V_1} = \frac{\text{Sin } \phi_2}{V_2} \qquad \text{(C.3.2)}$$

where

ϕ_1 = angle of incidence

ϕ_2 = angle of refraction

V_1 = velocity of wave in first material

V_2 = velocity of wave in second material.

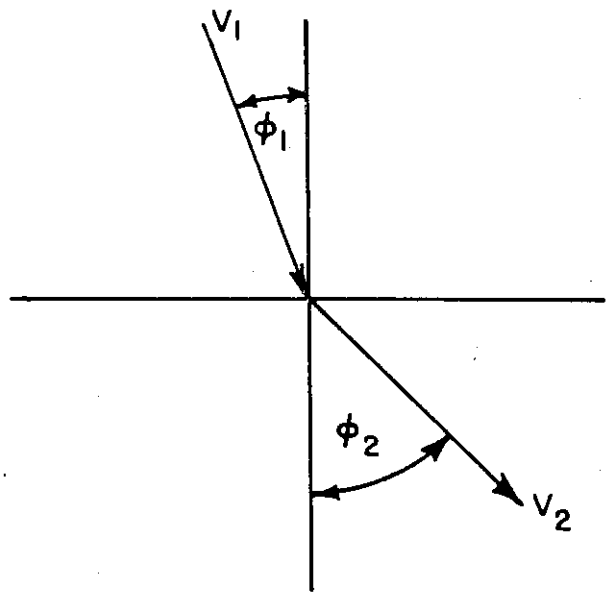

FIGURE C-4
GRAPHICAL PRESENTATION OF SNELL'S LAW

C.3.3 Skip Distance

As previously mentioned, the angle probes project a sound wave into the test specimen at some pre-designed angle of refraction. The beam, if uninterrupted by a flaw or discontinuity, will continue through the test specimen being reflected each time it strikes a surface as

shown in Fig. C-5. The first, second and third skip distances are shown, thus defining the term, skip distance.

When a sound wave is interrupted by a flaw oriented at 90^{0} to a free surface, the path followed by the sound wave is shown in Fig. C-6. The sound wave reflects off the free surface, then reflects off the flaw surface and is finally returned to the angle probe. Figure C-6 illustrates the mechanism by which flaws were located during the actual field inspection.

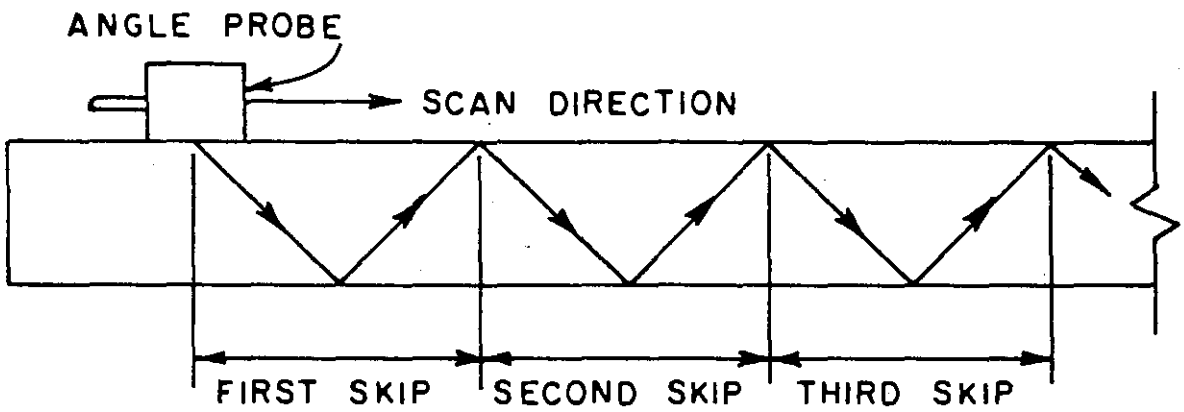

FIGURE C-5
ANGLE PROBE BEAM PATH AND SKIP DISTANCE IN TEST MATERIAL

C.3.4 Attenuation

Scattering of a sound wave due to large grain size within the test specimen, test surface irregularities, flaw surface irregularities, beam spread, or flaw surface size, can result in an attenuated signal[C3]. Due to the attenuation of the sound wave as it passes

through the test material, it becomes advantageous to locate all flaws within the first skip distance, Fig. C-5 and Fig. C-6.

C.3.5 Minimum Detectable Flaw

Theoretically, ultrasonic waves are not reflected effectively from flaws whose dimensions are less than the wavelength of the refracted ultrasonic waves. The wavelength of the angle probes selected for the field test was 0.065 cm., or 1/40 of an inch, which makes them sensitive to small flaws, but also susceptible to spurious defects such as grain boundaries. However, practice with the test equipment prior to field inspection eliminated confusion regarding these spurious indications.

C.3.6 Ultrasonic Couplant

A material must be provided through which the sound waves can travel from probe to test specimen. The material can be any liquid, semi-liquid, or paste which meets the criteria for a good ultrasonic couplant. A good ultrasonic couplant is one that provides a smooth surface on which to work, is easily applied, easily handled, non-corrosive to the test specimen and permits no air between the probe and test surface[C3].

The couplant chosen for the field test was Hercules Natrasol 250 HXR Powder mixed with water. The mixture, proportioned by weight, was 60 parts water to one part Natrasol powder. This mixture provided a moderately viscous couplant which could be applied in thin layers to overhead surfaces without dripping. The residue from this couplant

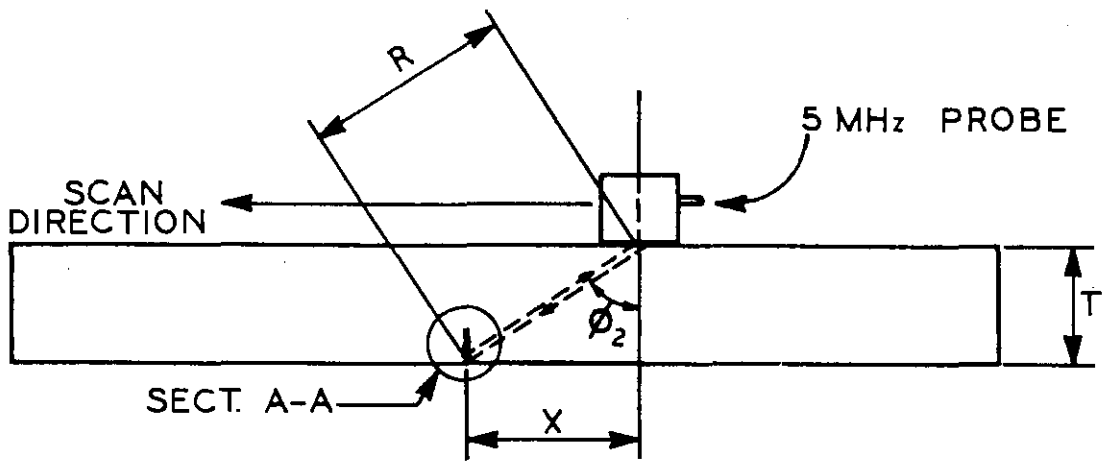

X= HALF SKIP DISTANCE // ϕ_2=ANGLE OF SOUND WAVE

T= MATERIAL THICKNESS // 2R=TOTAL DISTANCE TRAVELED BY SOUND WAVE

FIGURE C-6. COMPONENTS OF BEAM DATA (SECTION A-A)

ANGLE PROBE	45°		70°	
SECTION PROPERTIES	X	2R	X	2R
W30x99 T_F=0.67	0.67	1.90	1.84	3.92
W30x108 T_F=0.67	0.76	2.15	2.09	4.44
W30x99 T_W=0.522	0.52	1.48	1.43	3.05
W30x108 T_W=0.548	0.55	1.55	1.51	3.20

UNITS=INCHES

TABLE C-1. FIELD TEST CONSTANTS FOR ANGLE PROBES

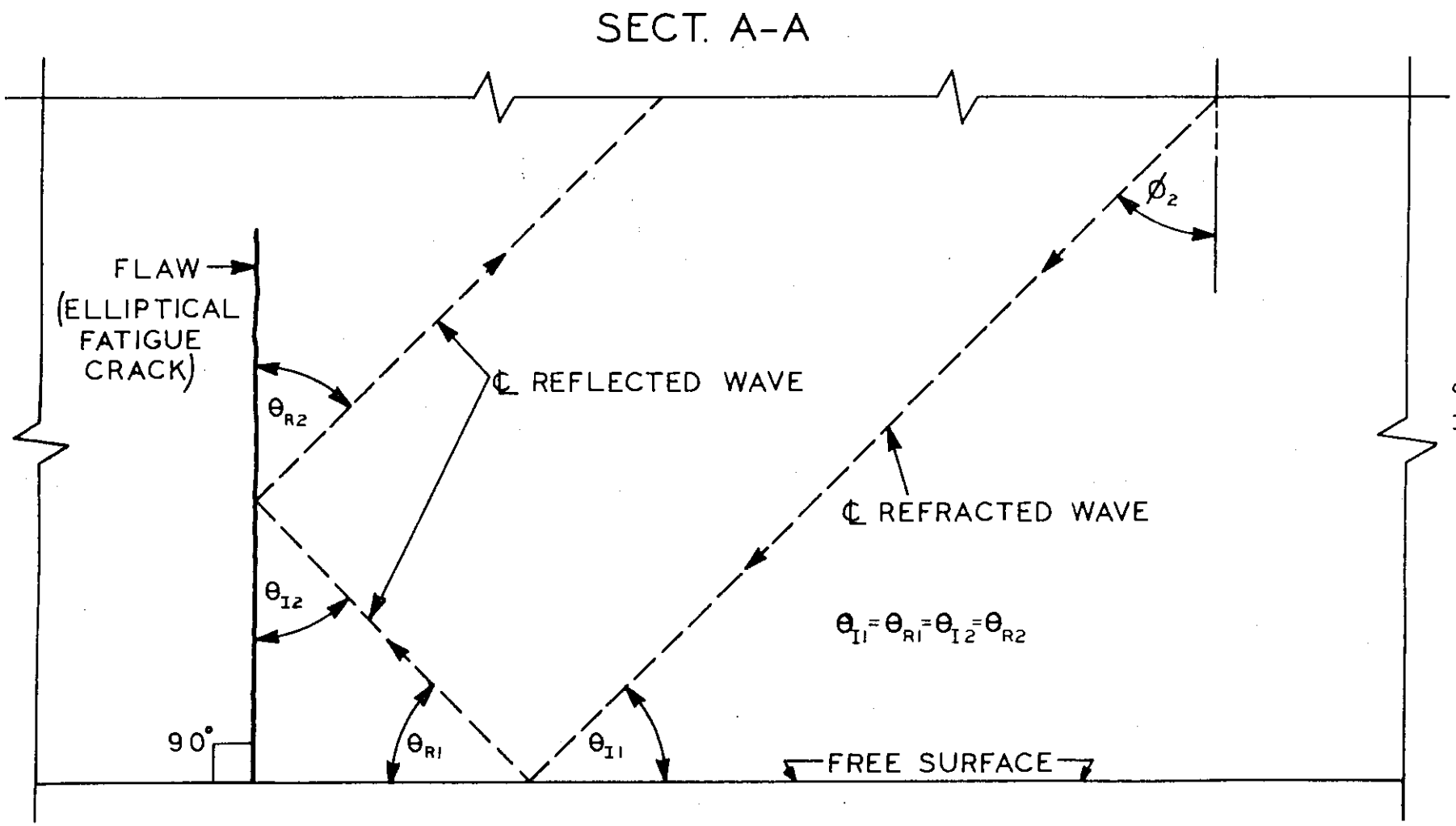

FIGURE C-6. (Cont.) COMPONENTS OF BEAM PATH (SECTION A-A)

literally dries up and blows away within an hour or two after it is applied. Ideally, the thinner the layer of couplant between probe and test specimen, the less susceptible is the sound wave to critical angles of refraction.

C.4 INSPECTION FOR FATIGUE CRACKS

C.4.1 Calibration of the Angle Probes

Accurate interpretation of field inspection results required careful calibration of the angle probes[C4,C9]. Calibration was accomplished by placing each respective angle probe on the calibration block as shown in Fig. C-7. Appropriate instrument adjustments were made to properly position the reflections created by the free surfaces of the angle calibration block. When properly calibrated, the free surface

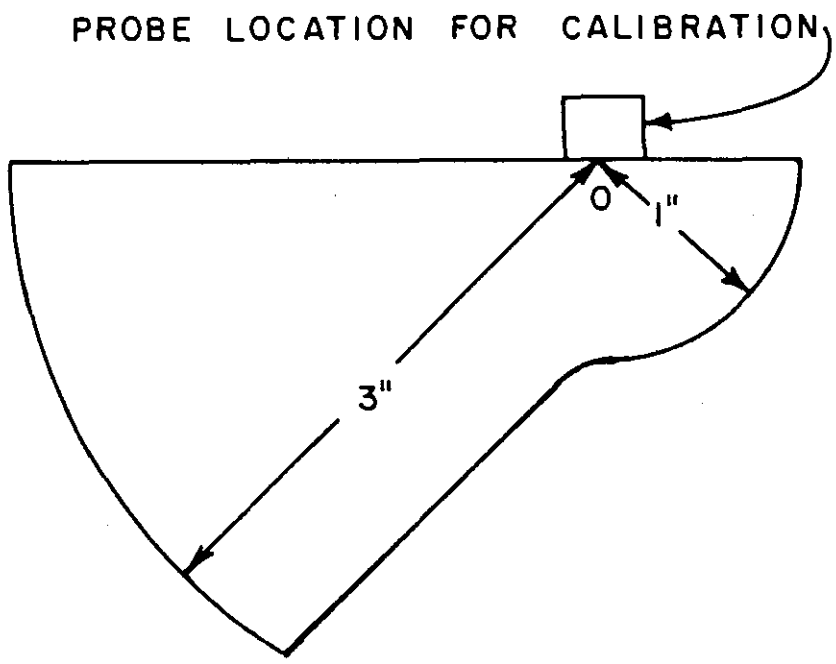

FIGURE C-7
ANGLE PROBE CALIBRATION BLOCK

reflections (for both the 45° probe and the 70° probe) occurred at 2 in. and 6 in. on the scope's horizontal scale.

C.4.2 Calibration of the Split-Crystal Normal Probe

The calibration block shown in Fig. C-8 was used in conjunction with the split-crystal normal probe. Appropriate instrument settings were made to properly position the free surface reflections created by each successive step. When properly calibrated, multiple reflections from each step coincided with the scope's horizontal scale[C9].

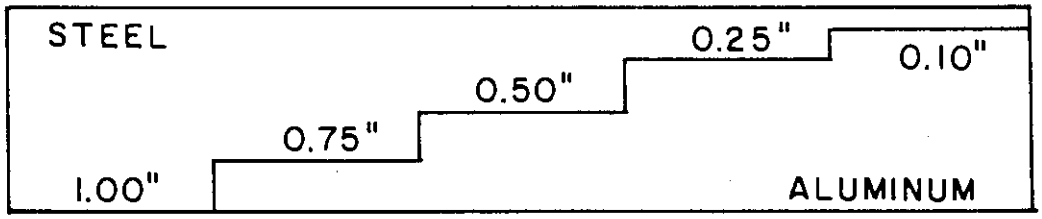

FIGURE C-8.
STEPPED CALIBRATION BLOCK

C.4.3 Technique

The inspection technique used in the field hinged on a thorough understanding of the beam's path and geometry. Figure C-6 and Table C-1 were used to facilitate field inspection.

Prior laboratory work indicated that due to the beam geometry and crystal size there was a finite area within which the probe must be positioned to effectively locate a flaw at the toe of the fillet

weld. Based on data from Table C-1 and laboratory experiments, scan areas for field inspections were developed, Figs. C-9, and C-10.

The reinforced concrete bridge deck completely encased the top cover plates and the outer surfaces of the top girder flanges. Before inspection of the top critical sections could take place, it was necessary to locate and permanently mark the ends of the cover plates. The split crystal normal probe was used to trace the fillet welds at the ends of the cover plates. There was no reflected wave when the probe was directly below a fillet weld around the cover plate or a shear connector. At all other locations there was a reflection from the smooth top surface of the flange. Lines were drawn on the flanges of the girders to designate the weld lines. Then the appropriate scan areas were located and marked.

Based on Fisher's work[C1], the fatigue cracks were expected to originate in the base metal at the toe of the fillet welds, at the ends of the cover plates. The flaws were expected to grow in an elliptical pattern through the thickness of the flange and outward in the direction of the flange width. The flaw surfaces were expected to be generally perpendicular to the horizontal flange surfaces, and perpendicular to the plane of the girder web. Therefore, the angle probes were primarily oriented parallel to the web. This positioning was designed to focus the sound wave at right angles to any fatigue crack, thus providing a maximum of returned energy. The probes were rotated about a vertical axis to inspect for flaws which might not be at right angles to the web.

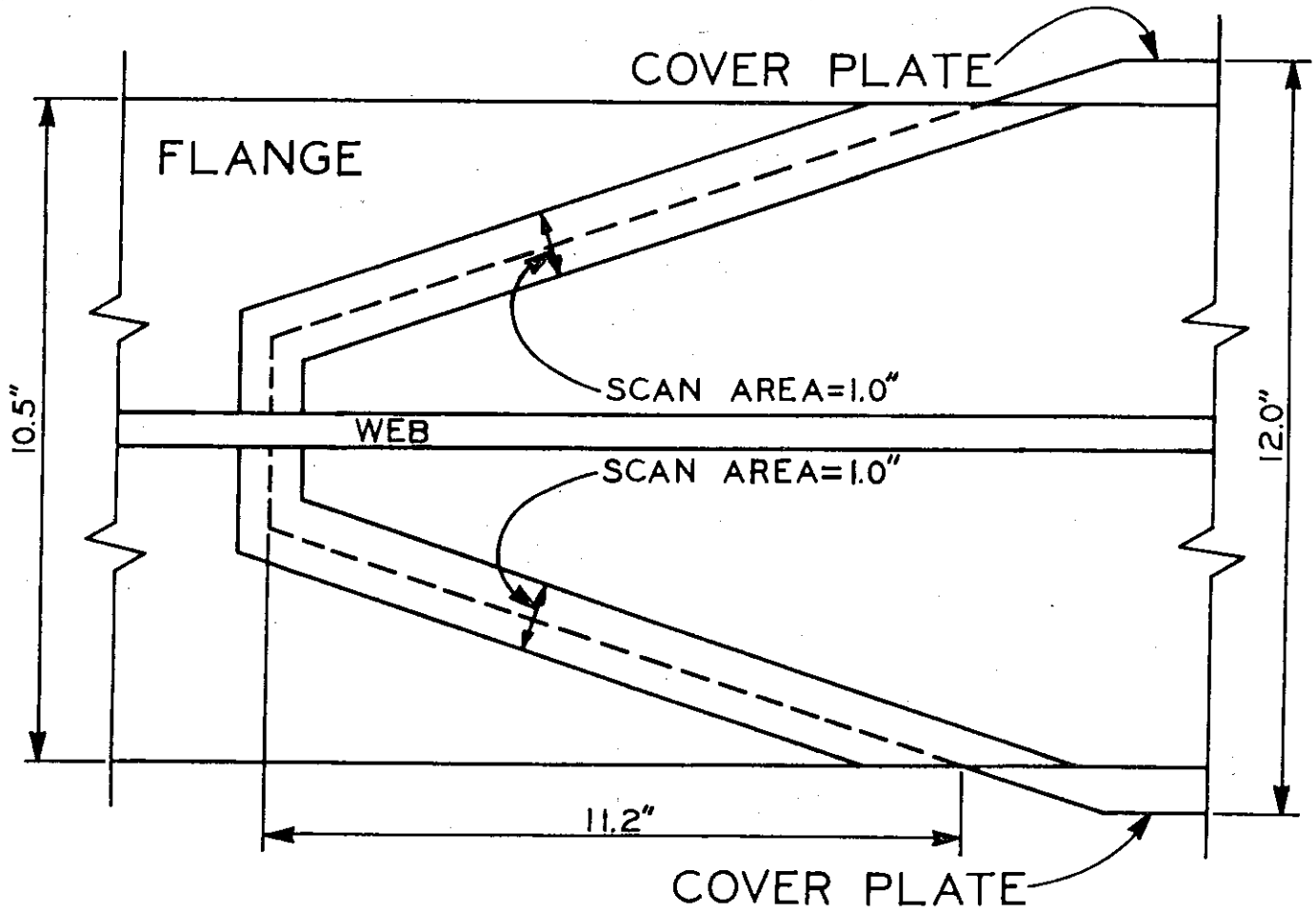

FIGURE C-9. SCAN AREA FOR 45° ANGLE PROBE

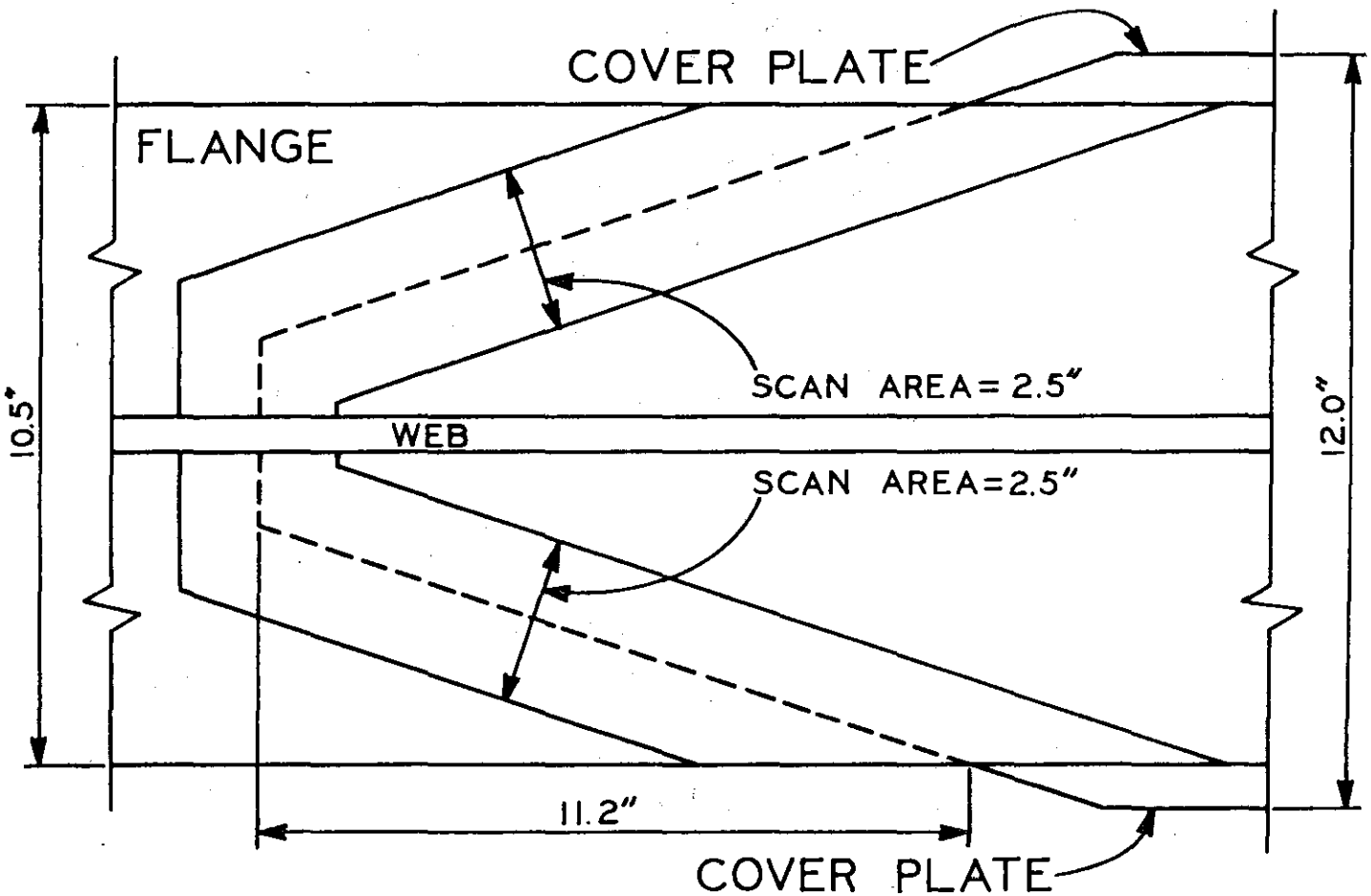

FIGURE C-10. SCAN AREA FOR 70° ANGLE PROBE

Crack lengths in the base metal were measured by the 6 dB method[C4]. The angle probe was positioned near the crack such that a maximum of energy would be returned to the probe. Instrument adjustments were made so that the return signal amplitude registered 10 dB. The probe was then moved parallel to the plane of the crack until the return signal amplitude dropped 6 dB. At this point the centerline of the sound path should have been located at one end of the crack being measured. The probe's position was marked on the girder flange and the process was repeated at the opposite end of the crack. The distance between the two respective marks was the ultrasonically indicated flaw length.

C.4.4 Limitations

Physical limitations impaired the effectiveness of the ultrasonic inspection. As was seen in Figs. C-9 and C-10, the web and web-flange fillets obscured inspection of an area approximately 0.75 in. in width directly beneath the web. Extra time was required to manuever around additional measuring devices placed on the bridge girders to monitor bridge behavior.

The presence of the weld itself makes it difficult to detect fatigue cracks at the toe of the fillet weld when scanning from the back side of the weld. This is due to the fact that there is no flange surface to reflect the sound wave, Fig. C-11.

There is serious doubt about the ability of ultrasonic inspection to detect a crack at the toe of the fillet weld at the end of the

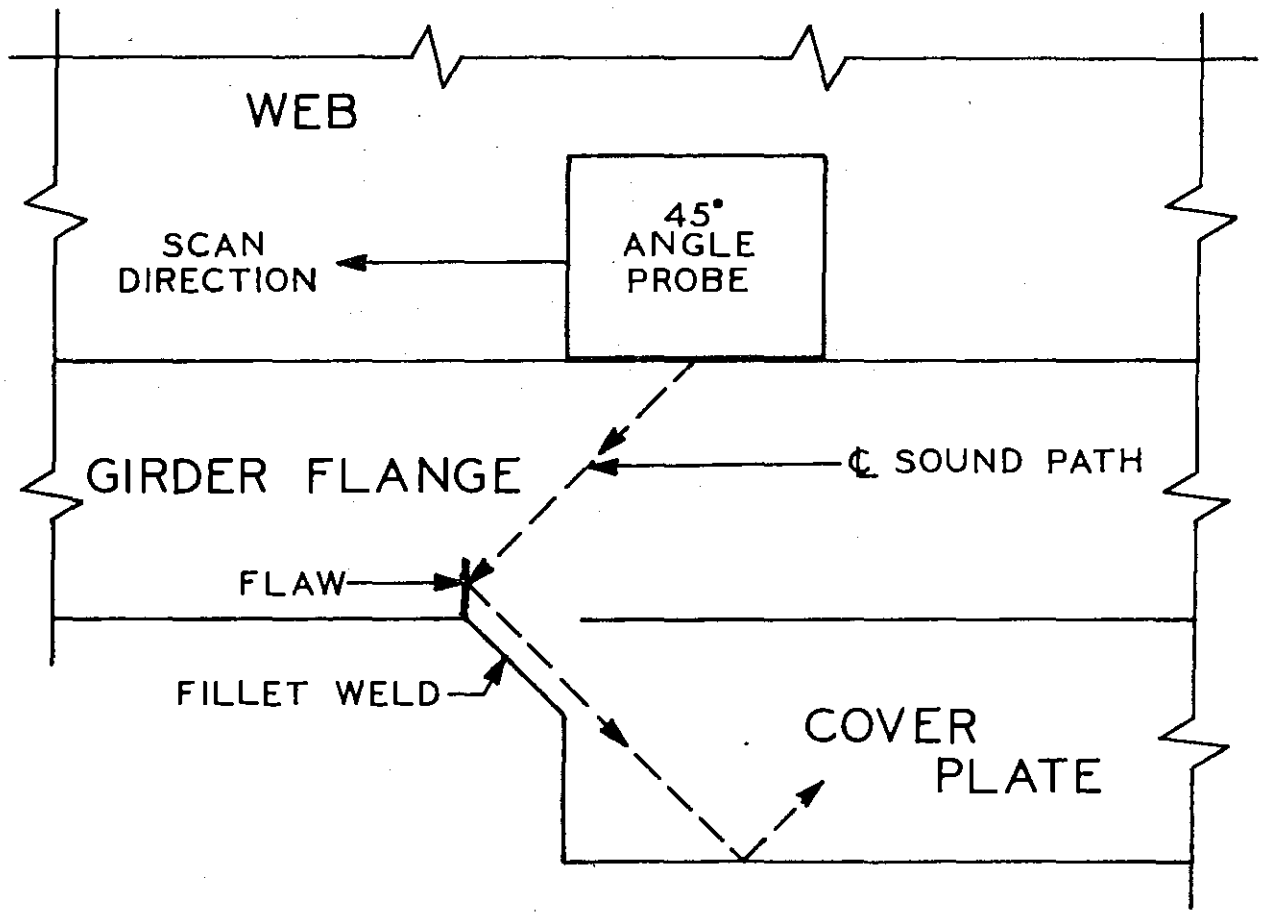

FIGURE C-11. SOUND PATH WHEN EXAMINING FROM HEEL SIDE OF FILLET WELD

cover plate in the top flange in this bridge. As can be seen in Figure C-12 the weld detail provides no suitable surface for reflection of the wave.

Although the probe can be rotated to find cracks which are not perpendicular to the axis of the beam, it cannot be rotated to compensate for a crack that is not perpendicular to the bottom face of the flange. If a crack is not perpendicular to the face of the flange the reflected wave which doubles that corner is not parallel to the transmitted wave and does not return directly to the probe. In cases where the deviation from 90 degrees is small the width of the ultrasonic beam is great enough that part of the wave is received. However, if the deviation is more than a few degrees the reflection may be completely missed.

Inspection of the large area of weld material proved to be a tedious process requiring a great deal of time. During each full inspection, 550 inches of weld material were scanned. The process took approximately 9.5 hours to complete.

Mechanical limitations inherent to ultrasonic inspection are briefly touched upon in the preceding sections. In-depth study can be obtained from the Non-destructive Testing Handbook[C3].

C.5 PRESENTATION OF FIELD DATA

C.5.1 Introduction

Each ultrasonic inspection for fatigue cracks was assigned an inspection number. Table C-2 is a listing of the test numbers at the corresponding number of fatigue cycles. Inspection "Number 1" was

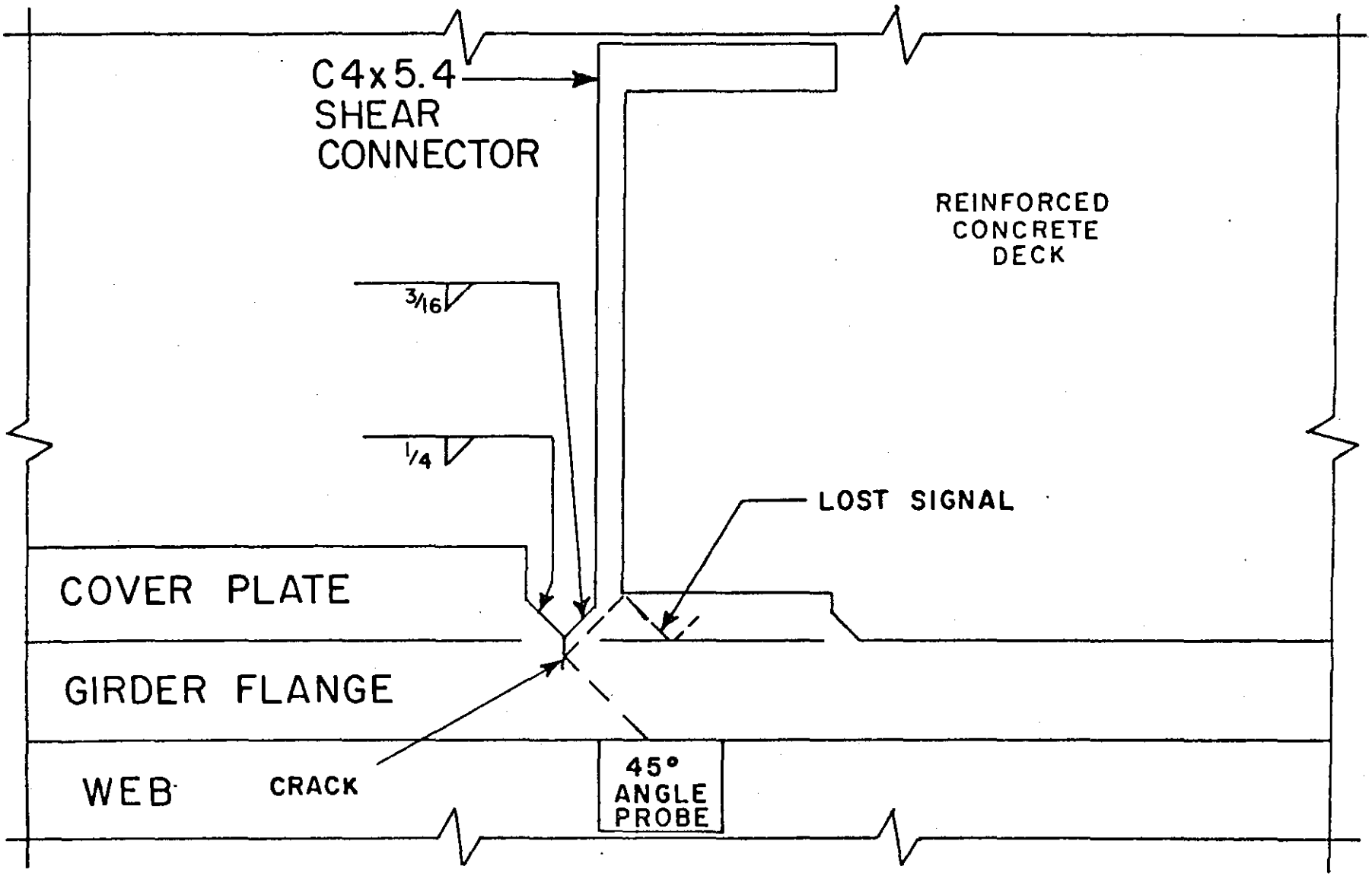

FIGURE C-12. SUSPECTED FLAW ORIGIN IN TOP CRITICAL SECTIONS

TEST NUMBER	DATE	10^3 CYCLES OF LOAD	SECTION NUMBER															
			2.1 B		2.2 B		2.3 B		2.4 B		6.1 B		6.2 B		6.3 B		6.4 B	
			N	S	N	S	N	S	N	S	N	S	N	S	N	S	N	S
1	8/12	0																
2	9/2	19.53							(0.25)		(0.20)			(0.25)		(0.25)	(0.25)	(0.25)
3	9/7	75.40							(0.50)							(0.50)	(0.40)	(0.50)
4	9/12	95.06	(0.25)				(0.25)		(0.50)	(0.25)	(0.25)	(0.25)		(0.25)		(0.50)	(0.75)	(0.70)
5	9/20	215.39	(0.25)				(0.25)		(1.00)	(0.25)	(0.25)	(0.25)		(0.25)		(0.50)	(0.90)	(1.00)
6	9/24	287.0	(1.25)		(1.30)	1.00	(1.25)	(1.50)	(1.50) 0.25	(1.50)	(1.50) 0.80	(1.50) 0.60	(1.50)	(1.50) 1.05	(1.30)	(1.50)	(1.50)	(1.00)

CRACK SIZE = INCHES

( ) = CRACK AT JUNCTION OF FILLET WELD & COVER PLATE, REMAINING VALUES ARE BASE METAL FATIGUE CRACKS.

N = NORTH SIDE OF GIRDER FLANGE S = SOUTH SIDE OF GIRDER FLANGE

TABLE C-2. ULTRASONIC CRACK MEASUREMENTS AT BOTTOM CRITICAL SECTIONS

7	9/25	337.5	(1.50) 0.70	(1.50)	(1.50)	1.50	(1.50)	(1.50)	(1.50) 0.25	(1.50) 0.25	1.85	1.80	0.55	1.05	(1.50)	(1.50) 0.25		(1.50) 0.25
8	9/25	348.7			(1.50)						2.05	2.00		1.20				
9	10/3	360.87	0.85		0.25	1.50	(1.50)	0.25	0.70	0.25	2.55	2.30	0.75	1.35	0.25	0.25		0.25
10	10/4	380.0	0.85		0.45	1.90					2.70	2.30	0.75	1.45				
11	10/4	402.05	0.85		0.60	2.10	(1.50)	0.25	0.70	0.25	2.90	2.60	0.80	1.60	0.50	0.25		0.25
12	10/5	415.5	0.85		0.60	2.80	(1.50)	0.25	0.70	0.25	3.35	3.25	0.80	1.75	0.50	0.25		0.25
13	10/5	422.5				2.80					3.50	3.25						
14	10/5	437.8				3.50												
15	10/5	447.9									4.70	4.25						
16	10/5	453.0																
17	10/5	455.0				3.50					FAILURE							

TABLE C-2 (cont.) ULTRASONIC CRACK MEASUREMENTS AT BOTTOM CRITICAL SECTIONS

performed prior to any test loading. The inspection consisted of tracing and marking the cover plate weld lines, as well as a preliminary examination for fatigue cracks. One flaw was found at section 6.3A. The flaw was located beneath the fillet weld on the south side of the tapered portion of the cover plate. No additional cracking took place at this location.

C.5.2 Location of Fatigue Cracking In Bottom Critical Sections

Ultrasonic test "Number 2" provided the first indication of cracking in the bottom critical sections. It was noted that some separation had occurred between the transverse fillet welds and the ends of the bottom cover plates, Fig. C-13.

In detecting these cracks the ultrasonic wave was interrupted and followed a path represented by the double-headed arrows shown. The resulting peaks displayed on the ultrasonic inspection unit occurred at points between 2.4 in. and 2.9 in. depending on the girder being tested. Lengths of these cracks as indicated ultrasonically are shown in parentheses in Table C-2. At this point there was no apparent cracking of the base metal beneath the transverse fillet welds.

Ultrasonic inspection was continued at the ends of the cover plates in an effort to monitor the cracking of the welds. Cracking occurred at all eight bottom critical sections, completely across the junction of the fillet welds and the ends of the cover plates (Fig. C-14 and Fig. C-15). Portions of these cracks turned the corners at the ends of the cover plates and continued in the fillet welds along the tapered sections of the cover plates, Fig. C-16. To this point there still had been no apparent fatigue cracking in the base metal.

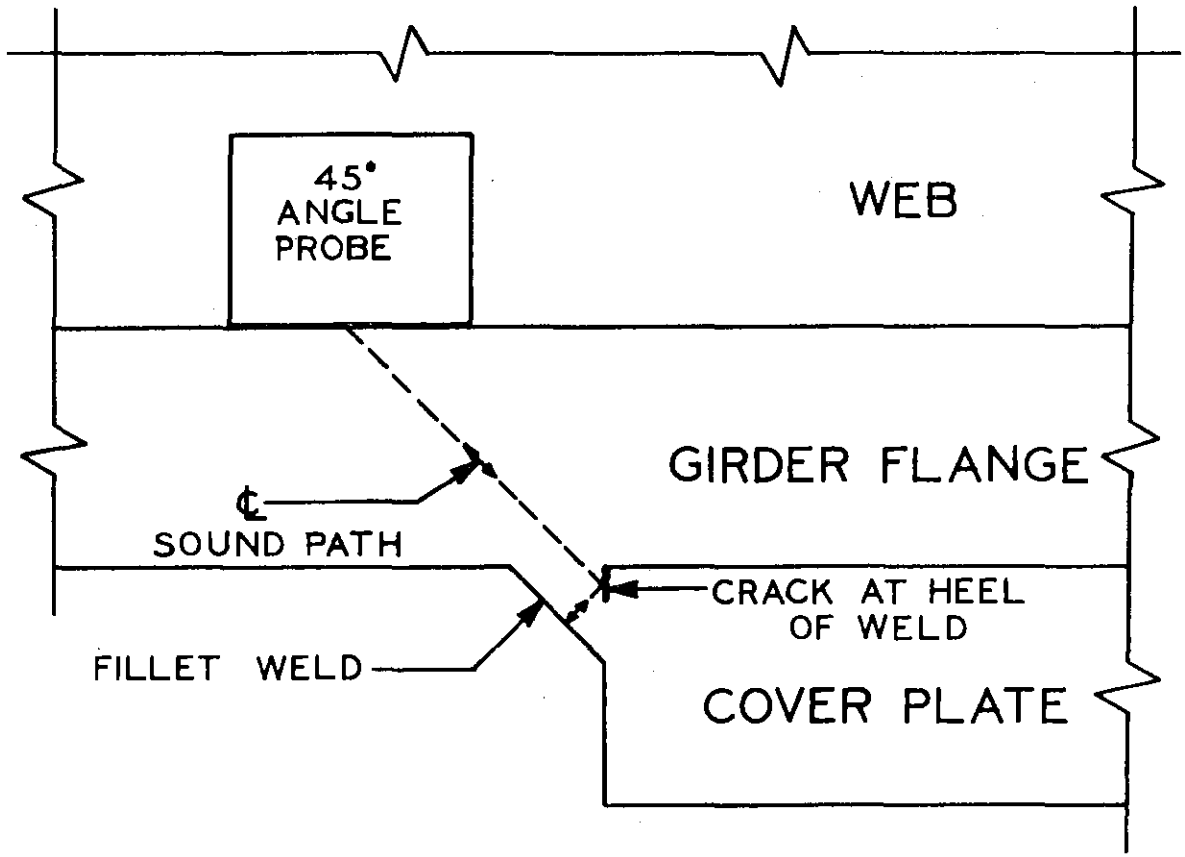

FIGURE C-13. SOUND PATH AFTER INITIAL FILLET WELD-COVER PLATE SEPARATION

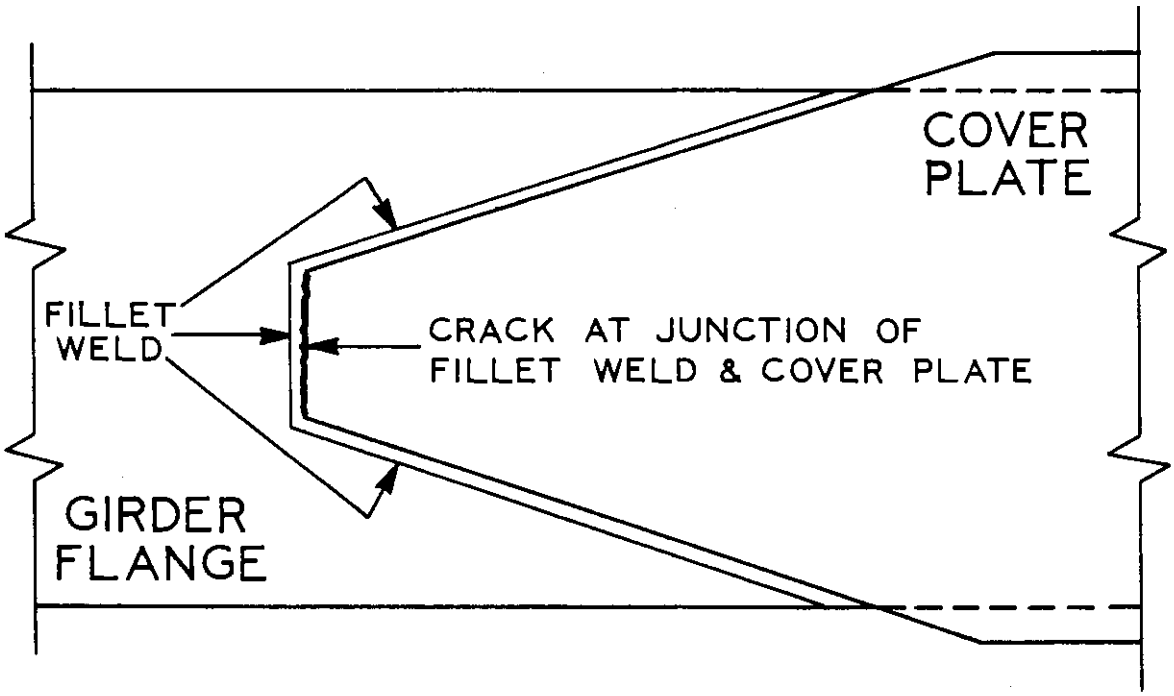

FIGURE C-14. EARLY CRACK GROWTH IN TRANSVERSE FILLET WELD

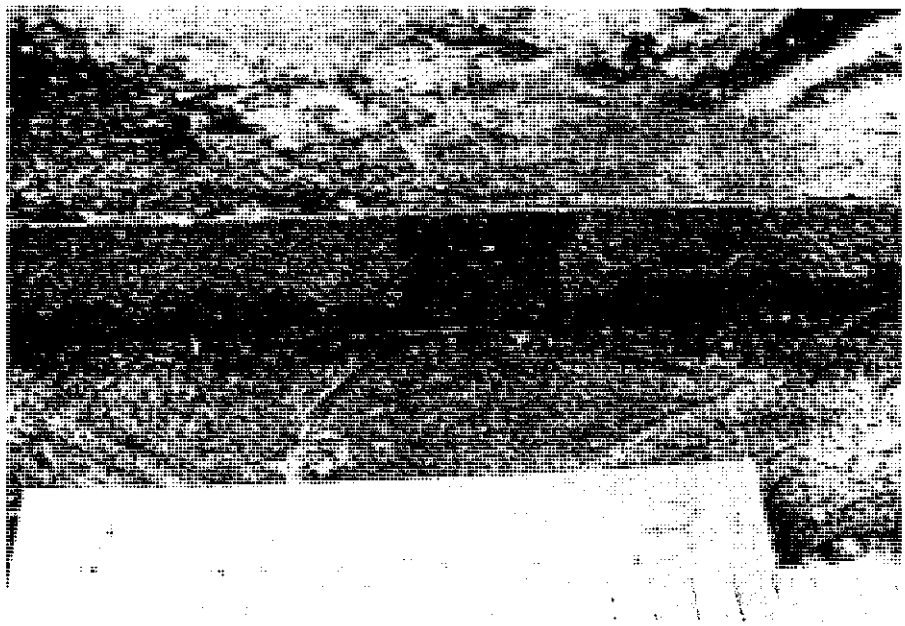

FIGURE C-15. CRACK AT JUNCTION OF FILLET WELD AND COVER PLATE, SECTION 6.1B

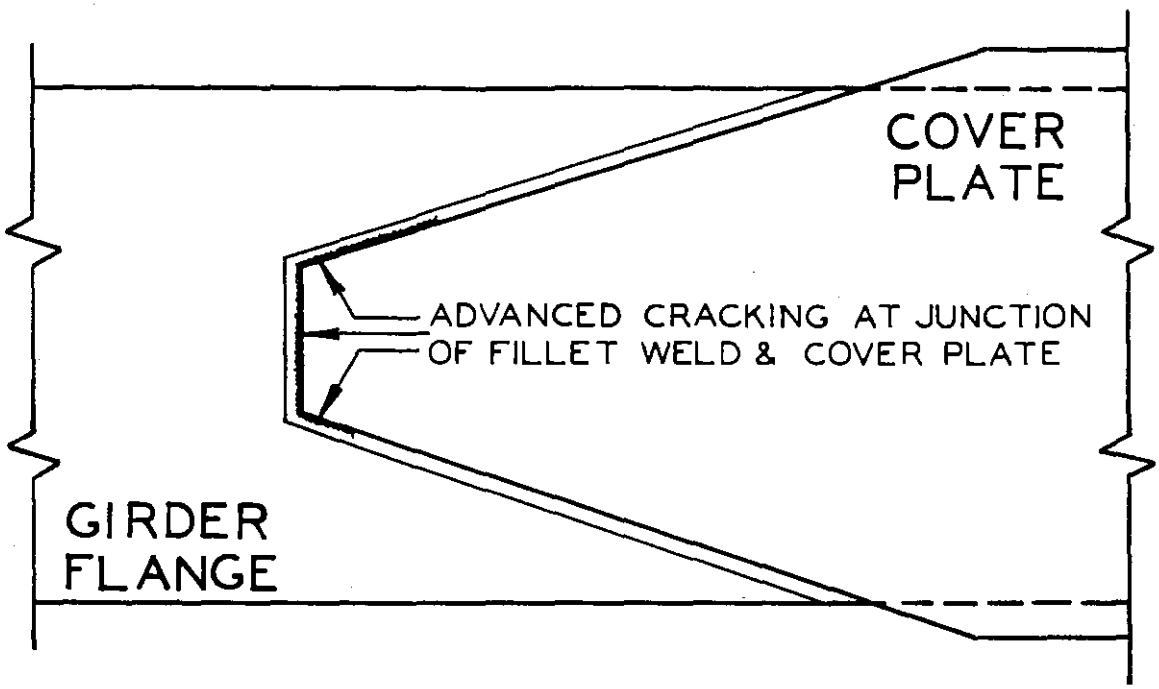

FIGURE C-16. ADVANCED CRACK GROWTH IN FILLET WELD

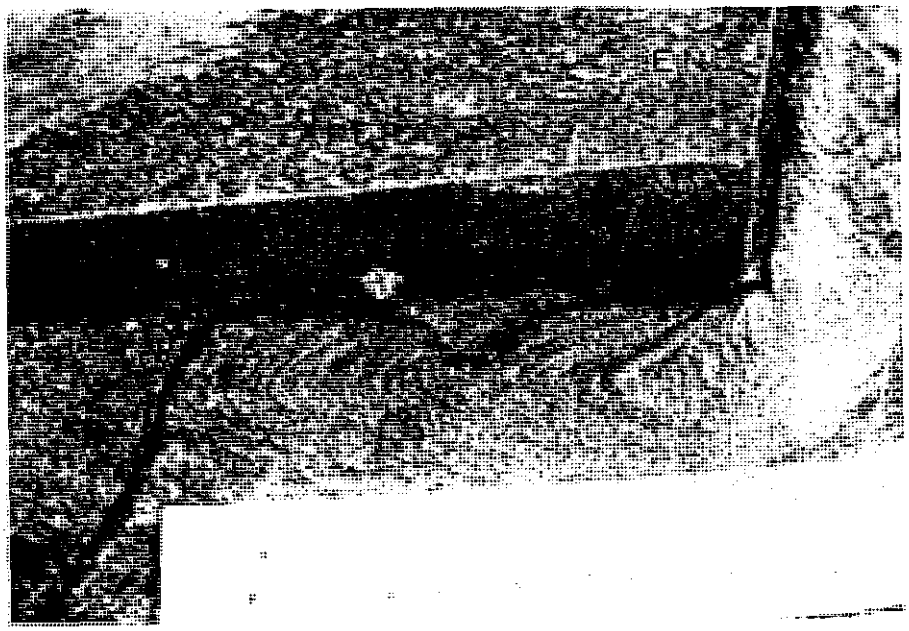

FIGURE C-17. FILLET WELD CRACK ALONG TAPERED PORTION OF COVER PLATE, SECTION 6.1B

Figure C-17 clearly shows the manner in which the cracks in the fillet welds eventually entered the base metal. The cracks traversed those portions of the fillet welds that ran along the tapered sections of the cover plates, and entered the base metal directly beneath the welds. This was the case for all eight bottom critical sections. The only notable differences were the positions along the tapered portions of the cover plates at which the cracks entered the base metal and the extent of the base metal fatigue cracking.

For the most part, beyond ultrasonic test "Number 6", Table C-2 is a log of fatigue crack growth in the respective girder flanges. It can be seen from Table C-2 that sections 2.2B, 6.1B and 6.2B exhibited the largest amounts of fatigue crack growth. This fatigue crack growth is displayed for the three respective sections in Figs. C-18 through C-26. Observation of the fatigue cracks was enhanced through the aid of dye penetrant. Note the locations at which the fillet weld cracks entered the girder flanges.

C.5.3 Location of Fatigue Cracks In Top Critical Sections

It had been determined prior to the full scale fatigue test that the top flanges were not as susceptible to fatigue cracking as were the bottom flanges, the measured test stress ranges were even smaller than those that were predicted prior to the full scale fatigue test. Therefore, ultrasonic inspections were stopped after the first inspection.

FIGURE C-18. SECTION 2.2B AT 337,500 CYCLES

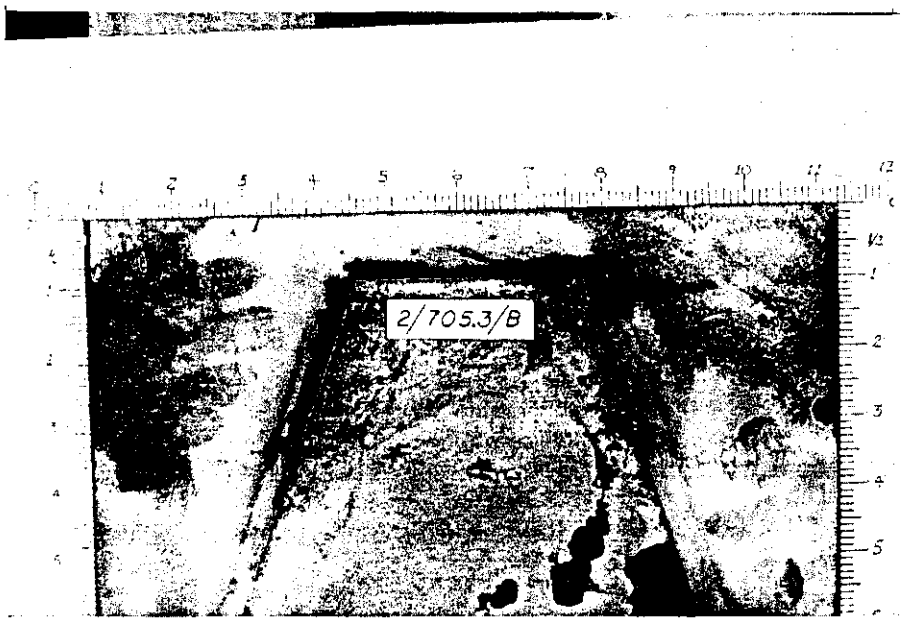

FIGURE C-19. SECTION 2.2B AT CONCLUSION OF FATIGUE TEST

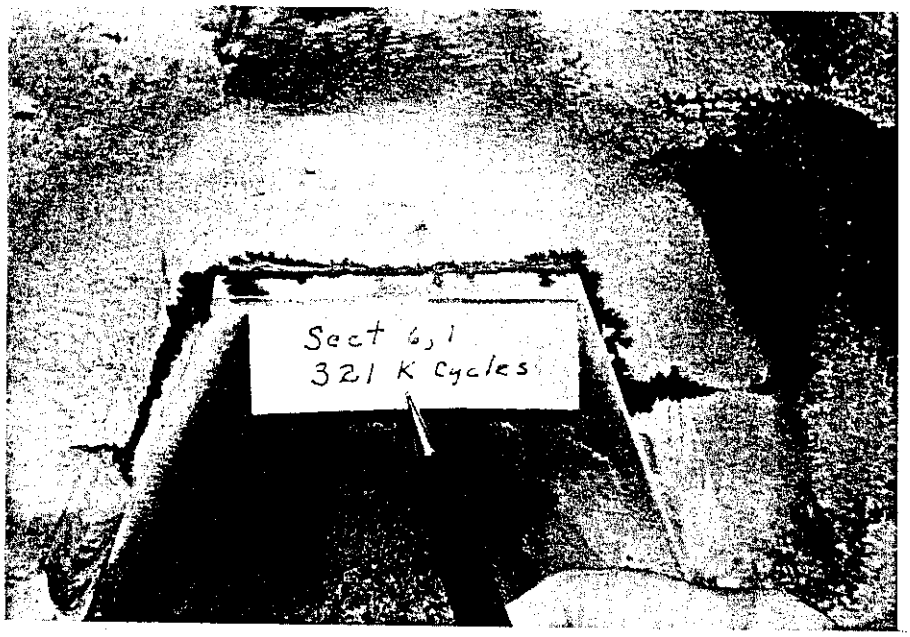

FIGURE C-20. SECTION 6.1B AT 321,000 CYCLES

FIGURE C-21. SECTION 6.1B AT 337,500 CYCLES

FIGURE C-22. SECTION 6.1B AT 402,000 CYCLES

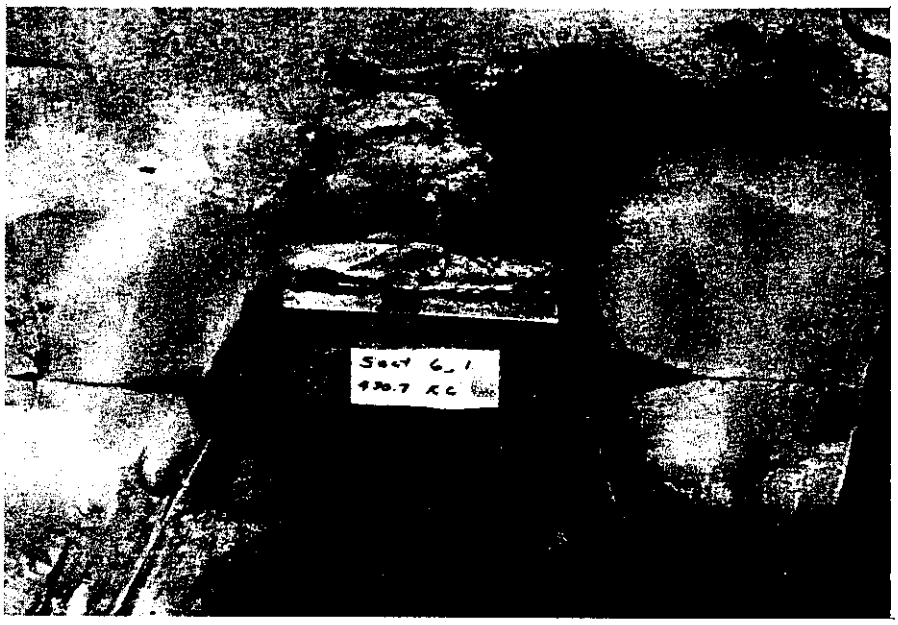

FIGURE C-23. SECTION 6.1B AT CONCLUSION OF FATIGUE TEST

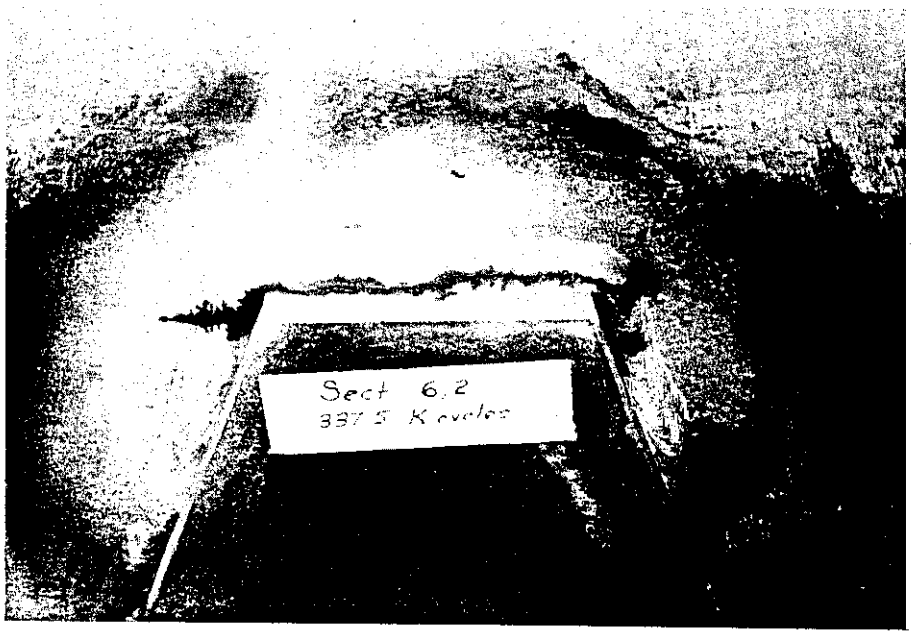

FIGURE C-24. SECTION 6.2B AT 337,500 CYCLES

FIGURE C-25. SECTION 6.2B AT 402,000 CYCLES

SECTION NUMBER / TEST NUMBER	2.1 A	6.2 A
1	0.00	0.00
12	6.02	6.25
13	6.32	6.65
14		7.65
15		8.80
16		FAILURE
17	8.32	
FINAL	FAILURE 462 KC	

CRACK SIZE = INCHES
KC = KILOCYCLES

TABLE C-3. ULTRASONIC CRACK MEASUREMENTS AT TOP CRITICAL SECTIONS

However, it was visually observed that at 415,500 cycles the top flanges were experiencing fatigue cracks at the ends of the cover plates. At this point during the test the loading of the bridge was stopped and a full ultrasonic inspection was performed on the top critical sections. Results of this and subsequent inspections are listed in Table C-3.

The cracking at the top critical sections was ultrasonically indicated to originate in the vicinity of the fillet welds which were used to connect the cover plates and the shear connectors to the girder flanges, Fig. C-12. Growth of the cracks proceeded outward toward the flange tips, and down the web in a direction toward the bottom flange, Fig. C-27 and Fig. C-28.

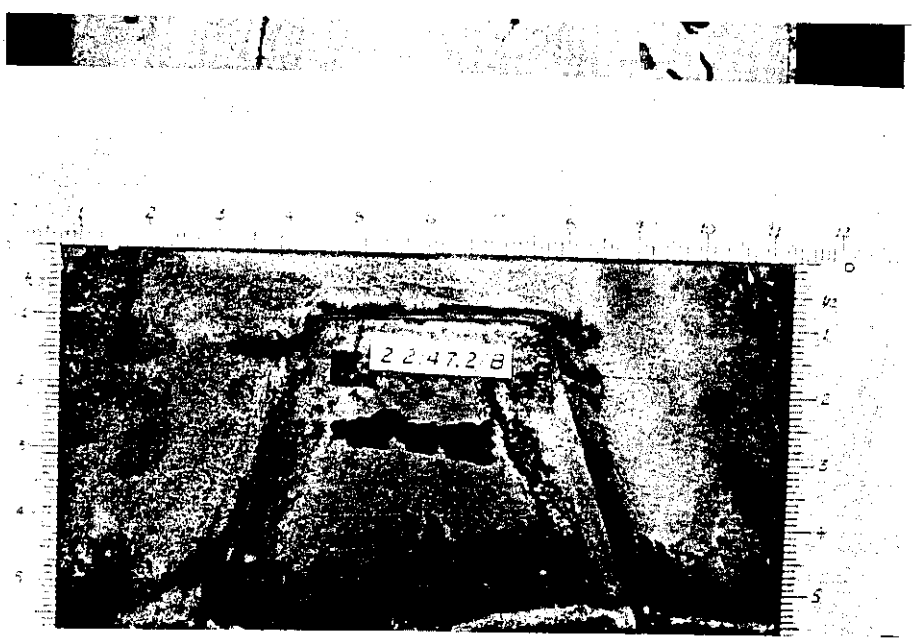

FIGURE C-26. SECTION 6.2B AT CONCLUSION OF FATIGUE TEST

FIGURE C-27. FATIGUE CRACKING AT SECTION 6.2A

FIGURE C-28. FATIGUE CRACKING AT SECTION 2.1A

C.5.4 Additional Fatigue Cracking

At approximately 373,500 fatigue cycles, the Butler-County bridge experienced a fracture at section 4.2B. The section had been subjected to a minimum stress of 0.0 ksi and a maximum stress of 32.3 ksi including ballast and dead load. No ultrasonic inspections had been performed at section 4.2B because the predicted life of this plain rolled beam was approximately 1.25 million cycles.

Fatigue cracking initiated at one of the heat numbers which had been rolled into the bottom flange, Fig. C-29. Heat numbers were spaced at 36 in. for the entire length of the bridge girder.

The failed section was removed and replaced with a bolted repair splice. A thorough ultrasonic inspection was conducted on the bottom flanges of all four girders for several feet on each side of section 4 but no additional cracking was detected. These regions were monitored frequently during the remainder of the test but no cracks were found. At 470,400 fatigue cycles a second complete fatigue failure occurred. Fatigue cracking had initiated at the heat number, 36 inches to the west of section 4.2B, Fig. C-30.

C.5.5 Ultrasonic Flaw Size vs. Actual Flaw Size

Sections 6.2B and 2.2B were separated in the laboratory to expose and measure the fatigue crack surfaces. Comparisons were made between the last ultrasonic crack measurements and the laboratory measurements. Three of the four comparisons shown in Table C-4 were in close agreement. The crack on the north side of section 2.2B was ultrasonically

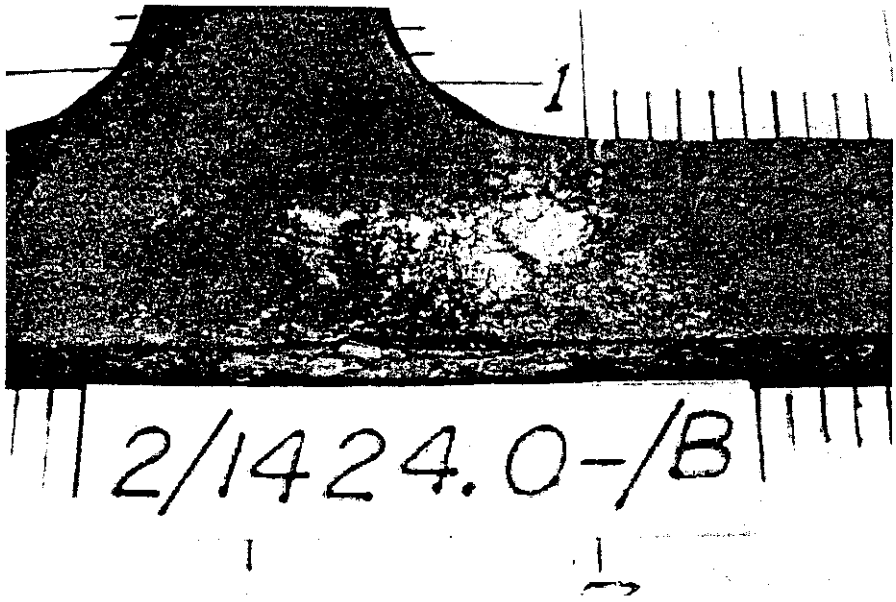

FIGURE C-29. FATIGUE CRACK INITIATION
AT SECTION 4.2B

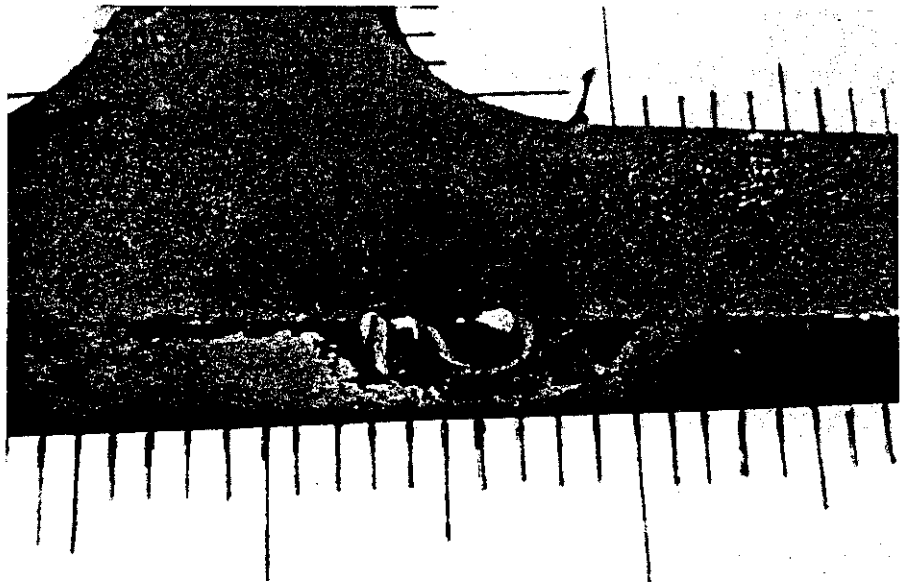

FIGURE C-30. FATIGUE CRACK INITIATION
36 INCHES WEST OF SECTION 4.2B

TABLE C-4
ULTRASONIC FLAW SIZE vs. ACTUAL FLAW SIZE

Flaw Size at End of Test

SECTION	ULTRASONIC MEASUREMENTS	LABORATORY MEASUREMENTS
2.2B N	0.60	1.00
2.2B S	3.50	3.50
6.2B N	0.80	0.80
6.2B S	1.75	2.00

N = North side of girder flange

S = South side of girder flange

measured to be 0.6 in. long, however, the crack was actually 1.0 in. long. When examining a crack of this size directly beneath a fillet weld, portions of the ultrasonic wave become attenuated. This attenuated signal may have resulted in the 40 percent difference between respective measurements.

REFERENCES

C1. Fisher, John W., et al., Report 102, "Effect of Weldments on the Fatigue Strength of Steel Beams," Highway Research Board, Washington, D.C. 1970.

C2. Bethlehem Steel Corporation, "Ultrasonic Testing Inspection for Butt Welds in Highway and Railroad Bridges," U.S. Department of Transportation, Washington, D.C.

C3. McMaster, Robert C. (Edited by), "Nondestructive Testing Handbook," The Ronald Press Company, New York, 1963.

C4. Summers, J. M., "Ultrasonic Inspection for Fatigue Cracks," A Thesis Presented to the Faculty of the Graduate School, University of Missouri-Columbia, May, 1974.

C5. McGonnagle, Warren J., "Nondestructive Testing," McGraw-Hill Book Company, Inc., New York, 1961.

C6. McGaughey, William C., "Nondestructive Testing of Weldments," Automation Industries, Inc., Danbury, Connecticut, 1968.

C7. Hinsley, J. F., "Nondestructive Testing," MacDonald and Evans, LTD, London, 1959.

C8. Hogarth, C.A. and Blitz, J. (Edited by), "Techniques of Nondestructive Testing," Chapters 1-9, 11 Butterworth and Co. (Publishers) Limited, Chapter 10 Crown Copyright, London, 1960.

C9. Operating Instructions, Model UJ Reflectoscope, Automation Industries, Inc., Danbury, Connecticut, 1974.

APPENDIX D

EXPERIMENTAL SETUP

D.1 INTRODUCTION

This appendix is concerned with the experimental setup which was employed during both the fatigue and dynamic test phases of the three-span composite highway bridge field tests. The vibration excitation systems, transducers, and electronic data acquisition systems employed during these field tests are presented here in detail. Additional information on the experimental setup employed during the dynamic tests is contained in reference[A1].

D.2 VIBRATIONAL EXCITATION SYSTEM

All of the field tests employed a closed-loop electrohydraulic structural vibration system. The vibrator was constructed by attaching weights to the piston rod of a servo-controlled hydraulic actuator. The closed-loop system provided complete control of stroke or acceleration and frequency of the hydraulic actuator which was a critical requirement of the field tests.

The hydraulic actuator was mounted in the center of a load distribution frame as shown in Fig. D-1. The load distribution frame was used to distribute the static and dynamic loads to the two interior girders and was tied down to these girders during the fatigue tests. However, the load distribution frame was not tied down to the bridge during the dynamic tests. This was possible since the maximum accelerations of the bridge deck during the dynamic tests never exceeded 0.16 g's.

The location of the hydraulic actuator and load distribution frame during both the fatigue test and dynamic tests are shown in Fig. 1-5.

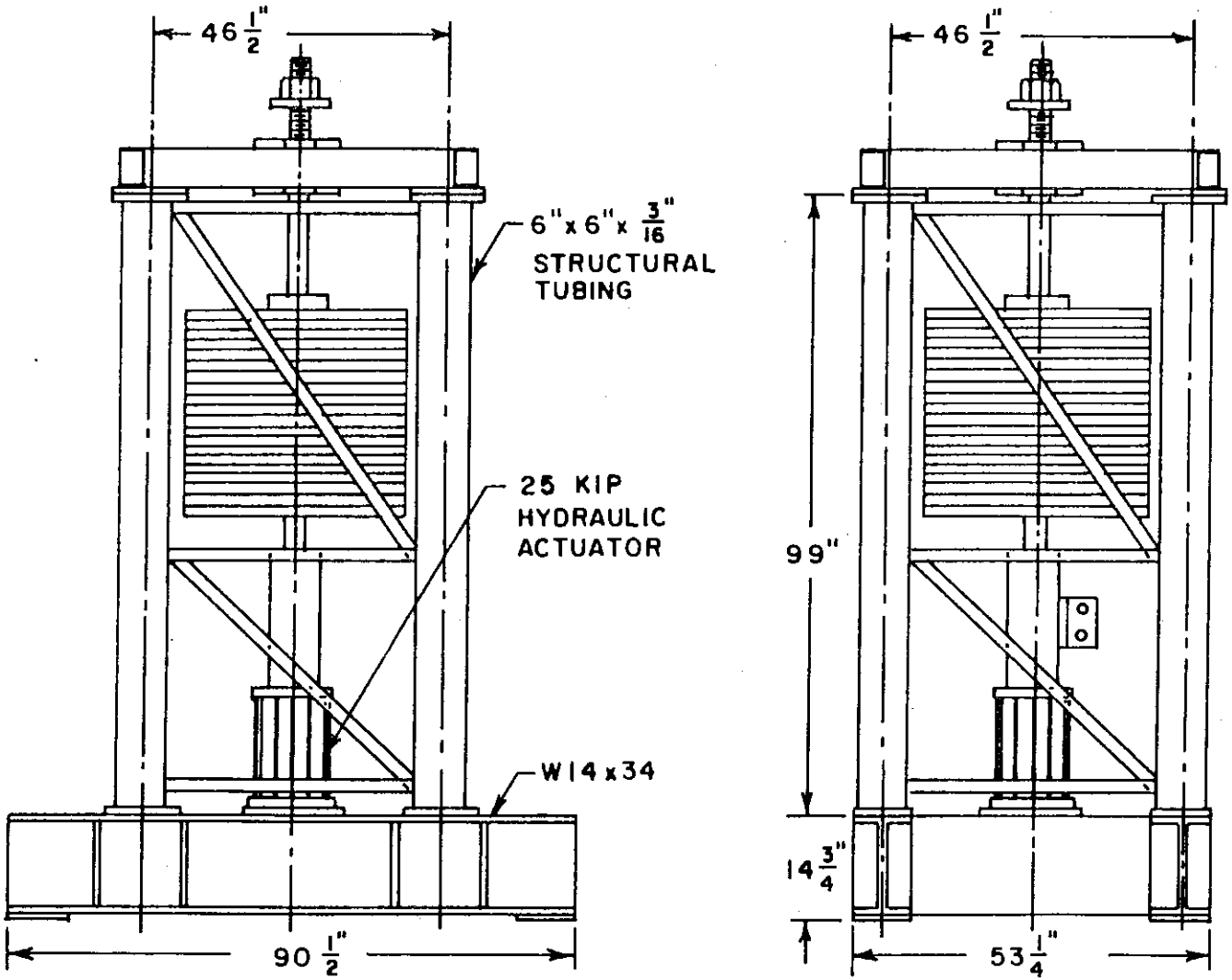

FIGURE D-1. HYDRAULIC ACTUATOR AND LOAD DISTRIBUTION FRAME

D.2.1 Ballast

During the fatigue test each span of the bridge contained 40 kips of ballast consisting of four 10 kip concrete modules arranged on the spans as indicated in Fig. 1-5. The concrete modules were composed of four 2.5 kip reinforced concrete slabs mounted on wooden blocks. The concrete modules were secured to the bridge deck by a chain attached to anchors in the deck to prevent their movement during the fatigue test. The method of support and anchoring of the ballast was chosen to minimize the effect of the modules on the stiffness and damping characteristic of the bridge.

D.2.2 Moving Weights

The moving weights employed during the investigation were fabricated from 36 in. x 36 in. by 1 1/4 in. steel plate. Twenty-one weights were used during the fatigue test, which in addition to the weight of the actuator rod plus other attachments gave a total moving weight of 9,760 lbs. The total moving weight during the dynamic tests was 1,115 lbs., which consisted of two weights, actuator rod plus other attachments.

D.2.3 Hydraulic and Electronic Control Systems

The vibration excitation systems employed for the fatigue tests and the dynamic tests are respectively shown in Figs. D-2 and D-3. Each of the vibration excitation systems consisted of a hydraulic section and an electronic control section. The hydraulic section, which was the same for both vibration excitation systems, was composed of two 35 gpm, 3,000 psi hydraulic power supplies, two 60 gpm hydraulic control manifolds, a 90 gpm high performance servo-valve and a 25 kip hydraulic actuator.

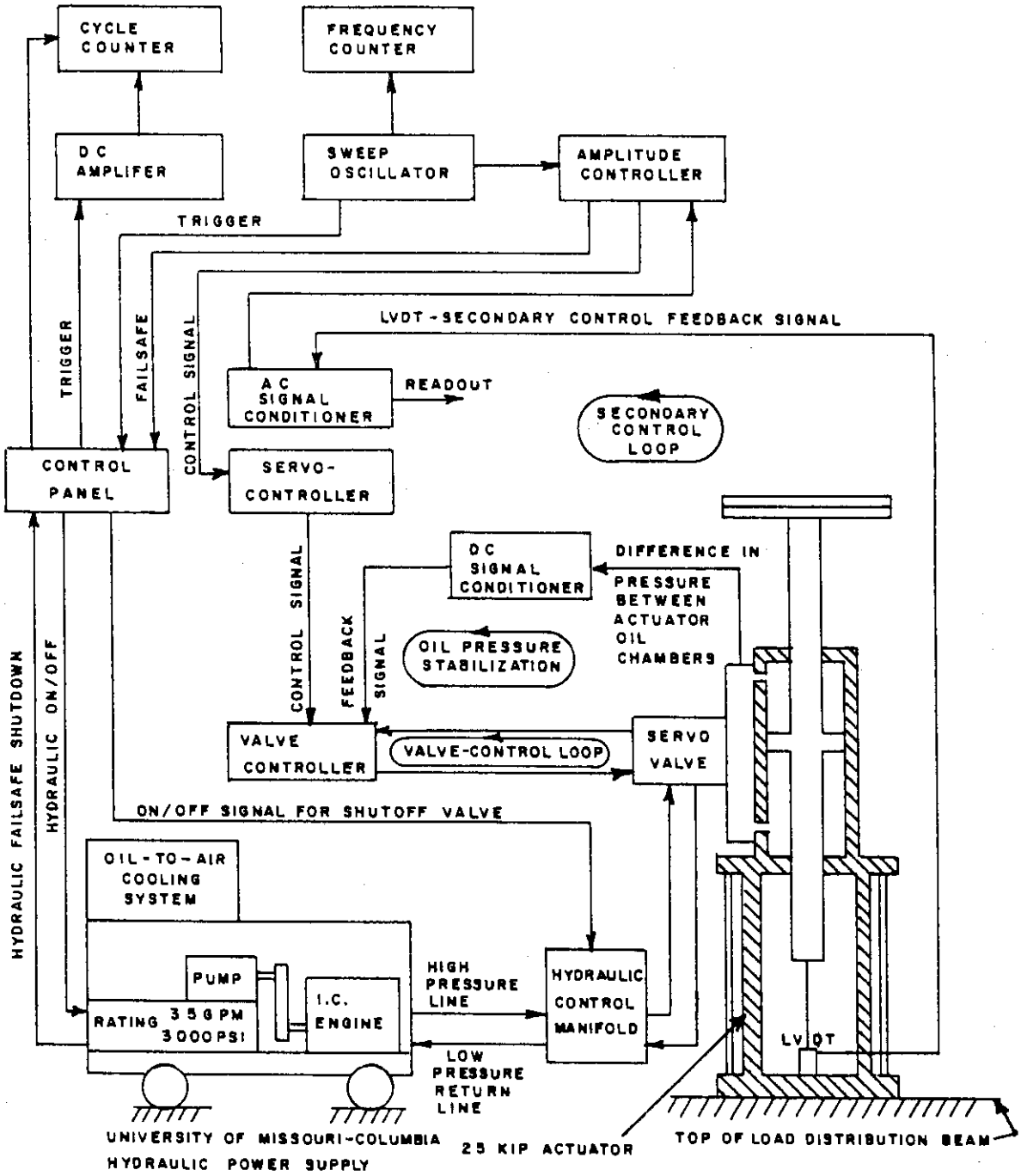

FIGURE D-2. SCHEMATIC OF VIBRATION EXCITATION SYSTEM DURING FATIGUE TEST

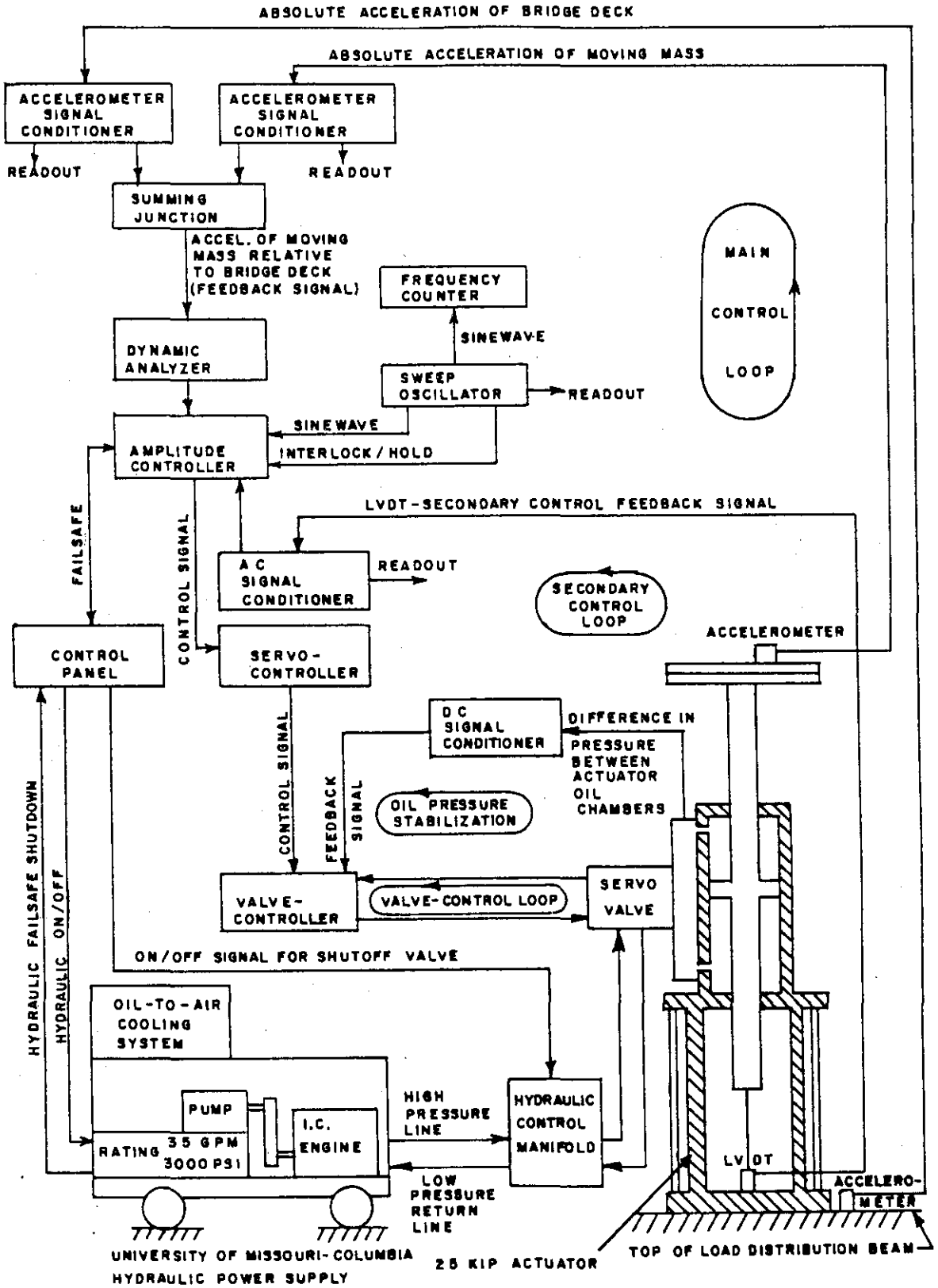

FIGURE D-3. SCHEMATIC OF VIBRATION EXCITATION SYSTEM USED DURING DYNAMIC TESTS

The electronic section for the dynamic tests was basically a closed-loop (feedback) electronic control system that was capable of automatic closed-loop control of the excitation force. Control of the excitation force was achieved by controlling the relative acceleration of the "moving mass" with respect to the base of hydraulic actuator. The electronic control system contained main and secondary control loops in which the main control loop was composed of an amplitude controller and the relative acceleration. The secondary control loop was composed of a servo-controller and an LVDT.

The electronic control system for the fatigue test differed from the electronic control system for the dynamic tests in that there was only a single control-loop, which provided closed-loop control of the stroke of the actuator. Control of the stroke of the actuator proved to be satisfactory for achieving and maintaining the excitation levels needed to conduct the fatigue test.

D.3 TRANSDUCERS

D.3.1 Accelerometers

Two piezoresistive 25-g accelerometers were used only during the dynamic tests. One of the 25-g accelerometers was attached to the top of the "moving mass" as shown in Fig. D-3. The function of this accelerometer, denoted as the control accelerometer, was to sense the absolute acceleration of the "moving mass". The other 25-g accelerometer was located on the test frame near the base of the hydraulic actuator as illustrated in Fig. D-3. This accelerometer, called the reference accelerometer, sensed the absolute transverse acceleration of the bridge deck at the location of the test frame. The relative difference in the

acceleration sensed by the control and reference accelerometers was used to control the excitation force being applied to the bridge.

Servo-accelerometers were used to sense transverse accelerations of the bridge during the dynamic tests. The type of servo-accelerometers employed was based on the "Q-flex" design and had a range of ± 15 g's.

The locations where accelerometer measurements were made during the dynamic tests are given in Fig. 1-8.

D.3.2 Deflection Gauges

Double cantilever beam type deflection gauges were designed for this study to sense the transverse dynamic deflections at various locations on the bridge during both the fatigue and dynamic tests. The deflection gauges were attached to the underside at the bottom flange of the bridge girders and were located parallel with the girders as shown in Fig. D-4. The ten locations chosen for the deflection gauges are illustrated in Fig. 1-7.

As illustrated in Fig. D-4, the deflection gauges were predeflected by pulling the free ends of the gauges downward five inches from their initial straight position and then securing the free ends of the gauges in this position by means of a music wire which was attached to an earth anchor. The electronic sensing element employed for the deflection gauges was a Wheatstone bridge composed of four 120 ohm strain gauges arranged in such a manner that only bending strains could be detected.

D.3.3 Strain Gauges

The strain gauges utilized for this study were 120 ohm gauges and they were attached to the bridge with an epoxy adhesive after proper preparation of the surface of the steel girder in accordance with Micro-Measurement Instruction Bulletin B-137-3 dated August 1974.

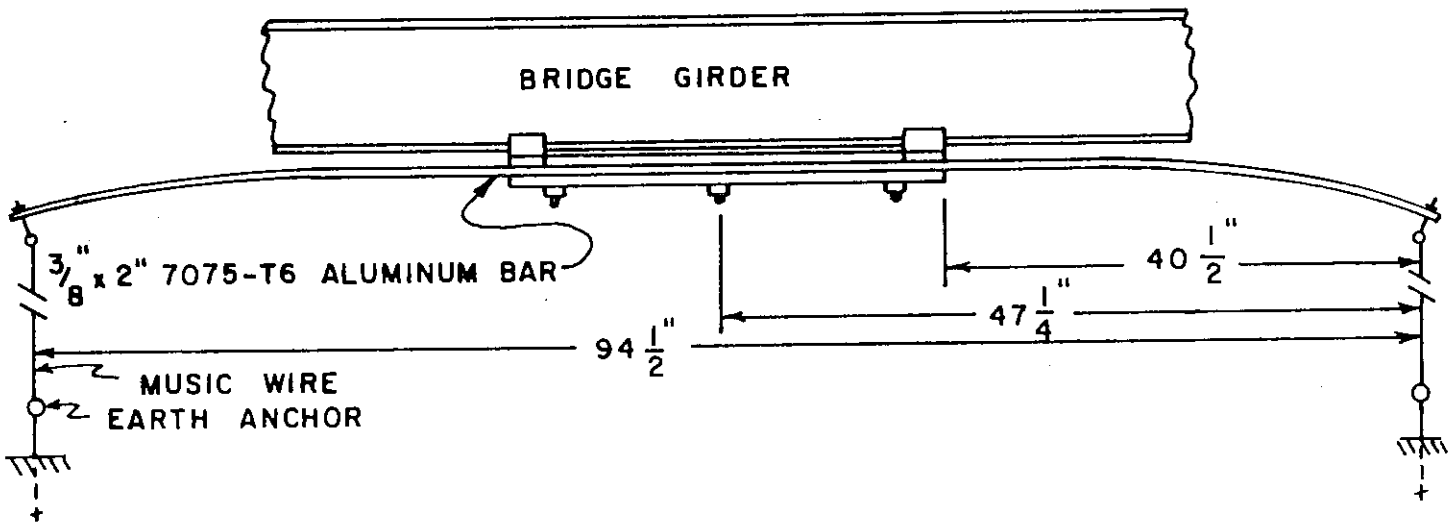

FIGURE D-4. DEFLECTION GAUGE INSTALLATION

The locations of the strain gauges on the bridge girders and on reinforcing bars in the bridge deck are shown in Fig. 1-6.

D.3.4 LVDT

The hydraulic actuator had a LVDT located inside the static positioning chamber which sensed not only the static position of the actuator rod, but also its dynamic displacement. A description of the function of the LVDT in the feedback loops of the control systems associated with both the fatigue and dynamic test is contained in Art. D.2.3.

D.3.5 DC Differential Transformer

Six DC differential transformers (DCDTs) were mounted on the bridge at the field splice locations in the east end of the bridge as illustrated in Fig. D-5. The DCDT's were attached between the bottom of the bridge deck and the top flange of a girder as shown in Fig. D-6. The DCDT was used to measure the slippage between the deck and a girder at a field splice location.

D.4 ELECTRONIC DATA ACQUISITION SYSTEMS

This section presents the data acquisition systems used during the field tests. The presentation is broken down into a separate discussion of the signal conditioning systems employed for the accelerometers, strain gauges, deflection gauges, DCDTs and LVDT. The presentation concludes with a discussion of the data recording and monitoring systems utilized throughout the field tests. A photograph of the data acquisition system is shown in Fig. D-7.

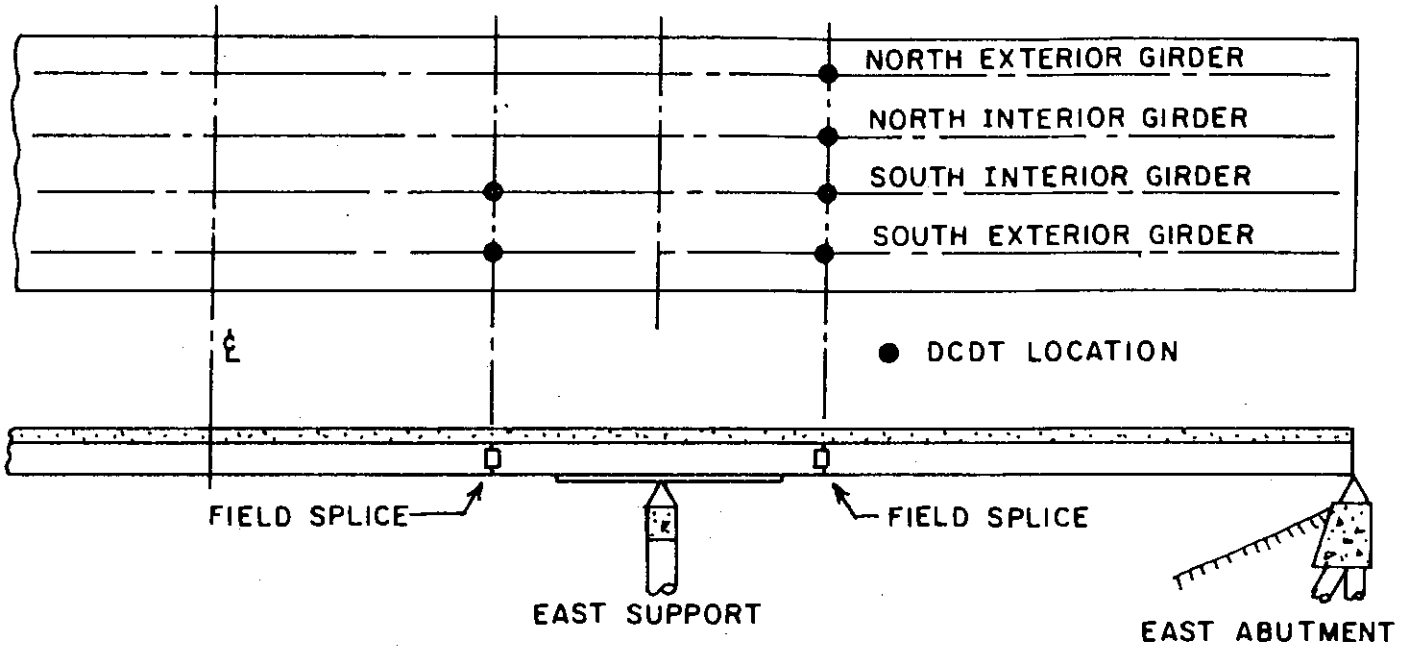

FIGURE D-5. LOCATION OF DCDT'S ON BRIDGE

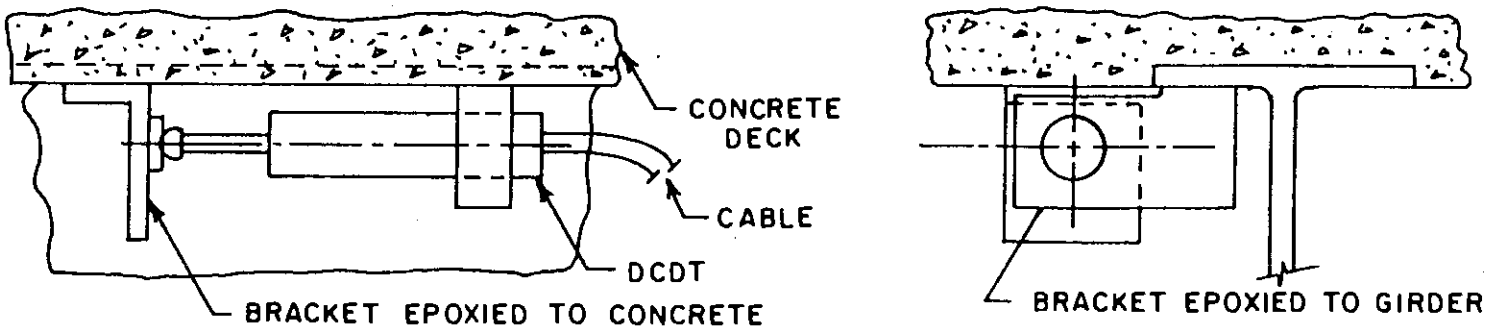

FIGURE D-6. ATTACHMENT OF DCDT TO BRIDGE

FIGURE D-7. DATA ACQUISITION SYSTEM

D.4.1 Signal Conditioning System

D.4.1.1 Accelerometer System

Two different signal conditioning systems were employed for the piezoresistive and servo-accelerometers. One system was used only for the sweep test and the other system was used with the Transient Response, Normal Mode and Frequency Response Curve Tests. Schematics of the two respective signal conditioning systems are given in Figs. D-8 and D-9.

It was necessary during the dynamic tests to filter the accelerometer signals. The signals from the servo-accelerometers were filtered with a low-pass filter with unity gain having a cut-off frequency of 10 Hz. As illustrated in Fig. D-8, the conditioned signals from the two piezoresistive accelerometers were fed to a difference junction whose output was the relative acceleration between the attached weights on the hydraulic actuator and the bridge deck. The relative acceleration signal was filtered by means of a tracking filter set for unit gain. The tracking filter used a 2.0 Hz bandpass filter with the centering frequency furnished by the sweep oscillator contained in the vibration excitation control system. During dynamic test No. 4, the tracking filter was replaced because of a malfunction with a low-pass filter with unity gain having a cut-off frequency of 10 Hz.

D.4.1.2 Deflection and Strain Gauges

The deflection gauges and 8 channels of the strain gauges were signal conditioned with a signal conditioning system furnished by the FHWA as illustrated in Fig. D-10. The 8 strain gauges connected to the FHWA system are those at sections 3 and 5 on the concrete deck. The signals from the FHWA system were fed to a specially modified 100-channel

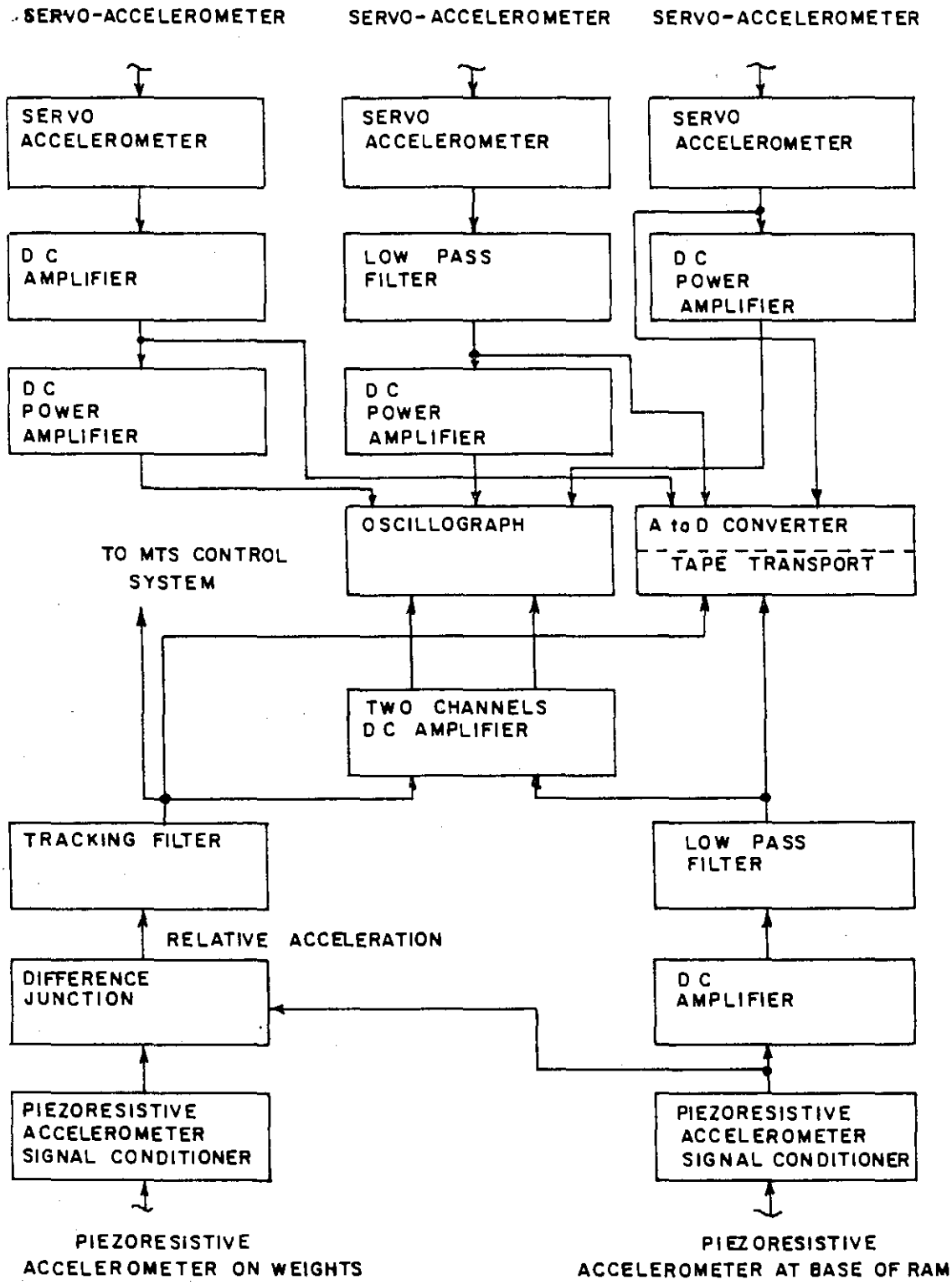

FIGURE D-8. DATA ACQUISITION SYSTEM SCHEMATIC FOR ACCELEROMETERS DURING SWEEP TEST

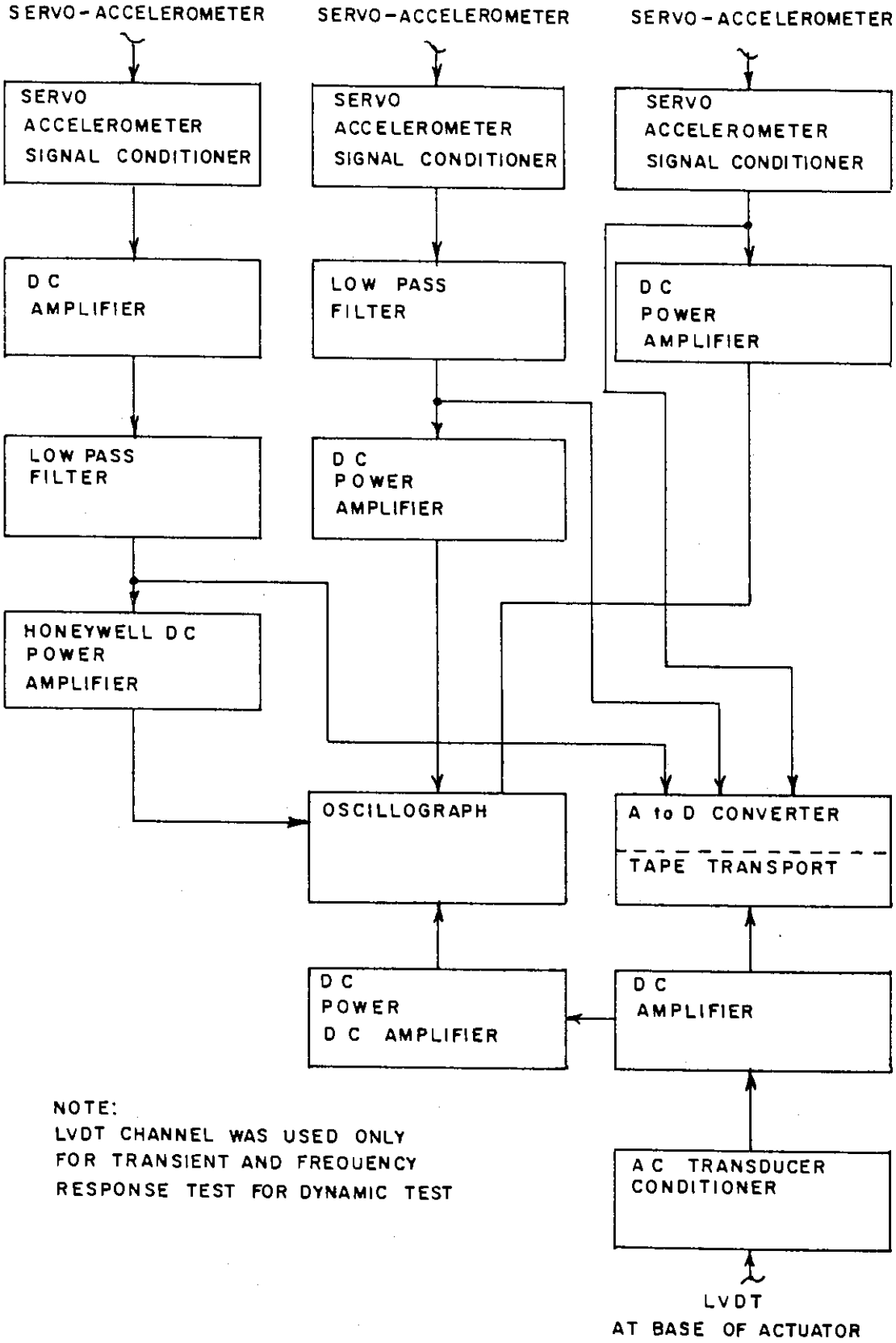

FIGURE D-9. DATA ACQUISITION SYSTEM SCHEMATIC FOR DYNAMIC TESTS

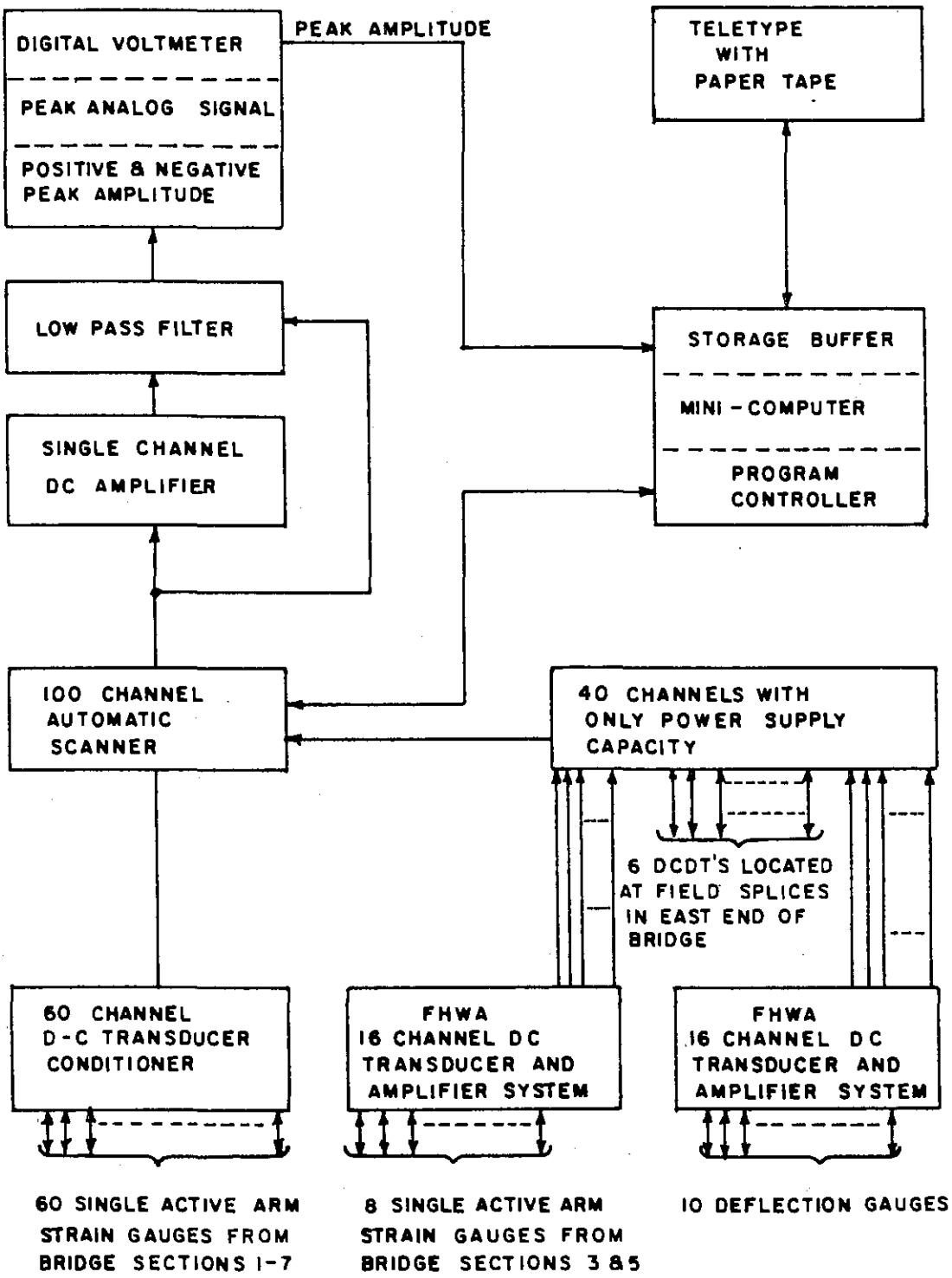

FIGURE D-10. DATA ACQUISITION SYSTEM SCHEMATIC FOR STRAIN AND DEFLECTION GAUGES

data acquisition system to be recorded. This recording system is discussed in Section D.4.2.1.

The remaining 60 channels of strain gauges were signal conditioned with the signal conditioning section of the 100-channel data acquisition system as illustrated in Fig. D-10.

D.4.1.3 LVDT

The LVDT located in the base of the hydraulic actuator was signal conditioned with an AC transducer conditioner. The LVDT conditioned signal was recorded during some parts of the first dynamic test.

D.4.1.4 DCDT

The DCDT's were powered by the 100-channel data acquisition system as illustrated in Fig. D-10. The output signal from the DCDT's was fed back to the 100-channel unit to be recorded without further signal conditioning.

D.4.2 Data Recording Equipment

Three different data recording systems were employed during the field tests and they consisted of two separate digital recording systems, and an oscillograph system.

D.4.2.1 Digital Recording System

The primary digital recording system for the dynamic tests consisted of an analog to digital converter and a tape transport as shown in Fig. D-11. The analog to digital (A-D) unit converted a continuous analog signal into its discretized digital equivalent. The magnetic

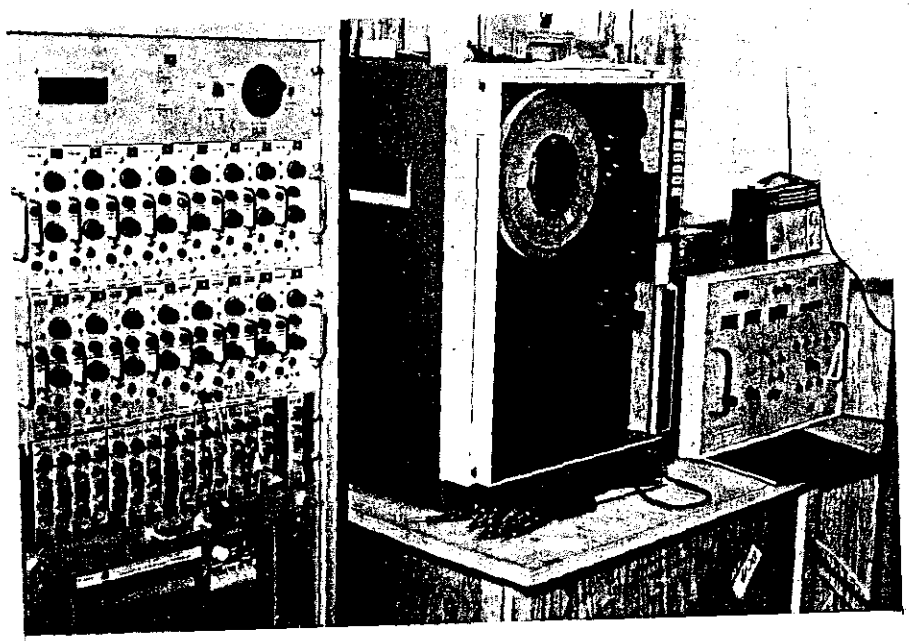

FIGURE D-11. FHWA SIGNAL CONDITIONING AND DIGITAL RECORDING SYSTEMS

tape drive unit wrote the discretized value onto a 9-track magnetic tape at a density of 800 bits per inch, a block size of 2,048 bytes and 12 bit binary. The two units used together formed a multi-channel, variable sample rate A-D recording system. During the dynamic tests, up to 5 channels of data were automatically scanned and sampled at a preselected rate of 70 or 100 samples per second.

The second digital recording system was a 100-channel data acquisitions system which was modified to be controlled by a Mini-Computer. A schematic of this system is shown in Fig. D-10. Each channel of this system was sequentially monitored by a channel scanner which was controlled and activated by a software program within the mini-computer. The signal from the channel scanner was fed to a filter, set up as a 16 Hz low-pass filter with unity gain. The analog output from the filter then went to a Peak Detector and Digital Indicator which detected either the maximum or the minimum peak of the analog signal. The peak value of the analog signal was then stored in digital form in the storage buffer of the mini-computer. When the required number of channels had been scanned and the peaks stored in the mini-computer's storage buffer, the digital recording system was then ready to output the data to a teletype which was equipped with a standard line printer and a paper tape punch. The software program of the mini-computer controlled the rate of output from the storage buffer and formatted the data for the teletype.

D.4.2.2 Oscillograph

A light-beam type oscillograph was used to obtain a graphical analog record of the signals from the accelerometers. The analog signals to the oscillograph were signal conditioned with a DC power amplifier in order

to accentuate the analog signals for proper graphical display on the strip chart and to provide the necessary current to drive the galvanometers.

D.4.3 Resonance Monitoring

The principle used for the detection of a resonant frequency was based on the 90° phase relationship that must exist between the steady-state harmonic excitation applied to the bridge by the hydraulic actuator, and the corresponding response at resonance. This phase relationship was established during the field tests with a Lissajous diagram. The Lissajous diagram was displayed on a dual beam oscilloscope. The signals associated with the LVDT, located in base of the hydraulic actuator, and a single deflection gauge connected to the oscilloscope as shown in Fig. D-12 were used to obtain the Lissajous diagram. The deflection gauge located on the south exterior girder of the center span, transverse position 1 in Fig. 1-7, was used to obtain the Lissajous diagram in 1st bending and 1st torsion during the dynamic tests and also during the fatigue test. In 2nd bending, during the dynamic tests, the deflection gauge located on the south exterior girder of the west end span, transverse position 1 in Fig. 1-7, was used to obtain the Lissajous diagram.

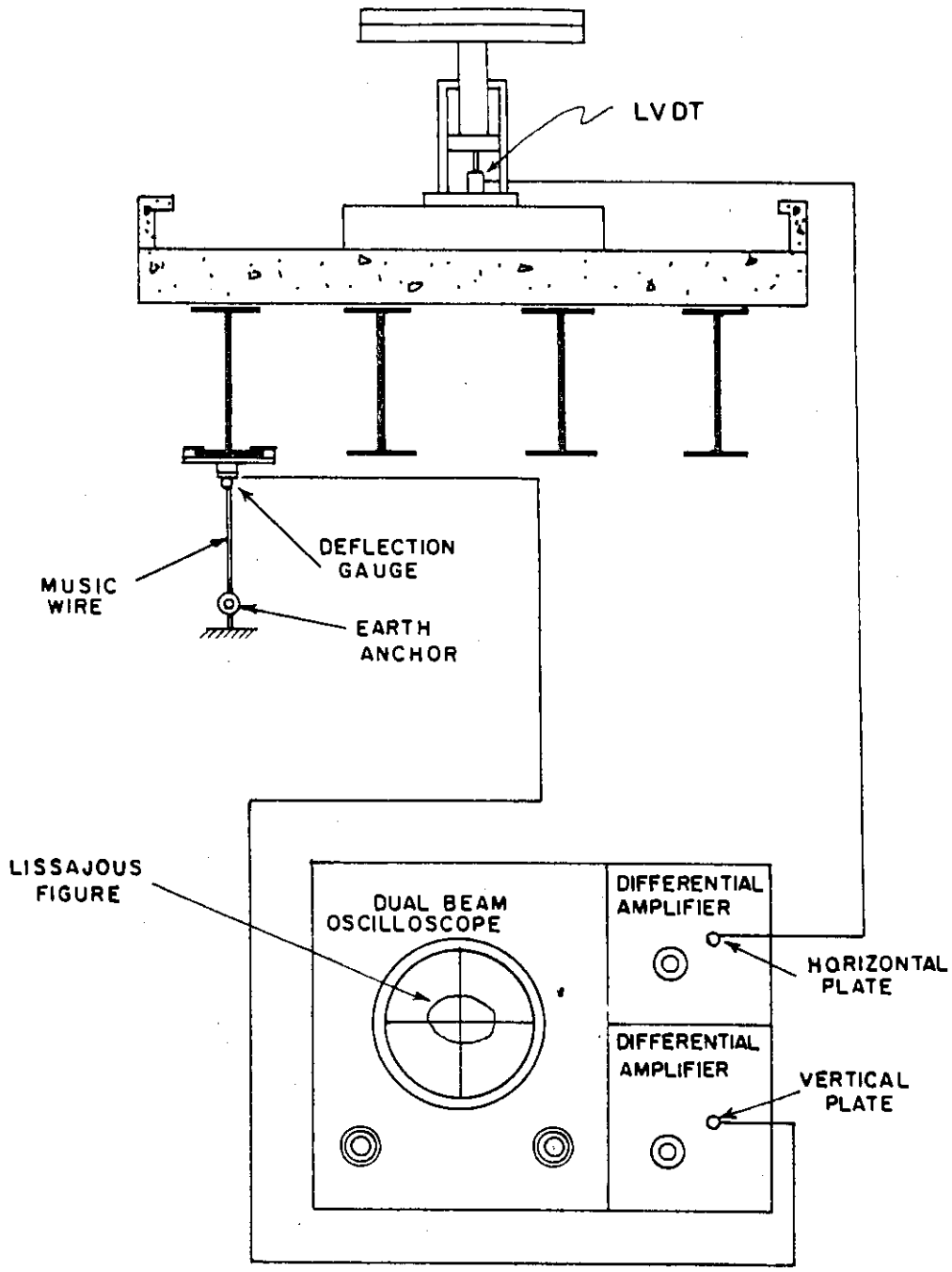

FIGURE D-12. RESONANCE MONITORING SYSTEM

APPENDIX E

ACOUSTIC EMISSION

E.1 INTRODUCTION

Acoustic emission sensors were utilized to monitor the growth of fatigue cracks in the bridge girders during the fatigue test. The intent in this study was to use off-the-shelf acoustic emission equipment which was readily available. Acoustic emission techniques have been successfully applied in testing pressure vessels, wire rope and gas pipelines[E1]. Work has been done at Battelle-Northwest to determine the applicability of acoustic emission techniques to assess the structural integrity of bridges[E1].

The concept of using acoustic emission to detect structural degradation in a bridge is promising. When a structure is under load, elastic stress waves called acoustic emissions are generated by plastic deformations which occur at imperfections in the material. These emissions can be detected by a piezoelectric sensor. The analog signals from the sensor are amplified and recorded in a form convenient for further analysis. In a bridge structure, one place these deformations can occur is at flaws in the weldments.

However, there are inherent problems in monitoring low level stress waves associated with the micro fracture events induced by fatigue loading and at the same time eliminating the background noise. Two

procedures used in the test to eliminate extraneous noise were gating and filtering of the analog signal. The filtering was done electronically at the amplifier stage. Also, at the outset of the acoustic emission monitoring, the incoming signal was gated, or inhibited, over a portion of the fatigue cycle.

E.2 EXPERIMENTAL PROCEDURE

The acoustic emission equipment for the test was leased from the Trodyne Corp. A block diagram of the equipment is shown in Fig. E-1. Eight sensors were used to monitor the acoustic emissions in the critical fatigue regions in the end spans of the bridge. Each sensor was clamped to the bottom flange of a steel girder within six in. of the end of a cover plate. Sensors 1, 2, 3 and 4 were in the west end span and sensors 5, 6, 7 and 8 were located in the east end span. Figure 4-2 in Art. 4.4 shows the locations of the eight sensors. In operation, the sensors were individually monitored by manually switching the gang signal adaptor. Fourteen sets of data were recorded during the course of the fatigue test. For each sensor an amplitude count of acoustic emission per second was made over a time interval of 150 seconds. The amplitude counts vs. time were recorded on an xy plotter. During the fatigue test the frequency of the ballasted bridge changed from 2.32 Hz at the outset of the fatigue test to 1.93 Hz at the conclusion of the fatigue test. In the time interval of 150 seconds during which acoustic emissions from each sensor were recorded, the bridge underwent

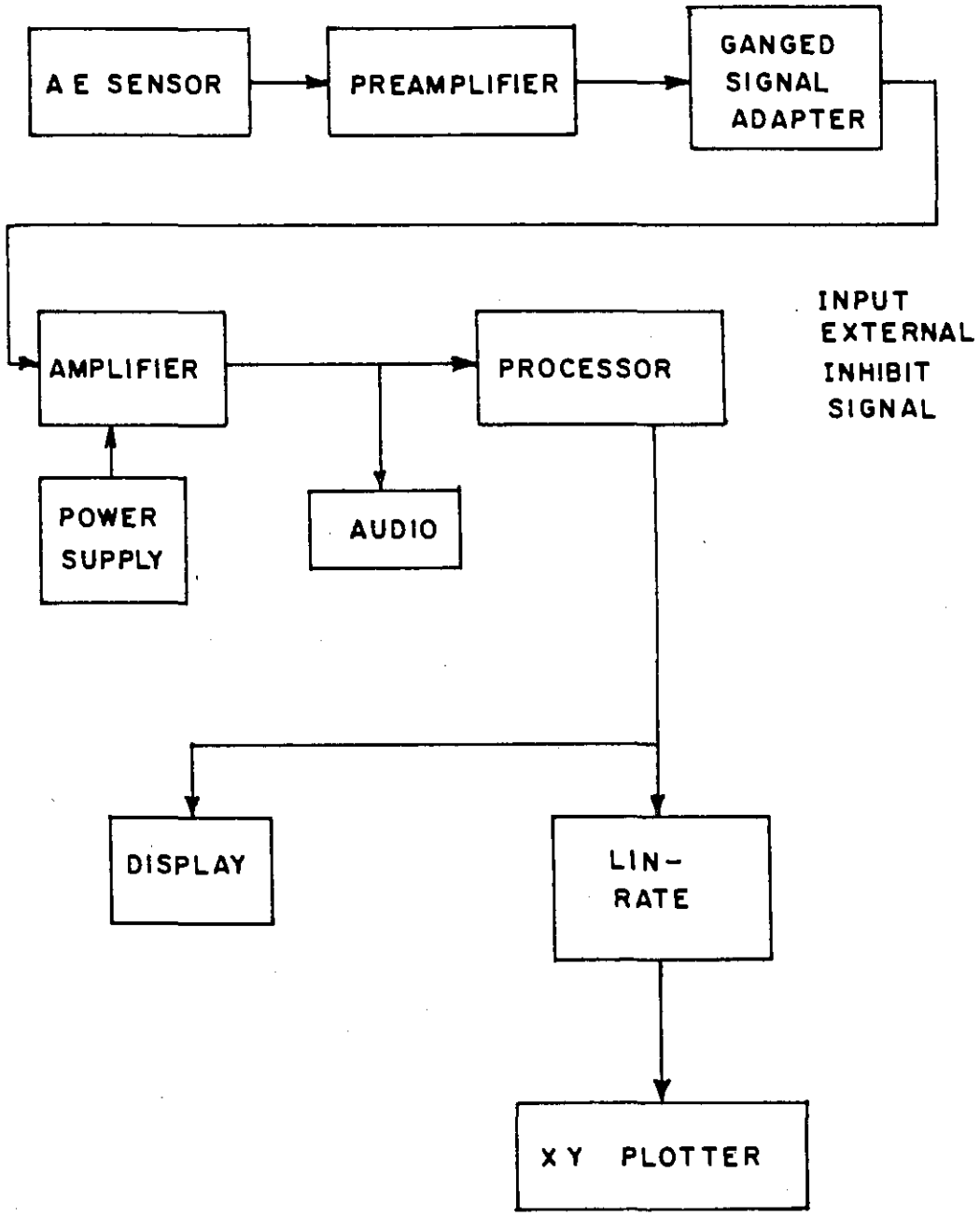

FIGURE E-1. BLOCK DIAGRAM OF ACOUSTIC EMISSION SETUP

approximately 300 cycles of vibration. The analog acoustic emission signals were amplified with gains ranging from 72 to 82 db to accommodate the ordinate values on the xy plotter. The filter was set to band pass frequencies in the 100 KHz to 400 KHz range. The resonant frequency of a sensor was 230 KHz.

In addition to being amplified and filtered, the analog signal was converted to an amplitude count which is analogous to a count of the oscillations in the sensor. The sensor converts low-level stress waves to transient electrical signals corresponding to the resonant oscillations of the piezoelectric element in the sensor. The amplitude count is based on a measured time interval which is proportional to the peak amplitude of the oscillations of the piezoelectric sensor.

Acoustic emission monitoring was initiated when the bridge had already accumulated 56,000 fatigue cycles. Prior to recording acoustic emission data, the signal was displayed on an oscilloscope. This revealed that during a portion of the bridge vibration cycle the acoustic emission signal appeared to contain a repetitive noise. The noise was thought to be due to the cyclic loading equipment. The repetitive signal was evident when the center span of the bridge was in its most upward position. Consequently the acoustic emission count was inhibited over that part of the vibration cycle. A deflection gauge at midspan in the bridge was used to sense the portion of the cycle over which the acoustic emission count was gated or inhibited.

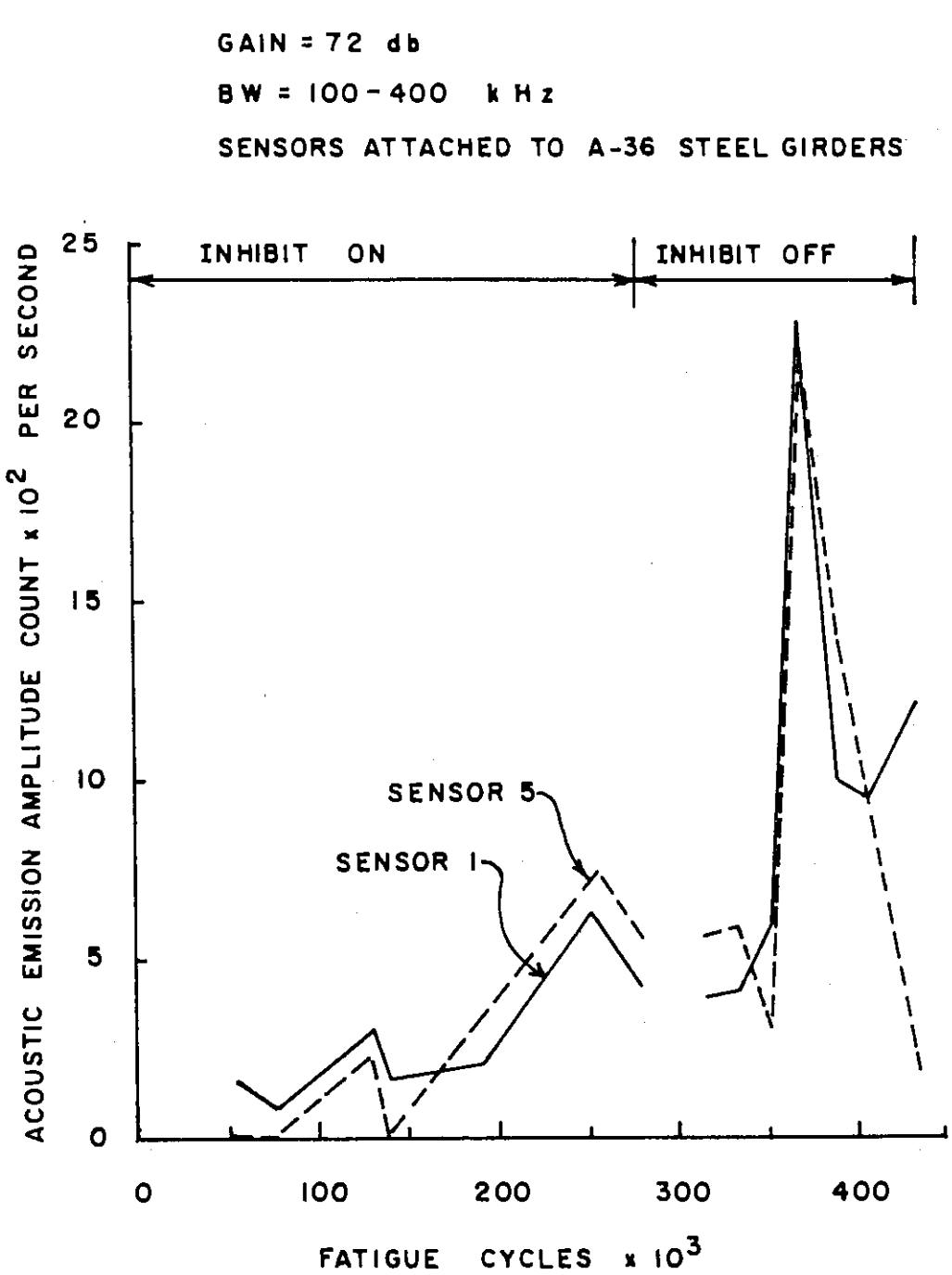

FIGURE E-2a. ACOUSTIC EMISSION AMPLITUDE COUNT DURING FATIGUE TEST

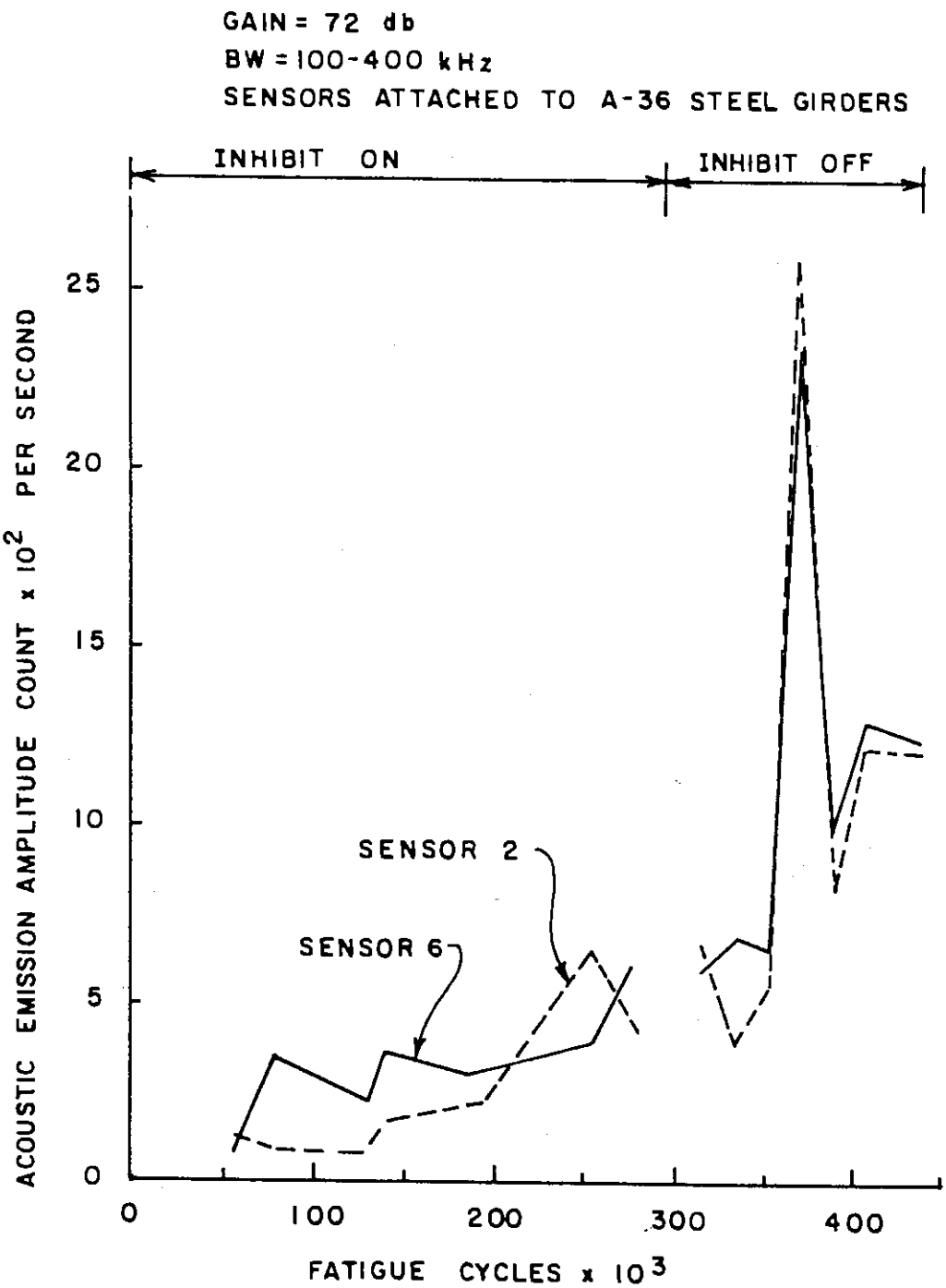

FIGURE E-2b. ACOUSTIC EMISSION AMPLITUDE COUNT DURING FATIGUE TEST

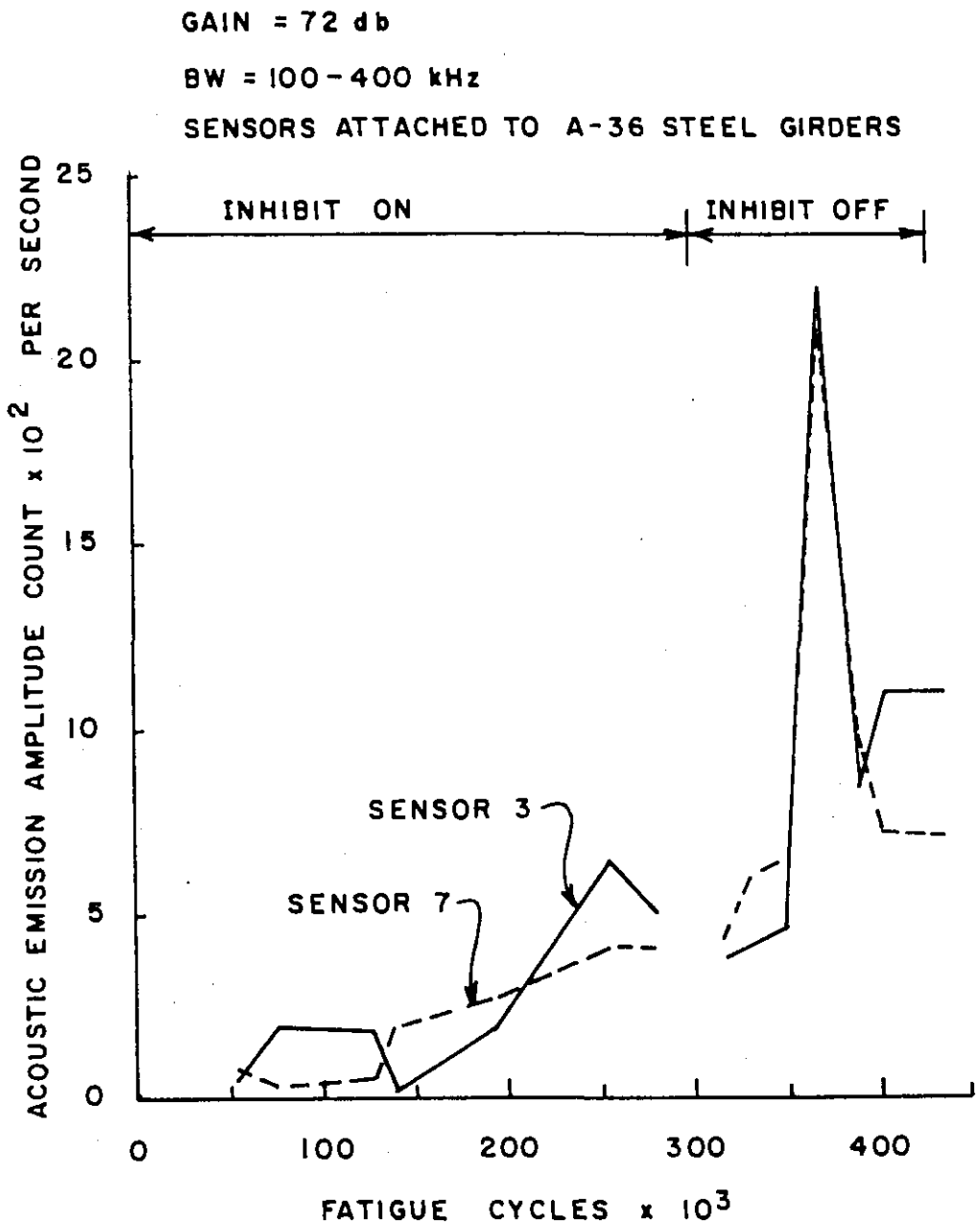

FIGURE E-2c. ACOUSTIC EMISSION AMPLITUDE COUNT DURING FATIGUE TEST

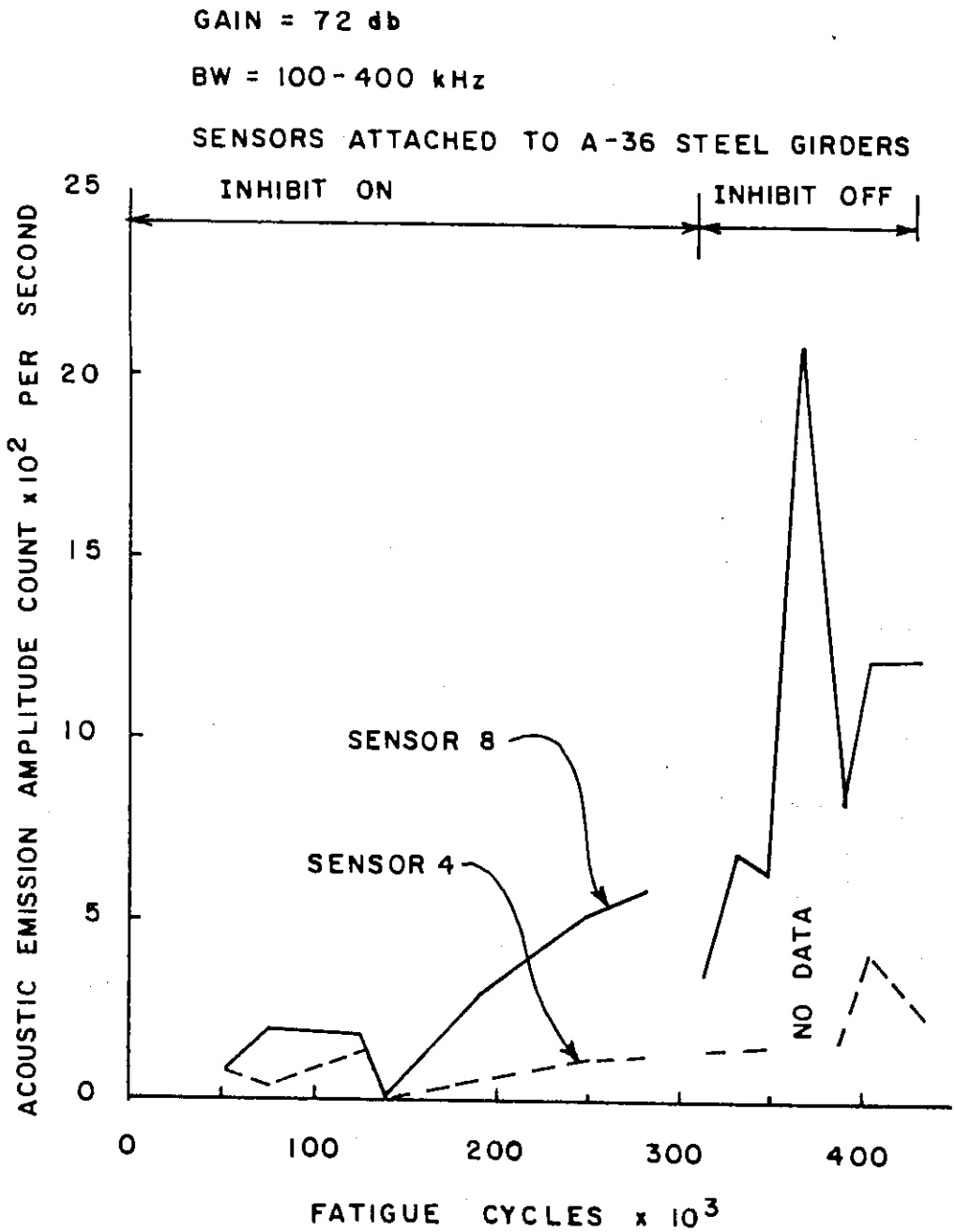

FIGURE E-2d. ACOUSTIC EMISSION AMPLITUDE COUNT DURING FATIGUE TEST

At 315,000 fatigue cycles the acoustic emission signals were found to be completely blocked out over the entire cycle. As a consequence, the inhibit circuitry was disconnected from the set up. Amplitude counts at 315,000 fatigue cycles and thereafter were made over the entire vibration cycle.

E.3 RESULTS

The xy graphs of amplitude count vs. time did not display the data in a form convenient for evaluating probable crack growth in the welds and base metal where the cover plates terminated. Hence the amplitude counts for each sensor were digitized and a mean value and standard deviation were calculated. The mean values for each of the 14 data sets for the eight sensors are shown in Figs. E-2a, E-2b, E-2c and E-2d. A comparison was made between the variations in amplitude count at a particular location and the crack growth as determined from the log of the ultrasonic inspections. There does not appear to be any positive correlation between the acoustic emission count and the crack growth based on ultrasonic measurements.

However, Figs. E-2a through E-2d show that the amplitude count from all sensors was at its maximum value at 370,000 cycles. This is attributed to the fracture that was occurring at midspan in the south exterior girder. The peak values for sensors 2 and 6 are slightly higher than those for the other sensors. Sensors 2 and 6 were located on the south interior girder approximately 60 ft. from the location of the impending fracture.

E.4 DISCUSSION OF RESULTS

The growth of fatigue cracks in the critical fatigue regions under cyclic loading was not discernible with the acoustic emission setup used in the bridge test. There are several factors which may have contributed to the lack of correlation between measured crack growth and acoustic emission count. The rate of crack growth was relatively slow. Consequently, the corresponding emission signal is known to be low and may even disappear. Extraneous noise from the hydraulic actuator and the movement of the bridge on its rockers and hinges at the supports tend to hinder the detectability of the acoustic emission signal. The repetitive noise observed in the signal at the outset of the acoustic emission measurements may have been due to the cracking of the concrete deck and curb. Concrete undergoing permanent deformation is reported to have emission signals that are higher than those from most metals.

All eight sensors were able to detect the critical crack growth at midspan in the bridge. The high level of signal recorded at the sensors located on other girders indicates that the stress waves radiating from that fracture were not significantly attenuated.

The use of acoustic emission sensors to monitor fatigue crack growth in bridges has some potential. One of the shortcomings observed from the results of the setup used in this study could be overcome by using triangulation procedures to determine the location of the cracks within a structure. Instrumentation to discriminate between

extraneous noise and the desired acoustic emission signal is sorely needed. A further refinement which would provide a means of distinguishing between acoustic emission signals from concrete and steel would also prove useful.

REFERENCES

E1. Liptai, R. G. and Harris, D. O., "Acoustic Emission - An Introductory Review," Materials Research and Standards, MTRSA, Vol. II, No. 3, p. 8.

APPENDIX F

COMPOSITE COMPUTATION

F.1 INTRODUCTION

Strain gauges on the top and bottom flanges of the steel girders at seven sections across the bridge were scanned and recorded regularly during the fatigue loading. These readings were made with the aid of a peak detector so that only the maximum and minimum strain values during a load cycle were recorded. By assuming that the top and bottom gauges on a given beam both reached extreme values at the same instant and properly matching maximum and minimum values, it was possible to find simultaneous strain readings in the top and bottom flanges at the instant of maximum positive bending and the instant maximum negative bending. From these measured strains, it was possible to calculate maximum and minimum fiber stresses in each flange of each girder. It was also possible to determine a great deal about the degree of composite action at each of these sections.

F.2 ANALYSIS

The composite analysis is based on the following assumptions:

1. The behavior of the girders under test loading was essentially elastic.
2. Plane sections in the steel beam remain plane after bending.

3. Plane sections in the slab and curb (if present) remain plane after bending.
4. An unknown amount of slip occurs at the interface between the slab and steel girder thereby producing a discontinuity in the strain distribution across the composite section.
5. The slab and girder remain in contact at all points thereby producing essentially the same curvature in the steel beam and the slab.

From elementary strength of materials it can be shown that the curvature of a homogeneous prismatic beam at any section is equal to the strain gradient and referring to Figure F-1, it is clear then that:

$$SG = \frac{SR_1 - SR_2}{d_b - 2t_f} \qquad (F.1)$$

where SR_1 and SR_2 are the strain readings from gauges 1 and 2, respectively, d_b is the depth of the steel beam, and t_f is the thickness of the beam flange.

Definition of terms:

A_b = Cross sectional area of steel beam

C = Axial force in slab and curb (if curb is present)

d_b = Depth of steel beam

d_c = Distance from centroid of steel beam to centroid of slab and curb (if curb is present)

E_s Modulus of elasticity for steel and transformed section, 29×10^6 psi

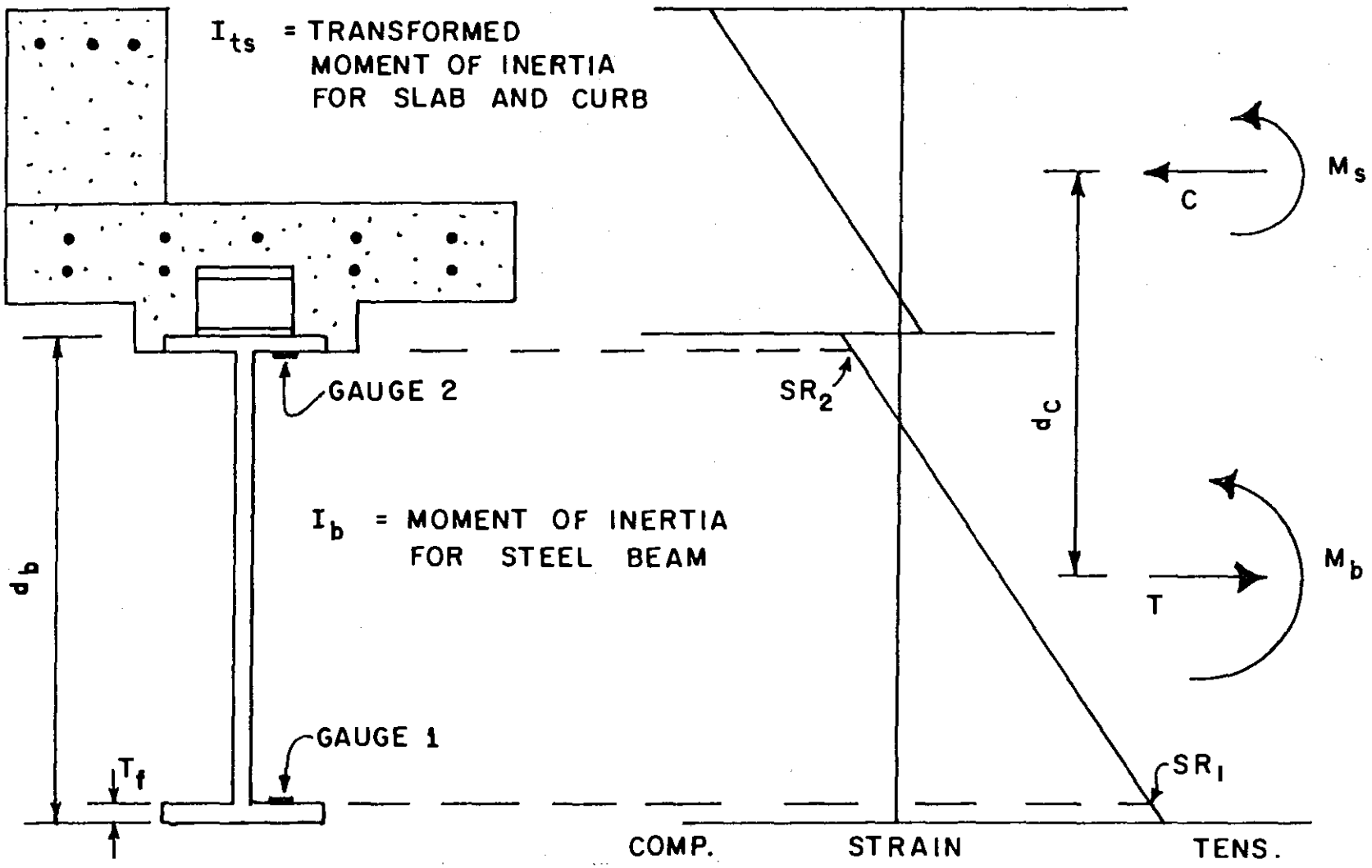

FIGURE F-1. MOMENT COMPONENTS

I_b = Moment of inertia of steel beam

I_{eff} = Effective moment of inertia for composite section during test.

I_{ts} = Transformed moment of inertia for slab and curb

M_b = Moment necessary to produce measured curvature in steel beam

M_s = Moment necessary to produce measured curvature in slab and curb (if curb is present)

M_t = Total moment in composite beam

SG = Strain gradient or curvature

SR_1 = Strain reading from gauge 1

SR_2 = Strain reading from gauge 2

T = Axial force in steel beam

t_f = Flange thickness.

Extreme fiber strains in the top and bottom flanges were calculated by extrapolating the strain gradient line to the surfaces of the flanges and the extreme fiber stresses are given by:

$$\text{Bottom flange Extreme fiber stress} = (SR_1 + SG\ t_f)\ E_s \qquad (F.2)$$

$$\text{Top flange Extreme fiber stress} = (SR_2 - SG\ t_f)\ E_s \qquad (F.3)$$

where E_s is the modulus of elasticity for steel. Since the steel section has a horizontal axis of symmetry and the two strain gauges are placed symmetrically about this axis, the axial force in the steel beam is given by:

$$T = \left(\frac{SR_1 + SR_2}{2}\right) E_s A_b \qquad (F.4)$$

where A_b is the cross sectional area of the steel beam. In order to satisfy horizontal equilibrium in the beam, C must equal and form a couple with T.

Again from elementary strength of materials for an elastic homogenous beam, the curvature is equal to M over EI, or:

$$\frac{M}{EI} = SG \qquad (F.5)$$

where M and I are the applied moment and moment of inertia respectively. From this it follows directly that:

$$M_b = SG\ E_s\ I_b \qquad (F.6)$$

where I_b is the moment of inertia of the steel beam, and:

$$M_s = SG\ E_s\ I_{ts} \qquad (F.7)$$

where I_{ts} is the transformed moment of inertia for the slab and curb.

If all the slab and curb are in compression or if it is assumed that the concrete can carry tension, calculation of the moment of inertia and centroidal location for the slab and curb is a straightforward process. However, if part or all of the concrete area is in tension, and the concrete is assumed to be incapable of carrying tension, the moment of inertia and location of the centroid become

a function of the axial force C, and their calculation becomes somewhat more laborious. Because there has been some speculation that concrete deck slabs do in fact carry some tension, the program for data analysis was set up so that calculations could be made either on the assumption that concrete carries tension or that concrete carries no tension, by inserting an operating parameter.

The total moment in the section then, is the sum of the moment in the steel beam, moment in the concrete deck, and the couple consisting of axial forces in the steel beam and deck.

$$M_t = M_b + M_s + (T \times d_c) \qquad (F.8)$$

where d_c is the distance between the centroid of the steel beam and the centroid of the deck with or without the curb as the case might be. Finally, it follows from Eq. F.5 that the effective moment of inertia in the bridge under test loading is given by:

$$I_{eff} = \frac{M_t}{E_s \; SG} \qquad (F.9)$$

These calculations were carried out for each girder at each of the seven instrumented sections for more than 100 data scans during the course of the fatigue test. In each case calculations were made for both the positive bending and negative bending halves of the loading cycle. Results were then plotted as a function of load cycles in order to observe changes in the behavior during the test.

Although the computer program was written so that the concrete could be considered to carry tension, or not, it turns out that for practical cases this assumption makes very little difference in the analysis. This is because in Eq. F.8 the M_s term is very small compared to the other two terms. Most of the contribution from tension in concrete appears in the T times d_c term which is automatically accounted for by the strain gauge measurements. Because this difference is so small, results for only one of these assumptions are presented. The assumption of a cracked section for calculating an M_s was used because this gives slightly more conservative results.

F.3 RESULTS

During the first several cycles of loading, the results tended to be somewhat erratic. This may have been partly due to some initial noise problems in the instrumentation. However, there is also strong evidence that the slab was nearly intact at the beginning of the test and there was progressive cracking during the first several thousand cycles. Because of the data sampling sequence significant changes in the cross section during a period of two or three minutes could have produced considerable scatter in the data.

By the end of 80,000 cycles, visual observations indicated that cracking had stabilized and the calculated moments of inertia became much more uniform. Except for the sections that actually fractured, there was very little change in these calculated effective moments of inertia during the remainder of the tests.

Table F-1 shows a comparison of these effective values with various calculated values. Missing entries in the table indicate strain gauges that became inoperative during the test.

It is clear that the curbs on girders 1 and 4 make a very large contribution which is not accounted for in design. There is also a significant degree of composite action even in those regions which contain no shear connectors. This, of course, is due to the fact that continuous reinforcing bars passing through these regions are anchored by the shear connectors in the positive moment regions. The high degree of composite action at the critical sections accounts for the fact that the stress ranges in the top flanges of those sections were subjected to much lower stress ranges than had been calculated. Load amplitude was controlled so as to make the stress ranges in the bottom flanges of these critical sections equal to the desired levels.

TABLE F-1 MOMENTS OF INERTIA

SECTION	GIRDER	CALCULATED Fully Composite	CALCULATED Cracked Slab Composite	CALCULATED Non-Composite	CALCULATED Design	EFFECTIVE VALUES FROM TEST Positive Bending I_{eff}	EFFECTIVE VALUES FROM TEST Positive Bending Percent of Design	EFFECTIVE VALUES FROM TEST Negative Bending	EFFECTIVE VALUES FROM TEST Negative Bending Percent of Design
1. Span 1 Midspan	1	16735	5898	3989	10422	15000	144	10800	104
	2	12863	5299	3989	11828	12900	109	8800	74
	3	12836	5299	3989	11828	12700	107	9700	82
	4	16735	5898	3989	10422	15000	144	10700	103
2. Critical Section Span 1	1	15788	5744	3989	3989	11100	278	6900	173
	2	13095	5671	4461	4461	11000	247	6800	152
	3	13095	5671	4461	4461	11400	256	7000	157
	4	16021	5782	3989	3989	12600	316	6500	163
3. First Pier	1	22922	9919	7429	7429	11100	149	9200	124
	2	20194	10825	8671	8671	13500	156	11900	137
	3	19899	10770	8671	8671	17700	204	12500	144
	4	23238	9974	7429	7429	12700	171	10400	140
4. Center Span Midspan	1	17606	6037	3989	11587	15800	136	8500	73
	2	13706	5431	3989	12226	12800	105	8200	67
	3	13484	5398	3989	12226	12800	105	8000	65
	4	17727	6058	3989	11587	15900	137	9100	79
5. Second Pier	1	22610	9865	7429	7429	11700	157	10000	135
	2	20194	10825	8671	8671	13000	150	10900	126
	3	19899	10770	8671	8671	14400	166	11300	130
	4	23087	9949	7429	7429	13900	187	11300	152
6. Critical Section Span 3	1	15788	5744	3989	3989	12400	311	6600	165
	2	13095	5671	4461	4461	8800	197	6700	150
	3	12767	5625	4461	4461	--	--	--	--
	4	15908	5764	3989	3989	--	--	--	--
7. Span 3 Midspan	1	16620	5878	3989	10422	15500	149	8300	80
	2	12946	5316	3989	11828	12100	102	--	--
	3	12416	5235	3989	11828	--	--	--	--
	4	16143	5802	3989	10422	14800	142	9500	91

APPENDIX G

A FATIGUE ANALYSIS OF FIELD DATA

G.1 INTRODUCTION

Fatigue cracks initiated at the heel of the welds at the joints between the weld and the end of the cover plate. These cracks then propagated around the end of the cover plate until at some point they turned into the fillet weld and subsequently entered the base metal of the bottom flange. The fatigue crack growth which occurred in the base metal during the full-scale fatigue test developed into elliptically shaped flaws. The depth of flaw to width of flaw ratio is shown in Fig. G-1. Figure G-2 shows actual fatigue crack characteristics during the early stages of growth. The flaw shown arrested at approximately 402,000 cycles but is a good example of the type of growth experienced by the bottom critical sections. Also shown is the weld flaw which probably caused the fatigue crack to turn into the weld at this location.

Figures G-2 and G-3 display radial color variations of the fracture surfaces. These variations termed "beach marks" are characteristic of fatigue crack growth and are thought to indicate the points at which the cracks temporarily ceased to grow. The discoloration is primarily due to the different rates of oxidation at the fracture surface as the fatigue crack propagates. However, attempts to correlate

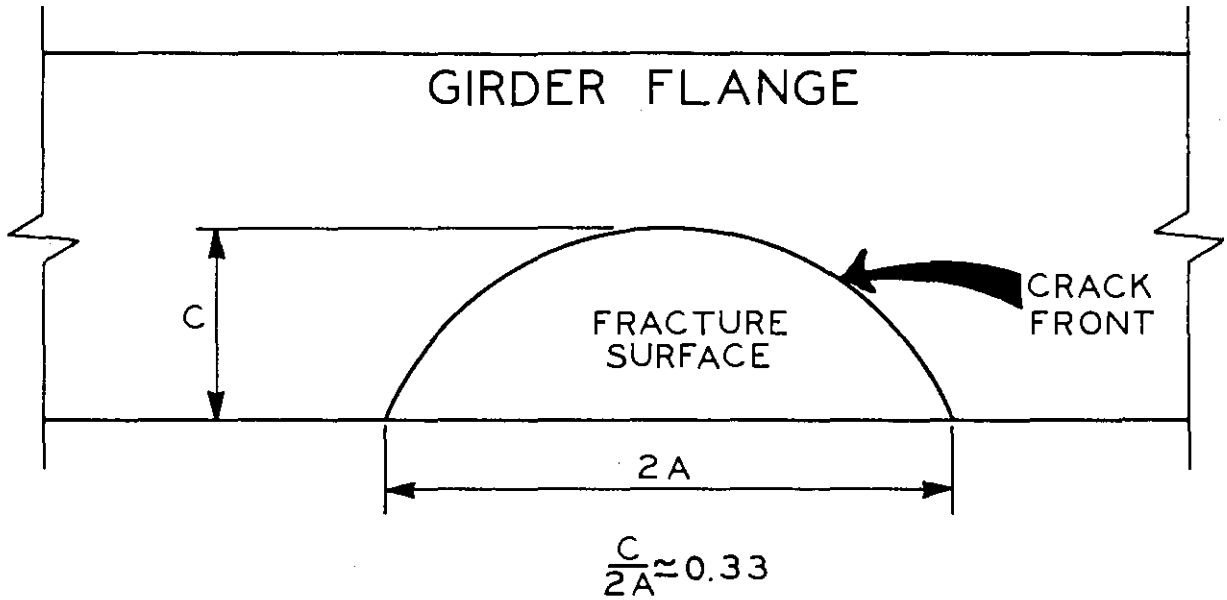

FIGURE G-1. ELLIPTICAL FATIGUE CRACK

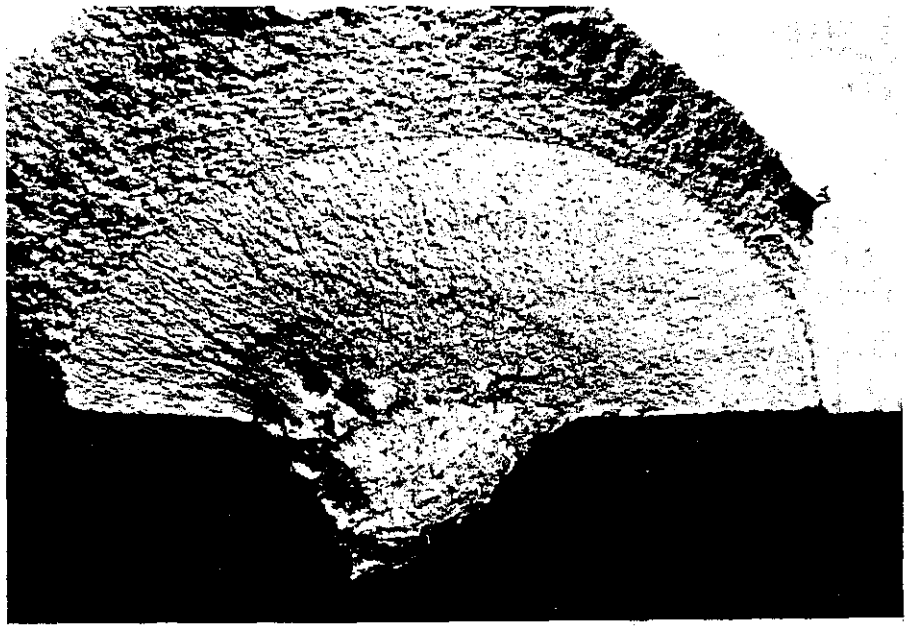

FIGURE G-2. CLOSE UP OF FRACTURE SURFACE
SECTION 2.2B

FIGURE G-3. BEACH MARKS, SECTION 2.2B

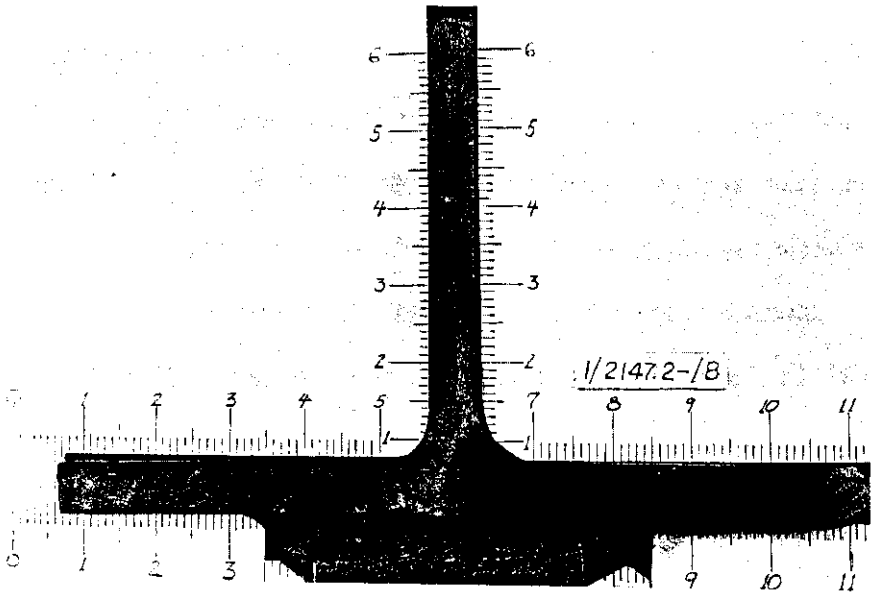

FIGURE G-4. BEACH MARKS, SECTION 6.1B

these beach marks with measured crack lengths and test load history were only partially successful.

Figure G-4 is a photograph of critical section 6.1B. The figure shows various stages of beach marking, but because the section was subjected to such high compressive stresses, burnishing of the surface caused the beach marks to be somewhat obscured.

G.2 APPLIED STRESSES AT CRITICAL SECTIONS

Strains were measured by electrical strain gauges located on the inner flange surfaces, five inches from the ends of the top and bottom cover plates. The recorded data were comprised of peak values of maximum and minimum strains with tensile strains indicated as positive values and compressive strains indicated as negative values. In the following discussion the word maximum implies, algebraically maximum values.

The resulting data were extrapolated to determine the strains at the outer flange surfaces and superimposed on the measured ballast dead load and the computed bridge dead load[G1]. Figures G-5 through G-9 show representative plots of maximum, mean and minimum stresses, plus appropriate ultrasonic inspection intervals and maximum base metal fatigue crack sizes for the critical sections.

G.2.1 Loading at Critical Sections

The top critical sections were subjected to a tension to tension fatigue loading (Table G-1). The average maximum stresses ranged

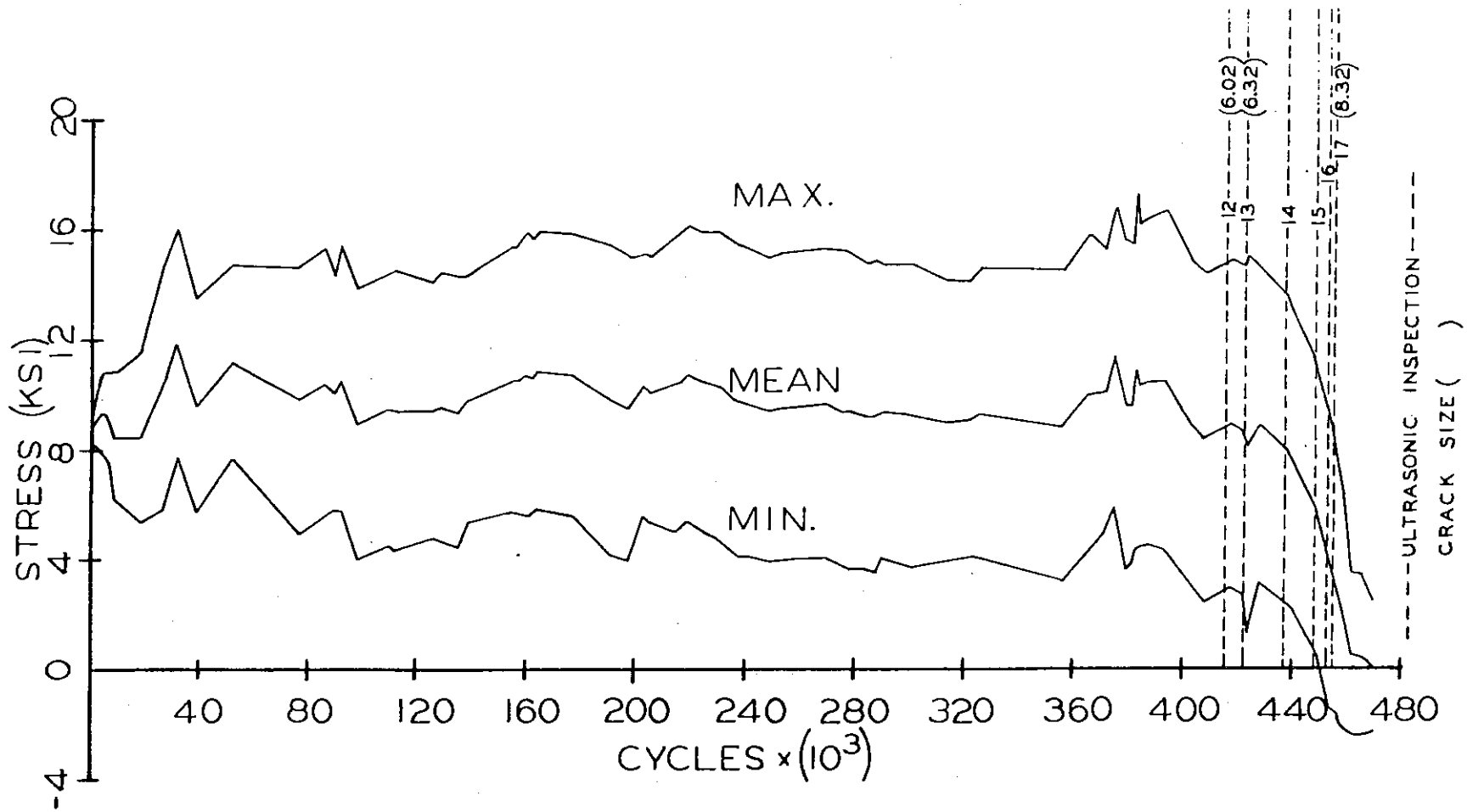

FIGURE G-5. FATIGUE STRESS AT SECTION 2.1A

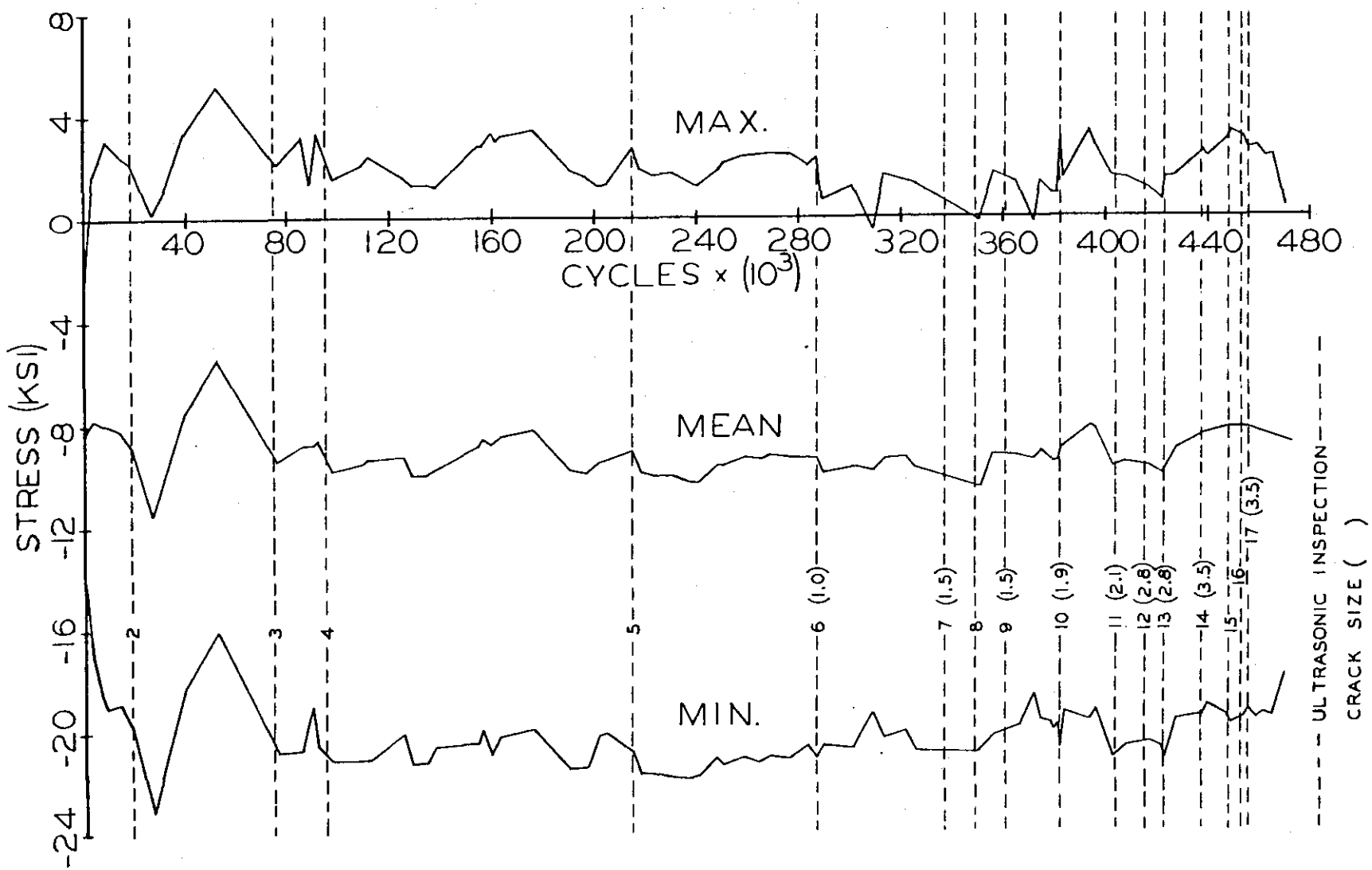

FIGURE G-6. FATIGUE STRESS AT SECTION 2.2B

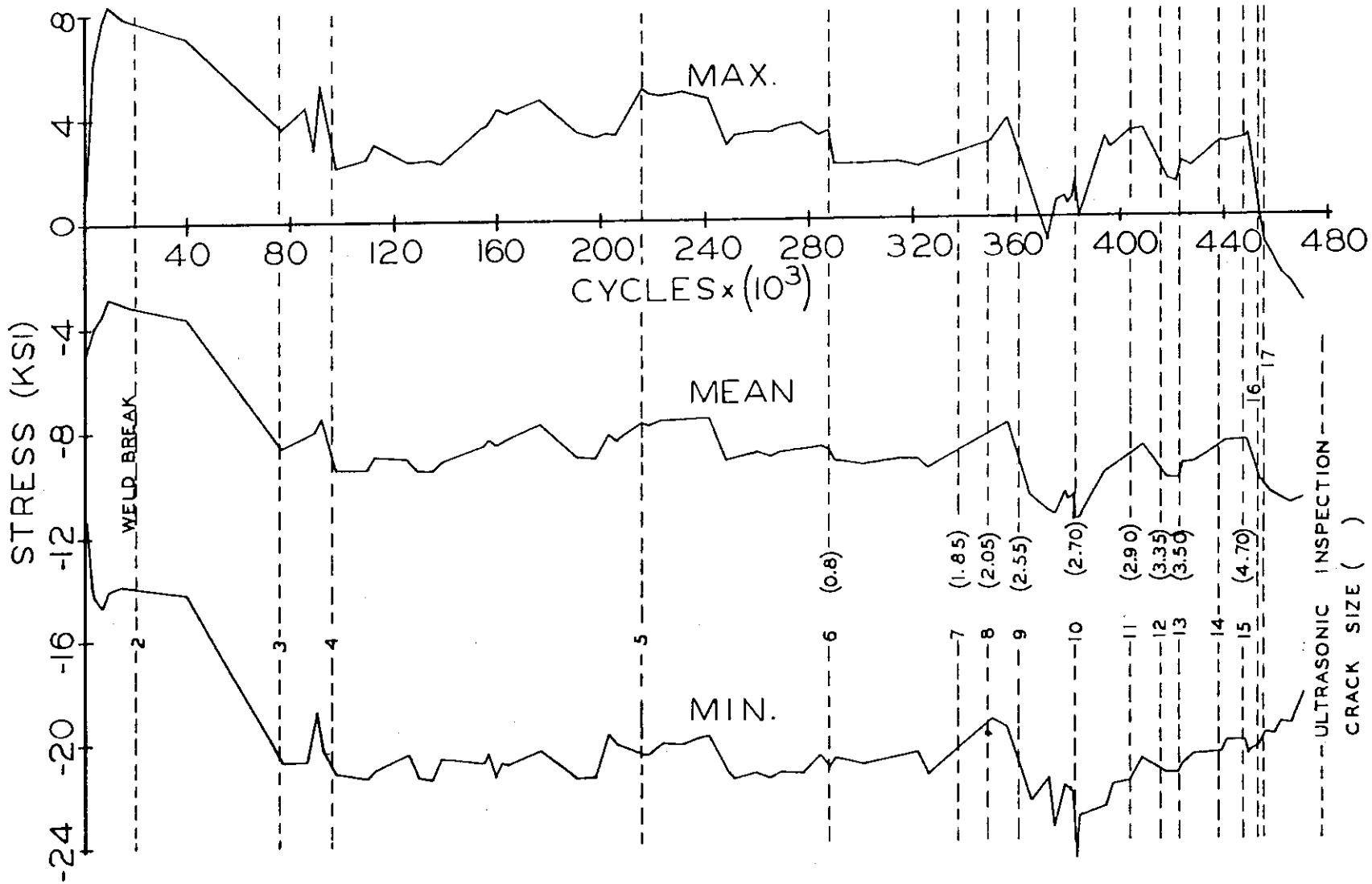

FIGURE G-7. FATIGUE STRESS AT SECTION 6.1B

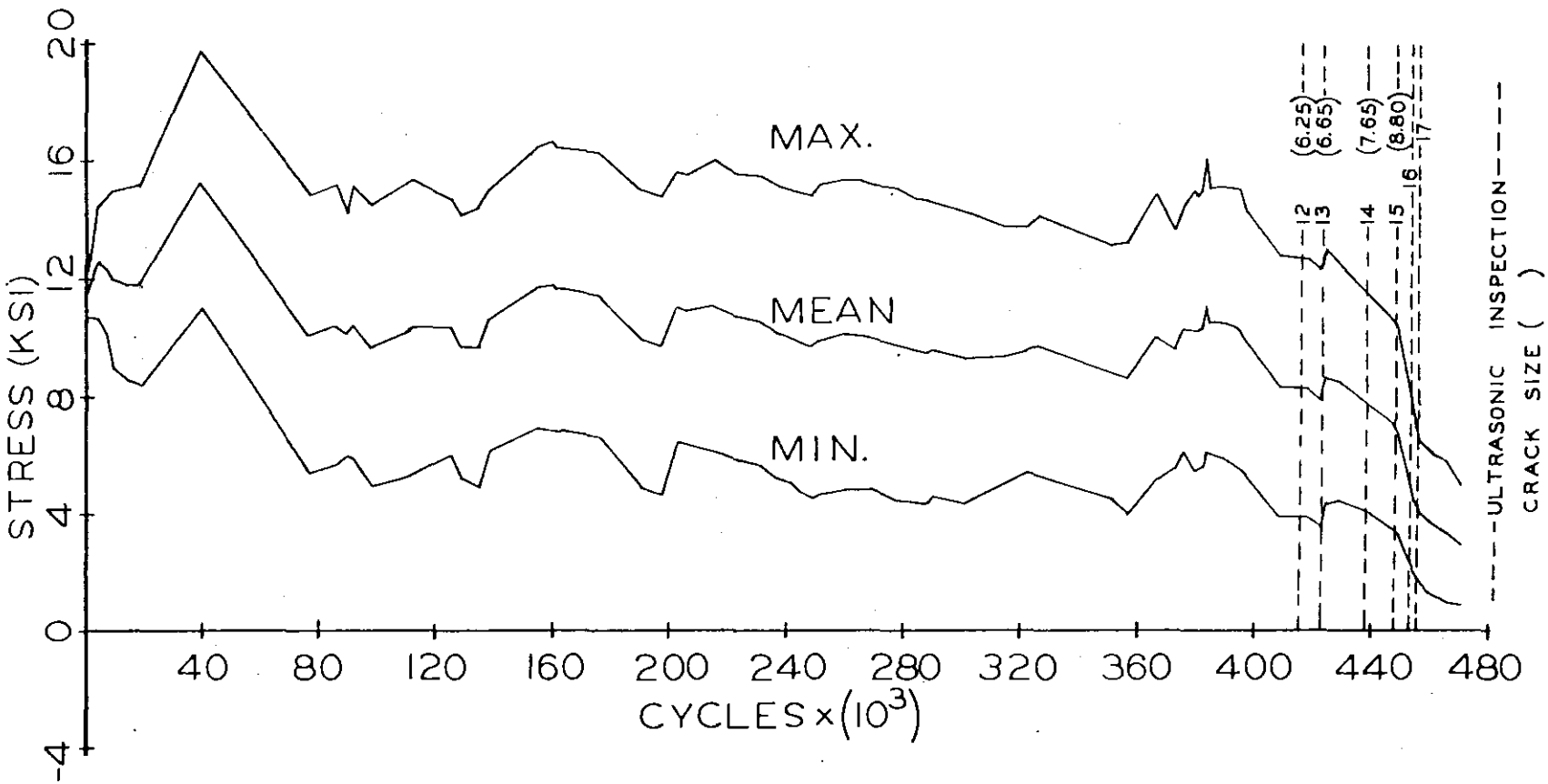

FIGURE G-8. FATIGUE STRESS AT SECTION 6.2A

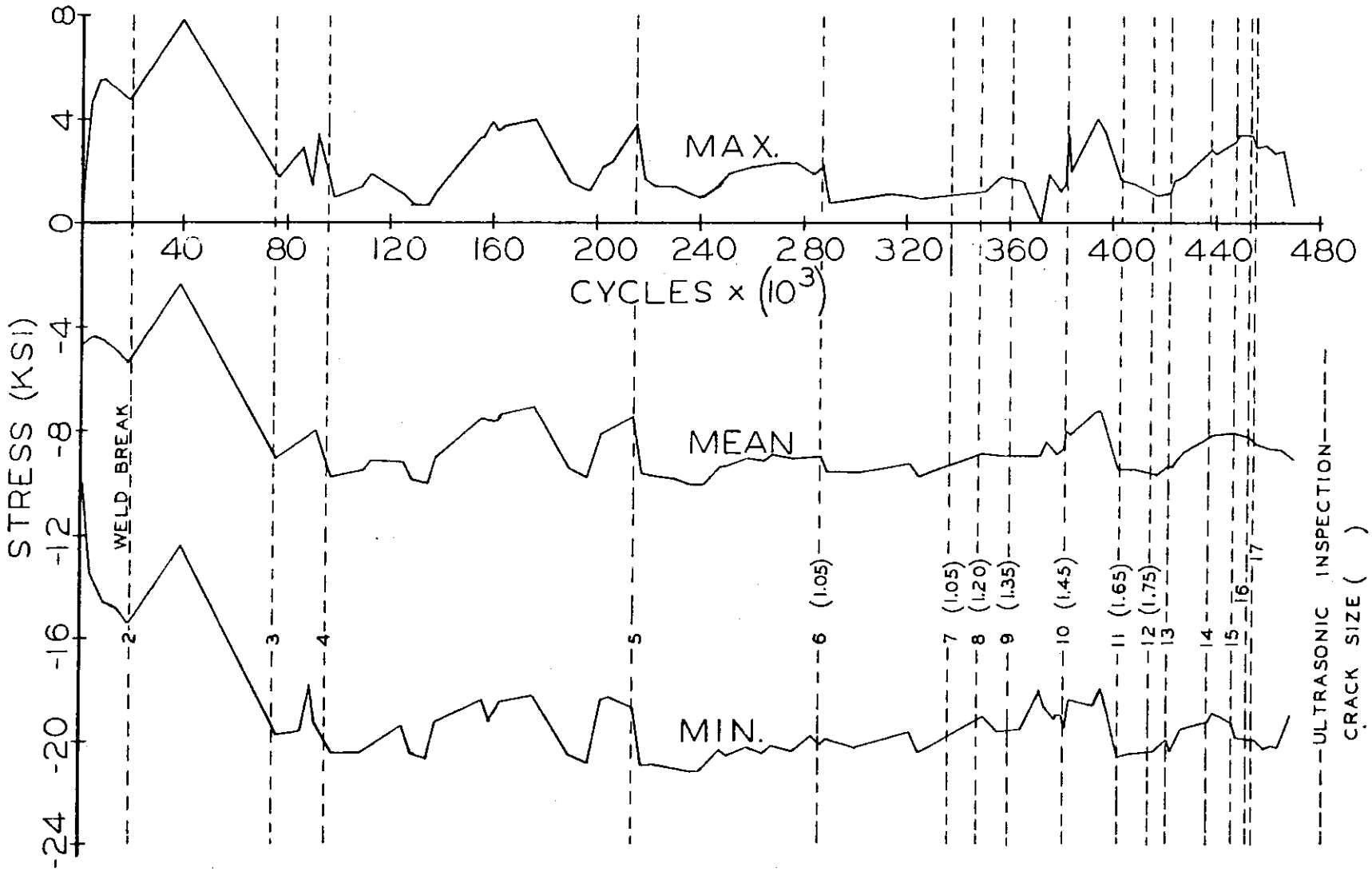

FIGURE G-9. FATIGUE STRESS AT SECTION 6.2B

SECTION NUMBER / STRESS	*2.1 A	2.2 A	2.3 A	2.4 A	6.1 A	*6.2 A
MAX (KSI)	14.57	15.18	14.57	13.64	15.33	14.74
MIN (KSI)	5.11	5.92	6.41	6.35	6.07	6.17
MEAN (KSI)	9.84	10.55	10.49	10.00	10.70	10.46
RANGE (KSI)	9.46	9.26	8.16	7.29	9.26	8.57

*SECTION FAILED

TABLE G-1. AVERAGE FATIGUE STRESS OVER TEST RANGE FOR TOP CRITICAL SECTIONS

STRESS \ SECTION NUMBER	2.1 B	2.2 B	2.3 B	2.4 B	*6.1 B	6.2 B	6.3 B	6.4 B
MAX (KSI)	3.55	2.07	1.58	1.63	3.38	2.64	1.85	1.83
MIN (KSI)	-21.70	-20.40	-19.52	-18.76	-19.98	-18.92	-18.15	-18.06
MEAN (KSI)	-9.08	-9.17	-8.97	-8.57	-8.30	-8.14	-8.15	-8.12
RANGE (KSI)	25.25	22.47	21.10	20.39	23.36	21.56	20.00	19.89

*SECTION FAILED

TABLE G-2. AVERAGE FATIGUE STRESS OVER TEST RANGE FOR BOTTOM CRITICAL SECTIONS

from 13.64 ksi to 15.33 ksi, while the average minimum stresses ranged from 5.11 ksi to 6.41 ksi. The bottom critical sections experienced an alternating fatigue loading (Table G-2). The average algebraically maximum stresses ranged from 1.58 ksi to 3.55 ksi, while the average algebraically minimum stresses ranged from -18.06 ksi to -21.70 ksi.

The stress range for a given section remained relatively constant throughout the fatigue test. Tables G-1 and G-2 demonstrate the variations in fatigue stresses between respective critical sections. The bottom critical sections were subjected to average stress ranges which varied from 19.89 ksi to 25.25 ksi. The top critical sections were subjected to average stress ranges which varied from 7.29 ksi to 9.46 ksi. Thus, stress ranges experienced by the bottom critical sections were 2.6 times those experienced by the top critical sections.

G.2.2 Residual Tensile Stress

It has been shown in prior tests[G2] that fatigue cracks occurred in the compression flanges of girders which had fillet weld connected cover plates, however, these fatigue cracks arrested as soon as they extended beyond the residual tensile stress zones. Cracks at sections 2.1B, 2.3B, 2.4B, 6.3B, and 6.4B also arrested after propagating a short distance from the weld.

Sections 2.2B and 6.2B displayed fatigue cracking which extended beyond the probable residual tensile stress zones. These two bottom critical sections were subjected to average maximum stresses of 2.07 ksi

and 2.64 ksi respectively. However, a combination of the maximum stresses, the residual tensile stresses, and the stress ranges at sections 2.2B and 6.2B was not sufficient to cause complete fatigue failure.

Section 6.1B, which did fail completely in fatigue, was subjected to a larger average maximum stress (3.38 ksi) than were sections 2.2B and 6.2B. In this case the increase in average maximum stress coupled with the residual tensile stress and the stress range was sufficient to cause complete fatigue failure of section 6.1B.

One bottom critical section did not follow this trend. Section 2.1B was subjected to the largest maximum stress (3.55 ksi) and the largest stress range (25.25 ksi), yet little fatigue cracking of the base metal took place at this section.

G.3 CORRELATION OF TEST RESULTS WITH PRIOR STUDIES

Recent developments in the field of fatigue[G2,G3] have indicated that stress range is the dominant stress variable when dealing with fatigue crack growth. Data from sections 6.1B, 6.2B and 2.1A were placed on a plot, Fig. G-10, developed from Fisher's equations for similar critical sections. This figure implies that with an average stress range of 23.36 ksi, section 6.1B should have failed at approximately 115,000 cycles. Figure 4-10 also implies that with average stress ranges of 9.46 ksi and 9.26 ksi, sections 2.1A and 6.2A should not have failed until 1,970,000 fatigue cycles and 1,830,000 fatigue cycles, respectively.

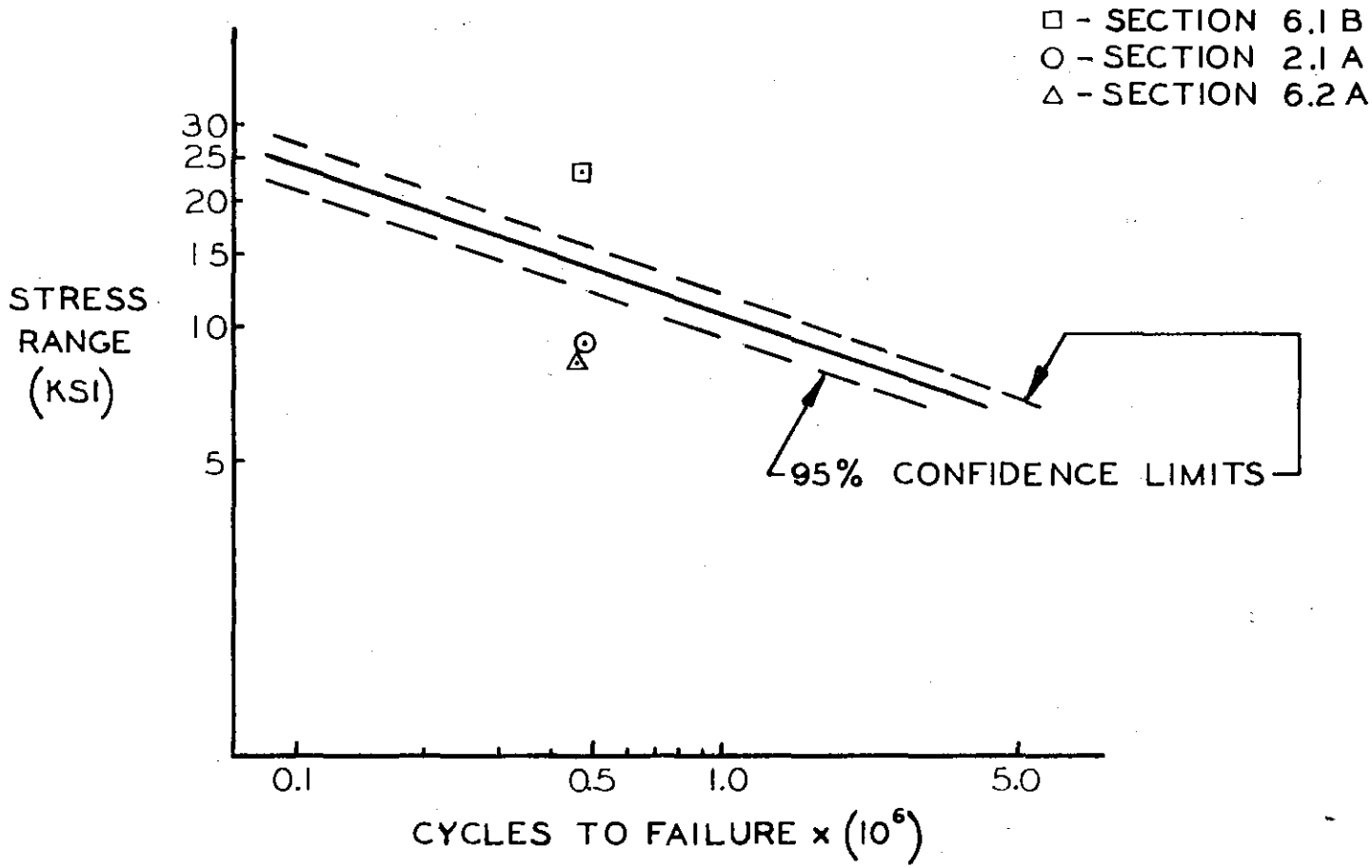

FIGURE G-10. FATIGUE STRENGTH OF END WELDED COVER PLATES

Fisher's experiments included minimum stresses from -6 ksi to 10 ksi, maximum stresses from 10 ksi to 30 ksi, and stress ranges from 8 ksi to 24 ksi. Table G-2 shows that section 6.1B did not experience maximum or minimum fatigue stresses within Fisher's experimental limits. The extended fatigue life of section 6.1B indicates that the small maximum stress experienced by each bottom critical section was a significant variable. Had greater maximum stress been developed in the remaining bottom critical sections, data indicate the possibility of additional complete fatigue failures.

Table G-1 shows that sections 2.1A and 6.2A experienced fatigue stresses within Fisher's experimental limits. The brief fatigue lives of section 2.1A and 6.2A can be partially attributed to the detail which existed at the ends of the top cover plates. Figure G-11 shows the toe-to-toe placement of the fillet welds which were used to connect the cover plates and the shear connectors to the top flanges. The sharp notch created by the fillet welds caused severe stress concentrations in the tension flanges. There is also some speculation that girder size may have played a role in the fatigue cracking of the top critical sections. The girders of the Butler-County bridge were much larger than those tested by Fisher.

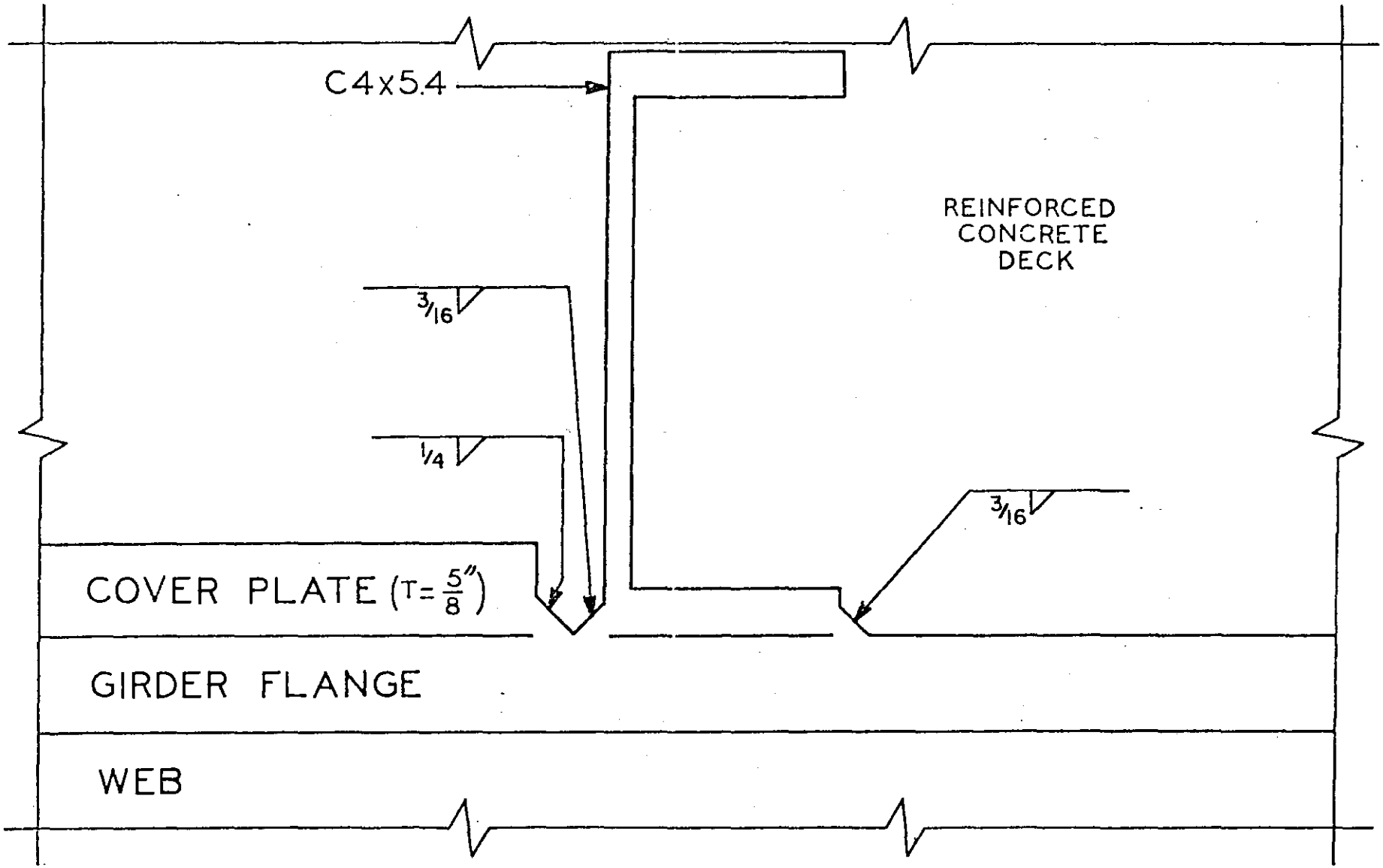

FIGURE G-11. TOP CRITICAL SECTION DETAIL

REFERENCES

G1. Salane, H. J., Duffield, R.C., McBean, R. P., Baldwin, J. W., and Galambos, T. V., "An Investigation of the Behavior of a Three-Span Composite Highway Bridge," Report 71-5, Missouri Cooperative Highway Research Program, Nov. 1971.

G2. Fisher, John W., et al., Report 102, "Effect of Weldments on the Fatigue Strength of Steel Beams," Highway Research Board, Washington, D.C., 1970.

G3. Fisher, John W., et al., Report 147, "Fatigue Strength of Steel Beams with Welded Stiffners and Attachments," Highway Research Council, Washington, D.C., 1974.